HAL
open science

Control and stabilization of morphologies in reactively compatibilized Polyamide 6 / High Density Polyethylene blends

Alexandra Fabre Argoud

▶ **To cite this version:**

Alexandra Fabre Argoud. Control and stabilization of morphologies in reactively compatibilized Polyamide 6 / High Density Polyethylene blends. Food and Nutrition. Université Claude Bernard - Lyon I, 2011. English. NNT : 2011LYO10242 . tel-00835910

HAL Id: tel-00835910
https://theses.hal.science/tel-00835910

Submitted on 20 Jun 2013

N° d'ordre : 242 - 2011

Année 2011

THESE DE L'UNIVERSITE DE LYON

Délivrée par

L'UNIVERSITE CLAUDE BERNARD LYON 1

ECOLE DOCTORALE MATERIAUX

DIPLOME DE DOCTORAT

(arrêté du 7 août 2006)

soutenue publiquement le 2 décembre 2011

par

Mme FABRE-ARGOUD Alexandra

CONTROL AND STABILIZATION OF MORPHOLOGIES IN REACTIVELY COMPATIBILIZED POLYAMIDE 6/HIGH DENSITY POLYETHYLENE BLENDS

Directeur de thèse : M. Paul SOTTA

JURY : M. René Fulchiron
        M. Yves Grohens (rapporteur)
        M. Guo-Hua Hu
        Mme Paula Moldenaers (rapporteur)
        M. Paul Sotta (directeur de thèse)
        Mme Lise Trouillet-Fonti (correspondant industriel)

Contrôle et stabilisation de morphologies de mélanges Polyamide 6 / Polyéthylène Haute Densité compatibilisés par voie réactive

Cette étude s'intéresse aux mélanges Polyamide 6 / Polyéthylène Haute Densité compatibilisés par voie réactive, plus particulièrement aux relations entre (1) la formulation, les paramètres de mise en œuvre en extrusion bivis corotative et (2) la morphologie et la microstructure des mélanges.

Des morphologies multi-échelles ont été observées en Microscopie Electronique à Balayage et en Transmission. A l'échelle micrométrique, les morphologies suivantes ont été développées : dispersion nodulaire, nodules étirés et co-continuité. Les paramètres procédés n'influençant pas le type morphologie, les régions correspondant aux types de morphologies ont pu être rassemblées sur des diagrammes ternaires. Dans le cas des mélanges compatibilisés, deux mécanismes de formation de ces morphologies sont proposés : (1) la réaction de compatibilisation très rapide et efficace entraîne la formation de nano-dispersions par instabilités d'interface et (2) le mécanisme classique de rupture/coalescence de domaines moins riches en copolymère permet de former des morphologies jusqu'à l'échelle micrométrique.
L'évolution de la taille maximale des domaines en fonction de la composition ainsi que la distribution de tailles ont été modélisés par des mécanismes de percolation.

La stabilité des morphologies en statique, sous cisaillement contrôlé et au cours d'une deuxième étape de mise en forme a ensuite été étudiée. Le copolymère formé à l'interface permet de stabiliser la taille des morphologies.

Enfin, une cristallisation à plus basse température a été mise en évidence en Calorimétrie Différentielle à Balayage lorsque les polymères sont confinés dans des domaines submicroniques.

Mots clés : *Polyamide – Polyéthylène – Mélange de polymères – Compatibilisation réactive – Extrusion – morphologie - Cristallisation*

Control and stabilization of morphologies in reactively compatibilized Polyamide 6 / High Density Polyethylene blends

This study deals with reactively compatibilized Polyamide 6 / High Density Polyethylene blends. More precisely, it focuses on the relationship between (1) the formulation, the processing parameters in corotating twin screw extrusion and (2) the morphologies and the microstructures of blends.

Multi-scale morphologies were observed by Scanning and Transmission Electron Microscopy. At the micron scale, the following morphologies were developed: nodular dispersions, stretched nodules and co-continuous morphology. As the processing conditions did not influence the types of morphology, the different morphological regions were reported in ternary diagrams. In the case of compatibilized blends, two mechanisms for morphology development have been proposed: (1) the compatibilization reaction, being very fast, leads to the formation of nano-dispersions by interfacial instabilities and (2) the standard break-up/coalescence mechanism of domains poor in copolymer could lead to the formation of morphologies up to the micron scale.
Both the evolution of the largest size as a function of the composition and the distribution of sizes were modeled using percolation concepts.

The stability of the morphologies was then studied either during static annealing or controlled shear or in a second step processing. The copolymer formed at the interface allows stabilizing the size of the morphologies.

Finally, crystallization at lower temperature was observed by Differential Scanning Calorimetry when the polymers are confined in submicron domains.

Remerciements

Cette thèse a été réalisée au sein du Laboratoire des Polymères et Matériaux Avancés (LPMA), Unité Mixte de Recherche CNRS/RHODIA (UMR 5268), dirigée par M. Ludovic Odoni et M. Didier Long. Ce travail a été effectué dans le cadre du projet DURAMAT du pôle de compétitivité AXELERA de la région Rhône-Alpes.

Je tiens tout d'abord à remercier chaleureusement mes encadrants Mme Lise Trouillet-Fonti et M. Paul Sotta pour leur soutien pendant cette thèse. Ces trois années ont été extrêmement enrichissantes tant sur le plan scientifique que professionnel. Un grand merci à vous deux.

Un merci particulier à M. Didier Long pour m'avoir aidé à « percoler », à Mlle Simona Ceccia pour sa contribution sur la cristallisation et pour les nombreuses discussions. Je remercie également Mme Louise-Anne Fillot pour les échanges sur les relations structure/propriétés et Mme Sandrine Rossi pour son aide indispensable et sa bonne humeur quotidienne.

Je souhaite également remercier Mme Paula Moldenaers et M. Yves Grohens pour avoir accepté d'être rapporteurs de ce travail, ainsi que les autres membres du Jury M. René Fulchiron et M. Guo-Hua Hu.

Ce travail n'aurait pu être mené sans la participation des équipes du Centre de Recherches et Technologies de Rhodia. Je tiens donc à remercier ici toutes les personnes qui ont contribué à cette étude avec un merci particulier à M. Vincent Curtil du laboratoire de transformation, dirigé par M. Olivier Chaubet, pour m'avoir transmis son goût et son expérience de la mise en œuvre des polymères. Je remercie également toute l'équipe de microscopie, Mlle Magalie Fontana, Mme Joëlle Guillaud-Saumur, Mlle Clémence Abadie, M. Rémi Sellier, M. Olivier Sanseau et Mme Nelly Bulgarelli, l'équipe de rhéologie, Mlle Séverine Dauffer, M. Léo Georges et Mme Magali Davezac, et enfin Mme Nadia Anik-Delon, Mlle Laetitia Tribolet, M. Frédéric Leguyader et M. Philippe Menez pour leurs analyses.

Je tiens également à remercier les équipes du Technyl Innovation Center du site de Belle Etoile qui m'ont accueilli avec beaucoup de sympathie de l'autre côté de l'autoroute, et plus particulièrement M. Franco Speroni, M. David Haeusler, M. Christophe Lapierre, M. Yannick Martinez et M. Fabrice Chavand. Merci également à Mme Charlotte Basire et M. Nicolangelo Peduto pour leur aide précieuse au début de ce travail.

Je souhaite remercier le Laboratoire des Matériaux Polymères et des Biomatériaux (LMPB) de l'Université Claude Bernard Lyon 1 pour leur collaboration avec le LPMA dans le cadre du projet DURAMAT : Mme Eliane Espuche, M. René Fulchiron, M. Fabrice Gouanvé, M. Mathieu Sabard et M. Gérard Seytre.

Un grand merci enfin à toute l'équipe du LPMA et du Laboratoire Avancé Innovation Matériaux (LAIM) pour tous les bons souvenirs que je garderai de ces trois années de thèse, avec un merci tout particulier à mes « collègues de promotion » Mlle Luisa Munoz et Mlle Clio Cocquet pour ses nombreuses idées d'animations « non-scientifiques » qui ont su créer une véritable unité entre les thésards. Je remercie également Mlle Caroline Fayolle et Mlle Chloé Epinat pour leur contribution à ce travail de thèse dans le cadre de leurs stages de fin d'études.

Merci à tous les thésards et post-docs, Elodie, Brice, Elian, Clio, Luisa, Agustin, Arnaud, Naji, Pauline, Grégoire, Chloé, Caroline, Coraline, Alain et Roberto pour leur bonne humeur et l'excellente ambiance qui règne au laboratoire.

Enfin, un grand merci à toi Maxime, pour ton soutien, ta présence à mes côtés… et ta patience pendant ces trois années. Je remercie également toute ma famille et mes amis pour leurs encouragements. Merci beaucoup enfin aux ruthénois et grenoblois d'avoir fait le déplacement pour être présents et m'épauler lors de ma soutenance.

Un grand merci à tous !

Résumé

Cette thèse a été réalisée dans le cadre du projet DURAMAT du pôle de compétitivité AXELERA. Elle s'inscrit plus précisément dans un sous-projet visant à développer de nouveaux matériaux base Polyamide aux propriétés barrières améliorées pour des applications réservoirs et conduits d'essence. L'objectif de cette thèse était donc d'étudier des mélanges Polyamide 6 / Polyéthylène Haute Densité compatibilisés par voie réactive.

En effet, le Polyamide (PA) est connu pour ses propriétés barrières, plus particulièrement sa bonne résistance aux hydrocarbures. Cependant, les groupements polaires qui constituent le Polyamide le rendent sensible aux solvants polaires comme l'éthanol. Les biocarburants aujourd'hui utilisés sur le marché automobile contiennent 10% en poids d'éthanol et ce taux pourrait augmenter dans les prochaines années. De plus, les normes de perméabilité aux essences deviennent de plus en plus restrictives. De nouveaux matériaux aux propriétés barrières améliorées aux essences contenant de l'éthanol doivent donc être développés. Pour cela, mélanger le Polyamide à un polymère apolaire barrière à l'éthanol comme le Polyéthylène (PE) semble être une stratégie intéressante. Les performances des mélanges dépendent des propriétés de chacun des constituants, de la composition et également de la morphologie [1]. Le défi est donc de contrôler et stabiliser une morphologie adaptée en fonction des propriétés visées. Ainsi, cette étude s'intéresse plus particulièrement aux relations entre (1) la formulation, les paramètres de mise en œuvre et (2) la morphologie et la microstructure des mélanges.

Chapitre I : Etude bibliographique

Le premier chapitre de cette thèse (page 19) présente une étude bibliographique. Une introduction aux mélanges de polymères qui décrit notamment la notion de miscibilité dans les mélanges est tout d'abord proposée. La majorité des mélanges de polymères comme les PA/PE étant immiscibles, ils présentent des morphologies multi-phasées comme des dispersions nodulaires, des dispersions étirées/fibrilles ou des morphologies co-continues. Le développement de ces morphologies d'après les mécanismes de rupture (Taylor) et de coalescence est ensuite décrit. Ces morphologies sont généralement grossières et présentent une faible adhésion entre les phases dans les mélanges immiscibles. Les propriétés d'un tel mélange sont donc faibles et non-répétables. L'objectif de la compatibilisation est de prévenir cette séparation de phases à grande échelle en introduisant un compatibilisant, constituant du mélange, qui va se localiser aux interfaces. Plus précisément, elle permet de diminuer la tension interfaciale, facilitant ainsi la

diminution de la taille caractéristique des morphologies. Elle limite également la coalescence et stabilise les morphologies. Enfin, elle augmente l'adhésion entre les phases à l'état solide, améliorant ainsi les propriétés finales. Deux voies de compatibilisation peuvent être distinguées : la compatibilisation physique (ajout d'un compatibilisant) et la compatibilisation réactive (formation in-situ du compatibilisant). Les paramètres influençant chaque type de morphologies, typiquement, l'effet de la compatibilisation et l'influence de la rhéologie des constituants du mélange sont ensuite détaillés. Plus particulièrement dans le cas des morphologies co-continues, différents modèles de prédiction de l'inversion de phase basés sur la rhéologie (viscosité et élasticité) ont été proposés dans la littérature et sont détaillés dans ce chapitre.

Dans une deuxième partie, nous nous sommes plus particulièrement intéressés aux mélanges PA/PE. Les différentes voies de compatibilisation de ce système proposées dans la littérature sont donc détaillées afin de choisir ensuite le système le plus efficace pour notre étude. Les morphologies et les propriétés associées dans ces systèmes sont ensuite présentées.

Cette étude bibliographique nous a permis d'établir les zones d'ombre de la littérature et donc de définir plus précisément les objectifs de la thèse :

1) Ainsi, dans la majorité des études de la littérature, l'objectif est de développer une morphologie donnée présentant une taille caractéristique ciblée en utilisant un minimum de compatibilisant. Dans nos mélanges PA6/PEHD, un compatibilisant classique Polyéthylène Haute Densité greffé Anhydride Maléique (PEHD-g-AM), connu pour être efficace a été utilisé. Cependant, une large gamme de compositions PA6, PEHD, PEHD-g-AM a été utilisée en extrusion bivis afin d'étudier l'influence relative de la composition et des paramètres de mise en œuvre sur le développement de tous les types de morphologies. De plus, des taux de compatibilisant standards, mais également des plus hauts taux ont été utilisés afin de mieux comprendre comment considérer le compatibilisant lors du design d'un nouveau mélange de polymères, ainsi que son rôle dans les mécanismes de développement des morphologies.

2) Concernant plus particulièrement la morphologie co-continue, les conditions pour développer et stabiliser ce type de structure dans les mélanges PA6/PEHD ne sont pas encore totalement décrites [2,3,4]. Une attention particulière a donc été portée au développement de la co-continuité.

3) Il apparaît dans la littérature que l'inversion de phase, et donc la co-continuité, peut être décrite par la théorie de la percolation [5,6,7,8]. Cependant, à notre connaissance, cette théorie ne semble pas avoir été directement utilisée afin de décrire quantitativement les tailles caractéristiques des morphologies (et également des distributions de tailles) [9,10,11,12,13,14]. Nous avons donc étudié ce point.

4) Les morphologies observées dans la littérature peuvent simultanément présenter plusieurs tailles caractéristiques [15,16]. Un des objectifs est donc de proposer un mécanisme global de développement de ces morphologies multi-échelles.

5) Enfin, un dernier aspect, important du point de vue applicatif, est la stabilité des morphologies, notamment après une seconde étape de mise en forme. Dans la littérature, des études se sont intéressées à la stabilité en statique [17,18], mais peu d'auteurs ont étudié la stabilité lors de la mise en forme [19]. Dans cette thèse, la stabilité des morphologies dans différentes conditions a donc été étudiée.

Chapitre II : Matériaux et techniques expérimentales

Un Polyamide 6 (PA6), trois Polyéthylène Haute Densité (PEHDs) de différentes viscosités et un compatibilisant standard Polyéthylène Haute Densité greffé Anhydride Maléïque (PEHD-g-AM) ont été utilisés. La compatibilisation est assurée par la réaction entre les groupements Anhydride Maléïque (AM) du compatibilisant et les groupements terminaux Amine (NH_2) du PA6. Le ratio molaire [AM]/[NH_2] varie de 0 à 13,7 dans les mélanges. Ces matériaux sont décrits précisément dans le chapitre 2 (page 71). La miscibilité entre le PA6 et le PEHD, et entre le PEHD et le PEHD-g-AM est notamment discutée dans ce chapitre, en termes de paramètres d'interaction de Flory.

Les outils de mise en œuvre utilisés pour la réalisation des mélanges sont ensuite présentés :
- Une extrudeuse bivis co-rotative de diamètre 34mm
- Une deuxième extrudeuse bivis co-rotative de diamètre plus important, 40mm
- Une mini-extrudeuse bivis co-rotative discontinue (10g/passe). Ce dernier outil nous a notamment permis de faire varier sur une large gamme les paramètres de mise en œuvre (témpérature, vitesse de rotation des vis et temps de séjour)

Les principales méthodes de caractérisation utilisées pendant cette thèse sont également présentées :
- Rhéométrie capillaire et dynamique
- Microscopie électronique :
  - A balayage (MEB) : dans ce cas, les échantillons sont observés après dissolution sélective de la phase minoritaire afin d'avoir du contraste entre les phases.
  - En transmission (MET) : dans ce cas, les échantillons sont observés sans aucune dissolution, mais après marquage du PA6.

La température de mise en œuvre étant élevée (290°C), notamment pour les PEHDs ; et le PA6 étant sensible à la reprise en eau, une étude de la stabilité des matériaux utilisés a tout d'abord été menée essentiellement par Analyses Thermogravimétriques (TGA) et Chromatographie d'Exclusion Stérique (SEC). Le PA6 est stable à ces températures élevées de mise en œuvre alors que les PEHDs évoluent au cours du procédé. Le comportement rhéologique des PEHDs extrudés, du PEHD-g-AM extrudé et du PA6 non extrudé a donc été pris en compte dans la suite de l'étude.

Chapitre III : Contrôle des morphologies des mélanges

Le chapitre 3 (page 103) traite du développement des morphologies dans les mélanges PA6/PEHD/PEHD-g-AM. Les morphologies observées en Microscopie Electronique à Balayage (MEB) après dissolution sélective de la phase minoritaire présentent des tailles caractéristiques allant de l'échelle nanométrique à l'échelle micronique.

Les morphologies à l'échelle micronique sont tout d'abord discutées. En augmentant le taux de PA6 dans le mélange, différentes morphologies ont donc été obtenues :
- Dispersion de PA6 dans la phase PE
- Dispersion étirée de PA6 dans la phase PE
- Co-continue
- Dispersion étirée de PE dans le PA6
- Dispersion de PE dans le PA6

Des clichés MEB représentatifs de ces morphologies sont présentés en Figure III-4 page 107.

Le développement de ces morphologies en extrusion est accéléré par la présence de compatibilisant.

Les paramètres procédé ainsi que le type d'outils n'influençant pas le type de morphologie, les régions correspondantes aux cinq types de morphologies ont été définies et rassemblées pour chaque PEHD sur un diagramme ternaire représentant les fractions volumiques en PA6, PEHD et PEHD-g-AM, indépendamment des outils de mise en œuvre utilisés. Ces diagrammes ternaires sont présentés en Figure III-5 page 110. De plus, les ratios de viscosités entre les phases ont moins d'influence sur la gamme de compositions d'inversion de phase qu'attendu d'après le modèle de prédiction de Paul et Barlow. La composition est donc le paramètre prépondérant dans le développement des morphologies à l'échelle micronique.

Comme attendu, en augmentant le ratio volumique compatibilisant sur PEHD, la morphologie devient plus fine (10 – 20 µm à ~1 µm). Par ailleurs, le taux de conversion des groupements Anhydride Maléïque (AM) au cours de la réaction de compatibilisation est supérieur à 80% d'après des caractérisations en Spectroscopie InfraRouge.

- Pour des ratios molaires [AM]/[NH$_2$] de 0,5 à 1,2, un taux de réaction de 80% signifie que 40 à 80% du PA6 serait sous forme de copolymère, donc ancré aux interfaces.
- D'après les tailles caractéristiques des morphologies à l'échelle micronique, on estime une fraction de l'ordre de 5% seulement des chaînes PA6 du mélange se trouvant sous forme de copolymère à l'interface des domaines de taille micronique.

En couplant ces deux conclusions, la question est donc : où se trouve la majeure partie des copolymères formés ? Pour y répondre, des observations à l'échelle nanométrique ont été réalisées en MET.

Des nano-dispersions à la fois de PE dans le PA6 et de PA6 dans le PE ont simultanément été observées dans les mélanges compatibilisés, correspondant à une grande quantité d'interface, en accord avec les taux de réaction élevés observés dans ces systèmes. Ces nano-dispersions (de l'ordre de 50nm) sont générées par des instabilités d'interface pendant l'extrusion réactive. En effet, la réaction étant extrêmement rapide, la tension interfaciale diminue fortement. Des instabilités d'interface, dues aux fluctuations thermiques apparaissent et augmentent ainsi la quantité d'interface disponible, permettant ainsi à de nouvelles espèces réactives d'atteindre l'interface et de continuer la réaction de compatibilisation. Il y a donc un renouvellement continu de l'interface, facilité par le cisaillement. Ce cisaillement permet ensuite d'extraire plus facilement les instabilités de la surface sous forme de nano-dispersions. Un schéma résumant ce mécanisme se trouve en Figure III-38 page 150. Cependant, cette rugosification de l'interface épuise petit à petit le potentiel de réaction et des interfaces pauvres en copolymère restent présentes dans le système. Ces interfaces forment donc de plus grand domaines, qui sont ainsi soumis aux mécanismes classiques de rupture et coalescence pour finalement former la morphologie à l'échelle micronique.

Des sous-dispersions ont également été observées dans les mélanges non-compatibilisés. Dans ce cas, la tension interfaciale étant très importante, tous les domaines sont soumis aux mécanismes de rupture et coalescence. La taille minimum observée dans ces systèmes est de l'ordre de quelques centaines de nanomètres et correspond bien à l'estimation de la taille minimum atteignable d'après la théorie de Taylor.

L'évolution de la plus grande taille caractéristique des morphologies en fonction de la fraction volumique en PA6, ainsi que la distribution de tailles (de la dizaine de nm au µm) dans un mélange proche de la co-continuité, ont été modélisés par des mécanismes de percolation. En normalisant les tailles observées expérimentalement par la tension interfaciale Γ, the volume réduit (V/Γ^3) en fonction de la fraction volumique en PA6 a été tracé sur un même graphe pour tous les mélanges présentant des viscosités proches (compatibilisés et non-compatibilisés). Ces graphes correspondent aux Figure III-42 page 158 et Figure III-44 page 159. La distribution de tailles d'un mélange proche de l'inversion de phase est présentée en Figure III-48 page 163. Les fits réalisés en utilisant les exposants caractéristiques de la percolation sont en adéquation avec les résultats expérimentaux.

La théorie de la percolation semble donc tout à fait adaptée et utile pour la description des mélanges de polymères. Elle permet en effet d'estimer qualitativement des tensions interfaciales en mesurant la taille typique des domaines et de prédire la plus grande taille caractéristique de la morphologie selon la composition du mélange. Un schéma résumant les mécanismes de formation des morphologies multi-échelles dans les mélanges compatibilisés et non-compatibilisés se trouve en Figure III-49 page 166.

Chapitre IV : Stabilité des morphologies

La stabilité des morphologies a ensuite été étudiée pour différents taux de compatibilisant dans le chapitre 4 (page 167). En effet, la stabilité des morphologies au cours d'une deuxième étape de mise en forme est un point clé du point de vue de l'application.

Différentes conditions ont été testées. Afin de mieux comprendre, des essais de recuit en statique et sous cisaillement contrôlé ont tout d'abord été réalisés. Les recuits en statique ont été réalisés à 290°C pendant 5 et 15 minutes sous un flux d'Argon en Calorimétrie Différentielle à Balayage (DSC). Les essais sous cisaillement contrôlé ont été réalisés dans un rhéomètre capillaire à 200 et 2000s^{-1}. Puis, la stabilité des morphologies a été étudiée dans des conditions réelles, au cours d'une deuxième étape de mise en forme :
- moulage par injection d'éprouvettes de traction et de plaques
- extrusion soufflage de bouteilles

Il a tout d'abord été observé que l'étirage était relaxé pendant le recuit en statique, indiquant ainsi que les morphologies étirées ne sont pas des morphologies d'équilibre. Des effets cœur/peau ont été mis en évidence dans les pièces mises en forme.

Il a ensuite été observé que le copolymère greffé formé in-situ stabilisait la taille des morphologies quelle que soient les conditions appliquées, en statique ou sous cisaillement. Une légère augmentation de la taille des domaines a tout de même été observée dans le cas des mélanges présentant de faibles taux de compatibilisant. En revanche, dans le cas de mélanges non compatibilisés, une importante augmentation de la taille des domaines due la coalescence est observée après recuit statique. Après cisaillement contrôlé ou seconde étape de mise en forme, cette coalescence est limitée par le cisaillement.

Les mélanges étudiés dans ce chapitre se situent à la frontière entre deux régions de morphologies différentes. Après une deuxième étape en température (en statique ou sous cisaillement), il a été observé que ces mélanges évoluaient vers l'une ou l'autre des morphologies. Cet effet a également été observé dans d'autres cas lors de la première étape de mélange, en faisant varier les conditions d'extrusion sur des mélanges à la frontière entre deux régions.

Les morphologies obtenues après recuit statique ont été reportées sur un diagramme ternaire. Les morphologies obtenues après une étape de cisaillement en température (quel que soit le type d'essais : cisaillement contrôlé, seconde étape de mise en forme) ont pu être rassemblées sur un seul et même diagramme ternaire. Les différents diagrammes sont présentés en Figure IV-31 page 203.

Chapitre V : Cristallisation des mélanges

Dans un dernier chapitre (page 205), les propriétés des mélanges dépendant également de la cristallinité, l'influence de la composition et de la morphologie sur le mécanisme de cristallisation et les taux de cristallinité obtenus dans chacune des phases PA6 et PE dans les mélanges a été caractérisée par Calorimétrie Différentielle à Balayage (DSC). La cristallinité est un point très important d'un point de vue applicatif.

La cristallisation se fait en trois étapes :
1) Germination
2) Croissance
3) Perfectionnement cristallin

La première étape peut être homogène ou hétérogène Dans ce dernier cas, les germes sont initiés sur des hétérogénéités (impuretés, interfaces…) et l'énergie à franchir pour initier la germination et donc la cristallisation est plus faible. Généralement, dans les polymères, la cristallisation par refroidissement depuis l'état fondu est initiée par des hétérogénéités présentes dans le fondu : germination hétérogène [20].

Les matériaux de références PA6, PEHDs et PEHD-g-AM ont tout d'abord été caractérisés avant et après mise en œuvre afin de déterminer quelles sont les meilleures références à utiliser dans la suite de l'étude. Des différences ayant été observées entre les thermogrammes des matériaux extrudés et non extrudés, nous avons donc choisi d'utiliser les références extrudées.

Le PA6 peut présenter deux phases cristallines : α et γ :

- La phase α est généralement considérée comme la phase thermodynamiquement stable. Elle est obtenue par refroidissement lent. Sa température de fusion observée expérimentalement est de 220°C. Le taux de cristallinité associé à cette phase α est de 17%.

- La phase γ est généralement obtenue par refroidissement rapide et sa température de fusion a été observée à 214°C. Le taux de cristallinité associé à cette phase γ est de 27%.

La cristallisation du PA6 bulk a expérimentalement été observée à 187°C.

Les caractéristiques des PEHDs et du PEHD-g-AM extrudés sont présentées dans le tableau suivant :

	T fusion	T cristallisation	Taux de cristallinité χ_c
PEHD 1	127°C	115°C	64%
PEHD 2	131°C	117°C	75%
PEHD 3	133°C	119°C	84%
PEHD-g-AM	128°C	116°C	66%

Tableau 1: Caractéristiques des PEHDs et du PEHD-g-AM extrudes.

L'influence de la composition et de la morphologie des mélanges PA6/PEHD/PEHD-g-AM a donc ensuite été étudiée dans chacune des phases PA6 et PE.

Cristallisation du PA6:

Selon le degré de confinement du PA6, différents comportements en cristallisation ont été observés :

- Lorsque le PA6 n'est pas confiné (taille des domaines typiquement supérieure à 2µm):
    - La phase PE diminue le taux de cristallinité du PA6 (de 44 à 35% typiquement).

    - La température de cristallisation est la même que dans le bulk.

    - La phase γ phase est favorisée.

- Lorsque le PA6 est confiné (taille des domaines typiquement inférieure à 2µm):
    - Le taux de cristallinité du PA6 diminue encore jusqu'à atteindre des valeurs de 29%.

    - La cristallisation est décalée à des températures plus basses et ce décalage devient de plus en plus important au fur et à mesure que la taille des domaines de PA6 diminue. La température de cristallisation peut atteindre 135°C au lieu de 187°C dans le bulk lorsque la taille des domaines de PA6 devient inférieure à 600nm (voir Figure V-8 *E* page 213).

    - Seule la phase α est formée.

<u>Cristallisation de la phase PE:</u>

Le PA6 n'influence pas le taux de cristallinité de la phase PE quelle que soit la composition du mélange. Ensuite, selon le degré de confinement de la phase PE, une cristallisation fractionnée a été observée (voir Figure V-12 page 219):

- **Pic 1:** T_c *1~ T_c PEHD bulk (~116°C)*. Ce pic correspond à la cristallisation de la fraction de phase PE qui constitue la matrice.

- **Pic 2:** Le pic 1 se divise en deux pics (T_c *2 (114°C)<T_c bulk*) uniquement dans le cas de morphologies dispersées étirées de PE dans une matrice PA6. Ce dédoublement pourrait être dû à un ralentissement de la cinétique de cristallisation dans les étranglements formés le long des domaines de PE étirés subissant les instabilités de Rayleigh.

- **Pic 3:** T_c *3 (105°C)<<T_c bulk*. Ce dernier pic est associé à la cristallisation de la fraction de phase PE confinée dans des domaines de tailles inférieures à 1µm typiquement. En effet, lorsque la taille des domaines devient plus petite que la distance typique entre sites de germination présents dans le bulk (cette distance est de l'ordre du µm d'après nos estimations), une fraction des domaines ne contient pas de site de germination entraînant une cristallisation à 116°C comme dans le bulk. La cristallisation du PE dans ces domaines est donc décalée vers de plus basses températures, auxquelles d'autres types d'hétérogénéités deviennent actives (comme l'interface avec le PA6).

<u>Conclusion</u>

Pour conclure, les relations entre (1) la formulation, les paramètres de mise en oeuvre et (2) la morphologie et la cristallisation de mélanges PA6/PEHD compatibilisés par voie reactive ont été établies. Il serait maintenant intéressant de caractériser les propriétés d'intérêt selon les différents types de morphologies dans ces systèmes. Cette étude pourra donc constituer une base pour le design de nouveaux mélanges de polymères présentant une morphologie contrôlée et stabilisée en fonction des propriétés visées.

Content

Introduction

This PhD work was performed in the "Laboratoire des Polymères et Matériaux Avancés (LPMA)", a joint research unit between the CNRS and Rhodia (UMR 5268). This study was done within the framework of the project DURAMAT labelized by the pole of competitiveness AXELERA of the region Rhône-Alpes. DURAMAT project includes several industrial (Rhodia, Arkema, IFP) and academic partners among which the LPMA. Its target is to develop new materials with reduced environmental impact. More exactly, this PhD belongs to the sub-project SP 3.2: Biofuel permeability of materials based on Polyamide for fuel tanks and pipes applications.

Polyamide (PA) is known for its barrier properties. In fact, it exhibits a high resistance to hydrocarbon products. However, the polar groups which constitute the polyamide make it sensitive to polar solvents such as ethanol. Today, the biofuels used in automotive market contain $10\%_{wt}$ ethanol, but this fraction may increase in the next years. Moreover, the future standards controlling the allowed fuel permeability will be more and more restrictive. Thus, new materials with improved barrier properties to alcoholised gas have to be developed.

At the beginning of 2000s, polymer blends constituted $36\%_{wt}$ of the total polymer consumption [1]. Reason for blending is essentially economy. In fact, it presents several benefits:

- New material with desired properties can be developed at a lower cost by compounding products which already exist and the composition can be adjusted to customer specifications.
- It is possible to extend material performance by blending an engineering polymer like Polyamide to a lower cost one such as Polyethylene.
- Specific properties such as impact strength or barrier properties can be improved.
- Blending could also be a way for polymer recycling, an essential challenge nowadays.

So, blending Polyamide with a non-polar polymer which will be impermeable to polar solvents seems to be a good way to develop materials with improved barrier properties to alcoholised gas. Polyethylene (PE), a common low cost polyolefin, is a good applicant.

According to L.A. Utracki [1], polymer blends' performances depend on (1) the properties of each component, (2) the composition and (3) the morphology. In order to well control the final properties, the morphology must be stable. Therefore, the challenge is to control and stabilize the required morphology according to the desired set of properties.

Most polymer blends, like PA/PE, are immiscible and therefore exhibit multiphase morphologies. According to droplet break-up and coalescence mechanisms during processing, various morphologies can be developed: nodular dispersion, stretched dispersion/fibrils and co-continuous.

The main objective of this work was to study Polyamide 6 (PA6) / High Density Polyethylene (HDPE) compatibilized blends and to make the link between (1) formulation and processing parameters and (2) the morphology.

A literature review focused on the case of morphology development in polymer blends, and on morphologies and associated properties in PA/PE blends is first presented in this manuscript. Thanks to this literature review, several aspects seem to be not fully described yet; this defined more precisely the objectives of the PhD.

After studying the stability of the raw materials used, the development of the different kinds of morphology in extrusion was studied in PA6/HDPE reactively compatibilized blends (compatibilized by MA-g-HDPE) over a broad range of compositions in order to study the relative influence of composition and process parameters. So, various parameters were studied: the composition, the compatibilizer amount, the rheological behavior and the process conditions including the temperature, the screw speed, the residence time and the materials feeding mode. Morphologies scaling from nanometer to micrometer scale were observed. Thus, one of the mains objectives was also to understand these sizes distributions and to propose a mechanism of formation of these multi-scale morphologies.

In a second part, the morphologies stability was studied using various amount of compatibilizer. In fact, the stability of the morphologies during a second step processing is a key point from the application point of view to insure reproducibility of properties in a final part. For better understanding, the stability was first studied under controlled conditions (static annealing and controlled shear). Then, experiments in real processes like extrusion blow molding and injection molding were performed.

In a last part, as crystallinity also plays an important role on properties, the influence of composition and morphology of the blends on the crystallization of PA6 and HDPE was also studied.

I. Literature review

1. Introduction

This literature review is focused on the morphology development in polymer blends. An introduction to polymer blends is done to give essential definitions about miscibility, multi-phases morphologies and compatibilization. Then, the influence of various parameters, including compatibilizer amount and rheology of polymers, on the various kinds of morphology is detailed. In a second part, we focus on PA/PE blends with the morphologies observed in the literature, the associated properties and their main applications. Finally, according to this literature review, the objectives of this PhD work are presented.

2. Introduction to polymer blends

This section presents the main aspects of polymer blends. Miscibility is first described. Then, multi-phases morphologies developed in immiscible polymer blends are presented. Compatibilization of immiscible systems and blends rheology are finally described.

2.1. Miscibility

To know the miscibility of a polymer blend is essential to reach the targeted properties. Polymer blends can be [21]:

- *Miscible:* In this case, average properties as compared to homopolymers which compose the blend are expected.

- *Immiscible:* Heterogeneous systems are obtained with sometimes interesting and unexpected properties, depending on compatibilization.

2.1.1. Definition

It is important to distinguish miscibility, which is a thermodynamic notion, from morphology which can be a non-steady state. The main reason for wanting to know polymer blend miscibility is not necessarily to produce miscible blends, but rather to adapt the formulation, the needed compatibilization and the processing parameters in order to develop precise morphologies to enhance desired properties. Contrary to solutions, polymer blends are mostly immiscible. The free energy of mixing is written as:

$$\Delta G_m = \Delta H_m - T\Delta S_m \qquad \textbf{Eq. I-1}$$

With:
- ΔG_m, the free energy of mixing
- ΔH_m, the enthalpy of mixing
- ΔS_m, the entropy of mixing
- T, the temperature

ΔS_m is related to the possible arrangements between components. The higher the molar mass of constituents, the lower the entropy of mixing. For macromolecules, ΔS_m is positive, close to 0 [21]. ΔH_m is related to the exothermic or endothermic nature of mixing.

The miscibility of polymer blends is related to Eq. I-1, so:

- "***A miscible polymer blend*** is defined as a blend, homogenous down to the molecular level, in which the domain size is comparable to macromolecular dimension, associated with the negative value of the free energy and enthalpy of mixing: $\Delta G_m \approx \Delta H_m \leq 0$"[22] and a positive value of the second derivative $\frac{\delta^2 \Delta G_m}{\delta \phi_d^2}$ (out of binodal, see Figure I-7) with ϕ_d, the volume fraction of the dispersed phase. In fact, ΔH_m negative means that it exists specific favourable interactions between the macromolecules [23].
- An ***immiscible polymer blend*** is a blend whose free energy of mixing is positive: $\Delta G_m > 0$ [22].

There are several methods to detect miscibility. The most widely used one is the calorimetric glass transition temperature T_g. It seems that blends which display a single T_g are miscible.

2.1.2. Flory-Huggins theory

Many theories were developed to report the observed phenomena concerning miscibility. The first thermodynamic description of a binary mixture containing polymer, and still used, was proposed by Huggins and Flory in 1941 [21,22,23]. In this model, the mixture is discussed as a regular solution ($\Delta H_m \neq 0$ and $\Delta S_{m,ideal} \geq 0$). This theory is mainly adapted to non-polar blends and describes the phase separation when the temperature decreases. Using this model, the free energy of mixing ΔG_m (per monomer) can be calculated:

$$\Delta G_m = kT \left(\underbrace{\frac{\phi_1}{N_1} ln\phi_1 + \frac{\phi_2}{N_2} ln\phi_2}_{\textit{Entropy of mixing}} + \underbrace{\chi_{12}\phi_1\phi_2}_{\textit{Enthalpy}} \right)$$

Eq. I-2

$$\text{Where } \chi_{12} = \frac{1}{kT} \left(\varepsilon_{12} - \frac{1}{2}(\varepsilon_{11} + \varepsilon_{22}) \right)$$

Eq. I-3

With:

- ϕ_1 and ϕ_2, volume fraction of each specie
- N_1 and N_2, polymerization degree of each polymer
- χ_{12}, Flory interaction parameter
- ε_{12}, ε_{11} and ε_{22}, interaction energies associated with the contact of corresponding monomer units. For Van der Waals interactions, ε_{12} depends on molecular polarizabilities p_i: $\varepsilon_{12} = -kp_1p_2$. So, $\chi_{12} \propto (p_1 - p_2)^2 > 0$. In the most basic case in which interactions are independent of temperature, $\chi_{12} \propto \frac{1}{T}$.

Polymers exhibit very high polymerization degree: $N_1 \approx N_2 \gg 1$, that means:

$$\Delta G_m = kT \left(\underbrace{\frac{\phi_1}{N_1} ln\phi_1 + \frac{\phi_2}{N_2} ln\phi_2}_{\text{}} + \chi_{12}\phi_1\phi_2 \right)$$

$$\downarrow Tends\ to\ 0$$

Eq. I-4

So, the free energy of mixing, as well as miscibility, highly depends on the Flory interaction parameter. By using this interaction Flory parameter, it is possible to well describe miscibility.

Let us consider the symmetric case $N_1=N_2=N$. Depending on the value of χ_{12}, ΔG_m present different behavior as a function of volume fraction of one blend component ϕ, as shown on Figure I-1.
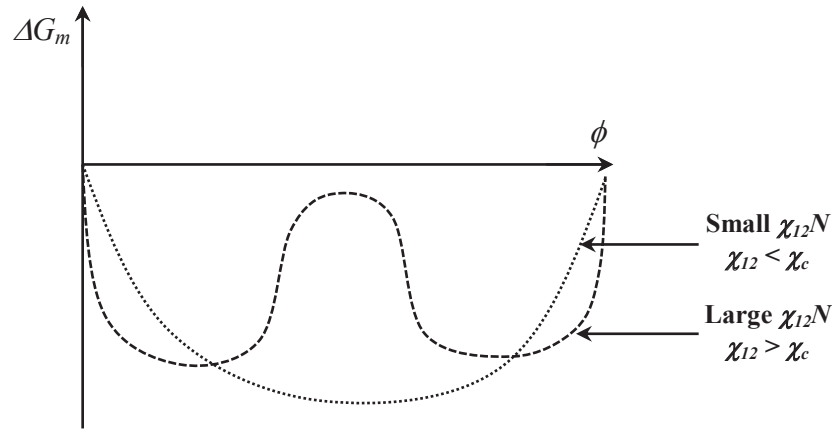
Figure I-1: Free energy of mixing as a function of blend composition.

Below a critical value of χ_{12} ($<\chi_c$), the mixture is stable, no phase separation occurs.

Above a critical value of χ_{12} ($>\chi_c$), ΔG_m has two minima as a function of volume fraction of one blend component ϕ given by:

$$\frac{\delta\Delta G_m}{\delta\phi} = 0 \quad \text{i.e.} \quad ln\left(\frac{1-\phi}{\phi}\right) = N\chi_{12}(1-2\phi)$$

Eq. I-5

$$\frac{\delta^2\Delta G_m}{\delta\phi^2} > 0$$

Eq. I-6

For a given value χ_{12} above χ_c, the two minima correspond to volume fractions ϕ_α and ϕ_β. Starting from the volume fraction ϕ between ϕ_α and ϕ_β, the system will separate in two phases of

fractions ϕ_α and ϕ_β (see Figure I-2). Outside the interval ϕ_α - ϕ_β, the mixture is stable. The location of ϕ_α and ϕ_β as a function of χ_{12} or $\chi_{12}N$ defines the so called binodal curve.
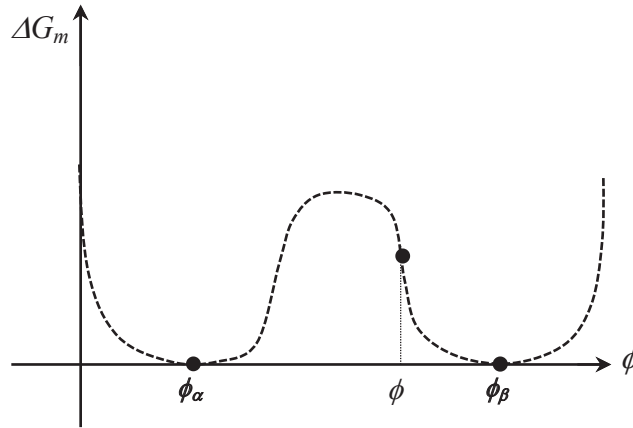
Figure I-2: Free energy of mixing in the symmetric case $N_1=N_2=N$ as a function of blend composition for $\chi_{12}>\chi_c$.

The curvature of ΔG_m determines the stability with respect to a local concentration fluctuation as illustrated in Figure I-3.
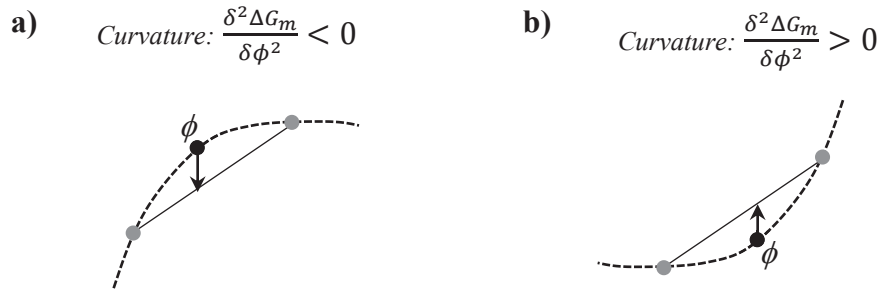
Figure I-3: Curvature of ΔG_m: a) negative, b) positive.

In the case of a negative curvature (a), the local concentration fluctuation leads to an energy gain. Thus, phase separation can be easily achieved: **the system is unstable**.

In the case of a positive curvature (b), there is an energy barrier to overcome to achieve phase separation: **the system is metastable**. This defines the metastability domain in which phase separation occurs via nucleation.

For χ_{12} above χ_c, the curve ΔG_m has also two inflexion points, defined by:

$$\frac{\delta^2 \Delta G_m}{\delta \phi^2} = kT \left(\frac{1}{\phi N} + \frac{1}{N(1-\phi)} - 2\chi_{12} \right) = 0 \qquad \text{**Eq. I-7**}$$

This leads to:

$$\frac{1}{\phi(1-\phi)} = 2\chi_{12}N$$

The location of the inflexion points defines the so called spinodal curve (Eq. I-8).
Figure I-4 shows the schematic phase diagram of $\chi_{12}N$ as a function of blend composition in the symmetric case $N_1=N_2=N$ according to the previously defined equations.
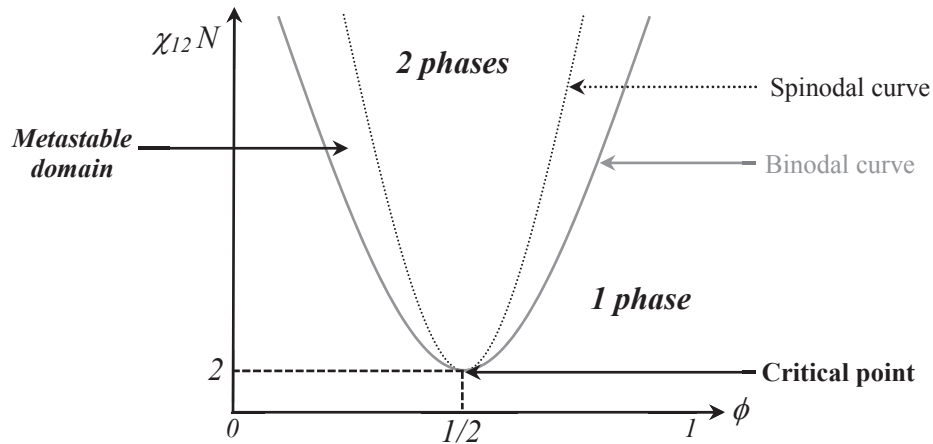
Figure I-4: Schematic phase diagram of the interaction parameter $\chi_{12}N$ in the symmetric case $N_1=N_2=N$.

This phase diagram can also be plotted as a function of temperature. As already written, in the most basic case in which interactions are independent of temperature, $\chi_{12} \propto \frac{1}{T}$. Thus, the phase diagram looks like this:
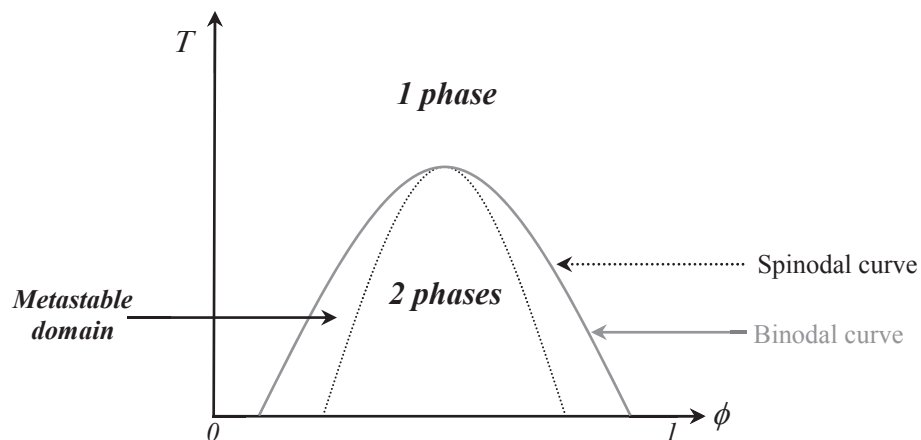
Figure I-5: Schematic phase diagram of the temperature T in the symmetric case $N_1=N_2=N$.

In the non-symmetric case ($N_1 \neq N_2$), the general behavior of ΔG_m for χ_{12} above χ_c is different from in the symmetric case as schematized in Figure I-6.
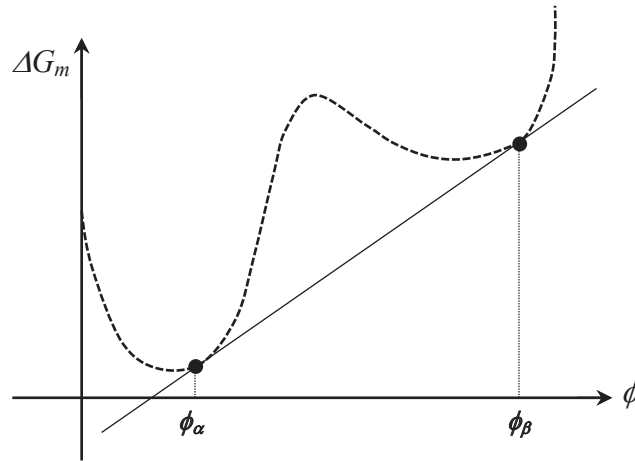
Figure I-6: Free energy of mixing in the non-symmetric case $N_1{\neq}N_2{\neq}N$ as a function of blend composition for $\chi_{12}{>}\chi_c$.

The volume fractions ϕ_α and ϕ_β of the two coexisting minima are determined by both following conditions:

1) *Equality of chemical potentials (same tangent):*

$$\mu_\alpha = \mu_\beta \text{ with } \mu = \frac{\delta \Delta G_m}{\delta \phi} \qquad \text{Eq. I-9}$$

2) *Equality of osmotic pressure (coinciding points):*

$$(\Delta G_m - \mu_\alpha \phi_\alpha) = (\Delta G_m - \mu_\beta \phi_\beta) \text{ with } \mu = \frac{\delta \Delta G_m}{\delta \phi} \qquad \text{Eq. I-10}$$

The critical point (as represented on Figure I-4) in terms of Flory interaction parameter is defined as:

$$\chi_c = \frac{\left(N_1^{-1/2} + N_2^{-1/2} \right)^2}{2} \qquad \text{Eq. I-11}$$

Note that in the symmetric case $N_1{=}N_2{=}N$, $\chi_c = \frac{2}{N}$ and $\phi_c = \frac{1}{2}$ as represented on Figure I-4.

2.1.3. General phase diagram of polymer blends

In general, polymer blends can present an Upper Critical Solution Temperature (UCST), a Lower Critical Solution Temperature (LCST) or both. Figure I-7 shows a schematic phase diagram of the temperature T as a function of blend composition for polymer blends [22].
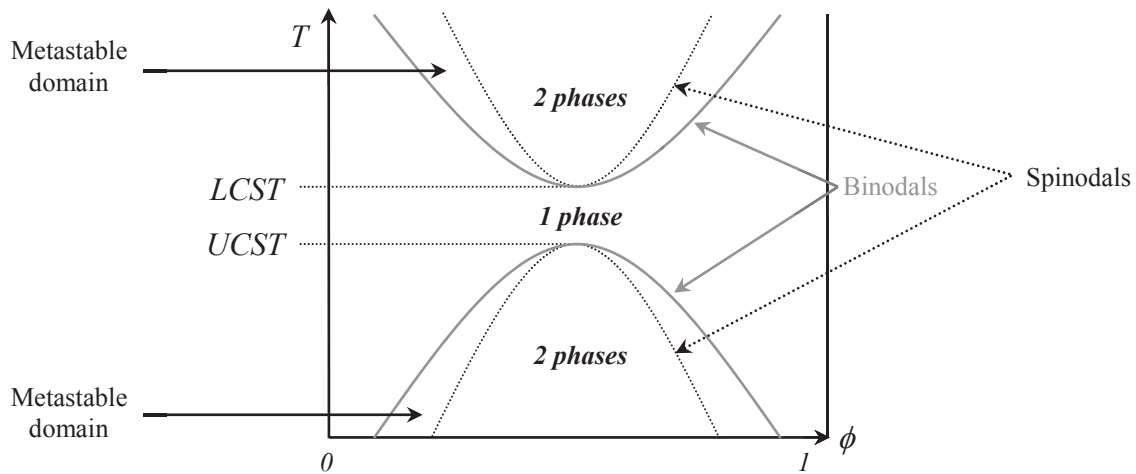
Figure I-7: Schematic phase diagram of temperature *T* for polymer blends.

There are three regions in a binary system:

- Miscible
- Metastable
- Immiscible

Flory theory as shown in Figure I-5 only predicts UCST (non-polar polymer blends, only Van der Waals interactions). According to the diagram of Figure I-7, a homogeneous system should present a phase separation when the temperature increases, showing the existence of LCST. LCST may be related to polar interactions (H bonds), to compressibility… which tend to stabilize the mixture at low temperature and to phase separate at high temperature [24].

2.1.4. Estimation of interaction parameter

From Eq. I-2, the Flory Huggins free energy ΔG_m can also be written per unit of volume (per cm^3) and is given by:

$$\Delta G_m = RT \left(\frac{\phi_1}{V_1} ln\phi_1 + \frac{\phi_2}{V_2} ln\phi_2 + \Lambda_{12}\phi_1\phi_2 \right)$$

<div align="right">**Eq. I-12**</div>

With:
- ϕ_1 and ϕ_2, volume fraction of each specie
- V_1 and V_2, molar volumes of polymer 1 and polymer 2 respectively
$V_1=v_1N_1$ and $V_2=v_2N_2$ with v_1 and v_2 the molar volumes of each monomer.

Dimensionally, χ_{12} and Λ_{12} are related by v, where v is the molar volume of one monomer molar volume (for same molar volume of both monomers):

$$\chi_{12} = \Lambda_{12}v$$

<div align="right">**Eq. I-13**</div>

The adimensional parameter χ_{12} can be calculated using Hildebrand equation, in terms of solubility parameters [22]:

$$\chi_{12} = \frac{\sqrt{V_1V_2}}{RT}(\delta_1 - \delta_2)^2 > 0$$

<div align="right">**Eq. I-14**</div>

With:
- V_1 and V_2, molar volumes of polymer 1 and polymer 2 respectively
- δ_1 and δ_2, the solubility parameters of polymer 1 and polymer 2 respectively

Hildebrand parameters provide one of the simplest guides to evaluate the miscibility.

In the case of polar systems, the Hansen solubility sphere can be used to determine solubility parameters.
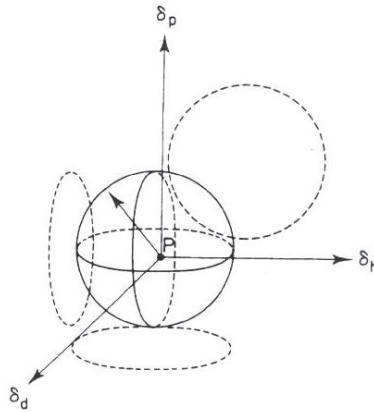
Figure I-8: Representation of the Hansen's solubility sphere [22].

In fact, Hansen defined a solubility parameter divided into three components:

$$\delta_i^2 = \delta_{id}^2 + \delta_{ip}^2 + \delta_{ih}^2$$

Eq. I-15

Dispersive interaction   *Polar interaction*   *Hydrogen bonding interaction*

The three components (dispersive, polar and hydrogen bonding) can be calculated using the groups contribution theory.

The phase separation takes place when a single-phase system undergoes a change of composition, temperature or pression, which forces it to enter in the metastable or in the spinodal region of the phase diagram in temperature (see Figure I-7) [22]. So, several mechanisms of phase separation exist [23].

2.1.5. Nucleation and growth
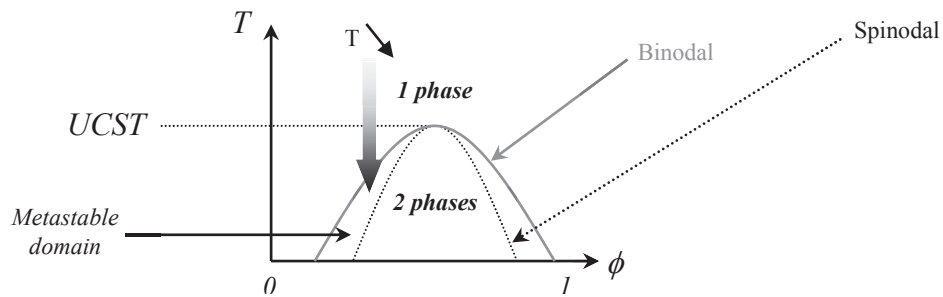
Figure I-9: Illustration of the first phase separation mechanism: Nucleation and Growth.

In the case of Figure I-9 (presence of UCST), the temperature is lowered from the miscible domain (1 phase) into the metastable domain. In this case:

1) The phase separation is initiated by local fluctuations of concentration. The activation energy of nucleation needed depends on interfacial tension and surface of the nucleus.

2) Then, the droplet grows by diffusion of macromolecules into these nucleated domains (function of time) approximated by Ostwald ripening equation:

$$\frac{dV_d}{dt} \propto \frac{\Gamma \phi_e V_m D_t}{RT} \text{ and } d \propto t^{1/3}$$ **Eq. I-16 and Eq. I-17**

With:
- V_d, the droplet volume
- Γ, the interfacial tension
- ϕ_e, the equilibrium concentration (solubility) at the given temperature
- V_m, the molar volume of the molecules which diffuse from the interface (corresponding to the droplet phase)
- D_t, the diffusion coefficient
- d, the drop diameter

3) Finally, there is coalescence of the formed droplets.

Ostwald ripening is a mechanism in which large droplets grow at the expense of small ones. In the case of polymer blends, $\phi_e \approx 0$. In fact, the solubility of a polymer A into a polymer B is ~0 because of large macromolecules. So, this process should be very very slow as compared to coalescence, and non-compatible with processing times for polymer blending.

2.1.6. Spinodal decomposition
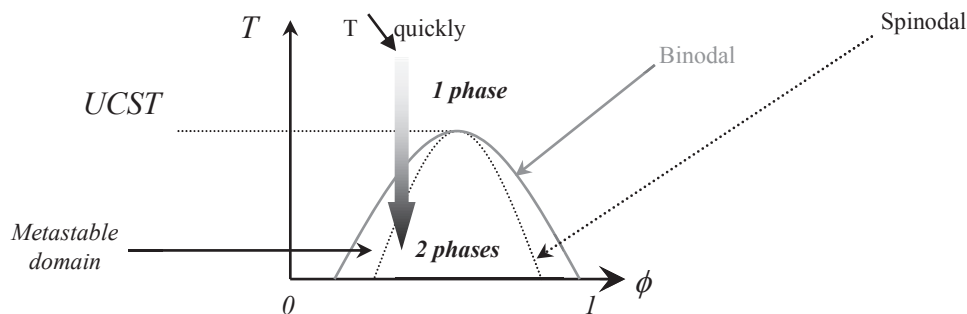
Figure I-10: Illustration of the second phase separation mechanism: Spinodal Decomposition.

Now, the temperature is quickly lowered into the immiscible domain (2 phases), leading to spontaneous phase separation. Contrary to "nucleation and growth" mechanism, the spinodal decomposition occurs uniformly throughout the material. Then, in the case of polymer blends, the size growth is highly controlled by coalescence.

In principle, this kind of phase separation would lead to more interconnected (co-continuous) morphology than Nucleation and Growth mechanism. Any variable, such as P, T, composition or applied stress can be used to generate such a structure.

2.2. Interfacial tension between immiscible polymer blends

The surface tension Γ_i of a polymer i in air is the reversible work required to create a unit surface area at given temperature T and given pressure P [25]:

$$\Gamma_i = \left(\frac{\delta G}{\delta A}\right)_{T,P}$$ **Eq. I-18**

With:
- G, the Gibb's free energy of the system
- A, the surface area

In immiscible polymer blends, interactions between the components 1 and 2 of the system are located at the physical boundary creating the interface. The energy required to separate the two components is defined as the work of adhesion [25]:

$$W = \Gamma_1 + \Gamma_2 - \Gamma_{12}$$ **Eq. I-19**

With:
- Γ_1 and Γ_2, the surface tensions of neat components 1 and 2 respectively
- Γ_{12}, the interfacial tension between both components 1 and 2

The interfacial tension corresponds to the energy required to create one unit area interface.

2.3. Multiphase morphologies in immiscible polymer blends

Most systems are immiscible polymer blends and the overall equilibrium would correspond to macroscopically separated phases. However, the multiphase morphologies obtained in practice result from kinetic mechanism which occurs during processing. The morphology is a **balance between drop break-up and coalescence**.

2.3.1. Drop break-up

Drop break-up was first described in Newtonian systems by Taylor's theory [9,21]. Then, still based on this theory, drop break-up was studied in viscoelastic systems like polymer blends.

2.3.1.1. Newtonian systems

Taylor proposed in 1950 a theory for drop break-up [9,21]. This theory studies the deformation and break-up of a **single Newtonian fluid droplet in a Newtonian liquid in a simple shear field**. Upon shearing, the drop is deformed into an ellipsoid as shown in Figure I-11.
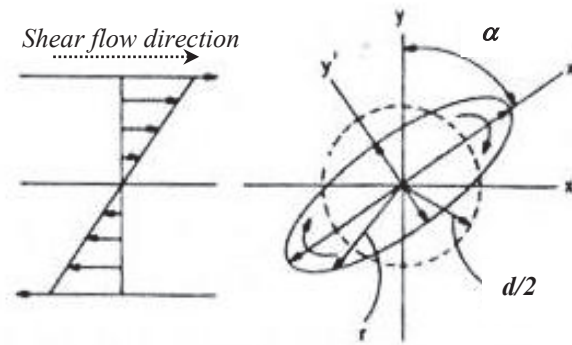
Figure I-11: Drop deformation under steady shear field in Taylor's theory [9].

Taylor modelized the size of this droplet using two parameters:

1) the viscosity ratio defined as:

$$R_v = \frac{\eta_d}{\eta_m}$$

Eq. I-20

2) the Capillary number representing the ratio between viscous forces and interfacial tension, defined as:

$$C_a = \frac{\dot{\gamma}\eta_m d}{2\Gamma}$$

Eq. I-21

With:
- η_m, the matrix viscosity
- η_d, the dispersed phase viscosity (viscosity of the fluid inside the droplet)
- d, the droplet diameter
- Γ, the interfacial tension
- $\dot{\gamma}$, the shear rate

The shear force defined as the normal stress difference across the interface between the drop and the matrix is given by:

$$\delta P_n = -4 \left(\frac{\dot{\gamma} \eta_m}{f(R_v)} \right) \sin(2\alpha)$$

Eq. I-22

With:

- $f(R_v) = \frac{16R_v + 16}{19R_v + 16} \approx 1$. In fact, by considering R_v varying from 0 to ∞, $f(R_v)$ ranges from 1 to 0.8.
- α, angle between the major axis of the ellipsoid and the direction perpendicular to the flow direction

This shear force tends to elongate the drop.

The interfacial force, which **tends to resist the deformation**, is given by the Laplace relation:

$$\delta P_i = \Gamma \left(\frac{1}{R_1} + \frac{1}{R_2} \right)$$

Eq. I-23

With:

- R_1 and R_2, the radii of curvature of the ellipsoid in Figure I-11.

By comparing interfacial and shear forces, Taylor obtained a relation that allows calculating the minimum droplet diameter d_{min} accessible under simple shear. The drop will deform until it breaks when the viscous shear force is larger than the interfacial force. So, the drop will break up when:

$$-\delta P_n > \delta P_i$$

Eq. I-24

This means:

$$4 \left(\frac{\dot{\gamma} \eta_m}{f(R_v)} \right) \sin(2\alpha) > \Gamma \left(\frac{1}{R_1} + \frac{1}{R_2} \right)$$

Eq. I-25

With, for small deformations:

- $\alpha \approx \pi/4$ at equilibrium (Newtonian conditions)
- $R_1 \approx R_2 \approx d/2 \, (= a/2)$ (see Figure I-11)

Thus, the condition for drop break up is:

$$2C_a = \frac{\dot{\gamma}\eta_m d}{\Gamma} \geq f(R_v)$$

Large droplets will break up into smaller ones until they reach the size d_{min}. So, the smaller droplet diameter accessible under simple shear stress is:

$$d_{min} = \frac{\Gamma(R_v + 1)}{\dot{\gamma}\eta_m \left(\frac{19}{16}R_v + 1\right)} = \frac{\Gamma}{\dot{\gamma}\eta_m}f(R_v)$$

Grace [26] used studies on model fluid systems of two liquid phases of high viscosity. The continuous phase viscosity ranged from 5 to 300Pa.s, the viscosity ratio (dispersed phase on continuous phase) from 10^{-6} to 950 and the interfacial tension between both phases varied from 1mN/m to 25mN/m. Based on these studies, he proposed the existence of a critical Capillary number Ca_{cr} defined as the minimum Capillary number sufficient to cause break up of a deformed drop [27].

Four regions can be defined [27]:
- Region 1: $Ca<<Ca_{cr}$: droplets do not deform
- Region 2: $Ca<Ca_{cr}$: droplets deform, but do not break
- Region 3: $Ca_{cr}<Ca<2Ca_{cr}$: droplets deform and break up
- Region 4: $Ca>2Ca_{cr}$: droplets deform into stable filaments

However, in the case of Newtonian systems, it has been shown that in pure shear, drop break up cannot be observed for viscosity ratios higher than 4 [26]. In elongational flow, drop break up can occur whatever the viscosity ratios [26,28].

The critical Capillary number was found to be dependent of the viscosity ratio R_v [27]:

$$log\left(\frac{Ca_{cr}}{2}\right) = c_1 + c_2 logR_v + c_3 (logR_v)^2 + \frac{c_4}{logR_v + c_5}$$

Depending on the flow type, the constants c_1, c_2, c_3, c_4 and c_5 of Eq. I-28 are summarized in Table I-1.

Flow	$1000c_1$	$1000c_2$	$1000c_3$	$1000c_4$	$1000c_5$
Shear	-506.0	-99.4	124.0	-115.0	-611.0
Elongational	-648.5	-24.42	22.21	-0.56	-6.45

Table I-1: Constants values for drop break up in Newtonian systems [27].

So, the critical Capillary number versus viscosity ratios can be plotted for Newtonian systems in case of both shear and elongational flows (Figure I-12).
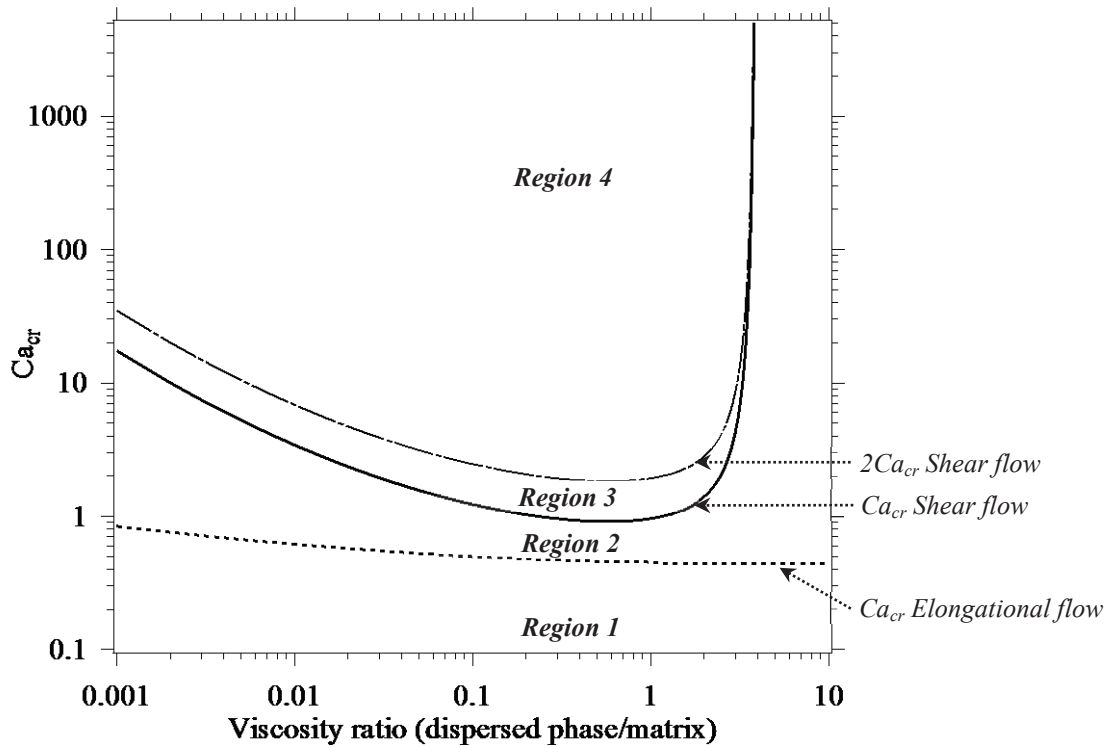
Figure I-12: Evolution of the critical Capillary number as a function of viscosity ratio in a shear flow (solid curve) and in an elongational flow (dashed curve) in Newtonian systems [27].

2.3.1.2. Viscoelastic systems

In the case of polymer blends, materials are not Newtonians but viscoelastics. In Taylor's model (Newtonian droplet in Newtonian matrix), polymer viscoelasticity is not taken into account. However, in polymer blends (viscoelastic systems), the evolution of the dispersed phase size with the viscosity ratio shows similar behaviour as in Newtonian fluids in some respects [29]. The diameter obtained by using Eq. I-27 can be considered as the minimal reachable size by the dispersed phase.

On the other hand, in a Newtonian system, it has been observed experimentally that the upper limit for particles disruption in pure shear is a viscosity ratio of 4 [26] whereas in a viscoelastic system, significant deformation and break up occur at higher viscosity ratio values (as high as 17 in case of PC/PP for example [29]). However, the break up becomes much more difficult as the viscosity ratio increases (i.e. as the matrix viscosity decreases or as the dispersed phase viscosity increases).

According to Wu [9], the size and shape of the dispersed phase in polymer blend are controlled by interfacial tension, rheological properties and deformation during mixing processing (such as extrusion). In this paper, PET/EP rubber and PA66/EP rubber blends (PA66 or PET as major phase: $85\%_{wt}$) processed by twin screw extrusion were studied. Both non compatibilized and compatibilized blends were used (by using carboxyl groups grafted EP rubber noted EPX rubber to reactively form in situ a copolymer with the matrix). To explain the morphology (size of the EP rubber dispersion) observed in this system where both matrix and dispersed phases are viscoelastic, and where the stress applied to the material is not pure shear, the author built his reasoning from Taylor's theory. Furthermore, he proposed to **extent the previous drop break-up condition to the case of a viscoelastic drop in a viscoelastic matrix**, by using the Weber number We.

$$We = 2C_a = \frac{\dot{\gamma}\eta_m d}{\Gamma} \geq \frac{F(R_v)}{\sin(2\alpha)}$$

<div align="right">**Eq. I-29**</div>

$\frac{F(R_v)}{\sin(2\alpha)}$ is an empirical function of:

1) the viscosity ratio R_v
2) the orientation angle α of the ellipsoid in the shear field
3) *and probably the elasticity*

In such a system, the orientation angle deviates from the Newtonian value ($\pi/4$). Moreover, the elasticity is not really taken into account. But, Wu considered that the entire matrix had the same elasticity and all the droplets had the same elasticity too. So, he made the **hypothesis that for a given system (given polymers and given composition), there was a given elasticity**.

The system studied in this paper fully respects this hypothesis:
- Given polymers: PET or PA66 as matrix and EP rubber as dispersed phase
- Given composition: 85%wt of matrix, which leads to a same kind of morphology: nodular dispersion of EP rubber.

To change the viscosity ratio in the system without changing polymers and process conditions, several molar masses of EP rubber dispersed phase were used.

Thus, by plotting the Weber number versus the viscosity ratio, Wu obtained a master curve as shown on Figure I-13.
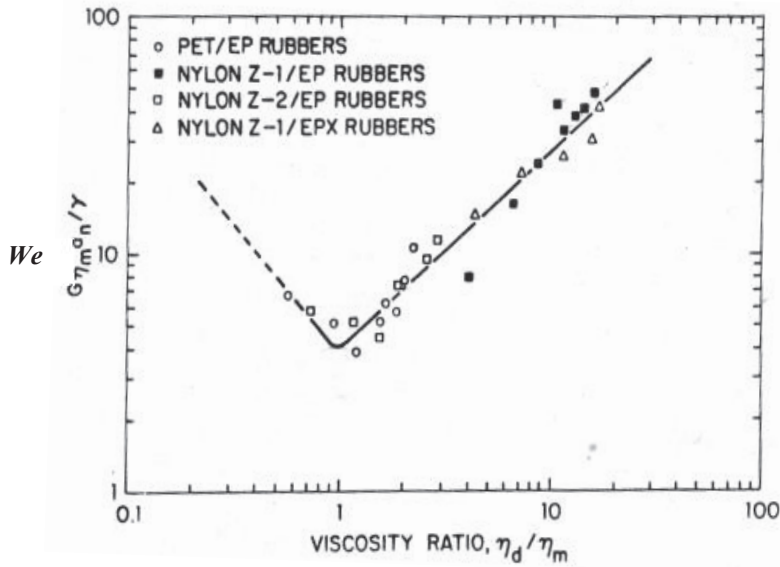
Figure I-13: Master curve of the Weber number *We* versus the viscosity ratio R_v obtained by Wu in PA66/EP rubber or PET/EP rubber blends (PA66 or PET as major phase: 85%wt) exhibiting nodular dispersion of EP rubber [9].

Each portion of the master curve was described with an equation which gives the interfacial and rheological influences on the size of dispersed phase:

For $R_v > 1$:

$$\frac{\dot{\gamma}\eta_m d}{\Gamma} = 4 \left(\frac{\eta_d}{\eta_m}\right)^{0.84} \qquad \text{Eq. I-30}$$

For $R_v < 1$:

$$\frac{\dot{\gamma}\eta_m d}{\Gamma} = 4 \left(\frac{\eta_d}{\eta_m}\right)^{-0.84} \qquad \text{Eq. I-31}$$

In this particular case, at given processing conditions and composition (that means $\dot{\gamma}$, η_m and Γ constant), the minimum of the curve (Eq. I-30 = Eq. I-31) corresponds to the smallest droplets size. It is obtained for a viscosity ratio of 1 and is defined as:

$$d_{min} = \frac{4\Gamma}{\dot{\gamma}\eta_m} \qquad \text{Eq. I-32}$$

Note that d_{min} equation is almost similar to Taylor's equation (Eq. I-27) for viscosity ratio R_v of 1. Thus, in the case of nodular dispersion morphology in viscoelastic polymer blends, the minimal droplets size should be quite well estimated by the value obtained for Newtonians systems by Taylor's theory.

According to Serpe et al [11], the Weber number *We* as defined by Wu [9] needs a correction in order to take into account the blend viscosity instead of the matrix viscosity, essentially when the dispersed phase fraction increases. The authors studied non-compatibilized PE/PA blends over a broad range of compositions. A rheometer was used for mixing. The velocity and the torque of this rheometer were used to calculate an average shear rate $\dot{\gamma}$ and the blend viscosity.

In this paper, contrary to Wu [9], various conditions were used:
- Various Polyethylenes (Medium Density Polyethylene MDPE and High Density Polyethylene HDPE) and Polyamides (PA11 and PA6) exhibiting different average molar masses
- Broad range of blends composition which leads to several kinds of morphology
- Several processing conditions: $\dot{\gamma}$ and temperature T

So, in these systems, viscosity ratio changes depending on the polymers used and processing conditions.

By plotting the Weber number versus the viscosity ratio, they obtained one master curve for each composition, parallel to Wu's equations straight lines as shown on Figure I-14. It appeared that at low dispersed phase concentration (PA or PE as dispersed phase), the nodular dispersion morphology obtained was nearly well described by Wu's equations [9]. It is consistent with the fact that Wu's equations were defined in systems exhibiting this kind of morphology.

Remarks about notations:

$G = \dot{\gamma}$: the shear rate
$\gamma = \Gamma$: the interfacial tension
$\eta_R = R_v$: the viscosity ratio
LV: Low Viscosity

Figure I-14: Weber number versus viscosity ratio at various dispersed phase concentrations in PE/PA blends and using a broad range of mixing conditions ($\dot{\gamma}$ and temperature *T*) [11].

Immiscible polymer blends like PE/PA blends behave like emulsions [11]. Therefore, at low dispersed phase concentration, the inter-particle distance is high and the deformation/break up of particles is controlled, in part, by the matrix viscosity (Taylor's theory). When the dispersed phase concentration increases, the coalescence probability increases too. In this case, according to emulsion models, the particles deformation may be controlled by the medium, that means by the blend viscosity. This is why Serpe et al. [11] proposed to modify Wu's equations (Eq. I-30 and Eq. I-31) using the blend viscosity instead of the matrix one. It was also necessary to make changes in order to have a correction for the effect of composition. In fact, the particle size increases when the dispersed phase concentration increases. The authors defined an empirical function to take this phenomenon into account:

$$F(\phi) = 1 - 4\underbrace{(\phi_d\phi_m)}^{+0.8}$$

Eq. I-33

Characteristic of thermodynamic
interactions during mixing

With:

- ϕ_d and ϕ_m, the volume fractions of dispersed phase and matrix respectively

Thus, the modified Weber number We^* is given by:

$$We^* = \frac{\dot{\gamma}\eta_{blend}d(1 - 4(\phi_d\phi_m)^{0.8})}{\Gamma} = f(R_v^*)$$

Eq. I-34

With:

- $R_v^* = \dfrac{\eta_d}{\eta_{blend}}$

- d is defined here as the number average particle diameter

By using this modified Weber number, **one** master curve was obtained (Figure I-15) over a broad range of compositions and processing conditions for a nodular dispersion morphology, which can be defined by the following equations:

For $R_v^*>1$:

$$We^* = 4\left(\frac{\eta_d}{\eta_{blend}}\right)^{0.84}$$

Eq. I-35

For $R_v^*<1$:

$$We^* = 4\left(\frac{\eta_d}{\eta_{blend}}\right)^{-0.84}$$

Eq. I-36

Figure I-15: Modified Weber number versus modified viscosity ratio [11].

For a given system and for a blend composition:

Eq. I-35 and Eq. I-36 are representative of viscosity change due to change of shear rate and temperature during mixing.

For given processing conditions:

Eq. I-35 and Eq. I-36 are representative of phase inversion.

Note that, on the plot of modified Weber number versus modified viscosity ratio (Figure I-15), the minimum of the curve does not correspond to the smallest particle size. In fact, several parameters vary along the ordinate axis (shear rate, particle size…).

We can also note that the data points which are not well aligned (Figure I-15) do not present a nodular dispersion morphology; they are closer to phase inversion with co-continuous morphology [11]. In fact, this graph is plotted for one kind of morphology: dispersion. However, this kind of study should be generally applicable for other types of morphology [9].
Serpe et al [11] also proposed to add the temperature influence on viscosities and thus, on particles size, by using Arrhenius equation.

To conclude, **drop break up in polymer blends exhibiting a dispersed morphology** has been studied during the last years, including both formulation and process parameters influence, in order to predict the minimal particle size reachable.

2.3.2. Coalescence

The coalescence also plays a key role in final morphology. In fact, if the particles break up, they may also merge. The coalescence process between two particles can be divided into four steps [21,30] as shown on the following diagram:

| STEP 1 | STEP 2 | STEP 3 | STEP 4 |

Approach of the two drops — *Deformation of the droplets due to the axial force and removal of the continuous phase trapped in the film between the droplets. (Drainage)* — *For a critical value of the gap thickness h_c, there is rupture of the film.* — *Evolution of the neck: Coalescence*
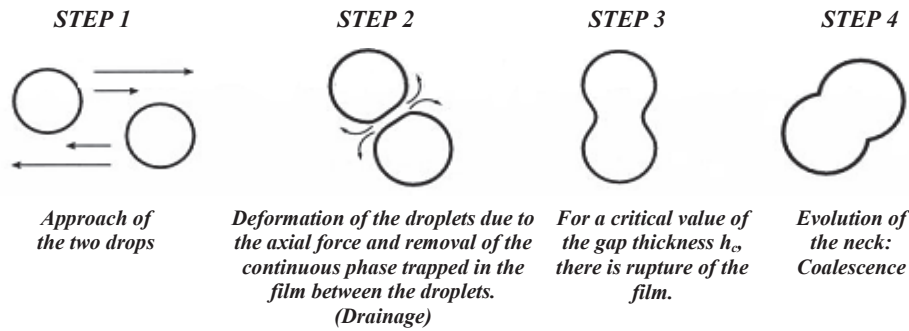
Figure I-16: Diagram of the coalescence process [21].

The coalescence can be observed and studied:

- *In quiescent conditions.* The material is subjected to annealing without any external stresses [21,30]. Forces affecting the droplets to approach themselves (step 1) can be Brownian motion, gravity or molecular forces (Van der Waals) [30,31].

- *Flow-induced coalescence.* This coalescence is generated by collision between two droplets which move at different velocities in the flow field [32]. So, typically, during extrusion, the droplets are brought together by the shear flow (step 1). This kind of coalescence is firstly controlled by the collision frequency, the contact force, the contact time (step 1) and then, by the drops flattening, film drainage (step 2), film rupture (step 3) and confluence (step 4) [33].

So, the first step of coalescence process to approach the drops themselves is controlled by various forces, depending on the conditions in which the coalescence is observed. Then, there are collisions between particles. We can note that only a few collisions result in coalescence, displaying the existence of a coalescence probability.

The coalescence time is defined as the time during which the distance between droplets decreases from the distance at the origin of coalescence to the critical distance until the film rupture. The coalescence strongly depends on the interfacial mobility, which allows the second step of matrix removal. Three cases were studied in the literature to estimate the coalescence

time: (1) immobile, (2) partially mobile and (3) mobile interfaces. In the case of immobile interfaces, the matrix cannot be easily removed from the space between the two droplets; there are "links" between both phases due to compatibilization for example. In the case of mobile interface, like polymer/polymer interface (without any compatibilizer), on the contrary, the matrix can easily be removed. The partially mobile interface is the intermediate case.

Under quiescent conditions, Fortelny et al [30] and Elmendorp et al [34] proposed equations for coalescence time in these three cases:

- Immobile interfaces:

$$t_c = \frac{3\eta_m R^2 F}{16\pi\Gamma^2 h_c^2}$$

Eq. I-37

- Mobile interfaces:

$$t_c = \frac{3\eta_m R}{2\Gamma} \ln\left(\frac{R}{2h_c}\right)$$

Eq. I-38

- Partially mobile interfaces:

$$t_c = \left(\frac{0.5\pi\eta_d F^{1/2} R^{3/2}}{(2\pi\Gamma)^{3/2}}\right)\left(\frac{1}{h_c} - \frac{2}{R}\right)$$

Eq. I-39

With:
- R, the droplet radius
- η_m, the matrix viscosity
- η_d, the dispersed phase viscosity
- F, the force affecting droplets (like gravity, Brownian motion or Van der Waals)
- Γ, the interfacial tension
- h_c, the critical value of the gap between the two drops, controlled by Van der Waals forces (~ few tens nm, typically)

This thickness h_c is defined as [33]:

$$h_c \approx \left(\frac{AR_{eq}}{8\pi\Gamma}\right)^{1/3}$$

<div align="right">Eq. I-40</div>

With:
- A, the Hamaker constant to define Van der Waals interaction parameter. For pure fluids, $A \sim 10^{-20}$ Joules, typically.
- R_{eq}, the equivalent radius:

$$\frac{1}{R_{eq}} = \frac{1}{2}\left(\frac{1}{R_1} + \frac{1}{R_2}\right)$$

<div align="right">Eq. I-41</div>

The equations governing film drainage between unequal particles (radii R_1 and R_2) are the same as those between equal particles of equivalent radius.

Typically, in quiescent conditions, the coalescence times for polymer blends (according to calculation) are between few tens and few hundreds seconds [30]. Experimentally, during high temperature (200°C) static annealing, the coalescence times was found to range from a few minutes to few tens of minutes in PE/PP compatibilized and non-compatibilized blends respectively [2].

Using this kind of theory, too high rates of coalescence are predicted, both in quiescent conditions and in flow-induced coalescence.

2.3.3. Balance between drop break up and coalescence

To study the relative roles of coalescence and single particle deformation in the final morphology after film extrusion, Gonzalez-Nunez et al [35] performed experiments on HDPE/PA6 blends in which they suppressed coalescence. Coalescence suppression was achieved by controlling either the concentration of minor phase (very low) or the level of interfacial interactions (very high by adding a lot of compatibilizer). The aspect ratio F was defined as:

$$F = \frac{4\pi A}{P^2}$$

<div align="right">Eq. I-42</div>

With, in 2D:
- A, the particles area
- P, particle perimeter

F=1 corresponds to a sphere.
F=0 corresponds to a fibre (maximal deformation).

By plotting the aspect ratio *F* of the dispersed phase versus the hot stretch ratio *HSR* (imposed during film extrusion), two regions were obtained as shown in Figure I-17:
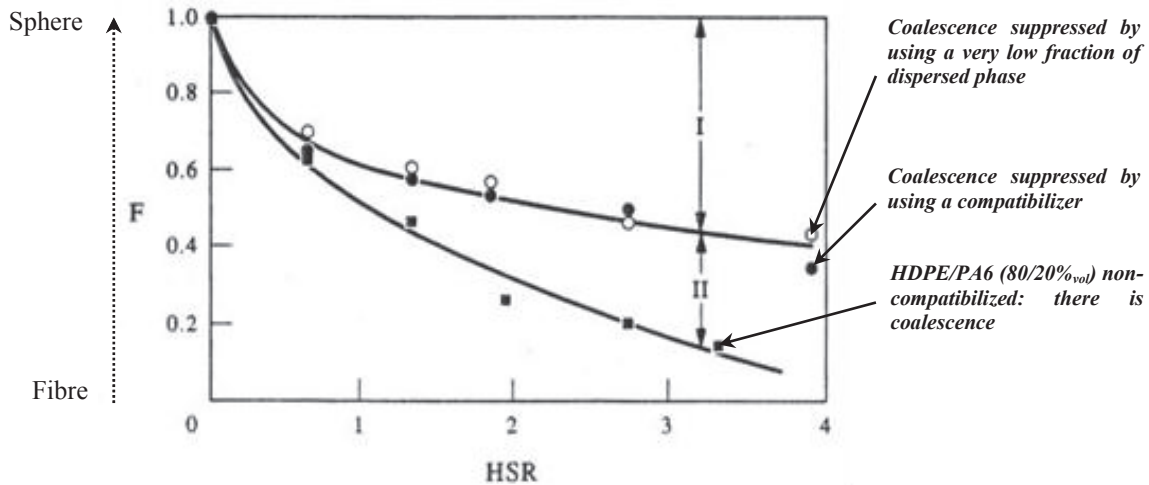
Figure I-17: Aspect ratio versus the hot stretch ratio (HSR) in HDPE/PA6 blends (80/20%vol) [35].

1) ***Region 1:*** Deformation in the absence of coalescence (only single particle deformation)
2) ***Region 2:*** Coalescence contribution

It is interesting to note that the two curves of the systems in which coalescence was suppressed superimpose. In non-compatibilized blend, in which there is coalescence, the PA6 dispersed phase is much more stretched (*F* decreases). Thus, the coalescence gives a significant contribution to the fibrillation of the minor phase. Moreover, the influence of coalescence on particle elongation is more and more pronounced with the increase of hot stretch ratio *HSR*.

We can add that these results also show that it is easier to stretch large particles (typically in the case of non-compatibilized blends) than smaller ones (typically in compatibilized systems).

So, besides the deformation and break-up of dispersed particles, coalescence is also very important in the morphology development. In fact, using Taylor's criterion (Eq. I-27), Willis et al [13] calculated a minimum value of the diameter in PA6/PP blends much smaller than the average diameter measured ($d_{calculated\ by\ Taylor's\ theory} < d_{measured}$).

Willis et al [13] used another model to describe their systems, Tokita's equation which is a balance between deformation, break up and coalescence:

$$r^* = \left(\frac{\Gamma}{\eta_m \dot{\gamma}}\right)\left(\frac{12P\phi_d + 48P^2\phi_d^2 E_{dk}}{\pi^2 \eta_m \dot{\gamma}}\right)$$

<div align="right">Eq. I-43</div>

With:

- r^*, the equilibrium particle size
- $\dot{\gamma}$, the shear rate
- Γ, the interfacial tension
- ϕ_d, the volume fraction of the dispersed phase
- η_m, the viscosity of the matrix
- P, the probability that two particles which have collided will result in coalescence
- E_{dk}, the macroscopic bulk breaking energy

Like in Taylor's equation (Eq. I-27), the interfacial tension is in numerator and both matrix viscosity and shear rate are at the denominator. However, Tokita's equation (Eq. I-58) also takes into account the influence of composition on the dispersed phase size. The condition to have particles break up is:

$$\eta_m \dot{\gamma} > E_{dk}$$

<div align="right">Eq. I-44</div>

The probability of particle-particle collision resulting in coalescence P is generally unknown. Elmendorp et al [34] proposed a way to estimate this probability depending on the interface mobility. Polymer/polymer interface (without any compatibilizer) is highly mobile which results in a larger probability of collisions resulting in coalescence. A mobile interface also enhances drainage, thus coalescence. Moreover, this probability is higher for small dispersed particles and decreases rapidly when the Weber number ($We = \frac{\dot{\gamma}\eta_m d}{\Gamma}$) increases.

2.4. Compatibilization of immiscible polymer blends

Mixing two polymers usually results in an immiscible blend which presents coarse morphology and poor adhesion between phases. Thus, the performances of this kind of system are very poor and irreproducible [25]. The objective of compatibilization is to prevent large scale phase separation. More precisely, the goals are [25]:

- **To reduce the interfacial tension** by decreasing the needed energy to create interface that facilitates the size reduction of dispersed particles.

- **To reduce coalescence**. In fact, the addition of a compatibilizer should decrease the interface mobility which results in a decrease of the probability of coalescence [34]. A significant coalescence inhibition seems to be only reached with a relatively high amount of compatibilizer to have a large interfacial coverage [36] (typically 0.3 chains/nm² in PA12/LDPE/MA-g-PE 30/68/2%$_{wt}$ exhibiting a nodular dispersion of PA12 of about 1μm). Huitric et al [36] proposed that steric repulsion played a predominant role in coalescence inhibition with the addition of compatibilizer. The compatibilizer seems to inhibit the drainage of the matrix between two drops, especially since the mobility of the matrix chains is reduced by their grafting.

- **To stabilize the morphology** during high stress and strain processing by limiting coalescence as detailed in the previous point.

- **To improve the adhesion** between the blend phases in the solid state: this facilitates stress transfer, hence improving mechanical properties.

Compatibilization can affect both morphology (size and shape of the phases of the blend) and microstructure (crystallinity, amorphous phase mobility…).

A majority of polymer blends are processed by extrusion. Without compatibilization, after this intensive mixing, the morphology of the immiscible blend formed is at the microscopic scale. This morphology which is not stabilized may coalesce during any subsequent heat or stress (like in a second step processing: injection molding, blow molding…). Coalescence may result in phase segregation at the macroscopic scale [37]. So, compatibilization is the way to promote the stabilization and the reproducibility of the morphology, and therefore of the properties (as checked with annealing experiments by Huitric et al. [36]).

The general idea of compatibilization is to add in the blend a component which will go to interfaces between incompatible polymers. Most generally, this interfacial agent is a copolymer. Nanoparticles can be used as well as compatibilizing agent as shown in recent studies [38,39].

2.4.1. Block copolymers

2.4.1.1. Structure of block copolymers

The block copolymers are macromolecules composed of two or more different polymers linked together by covalent bonding [40]. They can exhibit several architectures as illustrated in Figure I-18.

Di-block copolymer   Multi-block   Grafted block copolymer
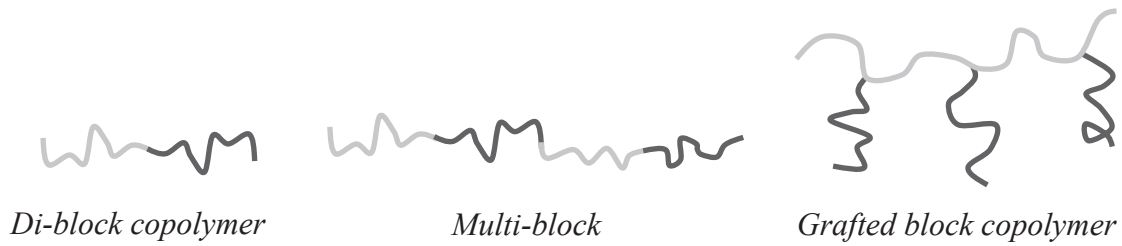
Figure I-18: Architecture of block copolymers.

In a block copolymer, the immiscible components cannot phase separate at a large scale because they are chemically linked to each other. Thus, they achieve nano-phase separation. The transition between disorder state and nano-separated state is called ODT (**O**rder **D**isorder **T**ransition).
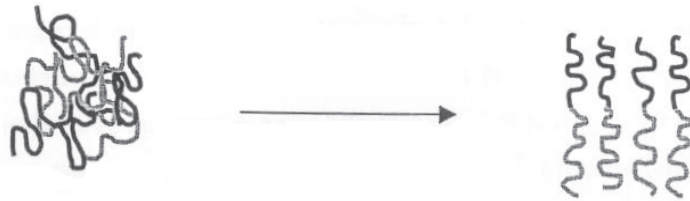
Figure I-19: Phase nano-separation of block copolymers in the melt [40].

The phase behaviour of a di-block copolymer may be controlled by the degree of polymerization N, the composition (fraction of each block) and the interaction parameter χ between the blocks (see *paragraph 2.1.2 Flory-Huggins theory page 21*). The strength of segregation of the two blocks is proportional to χN. A symmetric di-block copolymer is predicted to disorder (pass through its ODT) when $\chi N < 10$ [41]. Below the ODT, depending on the fraction of each block (f_A), the blocks would segregate into a variety of ordered structures as illustrated in Figure I-20.
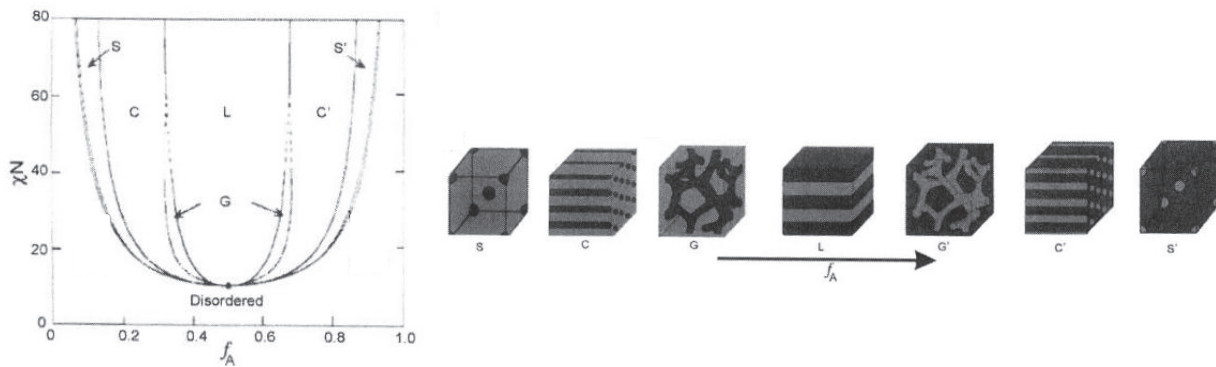
Figure I-20: Theoretical phase diagram of a di-block copolymer [41].

2.4.1.2. Interfacial coverage Σ

By considering the case of an immiscible polymer blend A/B with an interface saturated by a symmetric di-block copolymer A-b-B, the interfacial coverage Σ (number of chains par surface unit) of the symmetric di-block copolymer A-b-B is estimated [42,43]. The structure formed by the copolymer is lamellar. The concentration of block A is illustrated in Figure I-21.
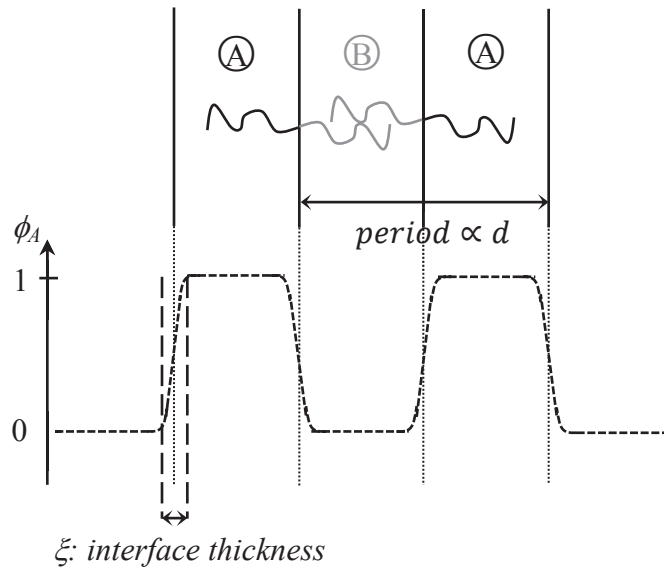
Figure I-21: Concentration profile of block A.

The interface thickness ξ is determined by the thermal fluctuations which allow one segment of B to penetrate in the domain rich in A. To calculate ξ, the energy required to mix one chain of B in A is first estimated. As the Flory interaction parameter χ (as detailed in *paragraph 2.1.2 Flory-Huggins theory page 21*) corresponds to the energetic cost to mix one monomer of B in A, the overall energetic cost would be generally of the order of kT (*k*, the Bolztmann constant; *T*, the temperature). Since χ is in unit of kT, the overall energetic cost may be written as:

$$g\chi \approx 1 \qquad\qquad \textbf{Eq. I-45}$$

With:
- *g*, the number of monomers

Figure I-22 shows a diagram of the penetration of a segment of B in the domain rich in A.

ξ: interface thickness
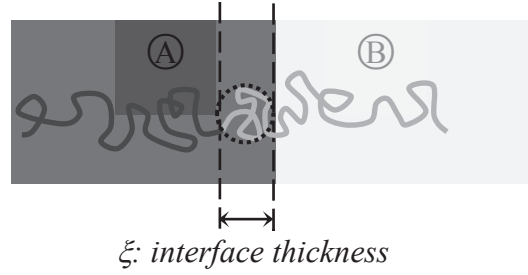
Figure I-22: Diagram showing the penetration of a segment of chain B penetrating in the domain rich in A.

The distance ξ on which a segment of B penetrates in the domain rich in A is defined as (assuming that this small portion of B chain is Gaussian):

$$\xi^2 \approx ga^2$$

<div align="right">Eq. I-46</div>

With:

- a, the length of one monomer

By combining Eq. I-45 and Eq. I-46, the interface thickness ξ is obtained:

$$\xi \approx \frac{a}{\sqrt{\chi}}$$

<div align="right">Eq. I-47</div>

The energy per unit surface γ is then estimated. γ is defined as the excess of energy stored in the interface and is given by:

$$\gamma \approx \frac{S_{unit}\xi\chi kT}{a^3} = \frac{kT}{a^2}\sqrt{\chi}$$

<div align="right">Eq. I-48</div>

With:

- S_{unit}, the unit surface ($S_{unit}=1$)
- a^3, the volume per monomer

A more precise calculation gives [42,43]:

$$\gamma = \frac{S_{unit}\xi\chi}{a^3} = \frac{kT}{a^2}\sqrt{\frac{\chi}{6}}$$

<div align="right">Eq. I-49</div>

This energy is directly linked to the interfacial tension between each block.

The volume occupied by a chain at the interface is illustrated in Figure I-23, with s the interfacial surface and d the chain length at the interface.
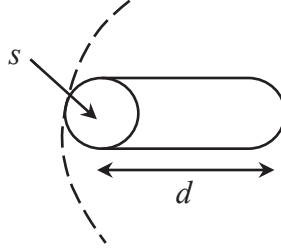
Figure I-23: Volume occupied by a chain at the interface.

As this volume also corresponds to the volume of each monomer a^3 multiplied by the number of monomers per chain N, the following equation is obtained:

$$Na^3 = sd \qquad \text{Eq. I-50}$$

Finally, the free energy per chain is given by:

$$\Delta F = \gamma s + \frac{3kTd^2}{2Na^2} \qquad \text{Eq. I-51}$$

The contribution of the surface energy γs tends to stretch the chains (to reduce s). The second term corresponds to the entropic cost for this chain stretching. So, by combining Eq. I-50 and Eq. I-51:

$$\Delta F(d) = \gamma \frac{Na^3}{d} + \frac{3kTd^2}{2Na^2} \qquad \text{Eq. I-52}$$

The equilibrium value of the chain length at the interface d_{eq} is obtained by minimizing the free energy per chain (Eq. I-52: $\frac{\partial \Delta F}{\partial d} = 0$) with respect to d:

$$d_{eq} \approx N^{2/3}a \left(\frac{\chi}{54}\right)^{1/6} \qquad \text{Eq. I-53}$$

Using this equilibrium value of the chain length at the interface, the interfacial coverage Σ can finally be estimated by:

$$\Sigma = \frac{1}{s} \qquad \text{Eq. I-54}$$

With:

$$s \approx N^{1/3}a^2 \left(\frac{\chi}{54}\right)^{-1/6} \qquad \text{Eq. I-55}$$

2.4.2. Compatibilization ways

L.A. Utracki [44] proposed a classification of compatibilization ways:
- Physical: a compatibilizer is added.
- Reactive: the compatibilizing species are chemically formed in situ.

2.4.2.1. Physical compatibilization

This compatibilization method presents different strategies [25,44]:
- Addition of a small quantity of a third component which is miscible with both phases (co-solvent).
- Addition of a small quantity of a copolymer exhibiting one part miscible with one phase and another part miscible with the other phase.

In A/B blend, a block copolymer A-b-B will generally locate at interfaces. The architecture of the copolymer (block, graft…) and the length of each block can induce different curvatures at the interface and thus can favour different morphologies.

According to Zhang et al [15], the architecture of grafted copolymers (density and length of grafts) at the interface also plays a role in the stabilization of morphology. They synthetized various PA6-g-PS copolymers (PA6 chains grafted on a PS backbone):
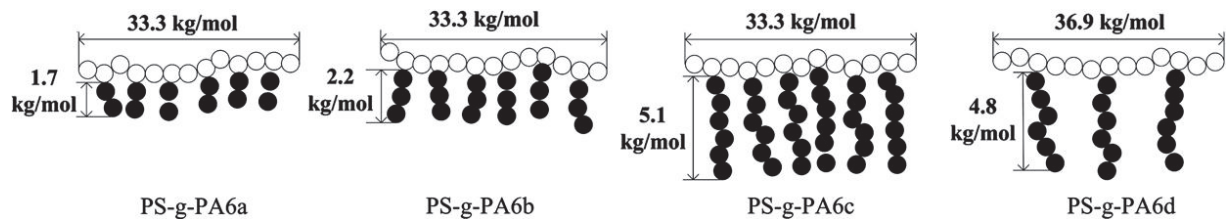
Figure I-24: Schematic representation of the molecular architectures and molar masses of the copolymers used [15].

They studied the influence of these copolymer architectures on the stability of PA6/PS blends morphology (50/50 and 40/60%$_{wt}$ containing 1%$_{wt}$ of copolymer) during high temperature static annealing. So, for a given number of grafts per backbone (comparing a, b and c), the longer the grafts (c), the higher compatibilizing and stabilizing efficiency. On the other hand, for a given backbone/graft composition (comparing b and d), graft copolymers having fewer and longer grafts (d) are more efficient.

In the case of block copolymer, to stabilize a co-continuous morphology (in PS/PE, PS/PMMA and FLPS/SAN blends) during static annealing, it was found that the most efficient architectures were di-block symmetric copolymer (blocks with a same length) [17].

The existence of an optimal molecular weight block copolymer may be due to a balance between the ability of the copolymer to reach the interface and its relative effectiveness as a compatibilizer [17]. In fact, chains of the copolymer must be able to entangle with each phase chains of the blend to insure efficient compatibilization, notably to insure blend final properties [16]. In the case of semi crystalline blends (like PA/PE), chains of the copolymer formed must be able to cocrystallize with each phase chains too. However, the efficiency of a block copolymer can be limited by the formation of micelles [45].

On the other hand, homopolymer chains must not be too long to be able to interpenetrate in copolymer brush at the interface [46]. Typically, to avoid macro-phase separation, the homopolymer must exhibit shorter or same length chains as the chains of the copolymer [40].

2.4.2.2. Reactive compatibilisation

The compatibilizing specie is generated in situ during the blending process [37,44]. Brown [37] classified various strategies for reactive compatibilization:

- Redistribution or "transreaction" to form block and random copolymers.
- Graft copolymer formation, by direct reaction of end-group of polymer A with pendent groups of polymer B for example.
- Block copolymer formation, by reaction between end-groups of each polymer for example.
- Crosslinked copolymer formation, by reaction of pendent functionalities of each polymer for example.
- Ionic bond formation to form block, graft or crosslinked structures.

To be efficient, compatibilization reaction must be compatible with the process used to produce blends. Most polymer blends are prepared by co-rotating twin screw extrusion, a continuous process exhibiting low residence times of the order of several tens of seconds typically. Thus, the compatibilization reaction has to exhibit high conversion rates and very fast kinetics. Another important aspect is the capability for reactive species to diffuse to interface.

2.4.2.3. Physical versus reactive compatibilization

Table I-2 summarizes drawbacks and advantages of the two kinds of compatibilization, physical and reactive [44]:

	Physical compatibilization	Reactive compatibilization
Advantages	• Control of added quantity in the medium • Copolymer structure is controlled	• Copolymer directly formed at the interface • Several structures are possible • One step transformation process
Drawbacks	• Copolymer diffusion to the interface • Copolymer can form micelles • Copolymer preparation	• Diffusion of reactive species to the interface • Reactive species excess • Low conversion rate if compatibilization reaction not fast enough

Table I-2: Comparison between physical and reactive compatibilization.

2.5. Parameters influencing the morphology

According to the balance between droplets break up and coalescence mechanisms, several kinds of morphology can be developed. As expected, the major component in a blend may constitute the continuous phase. Then, by increasing the dispersed phase amount, the coalescence probability increases and the droplets become larger. The phase inversion is preceded by elongation of the dispersed phase which will coalesce to form a continuous network [5]. Representative examples of these various kinds of morphology obtained in our systems in Scanning Electron Microscopy after selective minor phase etching are shown in Figure I-25.

Nodular dispersion   *Stretched dispersion*

Fibrils   *Co-continuous*
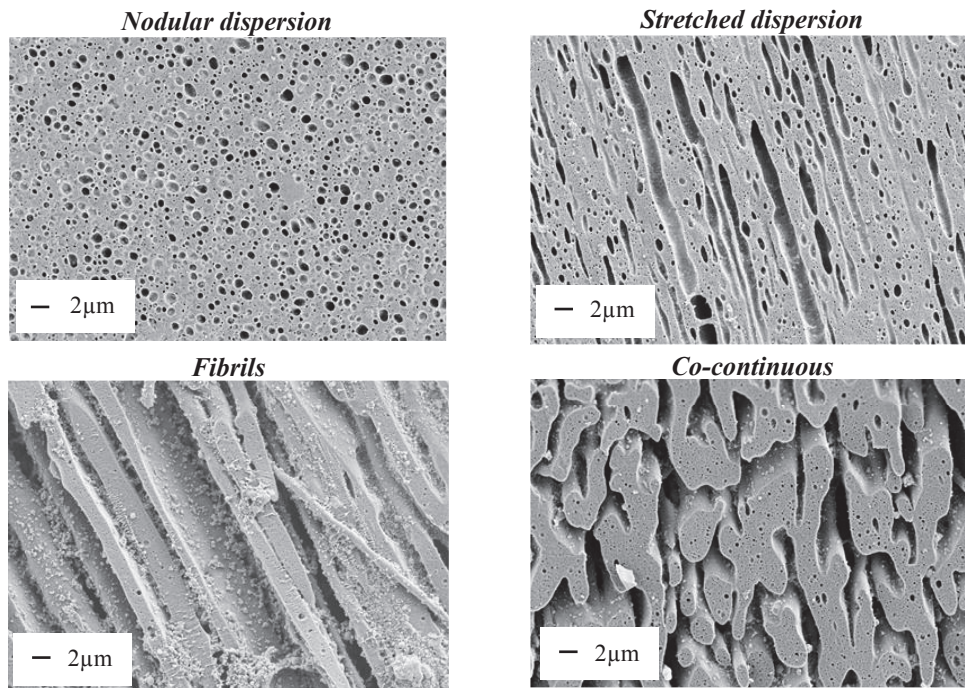
Figure I-25: Representative examples of the kinds of morphology obtained in immiscible polymer blends: SEM micrographs of our systems PA/PE after minor phase etching.

Stretched dispersion and fibrils differ in the aspect ratio: fibrils are several tens of micrometers long.

Controlling morphology is the challenge to design polymer blends with desired properties. This section describes more in details the kinds of morphology shown in Figure I-25 and the influence of various parameters:

1) *Influence of the compatibilizer*

2) *Influence of the rheology of polymers in the blend*.

In fact, the polymer blends are mostly prepared in the molten state, mostly by co-rotating twin screw extrusion. Thus, the rheological behavior of polymers during blend processing is an essential parameter in morphology development. Viscosity depends on the polymer itself and also on process parameters (shear rate and temperature). Many papers deal with the influence of extrusion parameters (temperature, shear rate, residence time, order of components addition) on rheology and morphology [9,19,35,47,48,49,50,51,52,53,54].

2.5.1. Nodular dispersion morphology

This kind of morphology was largely observed. In fact, it is facilitated by thermodynamic equilibrium.

2.5.1.1. Influence of the compatibilizer

By increasing the compatibilizer amount, the typical size of the dispersion decreases. The particles size reached is about few μm for uncompatibilized blends and less than 1μm for compatibilized systems typically [13]. This particle size reduction is due to the ability of the compatibilizer to reduce the interfacial tension between both phases (dispersed and matrix). Beyond a given compatibilizer amount, the interface is fully covered (see *paragraph 2.4.1.2 Interfacial coverage Σ page 47*) and no more effect is expected by adding more compatibilizer.

Macosko et al [16] proposed a diagram for morphology development according to the balance between break up and coalescence mechanisms in both compatibilized and non-compatibilized polymer blends (here PS/PMMA 70/30%$_{wt}$, P(S-b-PMMA) symmetric di-block copolymer used as compatibilizer) exhibiting a nodular dispersion morphology.
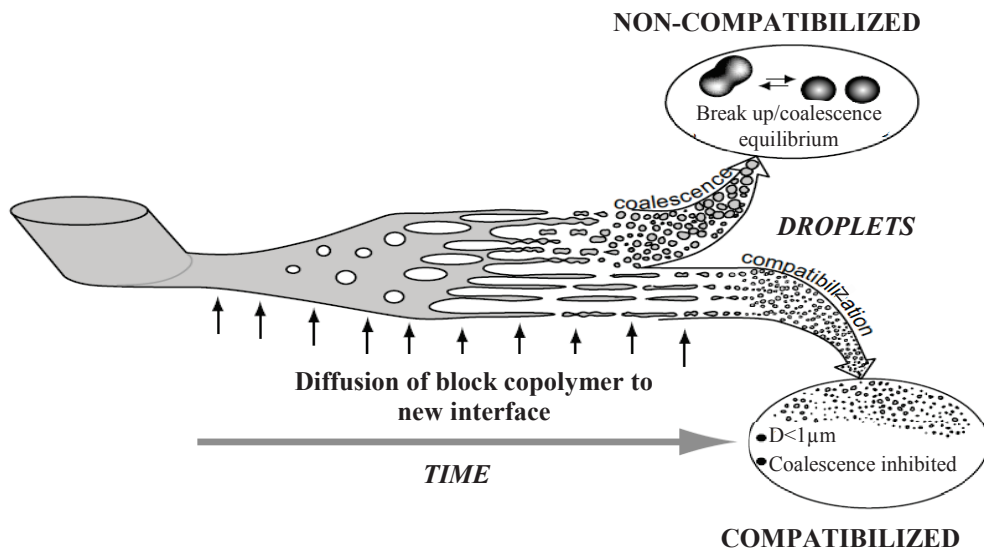
Figure I-26: Schematic of morphology development during melt blending [16].

In the case of compatibilized blends, this diagram was defined for system with physical compatibilization (addition of a di-block copolymer).

However, in the case of in situ reactive compatibilization, if the reaction is very fast with high conversion rate and if there is no limitation of reactive species diffusion to the interfaces, the reaction may be completed at the very early stage of extrusion. In this case, this diagram may be also valid.

2.5.1.2. Influence of the rheological behavior

According to Lee et al (without any compatibilizer, over a broad range of viscosity ratios) [55]:

- **For asymmetric blends** (one component in major concentration), the composition determines morphology: The major component may be the continuous phase. The rheology of phases should have an influence on the size of the dispersion. So, the dispersion is expected to be finer when the lower viscosity polymer is dispersed [56].

- **For symmetric blends** (50/50 $\%_{vol}$), the viscosity ratio controls morphology: The more viscous polymer may constitute the dispersed phase. In fact, from the point of view of the minimal energy dissipation principle in channel flow of two immiscible liquids, the component having lower viscosity is expected to form the continuous phase [55].

2.5.2. Stretched dispersion morphology

- In 1986, Utracki et al [57], studying the extrusion of non-compatibilized PA6/HDPE blends (PA6 as dispersed phase from 0 to 30%$_{wt}$), proposed a fibrillation mechanism. "The average diameter of the fibrils seems to be quite comparable to the average size of the original droplets, while their volume is many times larger". They concluded that the fibrillation, extensional mechanism, was associated with a specific shear-induced coalescence.

- In 1998, Huitric et al [10] proposed another mechanism. At low volume fraction of dispersed phase, the particles size at equilibrium is a compromise between break up and coalescence. When the volume fraction of dispersed phase increases, there is more coalescence, the droplets become larger and then, could deform into fibres. This kind of fibrillar morphology may be formed just before the phase inversion and thus, could be an indicator of co-continuity proximity [5].

2.5.2.1. Influence of the compatibilizer

According to Kamal et al [58], Rodriguez-Veloz et al [59] and Gonzalez-Nunez et al [35], the compatibilizer content has to be optimized in order to have a compromise between fibrils or platelets formation and phases adhesion. In fact, fibrils seem to be formed by drops elongation and it is easier to deform large particles (low compatibilizer content) than small ones (high compatibilizer content). On the other hand, a minimal compatibilization is needed to have sufficient adhesion between the two phases, to insure good final properties.

2.5.2.2. Influence of the rheological behavior

A study of Min et al [60] (PE/PS, PE/PC and PE/PA6 non-compatibilized blends) showed that the transition from drops to fibres would be controlled by the viscosity ratio ($R_v = \frac{\eta_{dispersed\ phase}}{\eta_{matrix}}$). With a viscosity ratio between 0.7 and 1.7, drops could be elongated into fibres with the shear stress in the flow direction. In the case of viscosity ratio larger than 2.2, droplets break-up was observed. These experiments were done in a capillary rheometer. However, we can imagine similar behaviour in the extruder die.

The schematic view of longitudinal phase morphologies at various viscosity ratios $\eta_d/\eta_m = \lambda$
(A) $\lambda < 0.7$
(B) $0.7 < \lambda < 1.7$
(C) $\lambda > 2.2$.
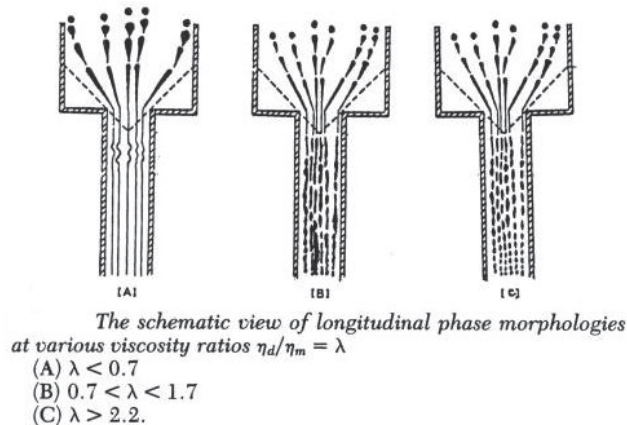
Figure I-27: Morphologies developed in a capillary as a function of the viscosity ratio [60].

2.5.3. Co-continuous morphology

This kind of morphology can be obtained [23]:
- kinetically through phase inversion under shear in ***immiscible*** blends (micrometer scale)
- thermodynamically via spinodal decomposition from ***miscible*** system, by quenching into the spinodal domain (nanometer scale) (see *paragraph 2.1.6 Spinodal decomposition page 29*).

So, in immiscible polymer blends like PA/PE, co-continuity is reached with phase inversion.

2.5.3.1. Description of phase inversion

Lee and Han [55] studied four non-compatibilized systems (PS/PMMA, PS/PC, PS/HDPE and PS/PP) with compositions 70/30, 50/50 and 30/70%$_{wt}$ prepared by co-rotating twin screw extrusion. At the end of each extrusion run, the screw was quenched to minimize variations of morphology and pulled out. So, the morphology of blends was followed all along the screw from the feed hopper to the exit of the die. Figure I-28 illustrates this morphology evolution along the screw.
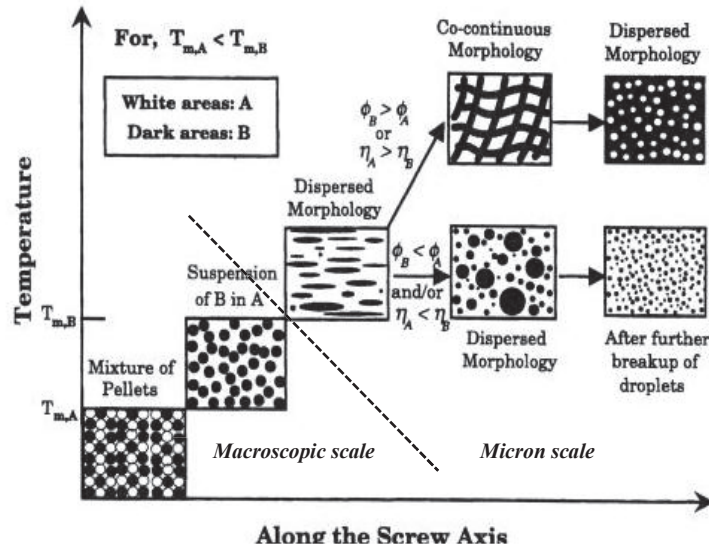
Figure I-28: Diagram of the morphology evolution along the screw [55].

In the diagram, polymer A which exhibits the lowest melting temperature melts first. A macroscopic dispersion of the polymer B which exhibits the highest melting temperature is first expected. Then, depending on the composition and the viscosity ratio, polymer B could remain in dispersed state, or phase inversion could occur. So, co-continuity is a transition between two states of dispersion. The authors underline the instability of this morphology in these non-compatibilized blends [55].

2.5.3.2. Percolation theory

Phase inversion and co-continuity can be described by the percolation theory [5,6,7,8]. Depending on balance between droplets break up and coalescence, as the concentration of the minor phase increases, droplets become close enough to behave as if they were connected until phase inversion is reached. As illustrated in Figure I-29, there is a composition range where co-continuity may exist.
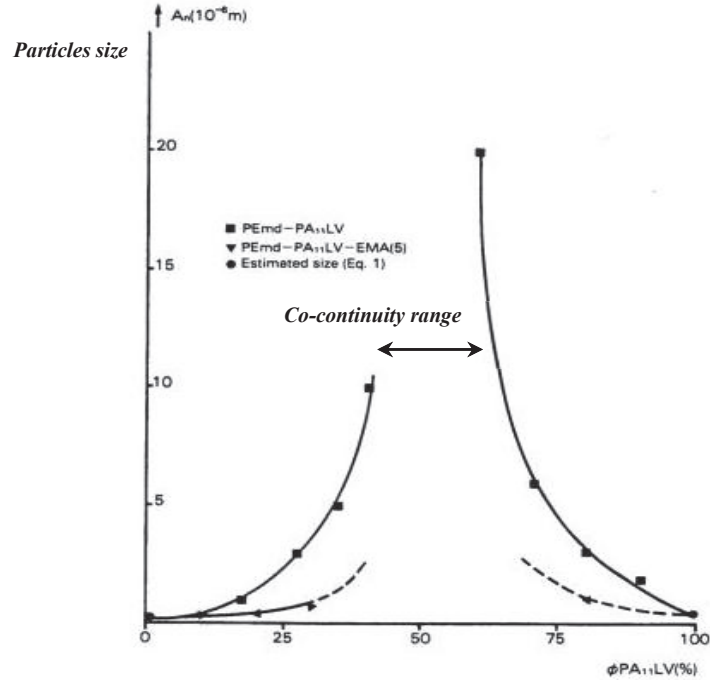
Figure I-29: Morphology as a function of composition in MDPE/PA11 compatibilized (by ethylene-maleic anhydride EMA) and non-compatibilized blends [11].

According to percolation theory, universal relationships in a form of power law can be found for a series of properties [8]:

$$P - P_{cr} \propto (\phi - \phi_{cr})^x \qquad \text{Eq. I-56}$$

With,

- ϕ, the volume fraction of one blend component
- ϕ_{cr}, the threshold volume fraction for the formation of infinite co-continuous morphology
- P, the property
- P_{cr}, the value of P at the critical volume fraction ϕ_{cr}
- x, the universal exponent

The value of the universal exponent x is characteristic of the property tested.

Many papers are dealing with percolation theory indirectly on different properties like electrical conductivity or mechanical properties [61,62]. However, to the best of our knowledge, the percolation theory does not seem to be used directly to predict quantitatively the characteristic size of the morphologies.

2.5.3.3. Influence of the compatibilizer

Bourry and Favis [5] studied physically compatibilized and non-compatibilized PS/HDPE blends over the full range of compositions. When a compatibilizer is added, the dispersed phase becomes less elongated, which shifts the percolation point to higher concentration of dispersed phase.
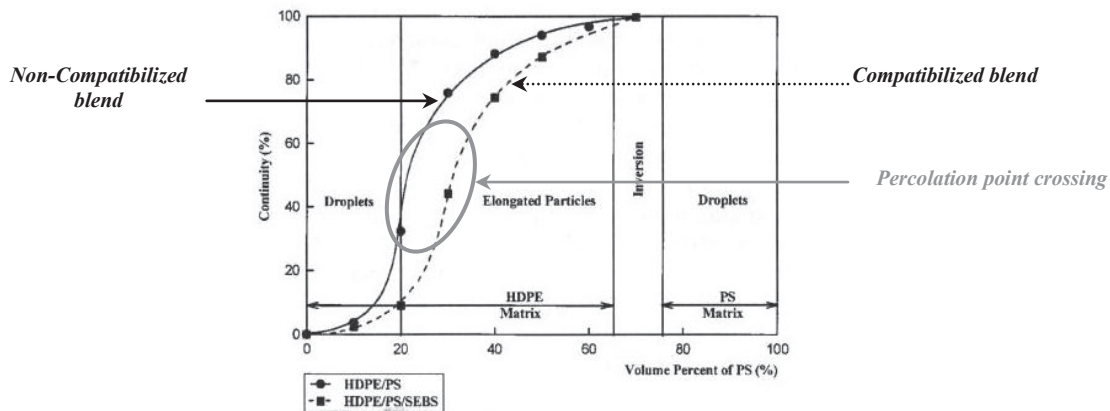
Figure I-30: Continuity of PS phase in HDPE/PS blends as a function of composition [5].

This shift in percolation threshold may be more precisely due to a limitation of coalescence in compatibilized systems.

Zhang et al [15] showed in PS/PA6 blends that by adding 1%$_{wt}$ of compatibilizer (grafted copolymer PS-g-PA6), the co-continuity domain was narrowed down and the lower limit of co-continuity domain of the more viscous component was shifted to a higher concentration. They explained this result by the greater tendency of the less viscous component to be the matrix. As co-continuity is developed by droplets coalescence, they also assumed that the **coalescence was reduced by adding a compatibilizer, consequently disfavoring the formation of co-continuous morphologies.**

Dedecker and Groeninckx [63] observed the same **narrowing of co-continuity domain by adding a compatibilizer** (functionalized polymer styrene-maleic anhydride) in PA6/PMMA blends due to coalescence reduction. They also observed a shift of co-continuity domain to lower amount of PA6 in both compatibilized and non-compatibilized blends when the molecular mass (M_w) of PA6 decreased (from 44 000 to 25 000g.mol^{-1}). This was due to the lowest viscosity of low molecular weight PA6 which tended to encapsulate PMMA [63].

Willis et al [13] studied the influence of adding a ionomer as compatibilizer in PP/PA6 and HDPE/PA6 blends over a broad range of compositions. The domain of existence of co-continuity was reduced with the addition of compatibilizer in PP/PA6 systems. On the contrary, in the case of **HDPE/PA6 blends, the co-continuous domain was still the same**, as shown on Figure I-31.
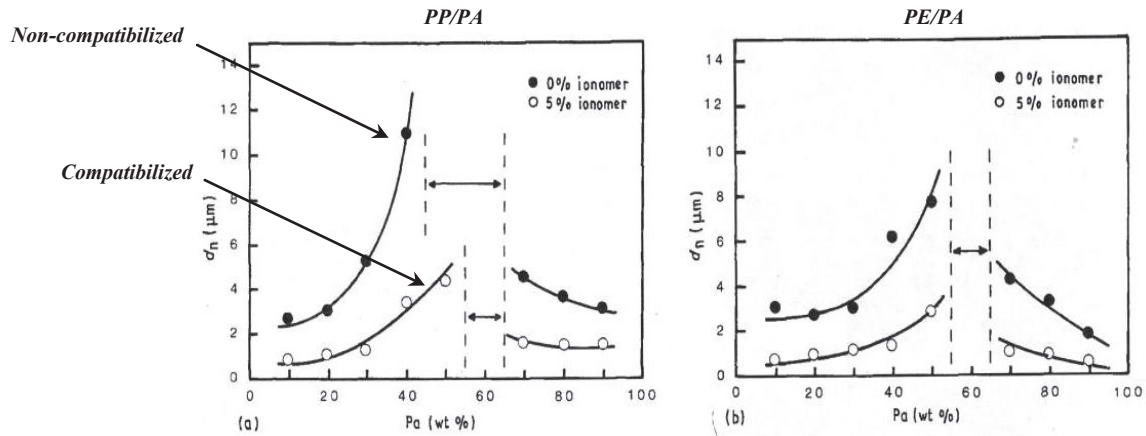
Figure I-31: Composition dependence of the size of the dispersed phase (measured by image analysis on SEM micrographs) in PP/PA blends with and without compatibilizer [13].

So, according to these studies, by adding compatibilizer, the co-continuity may be shifted to higher concentration of dispersed phase and the co-continuous range could be narrower. However, in some studies like Willis et al [13] work, compatibilized HDPE/PA6 compatibilized blends exhibit the same co-continuous range as in non compatibilized systems.

To explain the differences observed in the co-continuity ranges, Li et al [64] studied three kinds of interfaces in blends based on HDPE prepared in an internal mixer in order to propose a mechanism for co-continuity formation depending on lifetimes of both droplets and fibres. So, they studied compatible blends (HDPE/SEBS or HDPE/SEB) and found that the co-continuity was controlled by thread-thread coalescence. In the case of incompatible (HDPE/PS), they found that co-continuity was controlled by droplet-droplet coalescence. Finally, for compatibilized blends (HDPE/PS+compatibilizer SEBS or SEB), they found that co-continuity range was much narrower than in compatible blend. In this case, co-continuity was controlled by reduced droplet-droplet coalescence.

To conclude, adding compatibilizer to blends exhibiting co-continuous morphology could shift the percolation threshold to higher concentration of dispersed phase and reduce the composition domain of existence of co-continuity in some cases, depending on the kind of interface involved.

2.5.3.4. Influence of the rheological behavior: Phase inversion prediction models

Several models to predict phase inversion composition have been proposed in the literature [2,8,12,65]. The first model, based on viscosity ratios, was developed by Paul and Barlow in 1980 and generalized by Miles and Zureck in 1988 [66,67], with ϕ_i, the volume fraction of phase i and η_i, the viscosity of phase i:

$$\frac{\phi_1(vol)}{\phi_2(vol)} = \frac{\eta_1(\dot{\gamma})}{\eta_2(\dot{\gamma})}$$

Eq. I-57

Willis et al [13] used this model of phase inversion on polyolefine/polyamide (PP/PA6 and HDPE/PA6) compatibilized (using 5% ionomer) blends which gave a quite good prediction of the phase inversion.

Another model involving the viscosity ratios was developed in 1984 by Metelkin and Blekht [5,68]:

$$\phi_2(vol) = \left[1 + \frac{\eta_1}{\eta_2}\left(1 + 2.25ln\frac{\eta_1}{\eta_2} + 1.81\left(ln\frac{\eta_1}{\eta_2}\right)^2\right)\right]^{-1}$$

Eq. I-58

L.A. Utracki proposed in 1991 a model based on emulsion theory [8]:

$$\frac{\eta_1}{\eta_2} = \left(\frac{\phi_m - \phi_2}{\phi_m - \phi_1}\right)^{[\eta]\phi_m}$$

Eq. I-59

With:
- $\phi_m = 1 - \phi_{percolation}$, the maximum packing volume fraction, related to the percolation threshold volume fraction for emulsions
- $[\eta]$, the intrinsic viscosity, a measure of the hydrodynamic volume of the dispersed phase

So, most of the models to explain phase inversion only consider the viscosity ratio and predict that the less viscous phase would preferentially encapsulate the second phase to form the matrix [68]. By calculating the predicted phase inversion composition using these models, it appears that when the shear rate increases, the predicted composition is shifted farther and farther from the experimentally observed one [5]. So, these models seem to be representative of phase inversion only at low shear rates, which is not the case in a twin-screw extruder.

Bourry and Favis [5] considered the influence of elasticity on phase inversion considering dynamic shear properties of polymers (here HDPE/PS non compatibilized blends). The more elastic phase would tend to form the matrix (at sufficient concentrations). The polymers exhibit viscoelastic behaviour, intermediate between elasticity (reversible strain) and plasticity (non-reversible strain beyond elasticity threshold). Under dynamic shear, the complex shear modulus G^* (Pa) is defined as:

$$G^* = G' + iG''$$

With:

- G^*, the complex modulus
- G', the elastic modulus, representing the elastic part of the polymer behaviour
- G'', the viscous modulus (dissipative), representing the viscous part of the polymer behaviour

Bourry and Favis [5] proposed a model to take into account elasticity, using G' the elastic modulus and $tan\delta = \frac{G''}{G'}$, the loss angle. They considered two equations:

$$\frac{\phi_1(vol)}{\phi_2(vol)} = \frac{G_2'(\omega)}{G_1'(\omega)}$$

$$\frac{\phi_1(vol)}{\phi_2(vol)} = \frac{tan\delta_1}{tan\delta_2}$$

With:

- ϕ_1 and ϕ_2, the volume fractions of each polymer
- G', the elastic modulus
- $tan\delta = \frac{G''}{G'}$, the loss angle

Quite good predictions were obtained on PS/HDPE non-compatibilized blends using this last model [5].

The first normal stress difference (measured versus shear rate) can constitute an indication of elasticity effects. In quiescent conditions, the macromolecular chains hold a nearly spherical volume. Under shear, these spheres deform into ellipsoids whose long axis tends to rotate to the flow direction (anisotropy in normal forces). The elasticity of the polymer tends to bring back these ellipsoids to spheres.

The restoring force (directly proportional to elasticity) is maximum in the direction of the flow, which create a compression in this flow direction. This compression implies $\sigma_{11} < \sigma_{22}$. So, for a viscoelastic fluid, the application of a simple shear stress generates normal stress differences (contrary to Newtonian fluid).

According to the shear stress tensor:

$$\sigma = \begin{vmatrix} \sigma_{11} & \sigma_{12} & 0 \\ \sigma_{21} & \sigma_{22} & 0 \\ 0 & 0 & \sigma_{33} \end{vmatrix} \quad \begin{array}{l} \textit{Associated to a simple} \\ \textit{shear in direction 1 in} \\ \textit{(1, 2) plan} \end{array} \qquad \textbf{Eq. I-63}$$

The first normal stress difference is defined as:

$$N_1 = \sigma_{11} - \sigma_{22} \text{ (<0 because } \sigma_{11} < \sigma_{22}) \qquad \textbf{Eq. I-64}$$

According to Huitric et al [10], the relative elasticity of polymers only affects the strain recovery. Thus, for a viscosity ratio of 1:

- $|N_1(dispersed \cdot phase)| > |N_1(matrix \cdot phase)|$: a spherical dispersion is expected due to the strain recovery.
- $|N_1(dispersed \cdot phase)| < |N_1(matrix \cdot phase)|$: there is not strain recovery, which favors the preservation of a stretched dispersed/fibrillar morphology.

So, in the system studied by Huitric et al [10] (non-compatibilized PA12/LDPE blends), $|N_1(PE)| < |N_1(PA)|$ (lower elasticity of PE). That could explain an earlier transition to fibrillar morphology and then to co-continuity when PE is the dispersed phase than when PA is the dispersed phase.

As already described in the previous section (paper of Li et al [64]), we can note that in PA12/LDPE blends, thread-thread coalescence also seems to favor development of co-continuity at lower concentration of dispersed phase. However, in the case of PA12/LDPE systems, the development of fibers is explained by differences in elasticity between the dispersed phase and the matrix, whereas in Li et al work [64], the fibers formation is explained by a low interfacial tension in compatible blends.

So, even if they are immiscible, all the polymer blends have not the same behavior. Therefore, co-continuity may be a combination of all these effects: viscosity, elasticity and kind of interface. However, all the models presented in this section predict a unique composition for phase inversion, whereas, experimentally, there is often a broad range of compositions in which the phase inversion occurs. That shows the complexity of this phenomenon and the difficulty to design an universal model [68].

2.5.4. Coupling between parameters

So, we have seen in the previous paragraphs that several parameters influence the morphology in immiscible polymer blends including composition, rheology and process parameters. These parameters are often linked (such as viscosity which is affects by temperature and shear rate applied during blend processing). Thus, the final morphology depends on both formulation and process.

Rodriguez-Veloz et al [59] showed the **coupling existing between process parameters**. In fact, by studying the development of lamellar morphology by film cast of HDPE/PA6/Compatibilizer MA-g-HDPE (PA6 as the dispersed phase), the authors showed that the throughput was coupled with the temperature profile:

1) By increasing the throughput, the residence time decreased; there was a reduction of the drops break up.
2) Then, the temperature profile can be adapted to melt the PA at the end of the screw and therefore develop bigger particles easy to deform into platelets into the die.

Huang et al [69] study can illustrate the **coupling between formulation and process parameters**. PA6/HDPE/MA-g-HDPE compatibilized blend (12/85/3%$_{wt}$) with a viscosity ratio larger than 1 (between 3 and 7 depending on the HDPE used) was studied in extrusion film cast process in order to develop lamellar morphology of PA6 in HDPE. A lamellar morphology was developed despite this high viscosity ratio, adapting the screw profile and the screw rotation speed of the extruder. In fact, when the viscosity ratio increased (here by decreasing the viscosity of the matrix HDPE), the matrix imposed a lower shear stress to the dispersed phase. Thus, a higher shear rate (screw rotation speed and screw profile) should be used to increase the deformation of the dispersed phase in order to yield lamellar morphology.

3. Polyamide/Polyethylene blends

In this section, Polyamide/Polyethylene blends (PA/PE), which have been studied in this work, are presented in more details. The main benefits of this kind of blends will be first presented. Then, as it is an immiscible polymer blend, the compatibilizing systems observed in the literature for PA/PE will be detailed. Finally, the morphologies obtained in the literature and the associated properties will be described.

3.1. Benefits of Polyamide/Polyethylene blends

At the beginning, polyethylene was added to polyamide in order to improve impact resistance and to reduce moisture absorption of polyamide. On the other hand, polyamide was added to polyethylene to increase stiffness and barrier properties (especially to non-polar solvent) of polyethylene.

PA/PE blends are immiscible, so compatibilization is required. That immiscibility is precisely the reason why this kind of blends is interesting. In fact, average properties could be expected in case of miscible blends. On the contrary, in PA/PE immiscible blends, the formulation and the flow imposed to the polymers during processing may generate various morphologies which lead to different properties [70].

3.2. Compatibilizing systems for PA/PE blends

In the case of PA/PE blends, the most efficient compatibilization systems and so mostly observed in literature are reactive ones with addition of reaction initiator species. Table I-3 shows compatibilizers used in literature for PA/PE blends.

Reactive moieties	Reaction with	Nature	Remarks	Commercial name	Examples of literature
Maleic Anhydride MA	NH_2 end-group of PA	HDPE grafted maleic anhydride (or ethylene/MA copolymer)	• Water formed during this condensation reaction • A coupling agent (such as bisoxazoline) which reacts with anhydride and COOH of PA can be added.	Fusabond (DuPont), Orevac (Arkema), Polybond (Chemtura)…	[11,49,58,59,69]
Maleic anhydride	NH_2 end-group of PA	SEBS (block) grafted maleic anhydride	• Water forming • Elastomer: impact modifier	Kraton FG (Kraton)	[71] (PA/PP)
Epoxide	COOH and NH_2 end-group of PA	Ethylene/glycidyl methacrylate copolymer	• No water is formed during the reaction	Lotader GMA (Arkema)	[72,73]
Carboxyl moieties	NH_2 end-group of PA	Ethylene acrylic acid copolymer	• Water forming • A coupling agent can be added	Primacor 449 (Dow)	[74,75]
Ionic clusters	NH_2 end-group of PA	Terpolymer (80% PE, 20% of a mixture of methacrylic acid, partially neutralized with zinc ions (~70%) and isobutyl acrylate	• Ionic bonds: thermo-reversibility • Maybe, covalent bonds between non-neutralized COOH and amine moieties of PA (water formed)	Surlyn Ionomer 9020 (DuPont)	[35,47,48,76,77,78]

Table I-3: Reactive compatibilization systems for PA/PE blends in literature.

The reactions involved are the followings.

- Maleic anhydride with amine end-group of PA:
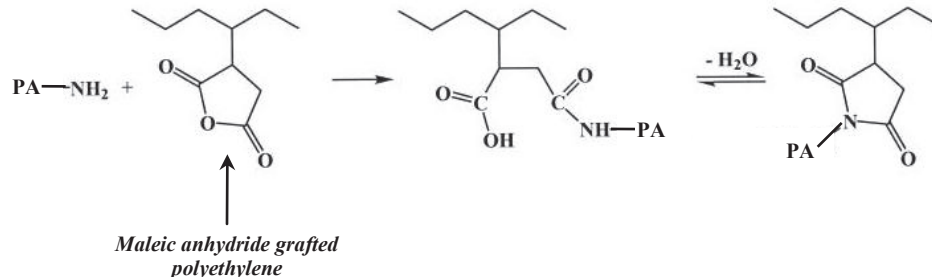
Figure I-32: Reaction between amine and maleic anhydride [21].

This reaction produces water, which could be harmful for Polyamide which is very sensitive to moisture. During blending process (like extrusion), a venting zone should be used in the barrel profile in order to eliminate the water produced.

In homogeneous conditions, the reaction between aliphatic amine and cyclic anhydride moieties (terminal groups on PS polymer chains) is very fast and nearly total with a conversion of 99% after 2 minutes at 180°C [79,80]. In static conditions, the reaction at the interface between two polymer phases is very slow. However, under flow conditions, (like in extrusion process), the reaction is tremendously accelerated (typically, multiplied by 1000), probably due to convection as well as the creation of fresh interface [79,80]. According to Orr et al [80], the reaction between amine and anhydride is not diffusion controlled at least on the processing time scale.

- Carboxylic acid moieties with amine end-group of PA:
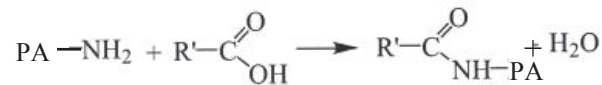
Figure I-33: Reaction between amine and carboxylic acid moieties [21].

This reaction also produces water and therefore, needs a venting zone during processing.

- Ethylene/glycidyl methacrylate copolymer with a) amine, b) carboxylic end-group of PA
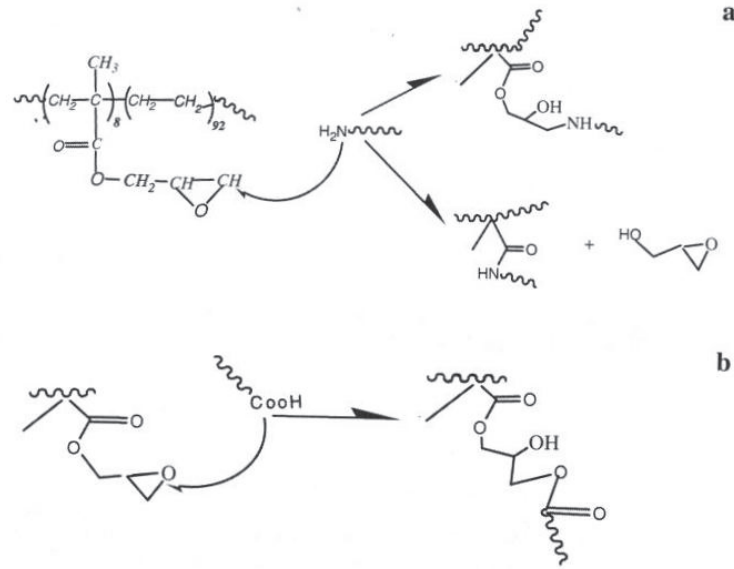
Figure I-34: Reaction between GMA (Glycidyl methacrylate) and a)amine, b)carboxylic acid [81,73].

Note that after reaction a), the amine of PA could react again with a new epoxide moiety.

Macosko et al [79,80] summarized the coupling kinetics in homogeneous conditions at 180°C of several Polystyrene (PS) with different terminal groups. Table I-4 shows the conversion reached after 2 minutes.

Group 1	Group 2	Conversion at 2min at 180°C	Reaction rate k (kg/mol.min)
Maleic Anhydride moieties	NH_2 end-group of PA	99%	$\sim 10^3$
Carboxylic acid moieties	NH_2 end-group of PA	0%	
GMA epoxy	NH_2 end-group of PA	1.8%	0.34
GMA epoxy	Carboxylic end-group of PA	9%	2.1

Table I-4: Reactivity between the various reactive groups for compatibilization [79,80].

It clearly appears that the most reactive pair is amine/maleic anhydride. So, **in this study, maleic anhydride grafted polyethylene is used as compatibilizer in PA/PE blends.**

3.3. Morphologies and associated properties in PA/PE blends

As already detailed, according to droplet break up and coalescence mechanisms during processing, various morphologies can be developed [82]: dispersed, stretched dispersed/fibrillar and co-continuity. This section describes the properties reached in PA/PE blends depending on the morphology.

3.3.1. Nodular dispersion morphology

According to Subramanian et al, "the properties of these systems are a function of their concentrations, the particle size, and the geometry of the dispersed polymer" [83].

This morphology generally result in average properties [83]. Blending a tougher polymer (like PE) to a more brittle one (like PA), as a fine dispersion allows an increase of impact resistance of PA [49]. Generally, blending PE and PA (with compatibilizer) allows intermediate mechanical properties (tensile and flexural strength). It also appears that tribological properties are improved by dispersing HDPE in PA6 [49].

3.3.2. Stretched dispersion morphology

Stretched dispersion of fibrillar morphologies can be extrapolated to 2 dimensions stretching processing (film cast process typically). In this case, we can talk about lamellar morphology. This kind of morphology was mostly developed in order to improve fuel barrier properties. In fact, PA exhibits high resistance to non-polar solvents diffusion. So, dispersed lamella of PA in PE may increase the tortuosity of the diffusion pathway and therefore barrier properties of PE. This system (Selar®) was developed by Dupont Company in the 1980s. However, this heterogeneous morphology brings about a decrease of mechanical properties [59].

3.3.3. Co-continuous morphology

Many authors took an interest in this particular structure. In fact, co-continuity may be interesting to reach properties compromises [84,4]. However, these compromises are not precisely described.

4. Objectives of the PhD

Polymer blends and more precisely Polyamide/Polyethylene blends have aroused a great interest for the last years. However, several aspects are not fully described yet. Thanks to this literature review, the objectives of the PhD were defined.

In most of the studies in the literature, the objective is to develop a given morphology with a given domain size with a minimum compatibilizer amount (typically less than 0.03%$_{wt}$ of Maleic Anhydride reactive moieties in the blend [69]). In this PhD work, we have studied PA6/HDPE compatibilized blends. A standard reactive compatibilizer Maleic Anhydride grafted High Density Polyethylene MA-g-HDPE, known to be very efficient, was used. More precisely, **we have investigated the development of the different kinds of morphologies in these blends in twin screw extrusion over the overall range of compositions** in order to study the relative influence of composition and process parameters. **We have used standard amounts but also high amounts of compatibilizers** (until 0.3%$_{wt}$ of Maleic Anhydride moieties in the blend) in order to form a lot of copolymer in our system and to understand how to consider the compatibilizer in the design of new polymer blends, and its role in the mechanisms of morphologies development.

More precisely about co-continuity, even if many papers have been dealing with blends and their morphologies, **the conditions to develop and stabilize co-continuous structures have not been fully described yet in Polyamide/Polyethylene blends** [2,3,4]. Particular attention has been turned in this work to the development of co-continuity.

In many papers, the size of the dispersed phase was measured and plotted as a function of blend composition [10,11,12,13,14]. The authors always observed an increase of size of the dispersed phase approaching the co-continuity, as shown in Figure I-35.
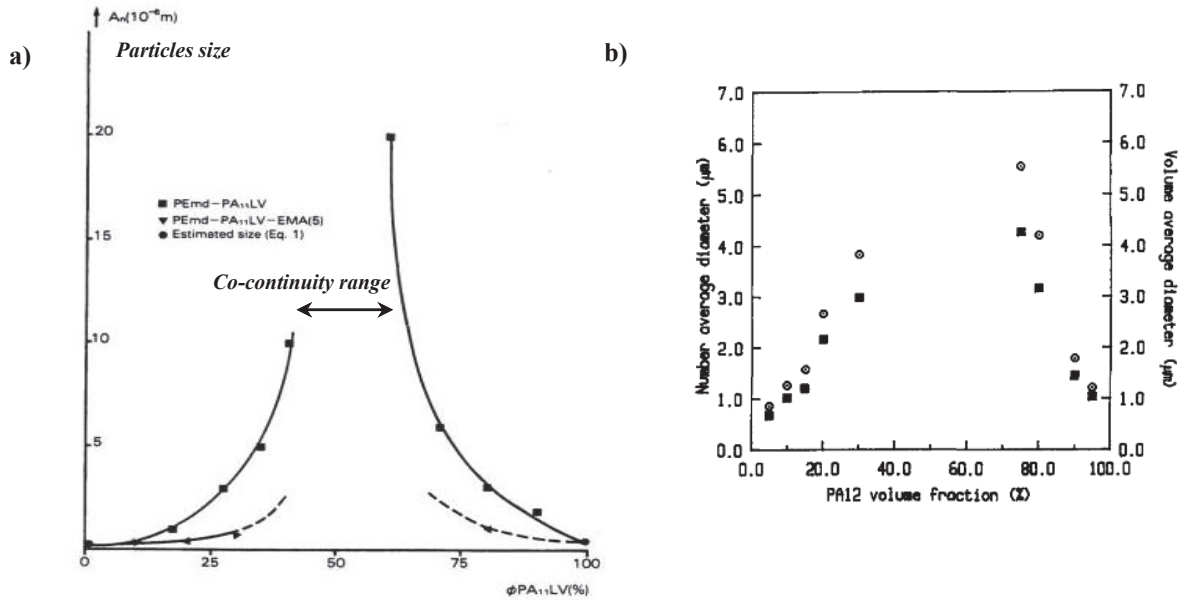
Figure I-35: Dispersed phase size as a function of composition: a) MDPE/PA11 compatibilized (by ethylene-maleic anhydride EMA) and non-compatibilized blends [11], b) LDPE/PA12 non-compatibilized blends [10].

Even if the authors assumed that, by increasing the dispersed phase amount, the probability of coalescence increased leading to larger particles, they did not explain quantitatively the values of the observed sizes neither the precise shape of the curves. Authors also plotted dispersed phase sizes distribution, but did not explain quantitatively the values of the observed sizes [9]. It has been claimed that phase inversion and co-continuity can be described by the percolation theory [5,6,7,8]. **However, this theory does not seem to be directly used to predict the characteristic size of the morphology (and also the distributions of sizes). In this work, we have investigated this point.**

In fact, in the case of compatibilized blends, the morphology can exhibit simultaneously various typical sizes as illustrated in Figure I-36.
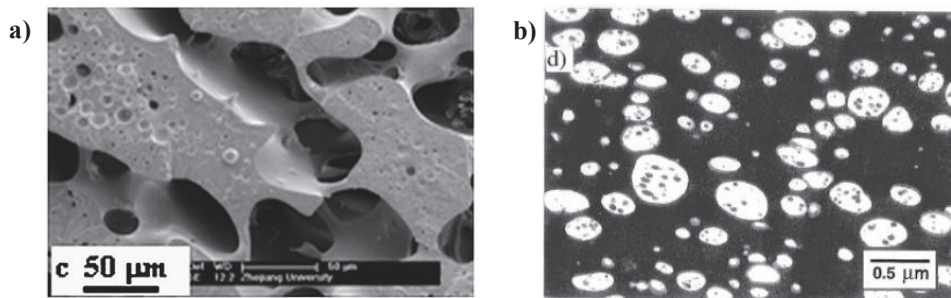
Figure I-36: a) SEM micrograph of PS/PA6/PS-g-PA6 (49.5/49.5/1%$_{wt}$) after etching of PS [15]. In this case, the morphology is co-continuous with sub-dispersions of PS in PA6. b) TEM micrograph of PS/PMMA/Compatibilizer P(S-b-MMA) (67/28/5%$_{wt}$) after staining of PS [16]. In this case, the morphology is a nodular dispersion of PMMA in PS matrix with both sub-dispersions of PS and PMMA.

The mechanisms proposed in the literature to describe the formation of the morphologies [55,16] focused on large scale morphology. Authors often assumed that the smallest particles were micelles of compatibilizer or trapped droplets [15,16]. Thus, a study over a broad range of compositions in PA6/HDPE reactively compatibilized blends may allow us to **propose a global mechanism for the development of the multi-scales morphologies.**

Finally, another aspect, important from the applicative point of view is the stability of the morphologies, notably during a second step processing. If some papers were dealing with stability in quiescient conditions [17,18], only a few papers focused on stability after a second step processing [19]. Thus, **to propose a more complete study about immiscible PA/PE blends morphology, a study of morphology stability was performed using various conditions.**

II. Materials and experimental

1. Introduction

This chapter presents materials used in this study: Polyamide 6 (PA6), High Density Polyethylene (HDPE) and the compatibilizer Maleic Anhydride grafted High Density Polyethylene (MA-g-HDPE). The miscibility between 1) PA6 and HDPE, and 2) HDPE and the compatibilizer MA-g-HDPE is discussed. The processing techniques used during this PhD to prepare the blends and the main experimental methods to characterize the rheological behavior and the morphology of these blends are then detailed.

In a second part, prior to focus on blends and morphologies development, the raw materials used were studied in more details. As the extrusion temperature (290°C) is very high, notably for HDPE and as PA6 is very sensitive to moisture, the stability of the polymers was checked before to prepare blends essentially by ThermoGravimetric Analysis (TGA), Size Exclusion Chromatography (SEC) and capillary rheometry. According to this stability study, a summary of rheological characteristics used is then presented.

2. Materials

Polyamide 6 (PA6) and High Density Polyethylene (HDPE) were used in this study. This section presents main characteristics of these polymers.

2.1. Polyamide 6 (PA6)

The Polyamide 6 (PA6) is a thermoplastic semi-crystalline polymer (crystallinity amount can reach 40 to 50%) obtained by polyaddition of ε-Caprolactam [85]. The molar mass of PA6 monomer is 113g.mol^{-1}. Figure II-1 shows the developed formula of PA6.
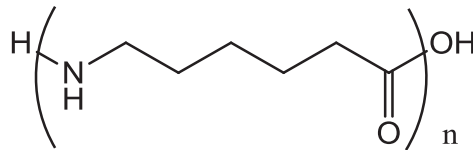
Figure II-1: Developed formula of PA6.

The crystalline phase of PA6 exhibits two polymorphic forms α and γ [86,87]:
-   α phase: generally considered to be the most thermodynamically stable phase as it is obtained by slow cooling [88]. It has a monoclinic structure. Its melting temperature is $T_m=223°C$.
-   γ phase: pseudo-hexagonal structure generally obtained by fast cooling [88]. $T_m=214°C$.

PA6 is a polar polymer in which hydrogen bonds are formed between amide groups of different macromolecular chains.

PA6, like other Polyamides, is sensitive to moisture and can absorb up to 9.5% in weight of water at saturation, at room temperature and 100% of hygrometry [85]. Water molecules break H-bonds, increase molecular mobility and thus decrease the glass temperature T_g.
Moreover, at high temperature (typically processing temperature), an excess of water according to the water content at the polycondensation equilibrium of PA6 (see Figure II-2), can induce chains alterations (hydrolysis). On the other hand, by decreasing the moisture amount below the equilibrium value, post-condensation of PA6 occurs leading to an increase of the average molecular masses.
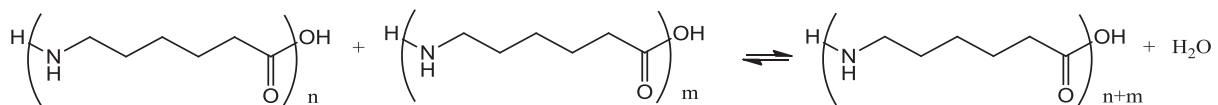
Figure II-2: Polycondensation equilibrium of PA6.

Thus, in any experiment which needs to heat the PA6 at higher temperature than its melting temperature T_m (notably to process it), the moisture content must be controlled. In our case, high molecular weight PA6 was used and the equilibrium moisture content was between 500 and 1000ppm.

2.2. High Density Polyethylene (HDPE)

High Density Polyethylene (HDPE) is also a thermoplastic semi-crystalline polymer (crystallinity amount can reach 85%). It is obtained by polymerization of ethylene gas, compressed at "low" pressure ($\leq$50 bar) which leads to the formation of linear macromolecular chains (HDPE can exhibit 1 or 2 short branching like -CH_3 for 1000 carbon atoms in the main chain) [89]. The molar mass of HDPE monomer is 28g.mol^{-1}. Figure II-3 shows developed formula of HDPE.
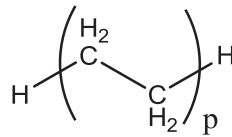
Figure II-3: Developed formula of HDPE.

The crystalline structure of Polyethylene is orthorhombic [90] and its melting temperature ranges from T_m=137 to T_m=145°C [91].

Contrary to PA6, HDPE is a non-polar polymer, insensitive to moisture.

2.3. Control of the moisture content

We have seen that moisture content in PA6 must be low and controlled for all experiments needing to heat PA6 at higher temperature than its melting temperature. So, PA6 was dried 12 hours under a primary vacuum in an oven at 90°C in order to reach the equilibrium moisture amount in our PA6 (between 500 and 1000 ppm) prior to any high temperature experiments. The moisture content in PA6 was then measured by coulometric Karl Fisher titration (*Mettler Toledo*). In order to apply the same thermal treatment to all materials, HDPEs and MA-g-HDPE were dried in the same conditions as PA6.

2.4. Miscibility between Polyethylene and Polyamide

Miscibility between Polyethylene and Polyamide was firstly studied. In fact, this parameter is useful to adapt the formulation, the needed compatibilization and the processing parameters in order to develop desired morphologies.

The interaction parameter χ_{12} between HDPE and PA6 was calculated using Hildebrand equation as described in *Chapter I section 2.1.4 Estimation of interaction parameter page 27* with V_1 and V_2, the molar volumes of polymer 1 and polymer 2 respectively; δ_1 and δ_2, the solubility parameters of polymer 1 and polymer 2 respectively:

$$\chi_{12} = \frac{\sqrt{V_1 V_2}}{RT}(\delta_1 - \delta_2)^2 \geq 0 \qquad \text{Eq. II-1}$$

Solubility parameter of PA6:

To determine the solubility parameter in case of polar systems (like PA6), the Hansen method which divides the solubility parameter into three components [92] was used as already detailed in *Chapter I*:

Dispersive interaction: $\delta_d = \frac{\sum F_{di}}{V_m}$ 　　　　　　　　Eq. II-2

Polar interaction: $\delta_p = \frac{\sqrt{\sum F_{pi}^2}}{V_m}$ 　　　　　　　Eq. II-3

Hydrogen bonding interaction: $\delta_h = \sqrt{\frac{\sum E_{hi}}{V_m}}$ 　　　Eq. II-4

With:
- E_h, the cohesive energy
- F, the molar attraction constants
- In the three components, V_m corresponds to the molar volume of PA6 and is defined as the ratio of the molar mass of PA6 monomer (113g.mol^{-1}) to its density (1.13g.cm^{-3}): $100 \text{cm}^3.\text{mol}^{-1}$ at room temperature.

Then, the solubility parameter was calculated using the following equation:

$$\delta^2 = \delta_d^2 + \delta_p^2 + \delta_h^2 \qquad \text{Eq. II-5}$$

The groups' contribution method was applied to estimate the value of the three terms and thus, the solubility parameter. Van Krevelen values at 25°C were used.

The molecule was divided into several groups with factors tabulated [92] as shown in Figure II-4.

- 1 group $-NH-$:
  - $F_d = 160\,J^{1/2}\cdot cm^{3/2}\cdot mol^{-1}$
  - $F_p = 210\,J^{1/2}\cdot cm^{3/2}\cdot mol^{-1}$
  - $E_h = 3100\,J\cdot mol^{-1}$

- 5 groups $-CH_2-$:
  - $F_d = 270\,J^{1/2}\cdot cm^{3/2}\cdot mol^{-1}$
  - $F_p = 0\,J^{1/2}\cdot cm^{3/2}\cdot mol^{-1}$
  - $E_h = 0\,J\cdot mol^{-1}$

- 1 group $-CO-$:
  - $F_d = 290\,J^{1/2}\cdot cm^{3/2}\cdot mol^{-1}$
  - $F_p = 770\,J^{1/2}\cdot cm^{3/2}\cdot mol^{-1}$
  - $E_h = 2000\,J\cdot mol^{-1}$
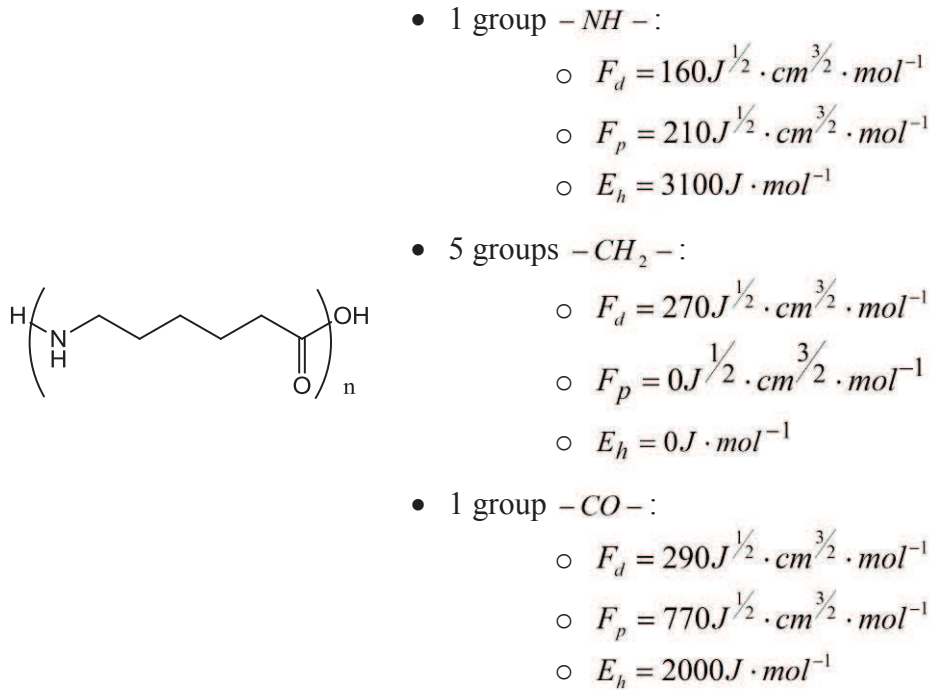
Figure II-4: Groups' contribution method for PA6.

According to these factors, the three terms of Hansen were calculated:

$$\delta_d = 18\ J^{1/2}.cm^{-3/2} \qquad \delta_p = 8\ J^{1/2}.cm^{-3/2} \qquad \delta_h = 7.1\ J^{1/2}.cm^{-3/2}$$

And the estimated solubility parameter using Eq. II-5 for PA6 is 20.9 MPa$^{1/2}$. This is in agreement with a tabulated value for PA6 of 21.5 MPa$^{1/2}$ [92].

Solubility parameter of HDPE:

In the case of HDPE, several values of solubility parameter are tabulated (from calculation or experiments) from 16 to 18.4 MPa$^{1/2}$ [92]. The groups' contribution method was also applied to compare the obtained value to the tabulated ones. For one ethylene monomer (two $-CH_2$ groups considered), with a molar mass of 28g.mol^{-1} and a density of 0.91g.cm^{-3}, the molar volume is 30.8cm^3.mol^{-1} at room temperature. The molar attraction constant tabulated for $-CH_2$ is $F=280$ MPa$^{1/2}$.cm^3.mol^{-1}. Thus, the estimated solubility parameter is 18.2 MPa$^{1/2}$. This calculated value from groups' contribution is close to tabulated ones.

According to these solubility parameters, the Flory interaction parameter was estimated (Eq. II-1) to be roughly of the order of 0.7 (for δ_{PE}=16 MPa$^{1/2}$ and δ_{PA}=21.5 MPa$^{1/2}$).

By using Eq. I-48 (*see Chapter I section 2.4.1.2 Interfacial coverage Σ page 47*), the excess of energy stored at the interface between PA and PE is estimated:

$$\gamma = \frac{kT}{a^2} \sqrt{\frac{\chi_{12}}{6}}$$

Eq. II-6

With:

- a, the size of one monomer, estimated using the following equation:

$$a^3 = \frac{V_m}{\mathcal{N}_a}$$

Eq. II-7

With V_m, the molar volumes of PA and PE monomers (respectively 100 and 30.8cm³/mol) and $\mathcal{N}_a$, the Avogadro's number.

Thus, it was found that a_{PA}=0.55nm and a_{PE}=0.37nm.

We consider an average size of monomer a=0.5nm in what follows.

- χ_{12}, the Flory interaction parameter, previously estimated to be roughly of the order of 0.7.
- k, the Boltzmann constant.
- T, the temperature.

So, at 290°C (extrusion temperature), **the interfacial tension between PA and PE was estimated to be of the order of 10.6mN.m⁻¹**, which is in agreement with values found for PA6/HDPE in the literature [93,94].

Thus, PA6 and HDPE are not miscible at room temperature and a compatibilizer is needed to insure final desired properties in blends.

2.5. Materials of the study

One Polyamide (PA6) and three High Density Polyethylene (HDPEs) of various viscosities were used during the PhD. As PA6 and HDPE are immiscible, one standard compatibilizer Maleic Anhydride grafted High Density Polyethylene (MA-g-HDPE) containing 1% in weigth of MA moieties was also used.

The compatibilization reaction between Maleic Anhydride (MA) moieties of compatibilizer and amine end-groups (NH_2) of PA6 is schematized in Figure II-5. It leads to the formation of grafted copolymer PA6-g-HDPE at the interface between the PA6 and PE phases during processing.
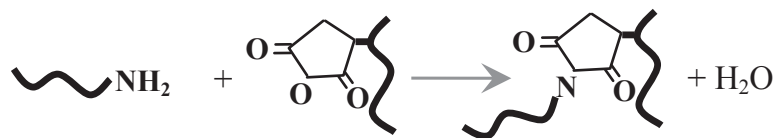
Figure II-5: Compatibilization reaction between MA moieties of MA-g-HDPE and amine end-groups of PA6.

The molar concentrations of NH_2 in PA6 and MA in the compatibilizer are respectively:
- [MA]=101mmol.kg^{-1}
- [NH$_2$]=40mmol.kg^{-1}

The molar ratios [AM]/[NH$_2$] in the blends range from 0 to 13.7.

2.5.1. Characteristics of neat polymers

The properties of neat polymers according to Size Exclusion Chromatography (SEC) (method described in 0), to supplier data and to literature [95,92] are shown in Table II-1 and in Figure II-6. SEC were performed by Olivier Boyron (CPE Lyon), Sabrina Paillet and Nadia Delon-Anik (Rhodia CRTL)

Materials	M_n (g/mol)	M_w (g/mol)	IP	ρ (g/cm^3) at T_{room}	ρ (g/cm^3) at 290°C	MFI
HDPE 1	29 300	145 300	5.0	0.94	0.72	15 (g/10min, 190°C, 21.6 kg)
HDPE 2	21 300	107 600	5.0	0.95	0.72	0.9 (g/10min, 190°C, 5kg)
HDPE 3	21 200	81 600	3.9	0.96	0.72	20 (g/10min, 190°C, 5kg)
MA-g-HDPE	26 000	75 700	2.9	0.95	0.72	
PA6	27600			1.13	0.96	

Table II-1: Properties of neat polymers according to supplier data, to literature [95,92] and to Size Exclusion Chromatography (SEC) measurements (absolute values). IP: Index of Polydispersity; MFI: Melt Flow Index.
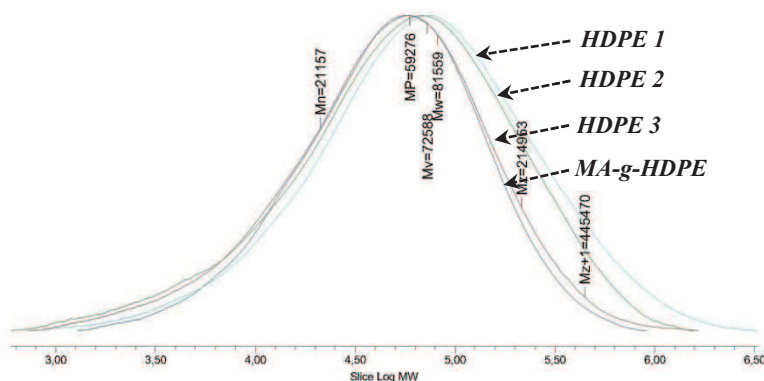
Figure II-6: Chromatograms of the three HDPEs and of MA-g-HDPE (SEC measurements, absolute values).

Concerning more particularly Polyethylene, HDPE 1 and HDPE 2 exhibit almost the same molecular mass distribution, so do HDPE 3 and MA-g-HDPE.

In neat compatibilizer, the concentration of MA moieties (1% in weight) corresponds to $2.9.10^{-3}$ moles of MA per mole of monomer (CH_2-CH_2). Considering the molecular mass of the overall MA-g-HDPE ($M_n \sim 26000 g.mol^{-1}$), there are ~930 monomers (CH_2-CH_2) in average per chain of compatibilizer. By combining both data, there are in average 2.7 MA moieties per chain of compatibilizer. Thus, there are about 350 monomers (CH_2-CH_2) between each grafted MA which represents a molar mass of $9800 g.mol^{-1}$.

2.5.2. PE phase definition

At the scale relevant in processing, the compatibilizer MA-g-HDPE and HDPE are considered to be miscible. **Thus, the overall HDPE+MA-g-HDPE amount corresponds to one phase, which will be denoted as the PE phase** in what follows, with index 1 (respectively 2 and 3) for HDPE 1 (respectively HDPE 2 and 3).

However, this compatibility at large scale between HDPE and MA-g-HDPE does not rule out a possible, at least partial, micellar organization of MA moieties in HDPE at the molecular level. The following section deals with the miscibility between MA moieties and HDPE chains in the PE phase more in details.

2.5.2.1. Interaction parameter

The Flory interaction parameter χ_{12} between HDPE chains and MA moieties was estimated using Hildebrand solubility parameters [92,22] (Eq. II-1).

Solubility parameter of MA:

Like PA6, MA moieties are polar molecules. So, the Hansen method which divides solubility parameter into three components [92] (Eq. II-2, Eq. II-3, Eq. II-4) was used.

Considering the molar mass of MA ($98 g.mol^{-1}$) and its density ($1.5 g.cm^{-3}$), the molar volume V_m of MA was found to be $65 cm^3.mol^{-1}$ at room temperature.

The groups' contribution method was applied to estimate the value of the three terms as shown in Figure II-7.
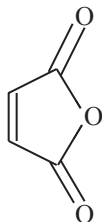
- 2 groups $-CO-$:
  - $F_d = 290 J^{1/2} \cdot cm^{3/2} \cdot mol^{-1}$
  - $F_p = 770 J^{1/2} \cdot cm^{3/2} \cdot mol^{-1}$
  - $E_h = 2000 J \cdot mol^{-1}$

- 1 group $=CH-$:
  - $F_d = 200 J^{1/2} \cdot cm^{3/2} \cdot mol^{-1}$
  - $F_p = 0 J^{1/2} \cdot cm^{3/2} \cdot mol^{-1}$
  - $E_h = 0 J \cdot mol^{-1}$

- 1 group $-O-$:
  - $F_d = 100 J^{1/2} \cdot cm^{3/2} \cdot mol^{-1}$
  - $F_p = 400 J^{1/2} \cdot cm^{3/2} \cdot mol^{-1}$
  - $E_h = 3000 J \cdot mol^{-1}$

Figure II-7: Groups' contribution method for MA.

According to these factors, the three terms of Hansen were calculated:

$$\delta_d = 13.5 \ J^{1/2}.cm^{-3/2} \qquad \delta_p = 17.8 \ J^{1/2}.cm^{-3/2} \qquad \delta_h = 10.4 \ J^{1/2}.cm^{-3/2}$$

And the calculated solubility parameter of Maleic Anhydride using Eq. II-5 is 24.6 MPa$^{1/2}$.

__Solubility parameter of HDPE:__

We remind the reader that in the case of HDPE, several values of the solubility parameter are tabulated from 16 to 18.4 MPa$^{1/2}$ [92]. The value estimated using group's contribution was 18.2 MPa$^{1/2}$.

__Interaction parameter between MA and HDPE:__

According to these solubility parameters, the Flory interaction parameter was estimated (Eq. II-1) to be roughly of the order of 1.2 (for $\delta_{PE} = 16$ MPa$^{1/2}$).

Thus, MA-g-HDPE may be considered as a polymer containing functional moieties not miscible with HDPE.

2.5.2.2. Dynamical rheometry

Results obtained in dynamical rheometry at 290°C in the linear viscoelasticity domain (shear amplitude of 4%) using a cone-plate geometry show a behaviour which could possibly indicate the presence of such micellar organization of MA moieties in HDPE (Figure II-8).
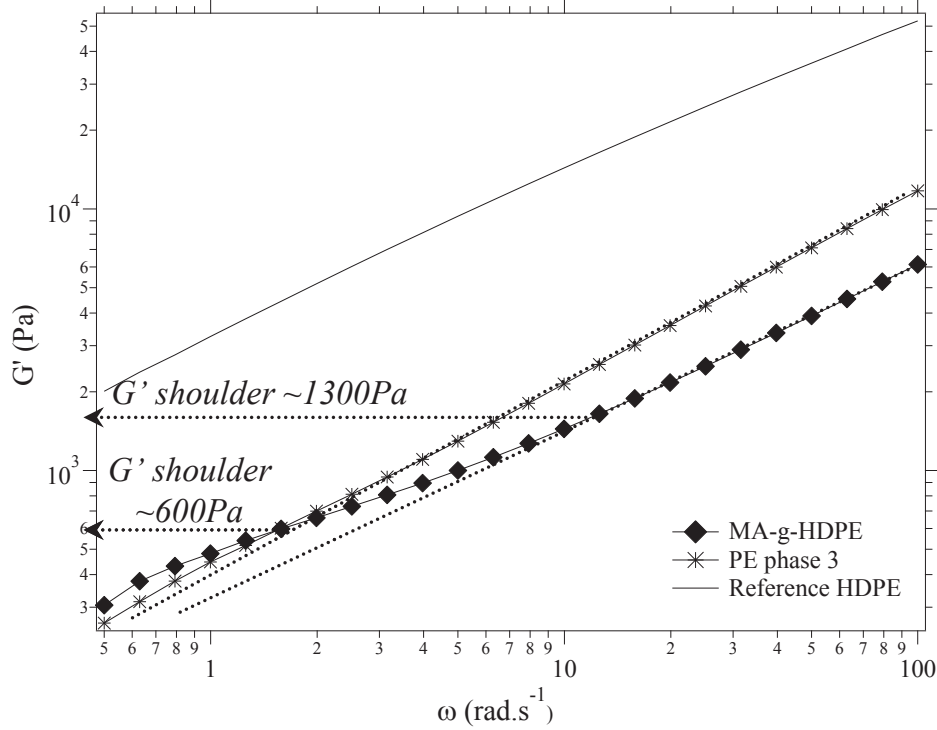
Figure II-8: Elastic modulus *G'* versus pulsation at 290°C for a reference HDPE, MA-g-HDPE and PE phase 3 (HDPE 3/MA-g-HDPE 60/40%$_{vol}$ processed by twin screw extrusion D34). Dotted curves are extrapolated from the high frequency regime.

As shown on Figure II-8, a shoulder of *G'* was observed at low frequency in both neat MA-g-HDPE and PE phase 3 (HDPE/MA-g-HDPE 60/40%$_{vol}$), in contrast to neat reference HDPE in which no shoulder was observed. This shoulder may be attributed to the form relaxation of MA micelles in HDPE [96,97]. By using these *G'* values, the average volume surrounding each micelle was estimated in both MA-g-HDPE and PE phase 3:

$$\delta^3 \approx {kT}/{G'} \qquad\qquad \text{Eq. II-8}$$

Then, the volume of the micelle ($V_{micelle}$) was calculated using the volume fraction of MA moieties:

$$V_{micelle} = \phi_{MA}(vol)\delta^3 \qquad\qquad \text{Eq. II-9}$$

80

In neat compatibilizer:

There is $1\%_{wt}$ of MA moieties. Considering a density of $0.95g.cm^{-3}$ for PE chains and $1.5g.cm^{-3}$ for MA, the volume fraction of MA is $\phi_{MA}(vol)=0.63\%$.

The average volume surrounding each micelle was estimated from Eq. II-8 to be $\delta^3 \approx 6000\ nm^3$, which gives an average distance between micelles of about 18nm and a micelle volume $V_{micelle}$ of about $38nm^3$.

On the other hand, the distance between micelles should be compatible with the chain length between grafts. We have seen that there are about 350 monomers (CH_2-CH_2) between each grafted MA which represents a molar mass of $9800g.mol^{-1}$. According to Fetters et al. [98], $\langle R_g^2 \rangle = 1.25 M_n$ (Å²) which gives a HDPE chain gyration radius R of 11nm. Thus, the estimated distance between micelles of about 18nm seems to be a little bit overestimated.

In PE phase 3 (HDPE/MA-g-HDPE 60/40%$_{vol}$):

There is $0.4\%_{wt}$ of MA moieties which corresponds to a volume fraction $\phi_{MA}(vol)=0.25\%$.

In this case, $\delta^3 \approx 13000\ nm^3$, $V_{micelle}$=33nm^3 and the distance between micelles is about 24nm.

As expected, the volume surrounding the micelles is larger in PE phase 3 than in neat MA-g-HDPE, due to the dilution of MA moieties in PE phase. Moreover, the micelle size remains almost constant.

The aggregation number of MA in micelles was estimated using the following equation:

$$N = \frac{V_{micelle}\rho\mathcal{N}_a}{M}$$

Eq. II-10

Considering the density ρ of MA ($1.5g.cm^{-3}$), M, the molar mass of MA ($98g.mol^{-1}$), $\mathcal{N}_a$, the Avogadro's number and $V_{micelle}$=35nm^3, the aggregation number of MA was estimated to be of the order of 300.

Thus, dynamical rheometry seems to indicate the existence of MA micelles in both MA-g-HDPE and PE phases. This is in agreement with the high interaction parameter χ_{12} estimated between MA and HDPE.

3. Experimental

This section presents the processing techniques and the experimental characterizations performed during this PhD.

3.1. Blends processing

We have seen in *Chapter I* that morphology of polymer blends is highly affected by processing conditions. On the other hand, to obtain blends with desired and reproducible properties, the morphology has to be stable during a second step processing during which a final product is produced, which is a key point for application. So, blends processing was performed in two steps:

1) Morphology development during blending by extrusion
2) Study of morphology stability using several conditions including controlled conditions and second step processing (extrusion blow molding and injection molding)

3.1.1. First step: blending

Three processing tools of different scales were used: two continuous tools (co-rotating twin screw extruders) and one batch system. Before blending, the materials were dried 12 hours in a primary vacuum oven at 90°C in order to reach the equilibrium moisture amount in PA6 (between 500 and 1000 ppm in our case).

3.1.1.1. Co-rotating twin screw extrusion (continuous tools)

Twin screw extrusion enables to continuously process materials in the molten state in a system screws/barrel. Various kinds of twin screw extruders can be found: co-rotating or counter-rotating systems and intermeshing screws or not. Intermeshing co-rotating systems are generally used to prepare polymer blends. In fact, they are efficient both for dispersive and distributive mixing. One of the main characteristics of co-rotating twin screw extruders is the screw profile modularity due to the large range of elements which can be placed along the screws. Two kinds of elements can be distinguished:

- Elements with direct thread (conveying) or inverse thread (restrictive)
- Blending elements (kneading blocks)

The modularity also comes from the possibility to add liquid, to feed the materials by open zones anyway along the screws…

In the case of polymer processing, the solid product is introduced at the beginning of the screws (pellets in this study).

Then, three functional zones can be distinguished along the screws [99]:
1) Solid conveying
2) Melting. This step is very fast, insured by the first restrictive element
3) Flow in the melt state

A simplified diagram of co-rotating twin screw extruder with intermeshing screws is presented in Figure II-9.
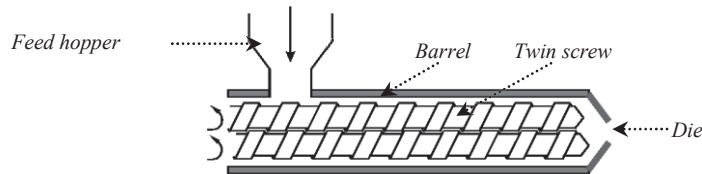
Figure II-9: Diagram of co-rotating twin screw extruder with intermeshing screws.

Various parameters are used to control extrusion process:
- Temperature profile.
- Shear rate which depends on both the screw profile and the screw speed. Generally, one can consider an average shear rate in twin screw extrusion of $100s^{-1}$.
- Residence time which depends on both the throughput and the screw speed.

The characteristic times of morphology development (drop break up, coalescence) and of reactive compatibilization have to be compatible with the residence time in extrusion (typically a few tens of seconds to a few minutes).

In this study, two co-rotating intermeshing twin screw extruders were used. The extruded strand obtained at the exit of the die was quenched in water and pelletized.

3.1.1.1.1. Twin screw extrusion D34

An extruder *Leistritz* of diameter 34mm and ratio length on diameter L/D of 35 was used with a die of diameter 2mm, using fixed processing conditions:
- Screw speed: 250rpm
- Throughput: 10kg/h

The barrel had ten temperature-controlled zones: eight cooled with air and two cooled with water (zones 4 and 8 in Figure II-10). The screw profile was designed with two « open » zones along the screws:
- An open zone after kneading blocks.
- A venting zone to eliminate the water produced by the compatibilization reaction.

Both open zones were used for sampling in the melt during extrusion.
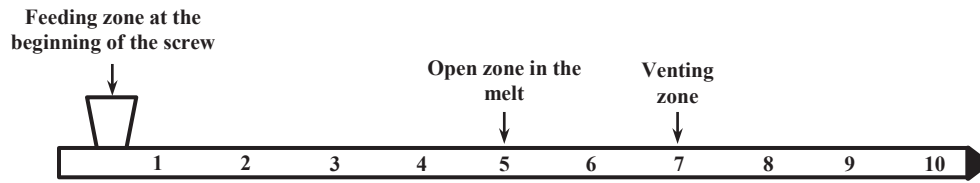
Figure II-10: Screw zones used in D34 extruder.

Two feeding devices were used, one containing the PA6 and the compatibilizer, one containing the HDPE. Both devices were placed in the feeding zone at the beginning of the screw.

The blends were prepared with Vincent Curtil and Michel Sorin in the team of Olivier Chaubet (Rhodia CRTL).

As the shear rate is an important parameter in blending and morphology development, the maximum shear rate into the 2mm die has been estimated. It is estimated as the shear rate on the wall of a capillary for a Newtonian fluid:

$$\dot{\gamma} = \frac{4Q_v}{\pi\left(D/2\right)^3}$$

The die of diameter 2mm is schematized in Figure II-11.
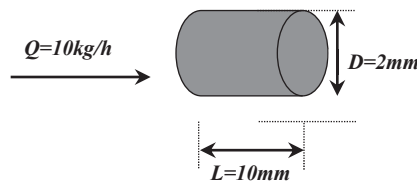
Figure II-11: Schematic representation of 2mm diameter die in extruder D34.

So, with a throughput of 10kg/h, using a density of about 1000kg/m^{-3}, the shear rate into the die is estimated to be of the order of 3500s^{-1}. Then, using the throughput, the section of the die and its length, the time during which the polymer is in the die and is submitted to this higher shear rate is estimated to be very short, of the order of 0.01s.

3.1.1.1.2. Twin screw extrusion D40

An extruder *Coperion* of diameter 40mm and ratio length on diameter L/D of 34 was also used with a die of diameter 5.2mm, notably to produce samples in larger quantity. The processing conditions used were the followings:
- Screw speed: from 180 to 300rpm
- Throughput: from 25 to 40kg/h
- Screw profile exhibiting higher shear rate than in D34 extruder

Like previously, the shear rate into the die can be calculated using Eq. II-11 for throughput from 25 to 40kg/h. It is estimated to be from 500 to $1000s^{-1}$.

In this case, the blends were prepared by David Haeusler in the team of Gérard Bradley, Niki Peduto and Franco Speroni (Rhodia TIC, BET).

In both cases (extruders D34 and D40), the average melt temperature of the blends at the exit of the die was about 290°C.

3.1.1.2. Batch mini-extrusion

Blends were also prepared using a batch mini-extruder (10 grams per run), *Microcompounder DSM Midi 2000*. It operates under inert atmosphere (N_2) but it is not completely tight. This tool allows controlling the residence time, independently from the screw speed, using a recirculating system as shown in Figure II-12.
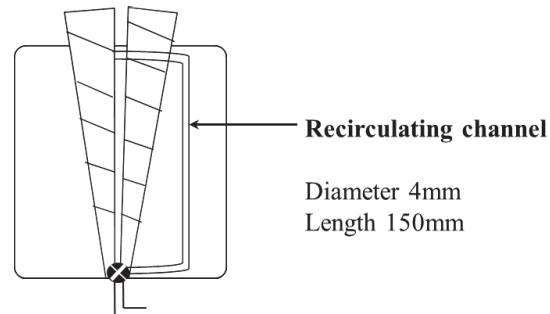
Figure II-12: Batch mini-extruder diagram.

The die characteristics are: diameter 4mm and length 35mm.
This mini-extruder was used to test a broad range of process conditions:
- Screw speed: from 10 to 200rpm
- Melt temperature: from 270 to 315°C
- Residence time: from 1 to 11min

3.1.2. Second step: study of the morphology stability

The morphologies stability was studied under various conditions. For better understanding, well controlled conditions were firstly used:
- Static annealing
- Controlled shear

Then, real processes exhibiting more complex flows and temperature profiles were tested:
- Extrusion blow molding
- Injection molding

The experimental conditions used in all these cases are described in the following section.

3.1.2.1. Static annealing experiments

In order to study the morphology stability under static conditions, heating rates of $70°C.min^{-1}$ from room temperature to 290°C followed by annealing at 290°C during 5 and 15 minutes under Helium flow were performed in Differential Scanning Calorimetry (DSC).

3.1.2.2. Controlled shear experiments conditions: capillary rheometer

The morphology stability was also studied using controlled shear rates at 290°C in a capillary rheometer (die 20/1: length 20mm and diameter 1mm). Prior to capillary experiments, materials were dried overnight at 90°C under primary vacuum. Before to start the test, the sample was put inside the rheometer barrel and left during 7 minutes for full melting at 290°C. This first step can be considered as a static annealing at 290°C. Then, the shearing test began using two shear rates:

1) $200s^{-1}$ during 10 minutes: order of magnitude of extrusion and extrusion blow molding shear rate.

2) $2000s^{-1}$: order of magnitude of injection molding shear rate during passage through the nozzle and of the die shear rate in twin screw extrusion. As the material quantity available in the capillary rheometer was not enough to conduct all the experiment during 10 minutes at $2000s^{-1}$, a shear rate of $50s^{-1}$ was applied with peaks at $2000s^{-1}$ after 1, 5 and 10 minutes.

Samplings were performed at the end of each experiment (after 10 minutes) for Scanning Electron Microscopy (SEM) observations. At the exit of the capillary rheometer, blends strands exhibiting very small diameter cooled rapidly at room temperature under air.

The characteristic times of this kind of experiment (annealing time and shear time) are estimated in the following section. The overall annealing time in static at 290°C is:

$$t_{static} = \textbf{17 minutes}$$

The time t_{shear} during which the polymer was submitted to shear rate is estimated for the die used (diameter of D=1mm and length of L=20mm) with v, the speed, Q_v, the throughput in volume and S, the section of the die:

$$t_{shear} = \frac{L}{v} = \frac{L}{Q_v/S}$$

Eq. II-12

Like for extruder die, the shear rate on the capillary wall for a Newtonian fluid is directly linked to the throughput in volume and to the section of the die by the following equation:

$$Q_v = \frac{\dot{\gamma}\pi(D/2)^3}{4}$$

Eq. II-13

Thus, the time t_{shear} is defined as:

$$t_{shear} = \frac{8L}{\dot{\gamma}D}$$

Eq. II-14

So, for:
- $\dot{\gamma} = 200s^{-1}, t_{shear} = 0.8s$
- $\dot{\gamma} = 2000s^{-1}, t_{shear} = 0.08s$

Thus, each experiment corresponds to 17 minutes of static annealing followed by shear at 200 and 2000s⁻¹ during respectively 0.8 and 0.08s.

Then, in order to study the morphologies stability during a real second step processing, the blends prepared by twin screw extrusion were transformed by extrusion blow molding and injection molding.

3.1.2.3. Extrusion blow molding

Bottles were made in extrusion blow molding (*Comec* machine) by Yannick Martinez in the team of Christophe Lapierre (Rhodia TIC, BET). This continuous process is used to produce hollow parts. The polymer is melted using a single screw extruder, then, a parison is formed using a tubular die. The mold closes on the parison and air is blown into the mold (mold temperature about 15 – 20°C) to flatten the polymer against the walls. The steps of this process are schematized on Figure II-13.
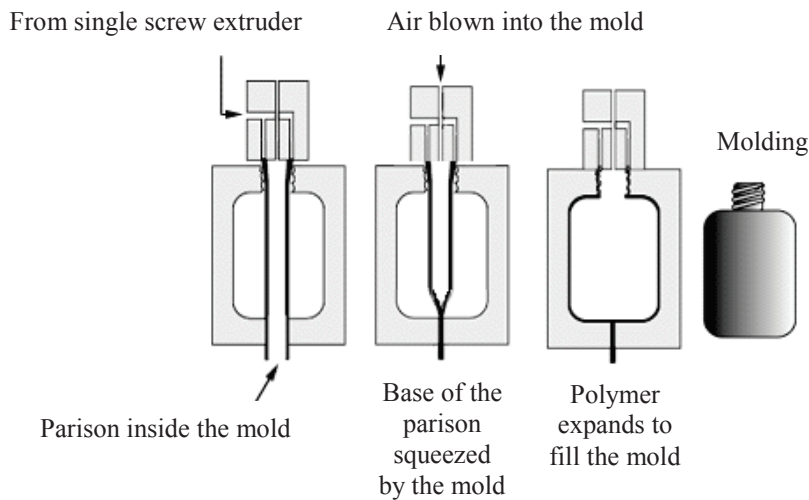
Figure II-13: Extrusion blow molding process diagram.

In term of processability, the polymer must be viscous enough in order to obtain a parison which does not flow and a constant thickness in the final part. Moreover, the crystallization kinetics must be slow enough to keep the parison in the molten state until the air blowing inside the mold.

3.1.2.4. Injection molding

Injection molding was used to produce tensile specimens and plates.

3.1.2.4.1. Tensile specimens

Tensile specimens with a thickness of 4mm were injected with Vincent Curtil (Rhodia CRTL), using an *Arburg* injection molding machine exhibiting a clamping force of 35 tons. Three injection speeds were tested: 26, 88 and 149mm/s. According to these injection speeds, the volume throughput in the mold Q_v was estimated to range from 18 to 110cm^3.s^{-1}.

The shear rate on the mold wall is defined as:

$$\dot{\gamma} \approx \frac{Q_v}{\left(h/2\right)^2}$$

With:

- h, the mold thickness

Thus, the shear rate on the mold wall ranged from 5 to 28s^{-1} in average, depending on the injection speed used.

The following temperature conditions were applied:
- Melt temperature: 280°C
- Mold temperature: 55°C except for neat PA6. In fact, PA6 was too difficult to turn out from mold at 55°C. Thus, a mold temperature of 65°C was used.

3.1.2.4.2. Plates

Plates of dimensions 100X100mm with a thickness of 0.8mm were also injected. They were injected by Fabrice Chavand in the team of Christophe Lapierre (Rhodia BET), using a *Demag* injection molding machine exhibiting a clamping force of 80 tons. Only one injection speed was used in this case: 170mm/s. The volume throughput Q_v was estimated to be 83cm^3.s^{-1}. By using Eq. II-15, the shear rate on the mold wall was estimated to be 520s^{-1}.

Then, the following temperature conditions were applied:
- Melt temperature: 270°C
- Mold temperature: 80°C

3.2. Rheological characterizations

The rheological behavior of materials was characterized using two techniques:
1) Capillary rheometry
2) Dynamical rheometry

3.2.1. Capillary rheometry

The raw materials were characterized at high shear rate from 10 to 5000s^{-1} by capillary rheometry (*Göttfert rheograph 2002*) using a die 20/1 (length 20mm and diameter 1mm) at extrusion temperature (290°C). The stability of the viscosity was first checked at 290°C during ten minutes at a constant shear rate of 200s^{-1} for each sample. Then, the variation of viscosity η versus shear rate $\dot{\gamma}$ was measured at 290°C.

3.2.2. Dynamical cone-plate rheometry

Dynamical rheometry *(Ares)* was also performed in order to characterize the rheological behavior of the materials in oscillatory mode, still at 290°C (the extrusion temperature). The rheometer imposes a sinusoidal strain. The material answer is a sinusoidal stress. As the polymers exhibit viscoelastic behavior, this answer is divided into two parts:
- An elastic component in phase with the strain: *G'*
- A viscous component in quadrature with the strain: *G''*

The complex modulus *G** measures the overall resistance of the material to the applied strain. It is defined as the sum of these two components (*G*=G'+iG''*). The loss angle can also be calculated using these values: *tanδ=G''/G'*.

A cone-plate geometry (diameter 25mm, cone angle 0.1rad) was used to perform these tests in order to keep the shear rate along the radius of the plate constant. The linear viscoelasticity domain was first determined performing strain sweeps at fixed temperature and frequency (290°C and 100rad.s^{-1}). Depending of the samples, the linear viscoelasticity domain could reach 25% of strain. However, to prevent any morphological changes during experiments, the strain amplitude chosen to stay in the linear domain was 4% [36]. Then, materials stability was checked by time sweeps at 290°C, strain amplitude of 4% and a frequency of 10rad.s^{-1}. The aim of these sweeps is to determine the maximum duration of the tests and so the lowest frequencies reachable without degrading the polymers. Finally, frequency sweeps were performed from 100 to 0.5rad.s^{-1} with strain amplitude of 4% to characterize the viscoelastic behavior of the materials.

3.3. Morphology characterization

The morphology can be studied by several techniques depending on the size of the characterized objects. In fact, different microscopy techniques allow reaching various ranges of resolution as schematized on Figure II-14.
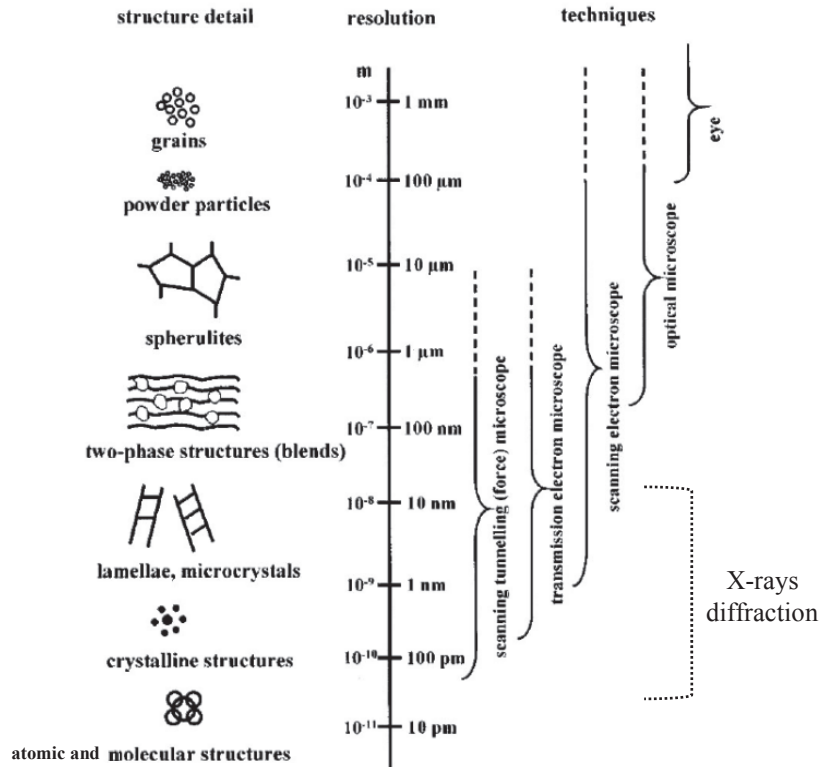
Figure II-14: Polymers' structures observable and associated microscopy techniques [100].

Within the framework of this study, the range of morphology sizes in blends is from tens of nm to tens of μm. Thus, electron microscopy is the most adapted technique.

Whatever the type of electron microscopy used (Scanning or Transmission), an electron beam is emitted by an electron gun and sent on the sample. Various electrons/material interactions are possible, bringing about modifications of the beam as illustrated on Figure II-15.
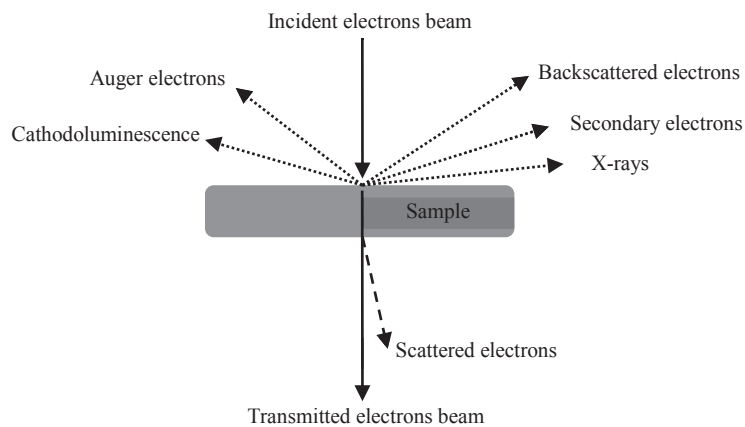
Figure II-15: Diagram of modifications of the primary electrons beam caused by various electrons/material interactions.

In Scanning Electron Microscopy (SEM), depending on the type of interactions, electrons are ejected from more or less superficial layers of the sample leading to different contrasts as illustrated on Figure II-16.

Incident electrons beam

Sample surface

Auger electrons
Secondary electrons
Backscattered electrons
Characteristic X-rays

X-ray continuum

Fluorescence X

Typical penetration depth ~ 1μm
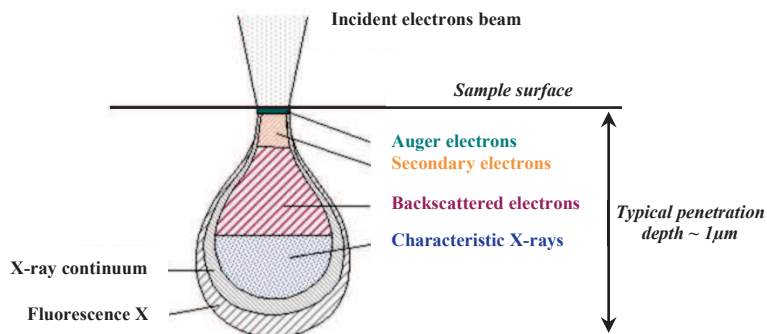
Figure II-16: Diagram of interactions between an incident electrons beam and the sample surface.

Thus, for example, as the secondary electrons are ejected from superficial layers of the sample, they will give topographic information.

In SEM, the radiations used depending on the detectors are:
- Secondary electrons: topographic contrast
- Backscattered electrons: chemical contrast essentially depending on atomic weight
- X-rays (X spectrometer coupled to SEM): cartography of chemical composition

In Transmission Electron Microscopy (TEM), the observation techniques are:
- Clear field: transmitted beam
- Dark field: backscattered electrons
- Diffraction: Scattered electrons

3.3.1. Scanning Electron Microscopy (SEM)

In this study, the blends morphology was mainly observed by Scanning Electron Microscopy (surface observation). A *Zeiss Ultra 55* microscope was used. The main advantage of this microscope is the ability to obtain micrographs at low accelerating voltage keeping a good resolution. This is particularly useful for polymer observation. In fact, as polymers are very sensitive to electron beam and can be damaged under the beam, this microscope allowed us observing the samples at low voltage to minimize their damage.

Concerning the method used to prepare the samples, blends pellets were first included in Epoxy resin (Araldite) and placed in an oven at 70°C overnight. Then, the surface was cryotrimmed at

-150°C (temperature lower than glass transition of both PA6 and HDPE) using a diamond knife in order to obtain a mirror surface.

In order to have contrast between phases, selective dissolution of the minority phase (in term of volume fraction) was performed:

- $\phi_{PA} < \phi_{HDPE+compatibilizer}$: PA6 phase was etched using formic acid at 90% at room temperature with stirring during 30 minutes
- $\phi_{PA} > \phi_{HDPE+compatibilizer}$: PE phase (HDPE + MA-g-HDPE) was etched. Toluene was first tested to solubilize the PE phase (stirring at 80°C for 2h). However, it only solubilized the amorphous part. As HDPEs used in this study exhibit about 80% of crystallinity, this solvent was not well adapted. Therefore, Decahydronaphthalene (Decalin) was used at 115°C with stirring for 1h30.

Finally, samples surfaces were metallized with Platinum.

Then, observation conditions were chosen in order to limit the sample degradation under the electron beam and to obtain a topographic contrast:

- Accelerating tension: 3keV
- Diaphragm: 20µm
- Secondary electrons. Two detectors were used:
  - SE2: mainly used
  - Inlens: used when an higher resolution was needed

The pellets obtained after extrusion were observed in the flow direction (denoted ‖) and perpendicularly to the flow (denoted ⊥) as shown on Figure II-17.
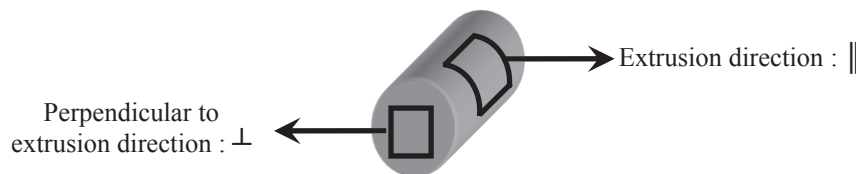
Figure II-17: Pellet diagram with SEM observations directions.

3.3.2. Transmission Electron Microscopy (TEM)

Transmission Electron Microscopy (*Technai Biotwin*) was also perfomed by Nelly Bulgarelli and Clémence Abadie (Rhodia CRTL) to characterize the morphologies at the nanometer scale without any phase etching on few samples. Ultrathin sections (100nm) were cut by ultramicrotomy at -150°C. PA6 phase was stained with phosphotungstic acid ($H_3PW_{12}O_{40}$) in order to improve the contrast between PA and PE.

4. Materials stability during processing

Prior to focus on blends, the stability of the materials (PA6, HDPEs and MA-g-HDPE) at extrusion temperature was first studied. The results obtained are presented in this section.

4.1. Stability of Polyethylene

As the extrusion temperature (290°C) is very high for HDPEs, ThermoGravimetric Analyses (TGA), Size Exclusion Chromatography (SEC) and capillary rheometry experiments were carried out to check the stability of Polyethylene.

4.1.1. ThermoGravimetric Analyses (TGA)

ThermoGravimetric Analyses (TGA) were performed on the three HDPEs and on MA-g-HDPE before any processing step at the extrusion temperature (290°C) by Daniel Alix (Rhodia CRTL). So, heating ramp from room temperature to 290°C was carried out at 50°C/min. Then, an isothermal plateau at 290°C during 30 minutes under air (to be in the most unfavourable conditions) was applied. The mass loss of each sample was followed during all the experiment duration. Obtained results are summarized in Table II-2.

	HDPE 1	HDPE 2	HDPE 3	MA-g-HDPE
Mass loss	6.2%	2.5%	2.2%	1.8%

Table II-2: Mass loss of Polyethylene (TGA).

Thus, HDPE 1 exhibited a larger mass loss than HDPE 2, HDPE 3 and MA-g-HDPE. As it is a commercial grade, formulated with various additives, the observed mass loss could be due to the degradation of PE additives in the formulation.

4.1.2. High Temperature Size Exclusion Chromatography (SEC)

Molecular masses distributions of the three HDPEs and of MA-g-HDPE were measured by High Temperature Size Exclusion Chromatography (SEC) before and after processing by Olivier Boyron (CPE Lyon) (method described in 0). These experiments were carried out both after twin screw extrusion (D34) and after batch mini-extrusion in order to determine if the type of process may have an influence on the possible degradation of Polyethylene. The results obtained are shown in Figure II-18 and summarized in Table II-3.

HDPE 1:
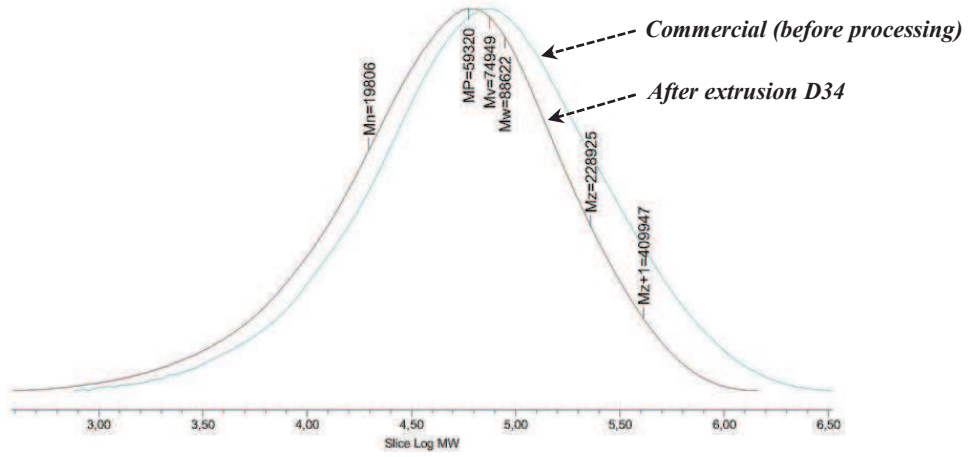
HDPE 2:
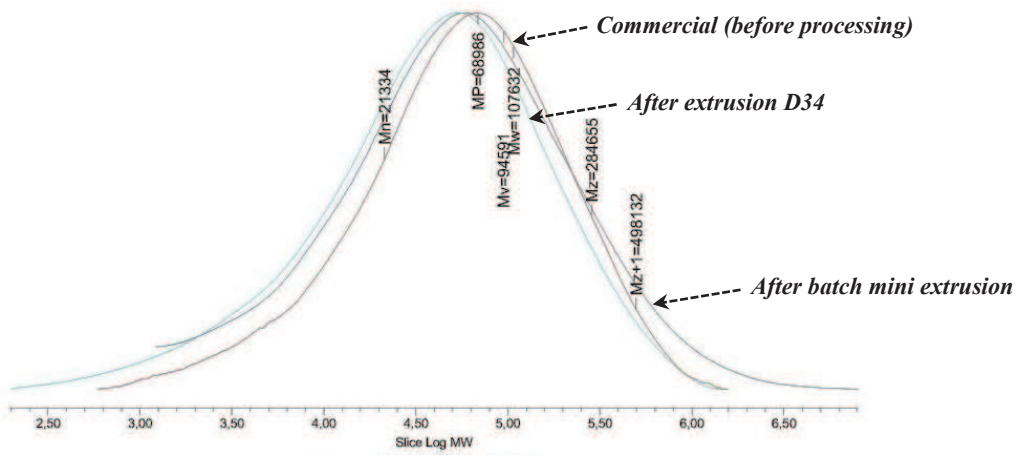
HDPE 3:
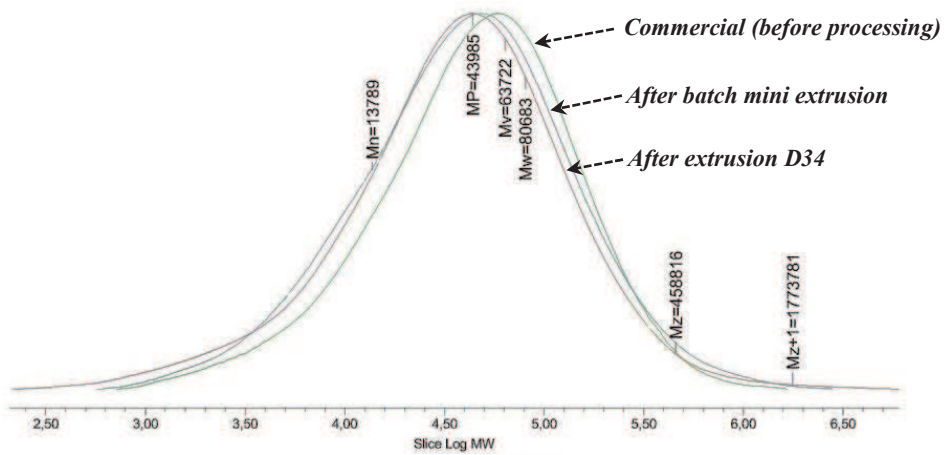
MA-g-HDPE:
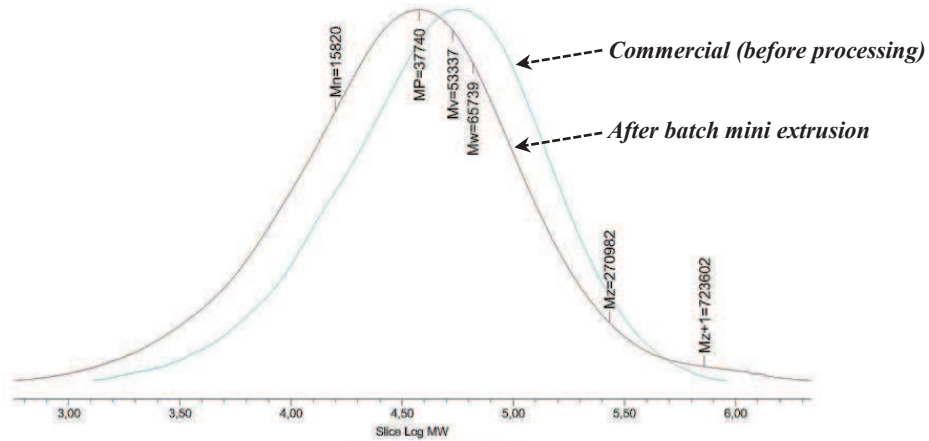
Figure II-18: Chromatograms of Polyethylene before and after processing (SEC measurements, absolute values).

		M_n (g.mol^{-1})	M_w (g.mol^{-1})	IP
HDPE 1	Commercial HDPE 1	29 300	145 300	5.0
	HDPE 1 after extrusion D34	19 800	88 600	4.5
HDPE 2	Commercial HDPE 2	21 300	107 600	5.0
	HDPE 2 after extrusion D34	11 300	87 700	7.7
	HDPE 2 after batch mini-extrusion	17 900	139 200	7.8
HDPE 3	Commercial HDPE 3	21 200	81 600	3.9
	HDPE 3 after extrusion D34	13 800	80 700	5.9
	HDPE 3 after batch mini-extrusion	17 700	82 500	4.7
MA-g-HDPE	Commercial MA-g-HDPE	26 000	75 700	2.9
	MA-g-HDPE after extrusion D34	24 300	120 600	5.0
	MA-g-HDPE after batch mini-extrusion	15 800	65 700	4.2

Table II-3: Molecular mass distributions (absolute values) of Polyethylene before and after processing.

Thus, according to Figure II-18 and to Table II-3, a decrease of the number average molecular mass (M_n) was observed after processing, often accompanied by an increase of the polydispersity index (_IP_). HDPEs and MA-g-HDPE evolved during these high temperature processes.

To compare both processes, Figure II-19 shows molecular mass distributions of HDPE samples after batch mini-extrusion and after extrusion D34.
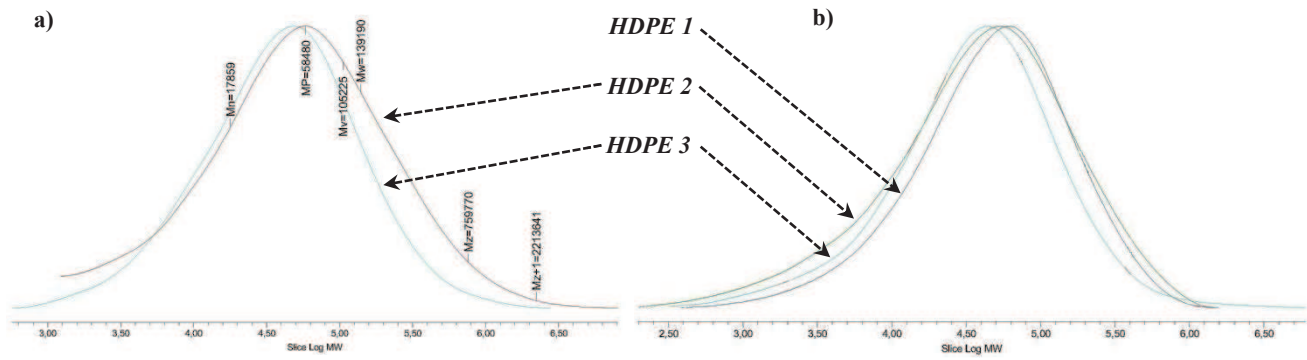
Figure II-19: Chromatograms a) after batch mini-extrusion and b) after extrusion D34 (SEC measurements, absolute values).

As shown on Figure II-19, after both processing tools, the average molecular mass of HDPE 1 was still larger than one of HDPE 2 and molecular mass of HDPE 2 was still larger than one of HDPE 3: $M_{HDPE\ 1} \geq M_{HDPE\ 2} > M_{HDPE\ 3}$.

4.1.3. Capillary rheometry experiments

The viscosity was also measured before and after extrusion at 290°C in order to check HDPEs evolution during processing. Figure II-20 shows the variation of the viscosity of raw HDPEs as a function of shear rate before and after twin screw extrusion (D34).
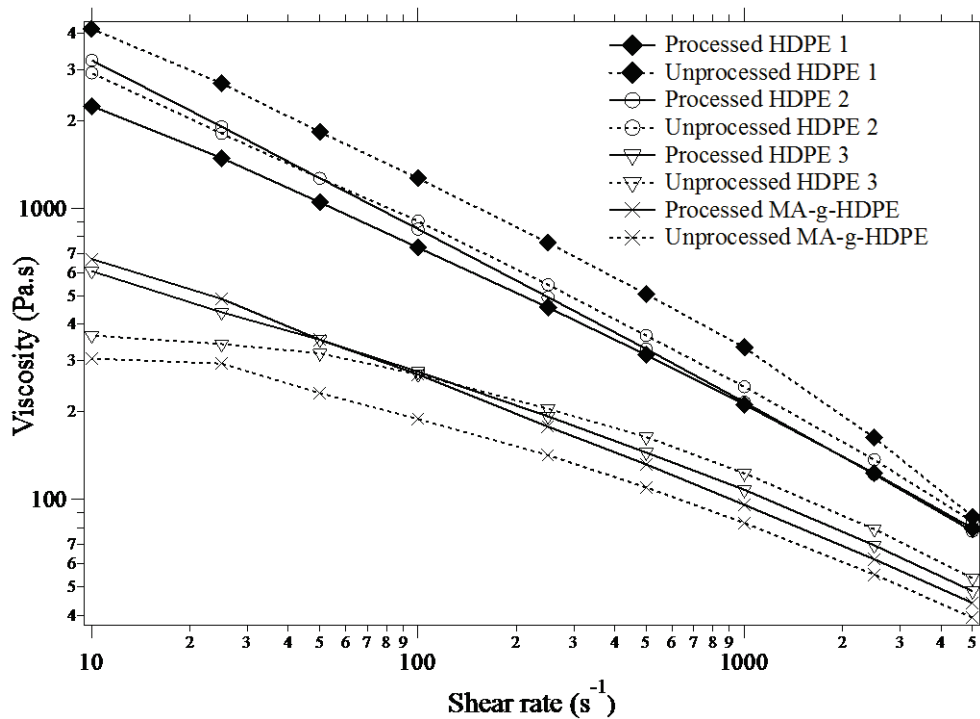
Figure II-20: Viscosity versus shear rate of commercial and extruded HDPEs at 290°C.

A large decrease of the viscosity after processing was observed in HDPE 1, which is in agreement with TGA results (Table II-2). As already explained, it is a commercial grade, formulated with various additives. This reduction of viscosity could be due to the degradation of PE additives in the formulation. SEC measurement on processed HDPE 1 actually showed a decrease of 39% on the average molecular mass M_w in comparison to the neat commercial HDPE 1 (Table II-3).

The viscosity of HDPE 2 was not affected during extrusion. We have also noted a quite small mass loss in TGA (Table II-2).

As regards HDPE 3 and MA-g-HDPE, the Newtonian plateau at low shear rates was lost after extrusion, which may be due to branching occurring during the process. This is qualitatively coherent with the increase of the Polydispersity Index (*IP*) during the process (Table II-3).

In addition, in the case of MA-g-HDPE, an increase of viscosity was observed after processing which is in qualitative agreement with the increase of M_w observed in SEC (Table II-3).

4.1.4. Conclusion on Polyethylene stability

To conclude on Polyethylene stability during processing (batch mini-extrusion and twin screw extrusion D34), small mass losses were obtained in TGA at 290°C, except for HDPE 1 (-6.2%). A large decrease of the viscosity of HDPE 1 after processing was also observed. On the other hand, only small differences were observed in the viscosity of HDPEs 2 and 3 after processing.

For all the HDPEs and the MA-g-HDPE, a decrease of the number average molecular mass (M_n) was observed in SEC after processing, most often accompanied by an increase of the polydispersity index (*IP*).

So, to take into account these changes in neat HDPEs and MA-g-HDPE, the parameters values of processed polymers will be considered to be representative of the materials when needed in the analysis.

4.2. Stability of Polyamide 6

As Polyamide 6 is very sensitive to moisture, the stability of this polymer during high temperature and shear process was studied.

The molecular mass distributions were measured by Sabrina Paillet and Nadia Delon-Anik (Rhodia CRTL) before and after extrusion (D34) by Size Exclusion Chromatography (SEC) in Polystyrene equivalents (method described in 0).

Figure II-21 shows the obtained molecular masses distributions.
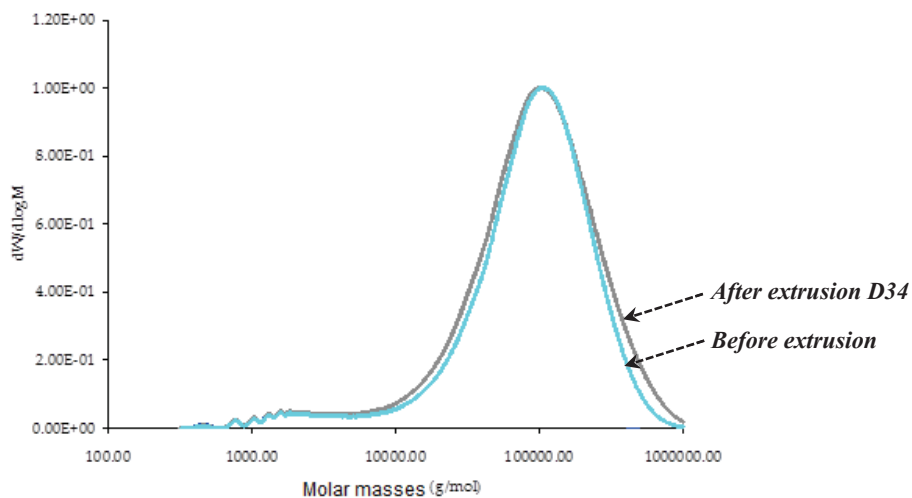
Figure II-21: Chromatograms of PA6 before and after extrusion D34 (SEC measurements in equivalents Polystyrene).

These SEC experiments did not show any significant effect of processing on PA6. In fact, we can just note a little increase of the polydispersity.

To conclude on the PA6 stability during processing, no significant evolution was observed.

So, the characteristics of neat unprocessed PA6 will be used in what follows.

5. Rheological characterization of raw materials

This section summarizes the rheological characteristics of raw materials measured by capillary rheometry. According to the study of polymers stability, in order to take into account the evolution of Polyethylene during processing, we have chosen to use the viscosities measured on HDPEs and MA-g-HDPE after extrusion. On the other hand, as PA6 does not seem to evolve much during processing, we have chosen to use the viscosity of unprocessed PA6. Figure II-22 shows the variation of the viscosity as a function of shear rate for:

- extruded HDPE
- extruded MA-g-HDPE
- examples of PE phases: HDPE/MA-g-HDPE 60/40%$_{vol}$
- unprocessed PA6
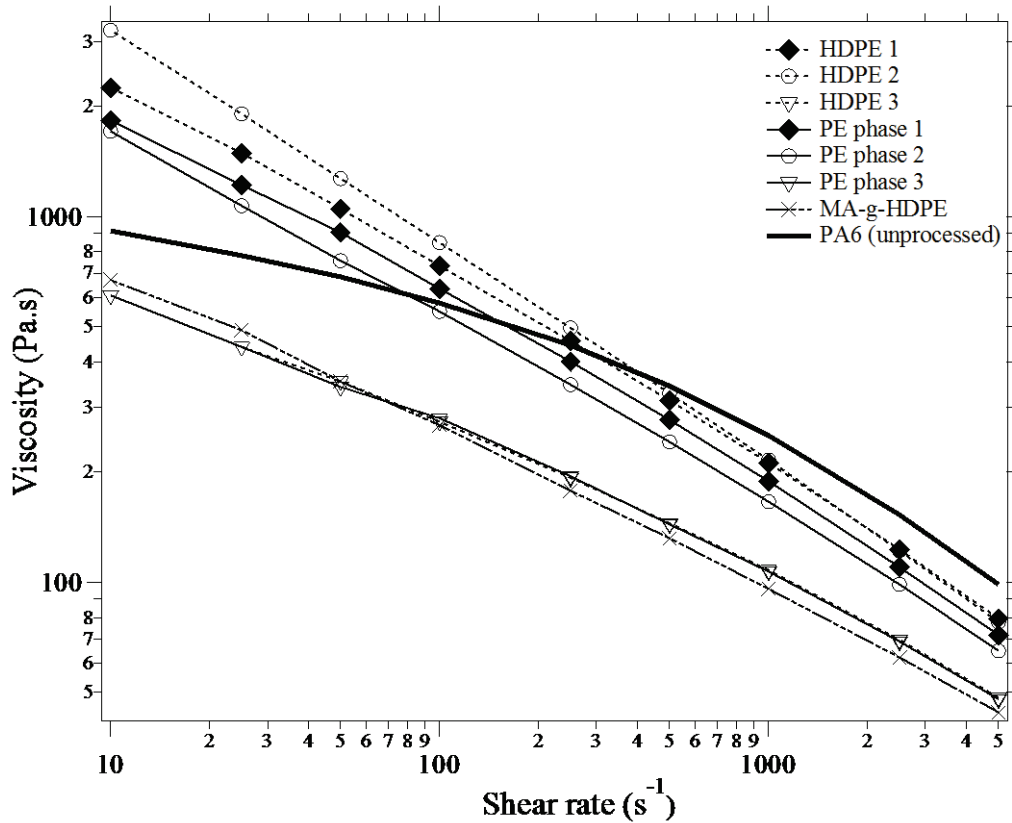
Figure II-22: Viscosity versus shear rate of unprocessed PA6, processed HDPEs, MA-g-HDPE and examples of PE phases (HDPE/MA-g-HDPE 60/40%$_{vol}$) at 290°C.

As shown in Figure II-22, by adding the compatibilizer to HDPEs 1 and 2, the viscosity of HDPEs 1 and 2 decreases. On the other hand, adding MA-g-HDPE to HDPE 3 does not change HDPE 3 viscosity, as expected from the molecular masses distributions in Figure II-18 and in Table II-3.

Thus, since HDPEs and MA-g-HDPE are considered to be miscible at the scale relevant in processing, the viscosity ratios between the two phases in the blends that must be considered are:

$$R_v = \frac{\eta_{HDPE+MA-g-HDPE}(\dot{\gamma})}{\eta_{PA\,6}(\dot{\gamma})} = \frac{\eta_{PE\,phase}(\dot{\gamma})}{\eta_{PA\,6}(\dot{\gamma})}$$

Eq. II-16

Then, two shear rates were considered:
- $100s^{-1}$: the order of magnitude of the average shear rate during extrusion
- $3500s^{-1}$: the order of magnitude of the shear rate in the most restrictive die (diameter 2mm) as calculated in *chapter II Materials and experimental section 3.1.1.1.1 Twin screw extrusion D34 page 83*.

The viscosity ratios obtained with the three PE phases (HDPE/MA-g-HDPE 60/40%$_{vol}$) at both shear rates were considered. They are reported in Table II-4.

	R_v at $100s^{-1}$	R_v at $3500s^{-1}$
HDPE 1	1.3	0.8
HDPE 2	1.5	0.7
HDPE 3	0.5	0.5
MA-g-HDPE	0.5	0.5
PE phase 1	1.1	0.7
PE phase 2	0.9	0.6
PE phase 3	0.5	0.5

Table II-4: Viscosity ratios R_v calculated using the viscosity of unprocessed PA6 and processed HDPEs and MA-g-HDPE at 100 and $3500s^{-1}$, at 290°C.

At high shear rate, all HDPEs and PE phases exhibit almost identical rheological behavior, which leads to viscosity ratios close to each other.

6. Conclusion

Thus, one Polyamide 6 (PA6) and three High Density Polyethylene (HDPEs) of different viscosity were used. The miscibility between PA6 and HDPE was discussed and the Flory interaction parameter was estimated to be roughly of the order of 0.7.

As PA6 and HDPE are immiscible, one standard compatibilizer Maleic Anhydride grafted High Density Polyethylene (MA-g-HDPE) was also used. HDPEs and MA-g-HDPE are considered to be miscible at the scale relevant in processing. Thus, the PE phase was defined to correspond to the overall HDPE+MA-g-HDPE amount. However, according to the estimation of the interaction parameter between MA moieties and HDPE chains and to dynamical rheometry experiments, MA micelles in HDPE seem to be formed.

The blends were prepared by twin extrusion using three different scales tools and various process conditions. Then, various conditions to study the stability of the morphologies were presented: static annealing, controlled shear experiments and second step processing (injection molding and extrusion blow molding).

The main experimental methods to characterize the rheological behavior and the morphology of the blends were then detailed. Capillary and dynamical rheometry were used in this study. To observe the morphologies obtained in the blends, Scanning Electron Microscopy (SEM) after selective phase etching of the minor phase was essentially performed. Transmission Electron Microscopy (TEM) without any phase dissolution was also carried out in some cases to complete the characterization.

In a last section, prior to focus on the blends and the morphologies development, raw materials used were studied in more details. As the extrusion temperature (290°C) is very high, notably for HDPEs, and as PA6 is very sensitive to moisture, the stability of the polymers was checked before to prepare blends essentially by ThermoGravimetric Analysis (TGA), Size Exclusion Chromatography (SEC) and capillary rheometry. It was shown that HDPEs and MA-g-HDPE evolved during processing. In fact, small mass losses were obtained in TGA at 290°C and a decrease of the number average molecular mass (M_n) was observed in SEC after processing, most often accompanied by an increase of the polydispersity index (IP). On the other hand, no significant evolution of PA6 was observed during processing. According to this stability study, a summary of the polymers rheological characteristics which will be considered to be representative of the materials was then presented (processed HDPEs and MA-g-HDPE, unprocessed PA6).

So, adding MA-g-HDPE to HDPEs decrease the viscosity of the HDPEs except for HDPE 3. The viscosity ratios (PE phase/PA6) obtained range from 0.5 to 1.5 at 100s-1. Obviously, this range is narrower at 3500s^{-1} (from 0.5 to 0.8).

III. Control of blend morphologies

1. Introduction

This chapter deals with the development and control of morphologies in Polyamide 6 / High Density Polyethylene reactively compatibilized blends. Several morphologies were observed in SEM: nodular dispersion, stretched dispersion and co-continuity. They exhibit characteristic sizes from nanometer scale to micrometer scale.

Morphologies at the micrometer scale are first discussed. As the process conditions do not influence the type of morphologies, the morphological regions are plotted in ternary diagrams for each HDPE, independently from the kind of tool. Dispersed/stretched dispersed and co-continuous structures are then discussed more precisely in term of Capillary number and of phase inversion models respectively. Finally, the influence of several parameters including processing conditions, compatibilization and viscosity ratios is detailed in order to determine the predominant factor in morphology development at this micrometer scale.

The compatibilization reaction conversion was determined and the quantity of in situ formed copolymer was estimated, which suggest the existence of morphologies at smaller scale. Thus, morphologies at the nanometer scale are then discussed. Firstly, the nano-dispersions are described in compatibilized systems. According to the literature, a mechanism of formation via interfacial roughening is proposed. The sizes observed experimentally in TEM are then compared to the estimated ones according to Taylor's theory. Morphologies at smaller scale in non-compatibilized blends are then discussed. The sizes observed experimentally are also compared to the estimated ones from Taylor' equation.

In a last part, the percolation theory is used to describe the characteristic sizes and the distribution of sizes obtained from the nanometer to the micrometer scale in our blends. Finally, as a conclusion, a global diagram to describe the formation of these multi-scales morphologies is proposed.

2. Obtained morphologies

PA6/HDPE/MA-g-HDPE blends were studied over a broad range of compositions. The morphologies obtained are represented using ternary diagrams in which each axis corresponds to the volume fraction of each polymer in the blends.

In the ternary diagrams, several particular regions, lines and points are considered to analyze the results obtained as shown in Figure III-1.
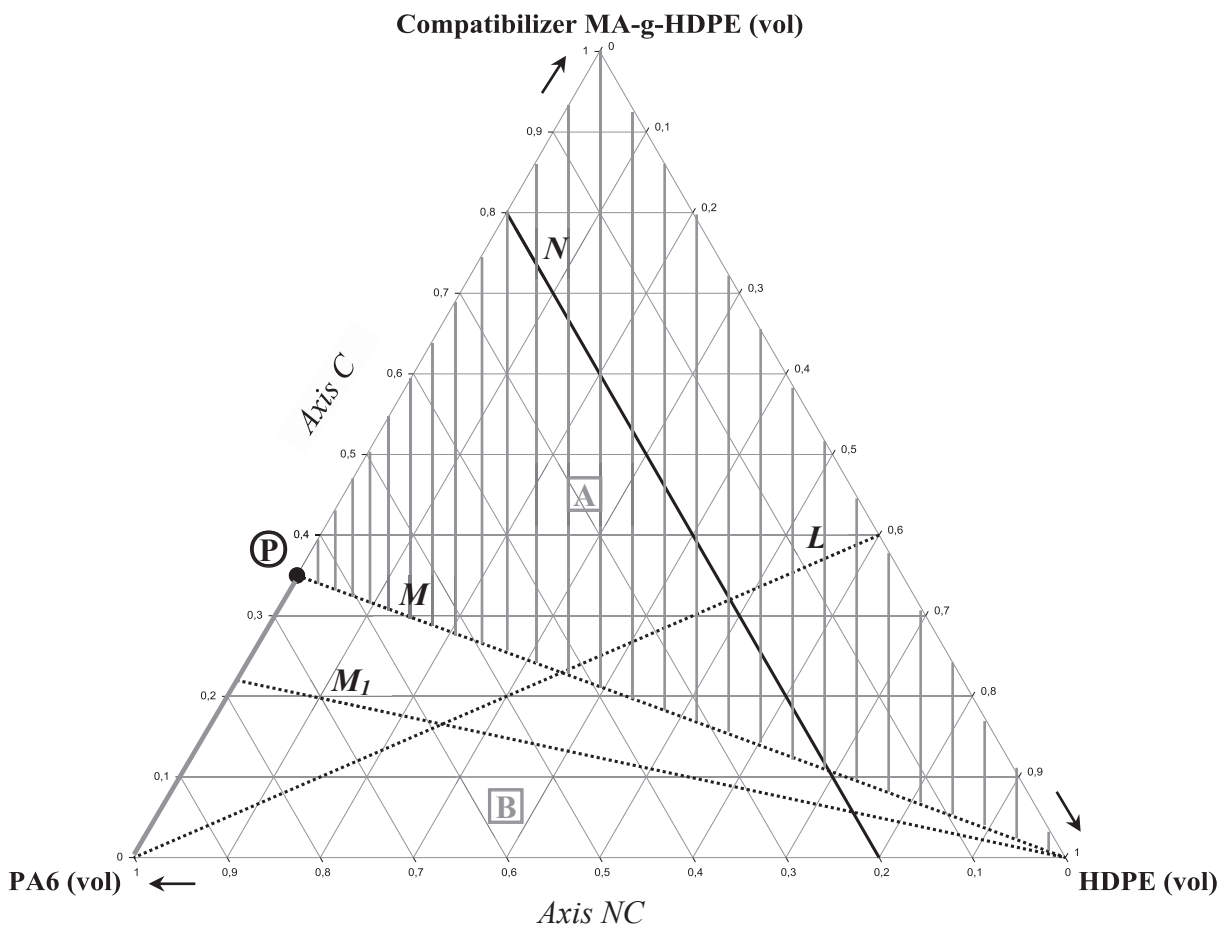
Figure III-1: Explanation of ternary diagram representation for PA6/HDPE/MA-g-HDPE blends.

- Along line **L** (which passes through PA6 vertex), the concentration of MA moieties in the PE phase (i.e. the initial chemical potential of MA moieties in the PE phase) is constant and equals to the concentration of NH_2 in the PA6 phase ($40 mmol.kg^{-1}$). Thus, whatever the blend composition, the interface is in contact with the same concentration of reactive moieties on each side, as illustrated in Figure III-2.

PE phase > PA6   PE phase < PA6

MA moieties ———▶   ——— NH_2 moieties
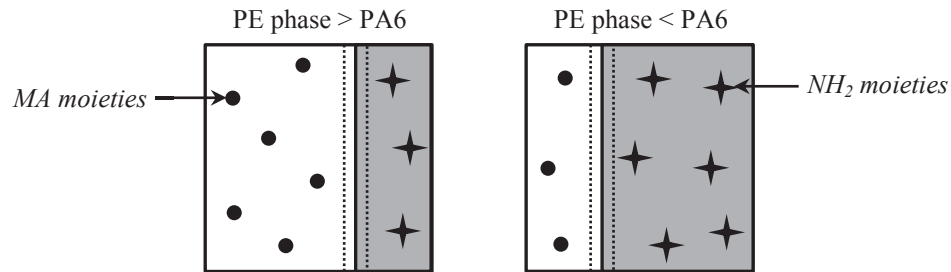
Figure III-2: Schematic diagram of PE phase-PA6 interface along line _L_ on Figure III-1.

- Along lines **M** or **M₁** (which pass through the HDPE vertex), the overall molar ratio $[MA]/[NH_2]$ in the blend is constant.
    - Line **M** corresponds to $[MA]/[NH_2]=1$, the stoichiometry
    - Line **M₁** corresponds to $[MA]/[NH_2]=0.5$

Thus, depending on the blend composition, the interface is not in contact with the same concentration of reactive moieties on each side. Blends on line **M** are illustrated in Figure III-3.

PE phase > PA6   PE phase < PA6

MA moieties ———▶   ——— NH_2 moieties
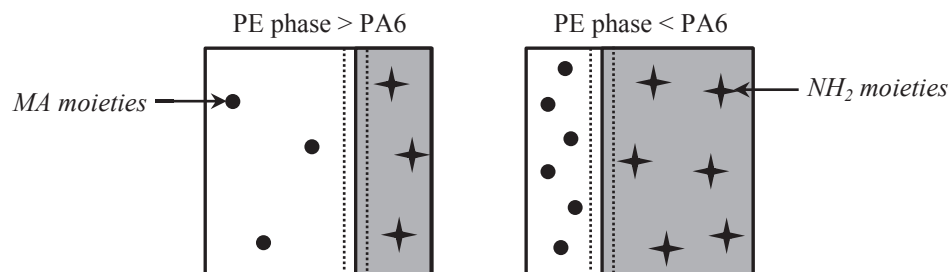
Figure III-3: Schematic diagram of PE phase-PA6 interface along lines _M_ on Figure III-1.

- At point **Ⓟ**, if the reaction conversion would be 100%, the obtained final system would contain only PA6-HDPE grafted block copolymer.

- Above line **M** (domain Ⓐ, hatched), there is an excess of MA moieties, which means that if the reaction would be fully completed, all PA6 chains would be under the form of copolymers anchored at interface.

- Below line **M** (domain ⬜B⬜), there is an excess of NH_2 end-groups, all PA6 cannot react. In domain ⬜B⬜, the obtained system contains both PA6 and HDPE homopolymers in addition to PA6-g-HDPE copolymers.

- Along the *Axis C*, (Compatibilized), there is no HDPE homopolymer is the blends. Only PA6 and MA-g-HDPE are added.

- Along the *Axis NC* (Non-Compatibilized), there is no compatibilizer MA-g-HDPE in the blends. There are only PA6 and HDPE homopolymer.

- Along the segment [Ⓟ - PA6] (in grey), all the chains of HDPE in PE domains are under the form of PA6-g-HDPE copolymers (if the reaction is completed).

- Along line **N** (any line parallel to MA-g-HDPE - HDPE axis), the PA6 volume fraction is constant. Only the concentration of MA-g-HDPE in the PE phase changes.

Figure III-4 shows representative examples of SEM micrographs of the different kinds of morphologies observed in PA6/HDPE blends. In what follows, the various morphologies will be represented in the ternary diagrams by regions filled with the same pictograms as in the small squares in Figure III-4 (dots, stripes, plain grey).

1) PA6 dispersion in PE phase

PA6/HDPE 3/MA-g-HDPE: 31/42/27%$_{vol}$

2μm

2) PA6 stretched dispersion in PE phase

PA6/HDPE 1/MA-g-HDPE: 38/38/24%$_{vol}$

2μm

3) Co-continuous

PA6/HDPE 1/MA-g-HDPE: 50/30/20%$_{vol}$

2μm

4) PE phase stretched dispersion in PA6

PA6/HDPE 1/MA-g-HDPE: 60/24/16%$_{vol}$

2μm

5) PE phase dispersion in PA6

PA6/HDPE 2/MA-g-HDPE: 63/15/22%$_{vol}$

2μm
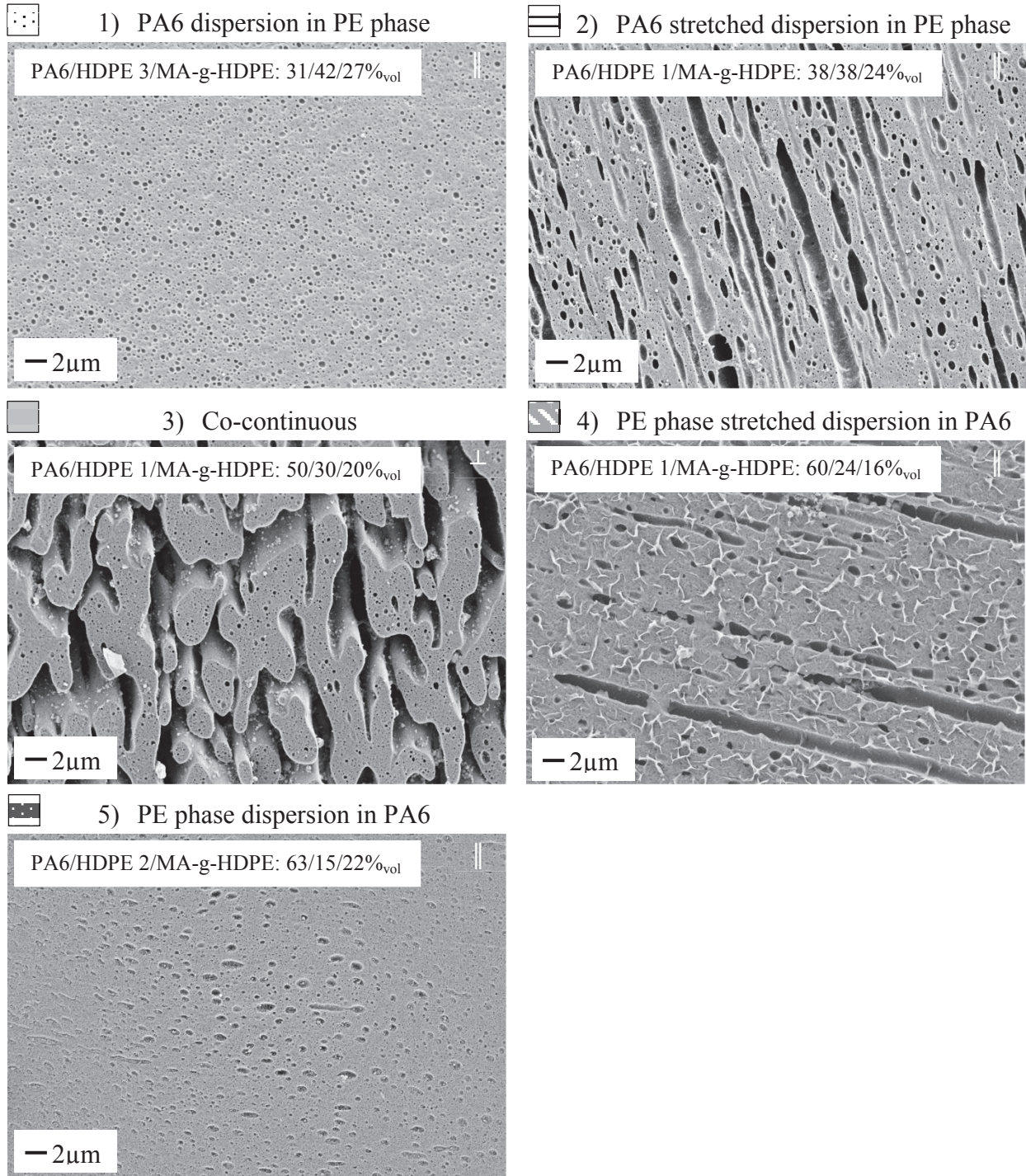
Figure III-4: Representative examples of SEM micrographs (x 2500) of the various types of morphology observed in twin screw extruder diameter 34mm: 1, 2: PA6 etched (formic acid); 3, 4, 5: PE phase etched (Decalin).

It is very important to notice that the morphology exhibits a broad distribution of sizes. This is particularly obvious at intermediate compositions close to phase inversion (Figure III-4 (3)). In this case, two characteristic sizes differing by almost two orders of magnitude are clearly visible.

107

The largest typical size ranges from 500nm to a few micrometers and the finest scale (nano-dispersion) is of a few tens of nanometers. The distributions of scales will be discussed in this chapter.

3. Morphology at the micrometer scale

In this section, we first focus on the morphology at the micrometer scale.

3.1. Ternary diagrams of morphologies

As the kind of processing tools and process conditions did not affect the type of morphology (this point is discussed in more details in *section 3.2 page 114*), the regions corresponding to the five types of morphologies in Figure III-4 were defined and summarized in ternary diagrams for the three HDPEs in Figure III-5 (a), (b) and (c). The investigated formulations correspond to the markers in Figure III-5. The different regions correspond to the morphologies shown in Figure III-4 using the same pictograms. The extrapolated boundaries between the different morphology regions are indicative limits. They are precise only between the investigated formulations (ie at the locations of the markers in Figure III-5).

Figure (b) — Ternary composition diagram. Axes: Compatibilizer MA-g-HDPE (vol) (top), PA6 (vol) (bottom left), HDPE 2 (vol) (bottom right). Labeled points F, D, G, E.
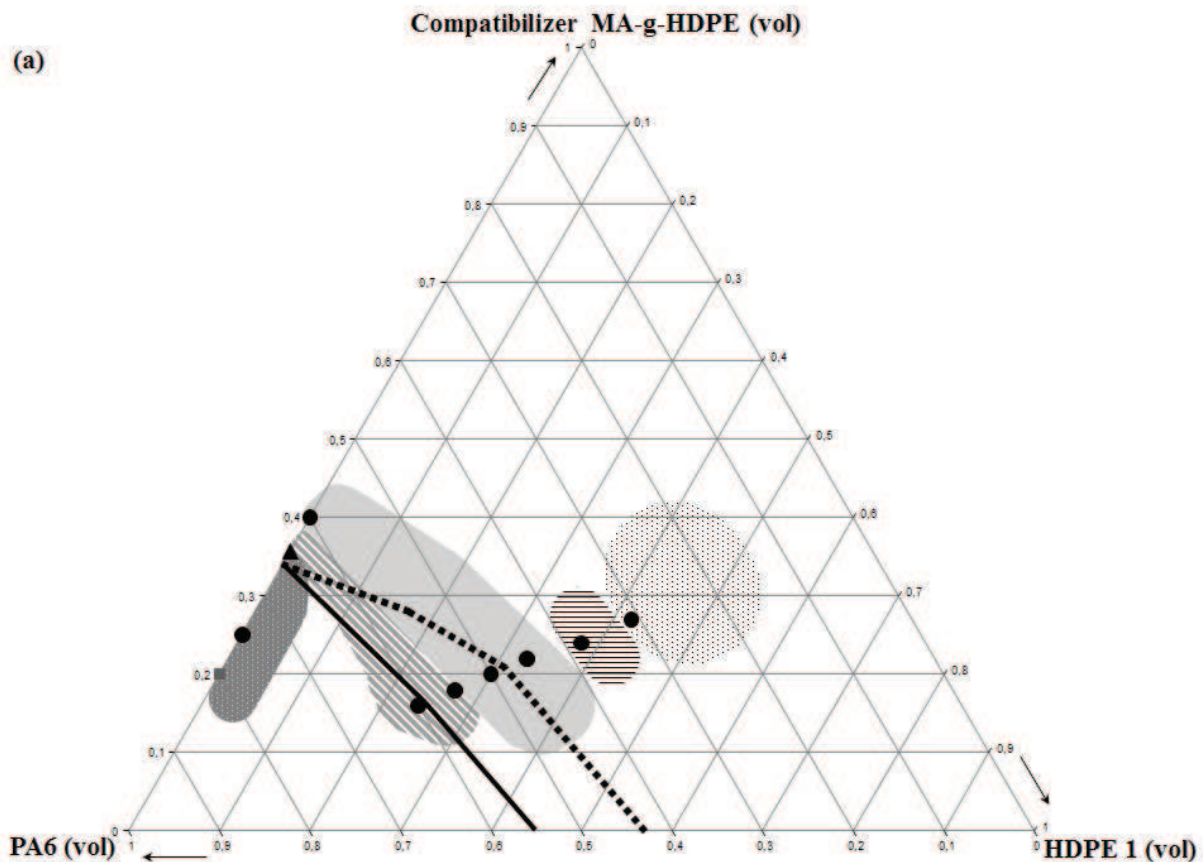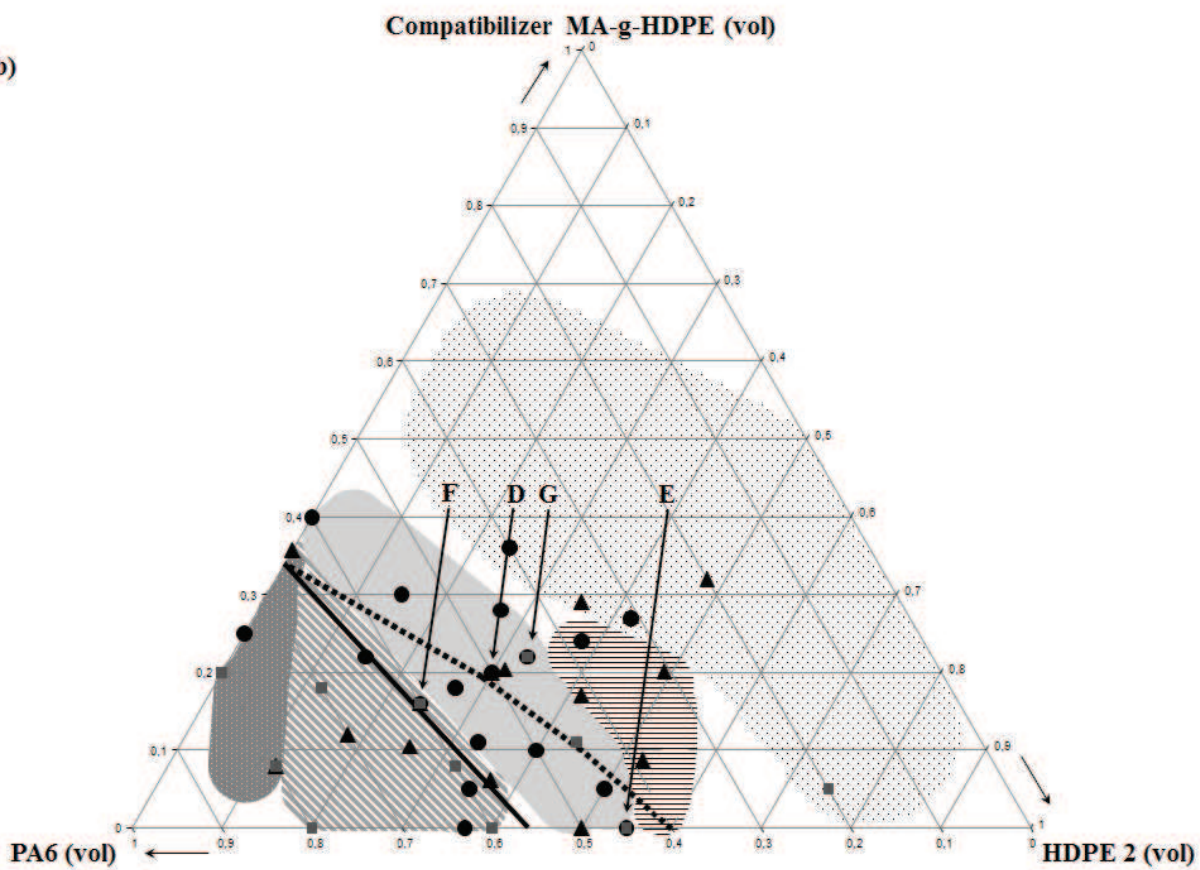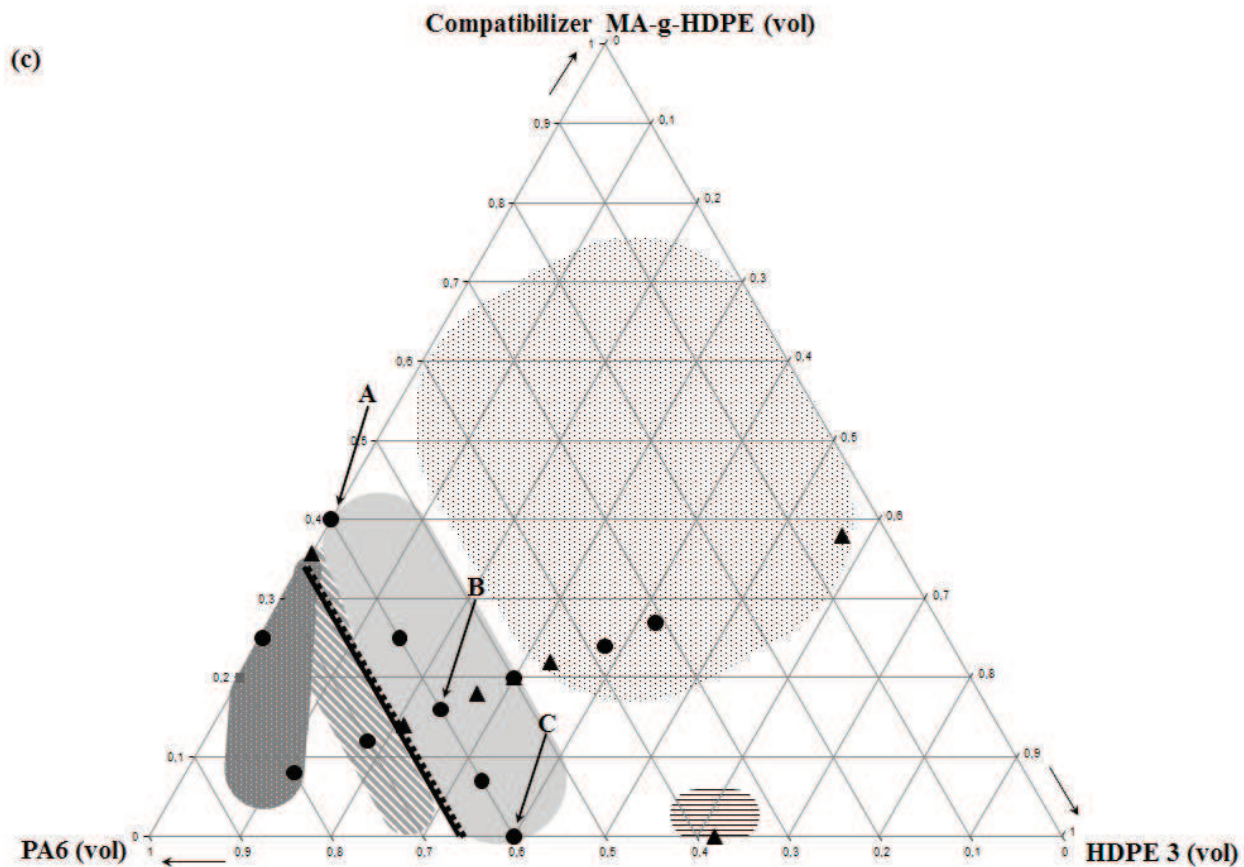
Figure III-5: Ternary diagrams of the morphologies obtained with (a) HDPE 1, (b) HDPE 2 and (c) HDPE 3.

● **: blends prepared in twin screw extruder diameter 34mm**
▲ **: blends prepared in mini extruder, various conditions**
■ **: blends prepared in twin screw extruder diameter 40mm**
Phase inversion compositions predicted by Paul and Barlow model (see *Chapter I Section 2.5.3.4 page 60*):
··· **: using viscosity ratios at 100s⁻¹ (order of magnitude of the average shear rate in extrusion)**
— **: using viscosity ratios at 3500s⁻¹ (shear rate in the extruder die diameter 2mm)**

HDPE 1 and HDPE 2 exhibit nearly similar results due to their very close rheological behavior (Figure II-22).

3.1.1. Dispersed and stretched dispersed morphology

In our system, the viscosity ratios range from 0.5 (PE phase 3, HDPE 3 and MA-g-HDPE as dispersed phase in PA6 matrix) to 2 (PA6 as dispersed phase in PE phase 3, HDPE 3 or MA-g-HDPE matrix) (*see Table II-4*). By using these values of viscosity ratios, the critical Capillary number Ca_{cr} defined as the minimum Capillary number sufficient to cause deformation and eventually break up of the dispersed phase can be estimated (Eq. I-28 in *Chapter I section 2.3.1 Drop break-up page 31*). In our case, a very narrow range of Ca_{cr} was found:

$$0.9 < Ca_{cr} < 1.4$$ **Eq. III-1**

This critical Capillary number is related to a minimum dispersed phase diameter D_{min} by:

$$D_{min} = \frac{2\Gamma Ca_{cr}}{\dot{\gamma}\eta_m}$$ **Eq. III-2**

With:
- η_m, the matrix viscosity
- D_{min}, the minimum dispersed phase diameter to observe dispersed phase deformation
- Γ, the interfacial tension (typically 1mN/m in compatibilized system as described in the literature for PA6/LDPE compatibilized using Maleic Anhydride [94,93,101] and 10mN/m in non compatibilized system as estimated in *Chapter II Materials and experimental section 2.4 Miscibility between Polyethylene and Polyamide page 74* using the Flory interaction parameter)
- $\dot{\gamma}$, the shear rate

At a shear rate of $100s^{-1}$ (order of magnitude of extrusion shear rate):
- For compatibilized blends: $D_{min}{\sim}50nm$
- For non-compatibilized blends: $D_{min}{\sim}500nm$

At a shear rate of $3500s^{-1}$ (order of magnitude of shear rate in the extruder die of diameter 2mm):
- For compatibilized blends: $D_{min}{\sim}6nm$
- For non-compatibilized blends: $D_{min}{\sim}60nm$

Thus, whatever the shear rate which would be considered to be representative of the process, at the micrometer scale, all the blends exhibit typical size of the dispersed phase larger than D_{min}. Thus, they are all able to deform into stretched dispersion morphology.

We assume that the stretched morphologies were notably obtained during the passage through the die. In fact, the shear rate applied was estimated to be $\dot{\gamma} = 3500 s^{-1}$. The time of passage through the die was estimated in *Chapter II section 3.1.1.1.1 Twin screw extrusion D34 page 83* to be t_{die}=0.01s. This time being very low, no stationary regime can be reached. In fact, the time of passage through the die was just 35 times longer than $\frac{1}{\dot{\gamma}}$. The maximum shear applied was estimated to be $\gamma_{max} = \dot{\gamma} t_{die} = 35 \gg 1$. Thus, the material was submitted to high shear and the morphology could be stretched. At the exit of the die, the strand was quenched in water. Note that the strand was also stretch during its cooling in water by a driving roller to be then pelletized.

As shown on the ternary diagrams (Figure III-5), in our case, stretched dispersions/fibrils were always observed near phase inversion which is in agreement with Huitric et al [10]. We can also note that stretched dispersion/fibrils were obtained over a broader range of compositions in non-compatibilized blends. This is particularly obvious with HDPE 2 (Figure III-5 (b)). In fact, we can easily imagine that it is easier to stretch the larger droplets obtained in non-compatibilized blends than the smaller ones in compatibilized systems.

3.1.2. Co-continuous morphology

As regards the co-continuous morphology, it was obtained at various PA6 volume fraction (from 45 to 65%$_{vol}$ of PA6) according to the three HDPEs used. Observed co-continuity domains were compared to predictions of phase inversion models proposed in the literature [12,8,65,2] as detailed in *chapter I section 2.5.3.4 Influence of the rheological behavior: Phase inversion prediction* models *page 60.* Models' predictions and experimental co-continuous formulations are plotted using the viscosity ratios at 100 and 3500s^{-1} or using the elastic modulus *G'* and loss angles *tanδ* at 10 and 100rad.s^{-1} in Figure III-6.

Paul and Barlow model:

$$\frac{\phi_1(vol)}{\phi_2(vol)} = \frac{\eta_1\left(\overset{\bullet}{\gamma}\right)}{\eta_2\left(\overset{\bullet}{\gamma}\right)}$$

ϕ_{PA} (vol)

$R_v = \eta_{PE\ phase}/\eta_{PA}$

Metelkin model:

$$\phi_2(vol) = \left[1 + \frac{\eta_1}{\eta_2}\left(1 + 2.25\ln\frac{\eta_1}{\eta_2} + 1.81\left(\ln\frac{\eta_1}{\eta_2}\right)^2\right)\right]^{-1}$$

ϕ_{PA} (vol)

$R_v = \eta_{PE\ phase}/\eta_{PA}$

At 10rad.s^{-1}   *At 100rad.s^{-1}*

Bourry model:

$$\frac{\phi_1(vol)}{\phi_2(vol)} = \frac{G'_2}{G'_1}$$

ϕ_{PA} (vol)

$R_{G'} = G'_{PA}/G'_{PE\ phase}$

Bourry model:

$$\frac{\phi_1(vol)}{\phi_2(vol)} = \frac{\tan\delta_1}{\tan\delta_2}$$

ϕ_{PA} (vol)

$R_{\tan\delta} = \tan\delta_{PE\ phase}/\tan\delta_{PA}$
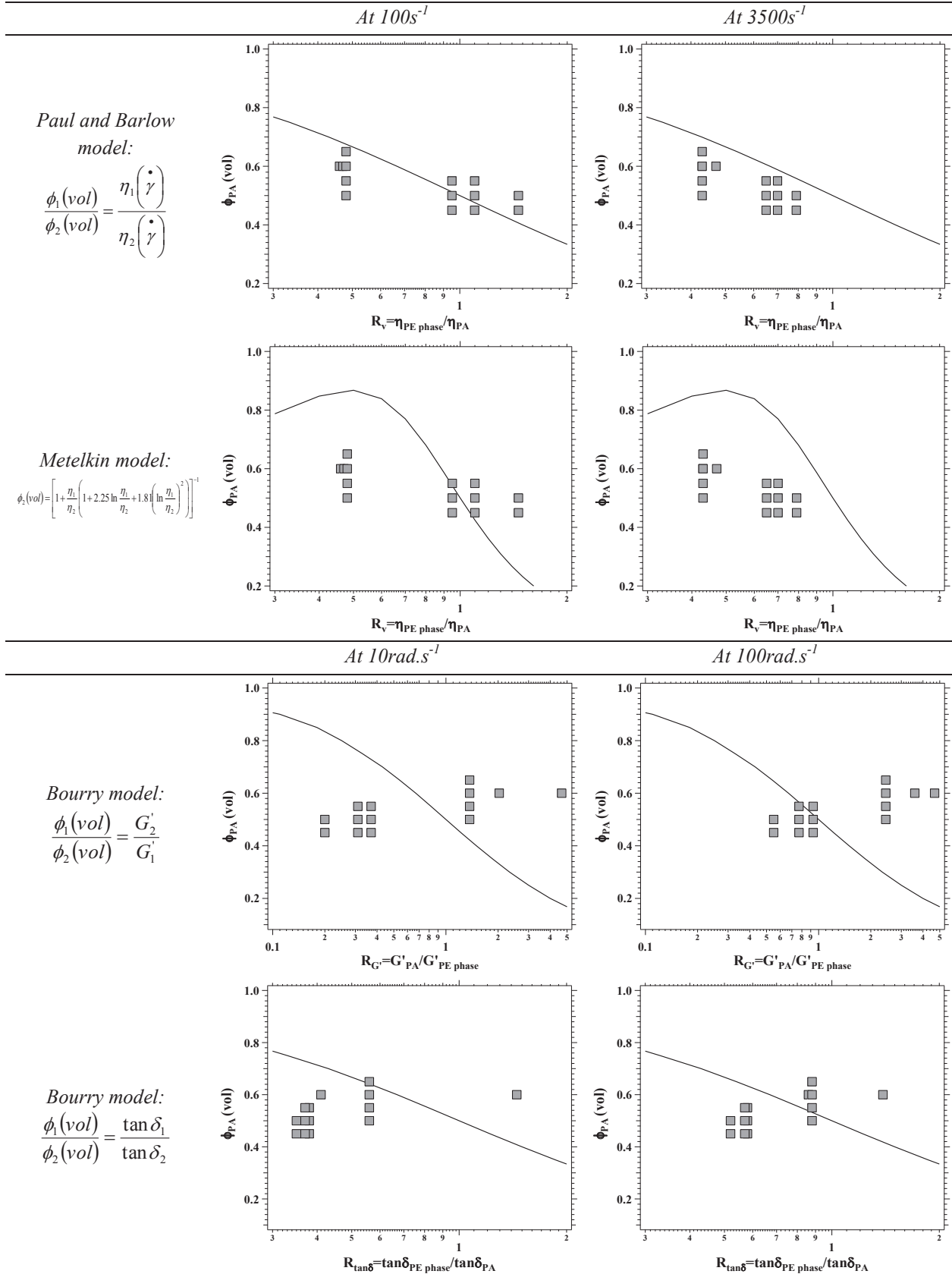
Figure III-6: Experimental co-continuous region (grey markers) and predictions of phase inversion models (black line).

The models based on elasticity ratios (elastic modulus *G'* and loss angle *tanδ*) clearly give an opposite evolution of the phase inversion composition as compared to the experimental data. Concerning the models based on the viscosity ratios, Metelkin predictions do not fit as well as Paul and Barlow ones. Thus, the phase inversion predictions of Paul and Barlow model taking into account the overall PE phase HDPE+MA-g-HDPE are represented on the ternary diagrams of Figure III-5 as a rough guide.

Concerning more precisely the co-continuity in the case of HDPE 3 (Figure III-5 (c)), since the viscosity ratios are similar at 100 and 3500s^{-1}, the same phase inversion compositions are predicted by the model at both shear rates. Moreover, since the compatibilizer does not influence the PE phase viscosity (Figure II-22), the model prediction follows a straight line.

On the other hand, for HDPE 1 and 2, the compatibilizer influences the viscosity of PE phases (Figure II-22). As the compatibilizer amount in the PE phase increases, the viscosity and thus, the viscosity ratio decrease which explains the curvature of the "phase inversion line" predicted by the model. Obviously, this curvature is less pronounced using the viscosity ratios at 3500s^{-1}. In fact, at this higher shear rate, MA-g-HDPE, HDPEs 1 and 2 exhibit quite the same viscosity (Figure II-22).

The ternary diagrams of the morphologies being established for the three HDPEs, the influence of various parameters including processing conditions, compatibilization and viscosity ratios on these morphologies at the micrometer scale will be discussed in the following sections.

3.2. Influence of processing on the micrometer scale morphology

The influence of the processing is divided into two parts. First, the kind of tools and extrusion parameters, including temperature, screw speed and residence time, were studied. Then, influence of materials feeding mode during extrusion was investigated.

3.2.1. Kind of tools and extrusion parameters

The influence of kind of tool was studied using the tools described in *Chapter II section 3.1 Blends* processing *page 82*):
- Two twin screw extruders (D34 and D40)
- One batch mini extruder

A broad range of process conditions was tested using this last batch mini extruder:
- Screw speed: from 10 to 200rpm
- Melt temperature: from 270 to 315°C
- Residence time: from 1 to 11min

3.2.1.1. Comparison between the tools

One blend with HDPE 2 (60%$_{vol}$ PA6 / 24%$_{vol}$ HDPE 2 / 16%$_{vol}$ MA-g-HDPE) (blend F on Figure III-5 (b)) was made using the three tools. Figure III-7 shows SEM micrographs of this blend processed using the three tools.

Twin screw extrusion D34 10kg/h, 250rpm   *Batch mini-extrusion 100rpm, 4min of residence time*   *Twin screw extrusion D40 40kg/h, 250rpm*
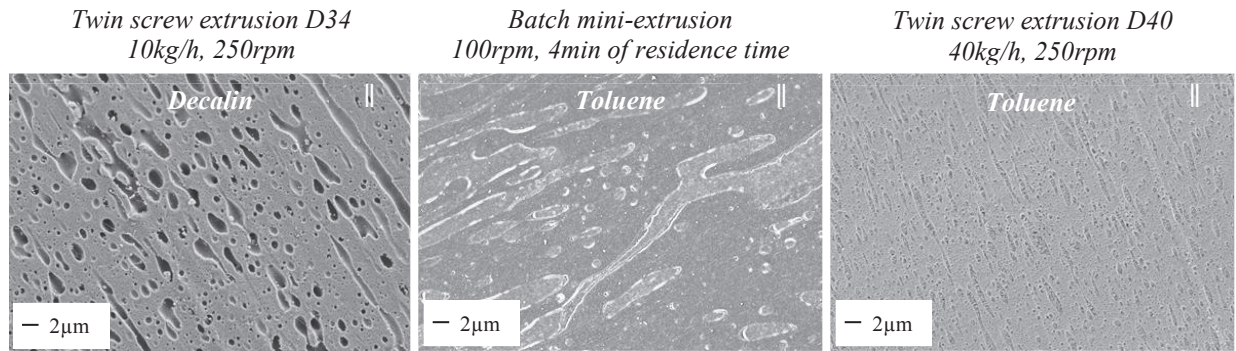
Figure III-7: SEM micrographs x2500 of blend 60%$_{vol}$ PA6/24%$_{vol}$ HDPE 2/16%$_{vol}$ MA-g-HDPE processed by the three tools at 290°C (PE phase etched).

The kind of morphology is PE phase stretched dispersion, close to co-continuous region in the three cases. However, domains size changes depending on the tool used. By taking blend processed by twin screw extrusion D34 as reference:
- The domains size after batch mini-extrusion is larger, which may be due to a smaller shear rate.
- The domains size after twin screw extrusion D40 is much smaller, which may be due to a larger shear rate.

Thus, the kind of tools, at least in the range tested here, does not seem to influence the kind of morphology but highly affects the size of the dispersed phase domains depending on the shear rate applied.

3.2.1.2. Influence of the extrusion parameters

In order to conclude on the influence of process parameters on the kind of morphology, two cases were considered:
1) Inside a region of morphology
2) At the boundaries between two regions of different morphologies.

3.2.1.2.1. Inside a region of morphology

Figure III-7 presents two examples of blends inside a region of morphology, D and E in Figure III-5 (b).
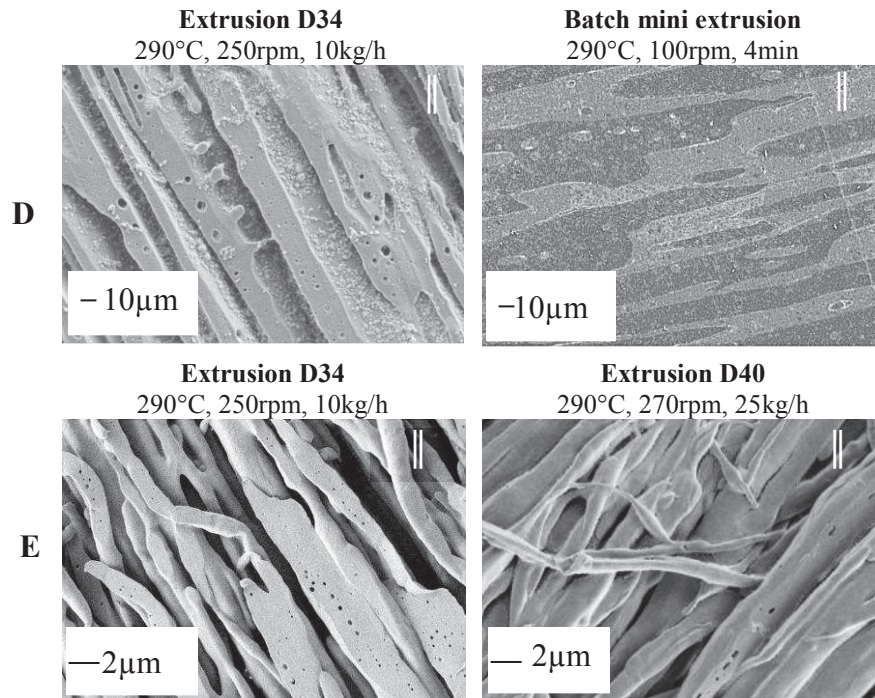
Figure III-8: Examples of SEM micrographs of formulations D (PA6/HDPE 2/MA-g-HDPE 50/30/20%ᵥₒₗ, PE phase etched with Toluene) and E (PA6/HDPE 2/MA-g-HDPE 45/55/0%ᵥₒₗ, PA6 etched with formic acid) in Figure III-5 (b) prepared at 290°C in the three processing tools inside the same morphology region.

Blend morphology does not depend on the kind of tool and thus, on the process parameters as shown on Figure III-8 with formulations D and E with HDPE 2 (Figure III-5 (b)).

3.2.1.2.2. At boundaries between two regions of different morphology

The kinds of tools and process parameters have an influence only in the second case, at the boundaries between two regions of different morphologies. In fact, at the frontier between a region of morphology 1 and a region of morphology 2, depending on the process conditions, the blend will exhibit morphology 1 or 2 as illustrated in Figure III-9 with formulations F and G (Figure III-5(b)).
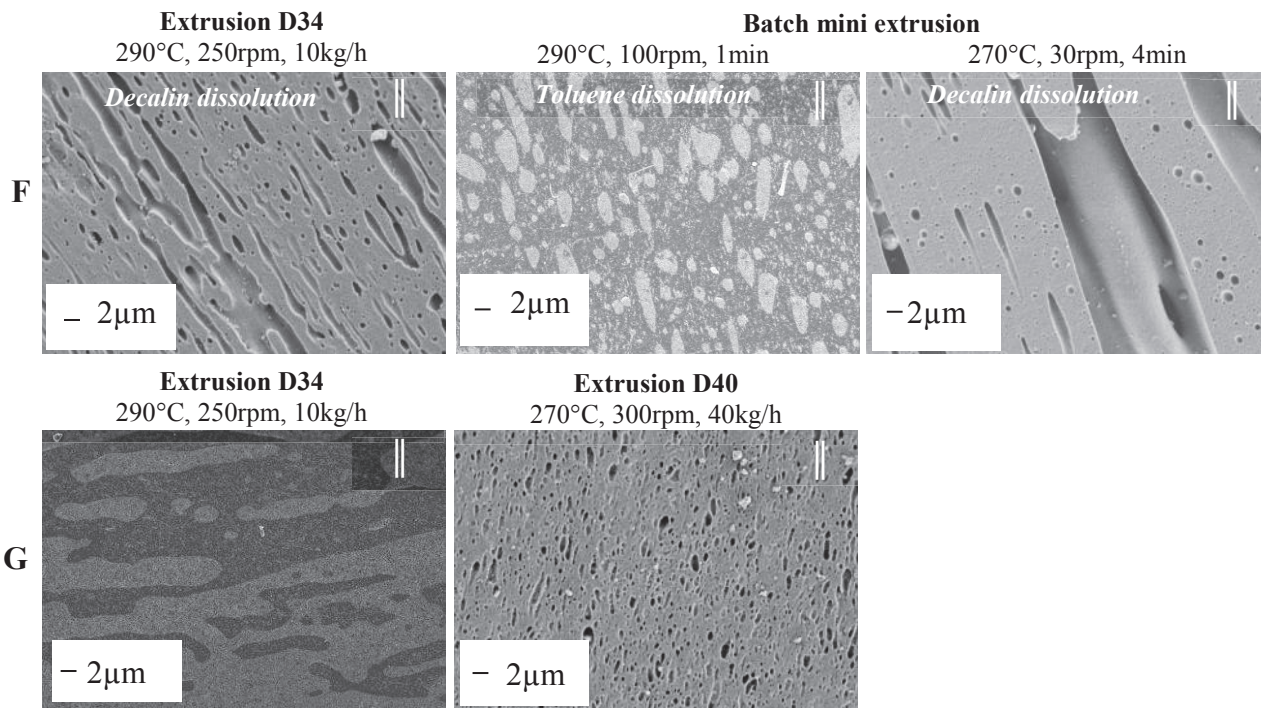
Figure III-9: Examples of SEM micrographs of formulations F (PA6/HDPE 2/MA-g-HDPE 60/24/16%$_{vol}$, PE phase etched with Decalin or Toluene) and G (PA6/HDPE 2/MA-g-HDPE 45/33/22%$_{vol}$, PA6 etched with formic acid) in Figure III-5 (b) prepared using the three processing tools and various conditions. These formulations are located at the boundaries between two regions of different morphologies on the ternary diagram.

In the case of formulation F in Figure III-9, the blend is at the boundary between PE phase stretched dispersion morphology region and co-continuous one. The blend made in twin screw extruder diameter 34mm exhibits PE stretched dispersion morphology with few domains still co-continuous. In batch mini extruder, depending on the conditions applied, the same formulation exhibits PE stretched dispersion or co-continuous structure with larger domains size.

In the case of formulation G in Figure III-9, the blend is at the boundary between co-continuous morphology and PA6 stretched dispersions. In twin screw extruder diameter 34mm, the obtained morphology is clearly co-continuous. Using twin screw extruder diameter 40mm, both throughput and shear rate are higher. Thus, the morphology becomes finer and is closer to PA6 stretched dispersion.

To summarize, the extrusion parameters do not influence the kind of morphology at least in the range of conditions and tools used (batch of 10g and twin screw extruders with diameters from 34 to 40mm), except at the boundaries between two different morphologies regions. At the boundaries, scale transposition conditions have been determined between twin screw extruder diameter 34mm and batch mini extruder to obtain the same morphology. **Thus, to be representative of twin screw extrusion diameter 34mm at 290°C, 250rpm and 10kg/h, the following conditions have to be used in batch mini extrusion: 290°C, 100rpm and residence times from 2 to 4min.**

3.2.2. Influence of the materials feeding mode

To study the influence of feeding mode, blend B in Figure III-5 (c) (PA6/HDPE 3/MA-g-HDPE 60/24/16%$_{vol}$) with a molar ratio [MA]/[NH$_2$] of 0.5 was prepared with six feeding modes. Two feeding devices were used. Morphologies obtained are summarized in Figure III-10.

feeding mode	x 1000: — 10μm	x 2500: - 2μm
D1: PA6+MA-g-HDPE *D2: HDPE* **Reference mode** 1)		
D1: HDPE *D2: PA6+MA-g-HDPE* 2)		
D1: PA6 *D2: HDPE+MA-g-HDPE* 3)		
D1: PA6+HDPE+MA-g-HDPE 4)		
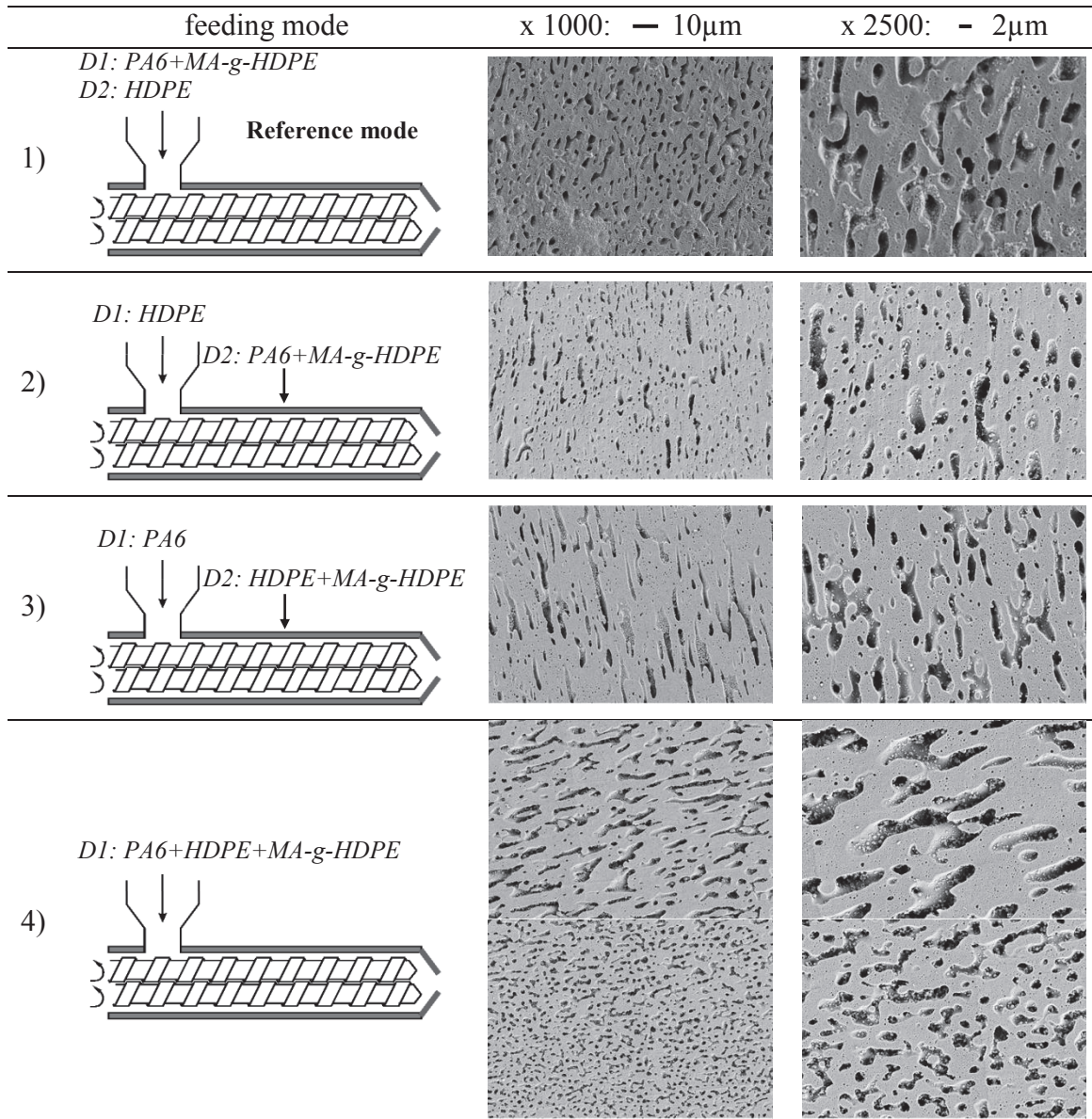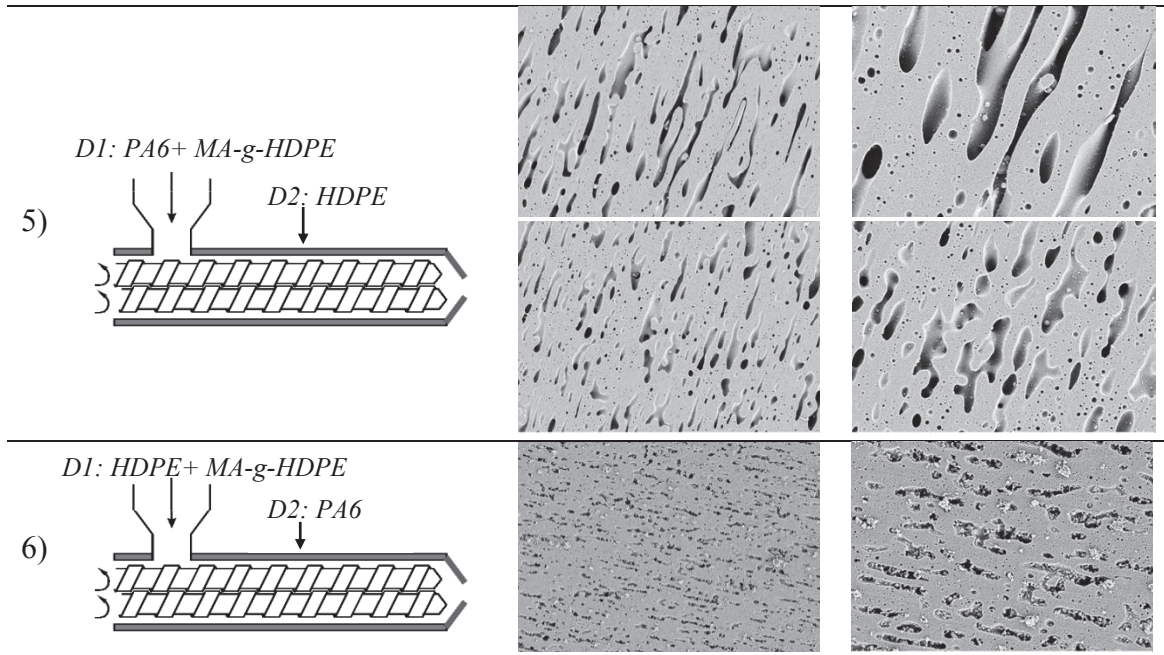
Figure III-10: SEM micrographs after PE phase etching of PA6/HDPE 3/MA-g-HDPE blend (60/24/16%ᵥₒₗ) prepared with six feeding modes (Blend B on Figure III-5 (c)).

According to Lee and Han [55], in the case of modes 1, 4 and 5, a macroscopic dispersion of PA6 in PE phase may first developed during extrusion, as the PE phase, which had the lowest melting temperature, melted first. Then, as PA6 was the major phase, a phase inversion occurred, leading to co-continous morphology.
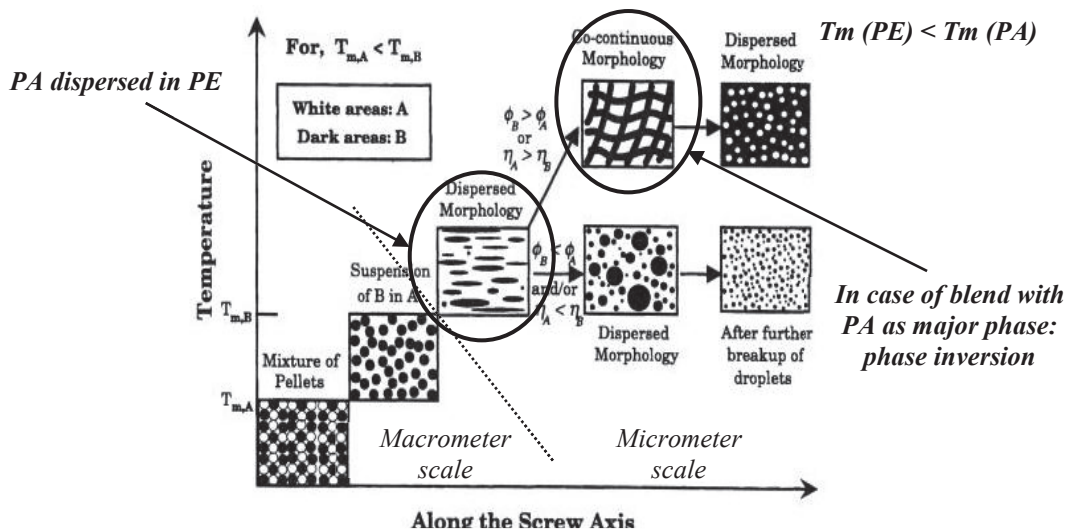
Figure III-11: Diagram of morphology evolution along the screw [55]. Comments in italic correspond to PA/PE blends.

In our case, independently of the evolution of morphology along the screw, formulation B tested here was in the compositions range of co-continuity and the compatibilizer may stabilize this morphology. **So, the materials feeding mode did not influence the morphology.**

However, the co-continuity showed size heterogeneities in the case of modes 4 and 5.

Even if in some cases (modes 2, 3 and 6), the compatibilization reaction can begin only in the middle of the screw due to later melt introduction of reactive species (PA6 or MA-g-HDPE), the final morphology was always co-continuous with the same domain sizes. **Thus, the compatibilization reaction seems to be efficient and fast enough**, that will be discussed in the next paragraph.

The feeding mode 5 is a particular case which may simulate physical compatibilization. In fact:
1) PA6 and MA-g-HDPE were first introduced at the beginning of the screw. As the compatibilization reaction may be very fast and as in this system without HDPE, the molar ratio $[MA]/[NH_2]$ was 0.5, PA6-g-HDPE copolymers may be formed in PA6 matrix. As PA6 was the major component, very small dispersion of compatibilizer (PE chains of the compatibilizer) in PA6 matrix may be formed.
2) Then, HDPE was added in the melt. Diffusion of HDPE homopolymer chains to already formed nodules of compatibilizer PE chains in PA6 matrix may occur. The morphology may be stabilized at once by the PA6-g-HDPE copolymers that were already present in the medium.

Finally, a co-continuous morphology as in the case of "reactive compatibilization" was obtained. However, size heterogeneities were observed. **So, the "physical compatibilization" seems to be a little less efficient than the "reactive compatibilization".**

3.3. Influence of the compatibilization on micrometer scale morphology

By following the formulations A, B and C with HDPE 3 in Figure III-5 (c), the **only changing parameter is the compatibilizer amount, or more precisely, the amount of MA moieties in the blends**. In fact, in these blends:
- A same PA6 content of 60%$_{vol}$ was used
- Viscosity ratio was always 0.5 (*Chapter II section 5 Rheological characterization of raw materials page 100*) whatever the shear rate and the compatibilizer amount
- Morphology was always co-continuous
- HDPE 3 and MA-g-HDPE exhibited very similar molecular mass distributions (*See Figure II-6 in Chapter II Section 2.5 Materials of the study page 76*)

Samplings in the melt during extrusion were performed on two formulations with and without compatibilizer (B and C respectively in Figure III-5 (c)) in order to determine the influence of the compatibilizer on the kinetics of morphology development as shown in Figure III-12. After samplings, the polymers were rapidly cooled in cold water in order to be quite representative of the strand cooling at the exit of the die.
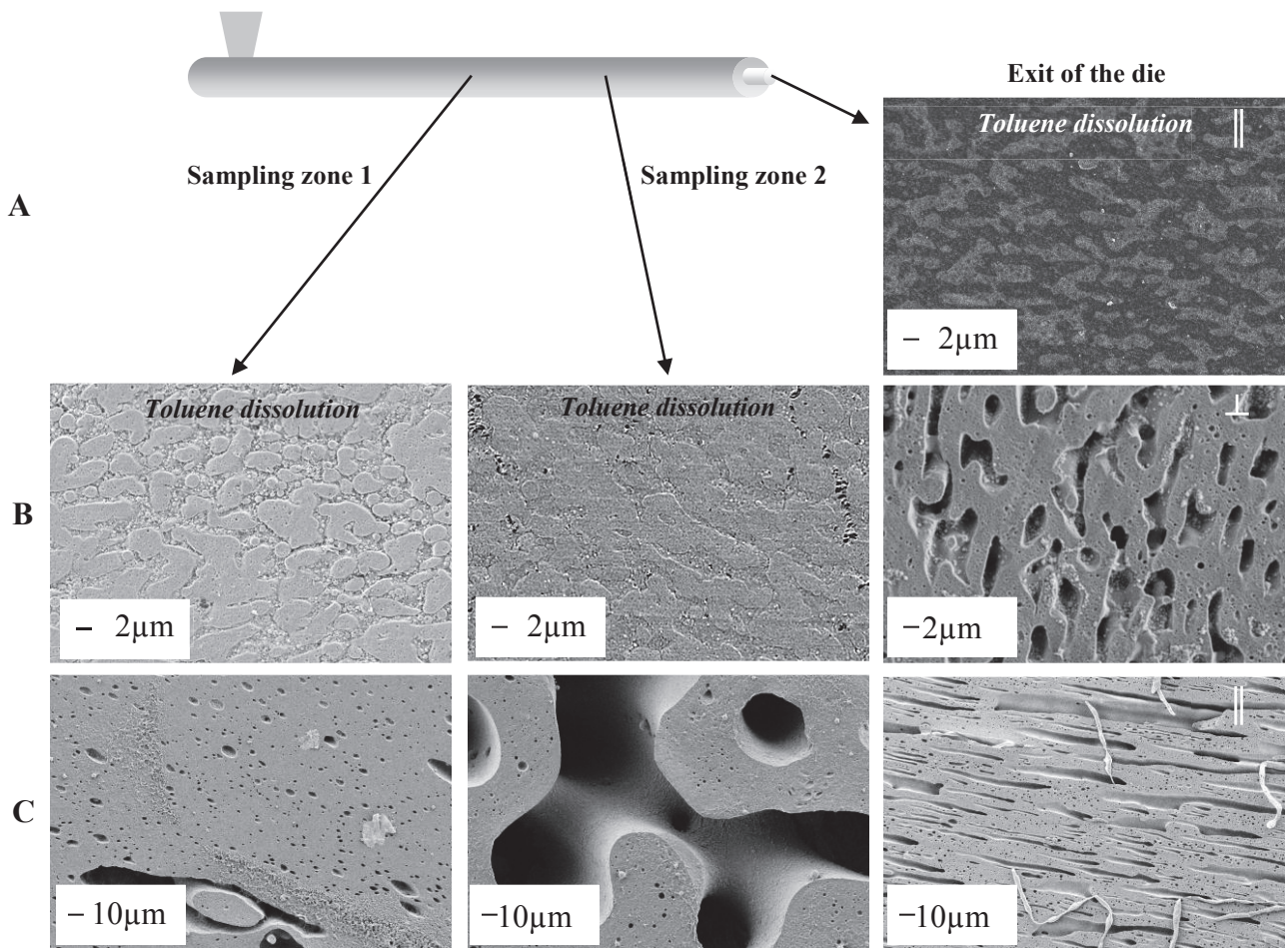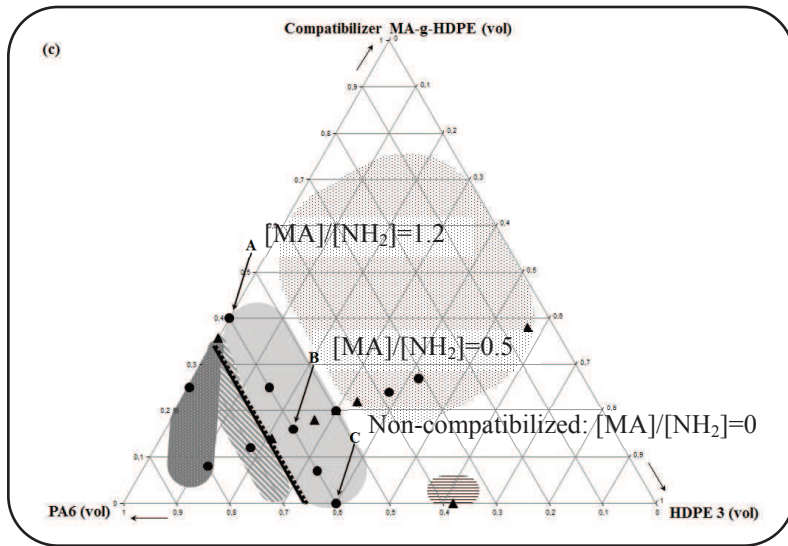
Figure III-12: SEM micrographs of A (PA6/HDPE 3/MA-g-HDPE 60/0/40%$_{vol}$), B (PA6/HDPE 3/MA-g-HDPE 60/24/16%$_{vol}$) and C (PA6/HDPE 3/MA-g-HDPE 60/40/0%$_{vol}$) formulations in Figure III-5 (c)) (PE etched using Decalin unless otherwise specified) along the screw and at the exit of the die.

As expected, by increasing the compatibilizer amount in PE phase, the interfacial area increases and the morphology becomes finer (from 10 – 20 µm to ~ 1 µm) [102].

Moreover, without compatibilizer (formulation C in Figure III-5 (c)), co-continuity was developed progressively along the twin screw. On the contrary, in compatibilized system, co-continuity was developed much earlier, close to the feeding zone. So, **the compatibilizer accelerated the morphology development and the reaction between amine end-group of PA6 and MA grafted moieties of compatibilizer to form a graft copolymer at the interface appeared to be very fast**.

Finally, in compatibilized blends, the morphology formed at the beginning of the twin screw remained unaltered until the exit of the die in spite of the high shear rate applied into the die ($3500s^{-1}$). Thus, in our case, **the compatibilizer also stabilized the morphology.**

Remark: the much coarser morphology osbserved in blend C (non-compatibilized) in sampling zone 2 may not be representative of the real size of the morphology inside the extruder. It may be due rather to coalescence after sampling during the cooling in water less controlled than after extrusion.

3.4. Influence of the viscosity ratios on micrometer scale morphology

The viscosity ratios measured are represented by black double lines corresponding to *Axis C*, *Axis NC* and *Line L* (see Figure III-1) in Figure III-13.
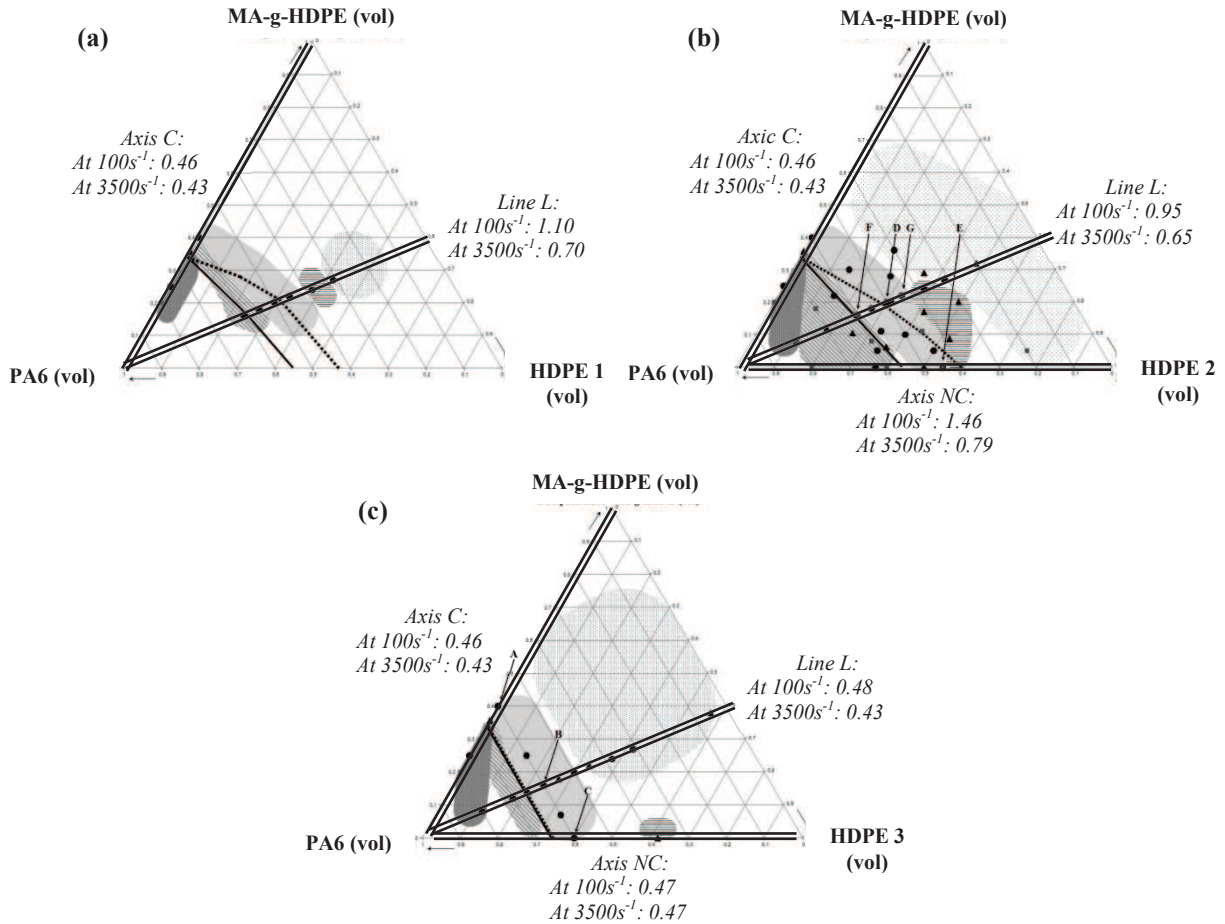
Figure III-13: Summary of known viscosity ratios for the three HDPEs.

Only blends with known phases rheological behaviours were used as illustrated in Figure III-13.

All the morphologies obtained with various compositions and the three HDPEs are then summarized in Figure III-14 which represents the PA6 volume fraction versus the viscosity ratios. The morphologies are represented using the same symbols as in Figure III-4:

- PA6 dispersion in PE phase
- PA6 stretched dispersion in PE phase
- Co-continuous
- PE phase stretched dispersion in PA6
- PE phase dispersion in PA6

The phase inversion compositions predicted by the model of Paul and Barlow (Eq. I-57) are also represented (black curve). This diagram is plotted using both shear rates:

(a) 100s^{-1}: order of magnitude of the average shear rate in extrusion

(b) 3500s^{-1}: order of magnitude of the shear rate in the extruder die of diameter 2mm

123

(a)

(b)
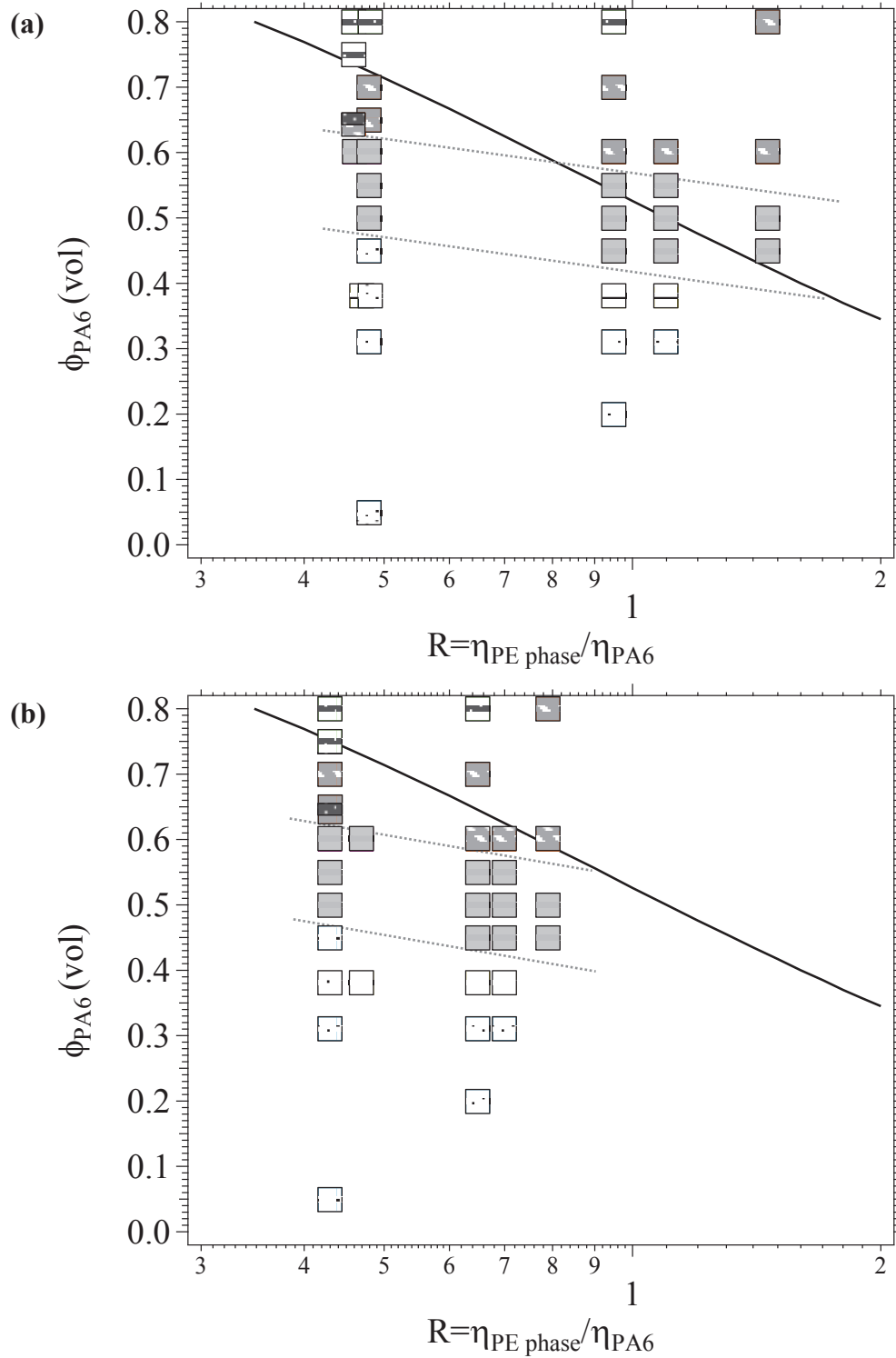
Figure III-14: Experimental data points showing the obtained morphologies: ☐ PA6 dispersion in PE phase, ☐ PA6 **stretched dispersion in PE phase,** ▨ **Co-continous,** ▨ **PE phase stretched dispersion in PA6 and** ▤ **PE phase dispersion in PA6, reported as** ϕ_{PA} **versus the viscosity ratio. In (a), the viscosity ratios at 100s^{-1} were used, in (b) at 3500s^{-1}. The dotted lines show the observed boundaries of the co-continuity region. The black curve corresponds to the phase inversion model of Paul and Barlow (Eq. I-57).**

124

At 3500s^{-1} (Figure III-14 (b)), the viscosity ratios range is narrower as shown in Table II-4 (*Chapter II Materials and experimental*). Thus, the experimental points are packed around a viscosity ratio of 0.6.

The composition range of PE phase stretched dispersion morphology is broader at high viscosity ratios. In fact, these high viscosity ratios correspond to the blends along *Axis NC* (Non-compatibilized) with HDPE 2. As already described, it should be easier to stretch the larger droplets obtained in non-compatibilized blends than smaller ones in compatibilized systems.

On the other hand, MA-g-HPDE (*Axis C*), HDPE 3 (*Axis NC*) and PE phase 3 (*Line L*) exhibited quite the same low viscosity ratio. Thus, depending on the PE phase used (MA-g-HDPE or HDPE 3 or PE phase 3), dispersions or stretched dispersions were obtained.

Whatever the shear rate used (100 or 3500s^{-1}), regarding the indicative boundaries of co-continuous domain, the Paul and Barlow's model seems to be quite consistent with the experimental data using the viscosity ratios at 100s^{-1}. **However, the viscosity ratio has less influence than expected by Paul and Barlow's model on phase inversion and thus co-continuity.**

So, the shear rate which should be taken into account to determine the effect of rheological behaviour on the morphology is the average shear rate in the extruder: 100s^{-1}. However, it is an average value of shear rate in twin screw extrusion. Locally along the extruder, depending on the screw profile, the shear rate applied can be higher.

3.5. Summary of the micrometer scale morphology

So, several kinds of morphologies were actually observed as the amount of PA6 increased in the blends from 1) to 5):
1) PA6 dispersion in PE phase
2) PA6 stretched dispersion in PE phase
3) Co-continuous
4) PE phase stretched dispersion in PA6
5) PE phase dispersion in PA6

The development of these morphologies was accelerated by the presence of the compatibilizer.

Extrusion parameters did not influence the morphology (except at the boundaries between two regions of different morphologies). Thus, all the morphological regions were summarized in ternary diagrams for each HDPE, whatever the tool and the process conditions used.

Stretched dispersions/fibrils and an increase of the domain sizes were observed near the phase inversion as schematized in Figure III-15, which is in agreement with Huitric et al. [10]. Thus, these morphologies indicate the proximity of co-continuity.
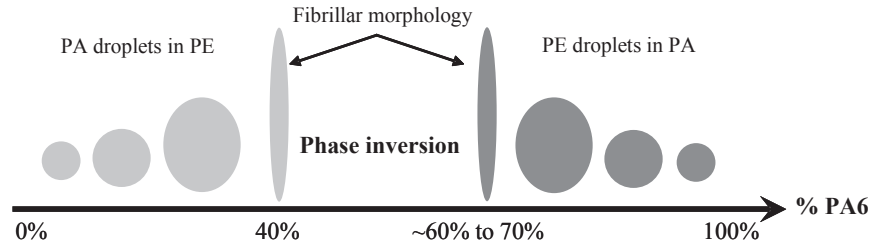
Figure III-15: Evolution of morphology as a function of blend composition.

We have seen that the stretching of the morphology should be essentially due to the high shear applied in the extruder die. However, note that by increasing the volume ratio compatibilizer / HDPE, the morphology became more stable during its passage through the die. At the exit of the die, the strand was quenched in water. Note that the strand was also stretch during its cooling in water by a driving roller to be then pelletized. So, these stretched morphologies are certainly not steady state morphologies and would relax to nodular dispersions or co-continuity depending on the blend composition, during a second heating step (without any shear).This will be studied later (see *Chapter IV*).

The viscosity ratios had less influence on the phase inversion compositions range than expected from the Paul and Barlow's model.

So, the composition (volume ratios PE phase / PA6) is the predominant parameter in the development of the micrometer scale morphology, which suggests a probable stability of the different structures.

The fraction of the compatibilizer was very large in most of the studied systems, which means that a large fraction of copolymer should be formed if the reaction conversion was high. Thus, we must check the conversion rate of the compatibilization reaction. This is discussed in the following section.

4. Conversion rate of the compatibilization reaction

Maleic Anhydride grafted High Density Polyethylene (MA-g-HDPE) was used as compatibilizer in PA6/HDPE blends. The compatibilization reaction is reminded in Figure III-16.
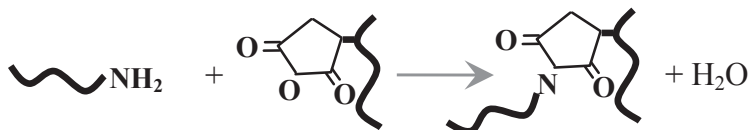
Figure III-16: Compatibilization reaction between MA moieties of MA-g-HDPE and amine end-groups of PA6.

According to the reaction scheme in Figure III-16, the stoichiometry between MA moieties of the compatibilizer and NH_2 end-groups of PA6 is 1.

In order to well describe the blends and then, the morphologies, the reaction conversion was first determined experimentally. Five blends with HDPE 3 were used as shown in Figure III-17.
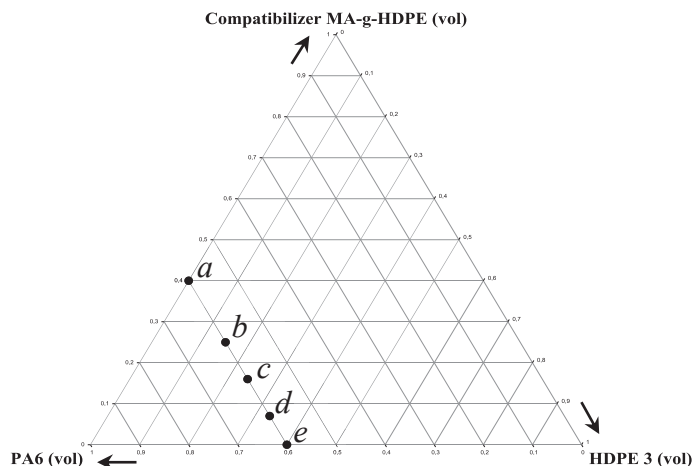
Figure III-17: Blends used to study the compatibilization reaction.

The common features of blends *a* to *e* in Figure III-17 (see also Figure III-5 (c)) are:
- A same PA6 content of 60%$_{vol}$
- A viscosity ratio always equals to 0.5 (*Chapter II Section 5 Rheological characterization of raw materials page 100*)
- Co-continuous morphology
- HDPE 3 and MA-g-HDPE exhibited very similar molecular mass distributions (*See Figure II-6 in Chapter II Section 2.5 Materials of the study page 76*)

Thus, the only changing parameter is the compatibilizer amount, or more precisely the amount of MA moieties in the blends.

Transmission Infrared spectroscopy (*Spectrometer Bruker Vertex 70*) was carried out in order to estimate the conversion MA moieties. Samples were firstly cryogrinded to obtain a fine powder. Then, KBr plates with fixed thickness and constant sample content were prepared. **This preparation method during which the samples are not melted one more time avoids any further reaction.** To estimate the compatibilization reaction conversion, the consumption of Maleic Anhydride moieties in the blends was determined. Thus, the decrease of the intensity of the characteristic absorption band of anhydride carbonyl in the IR spectra at 1791cm^{-1} was followed during the reaction [103,104,105,106].

First of all, the titration method of unreacted Maleic Anhydride moieties was validated using unreacted blends (known content of MA moieties). Thus, the same formulations as on Figure III-17 *a* to *e* were prepared by physically mixing pellets and cryogrinding (dry blends without any extrusion step). The obtained IR spectra are represented on Figure III-18.
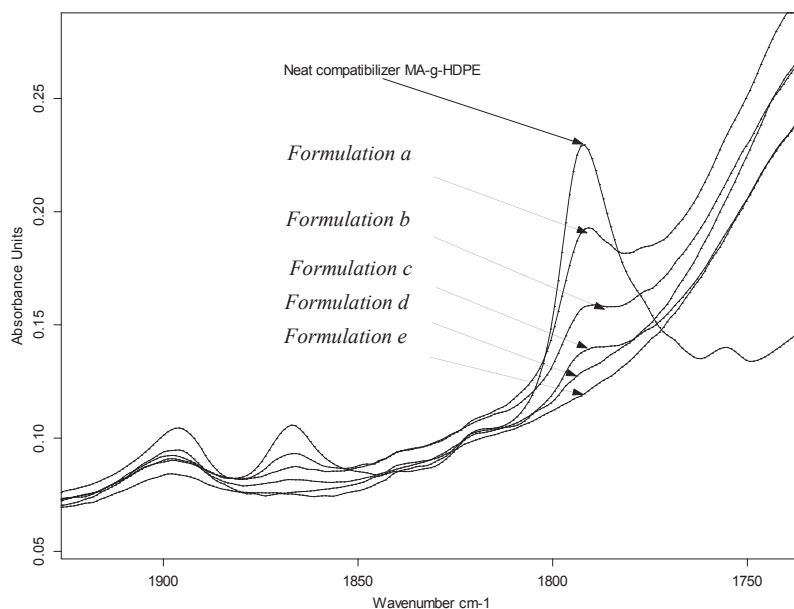
Figure III-18: IR spectra of unreacted blends *a*, *b*, *c*, *d* and *e* (Figure III-17).

As expected, by decreasing the compatibilizer amount in the sample, the area of the absorption band at 1791cm^{-1} due to anhydride carbonyl decreased. In blends with PA6, as blends with PA6 all contained the same PA6 amount, these absorbencies were normalized dividing them by the absorbance of a band due to PA6 at 1170cm^{-1} in order to eliminate the possible effect of sample thickness variation [104].

Figure III-19 shows the average surfaces (3 KBr plates and 3 IR spectra for each plate) measured for each dry blend including neat compatibilizer (1%$_{wt}$ MA) as a function of Maleic Anhydride content.
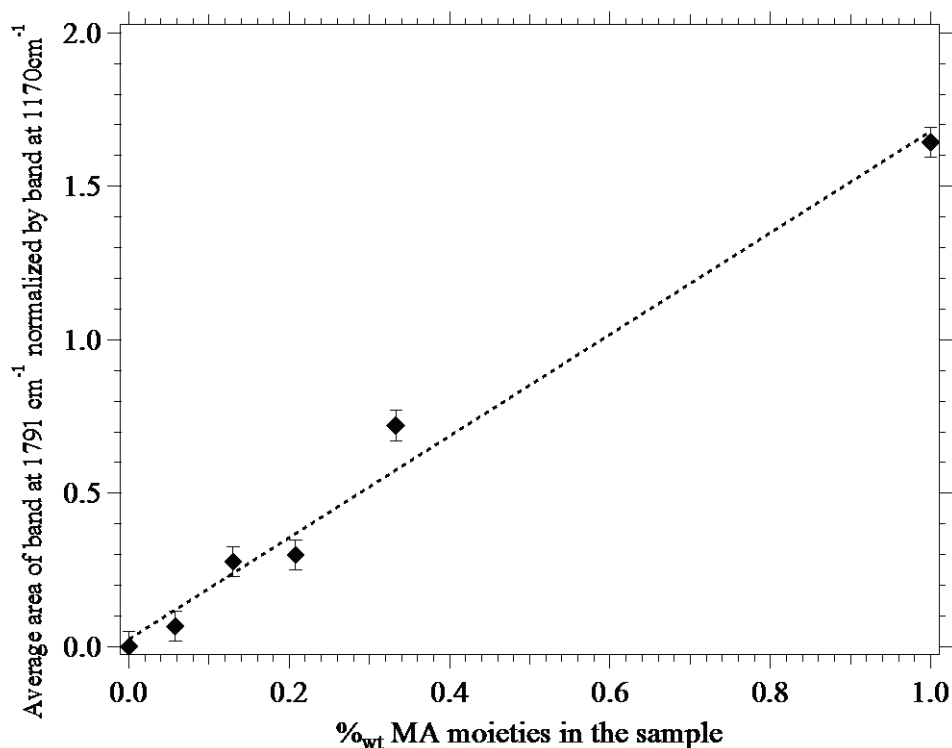
Figure III-19: Average 1791cm^{-1} band area normalized by absorbance of PA6 band at 1170cm^{-1} (except for neat compatibilizer) versus %$_{wt}$ of Maleic Anhydride moieties in the sample for unreacted blends and neat MA-g-HDPE.

There is quite good proportionality between the band areas and Maleic Anhydride content which shows method consistency.

Figure III-20 shows the carbonyl band at 1791cm^{-1} of reacted blends after extrusion D34. The areas measured in Figure III-20 were also normalized by the absorbance of the PA6 band at 1170cm^{-1}.No band was observed for blends *d* and *e* with the lowest amounts of compatibilizer due to detection limit.
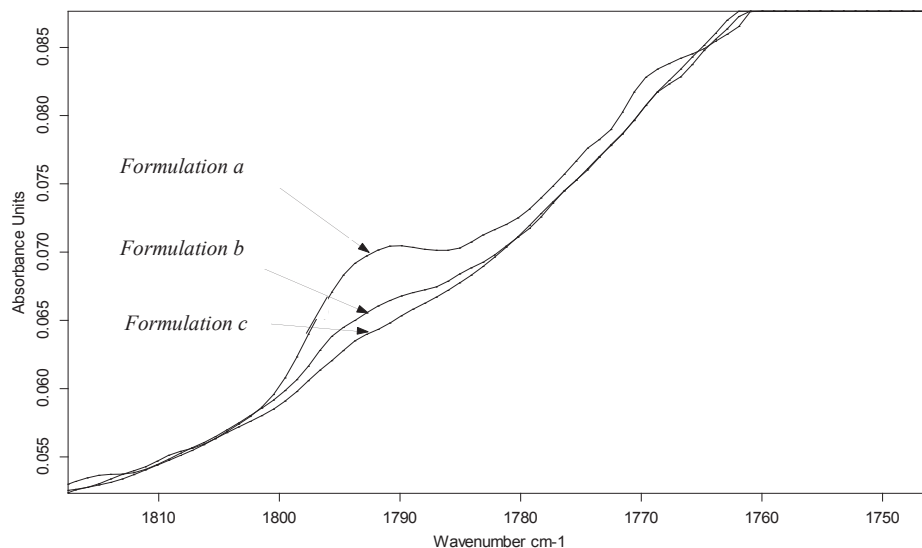
Figure III-20: IR spectra of reacted blends *a*, *b* and *c* processed using the extruder D34 (Figure III-17). Be careful that the vertical scale is amplified compared to Figure III-18.

Figure III-21 shows on the same graph the band areas of unreacted and reacted blends. It clearly appears that the amount of residual MA in the blend was much lower after extrusion, which indicates a high reaction conversion.
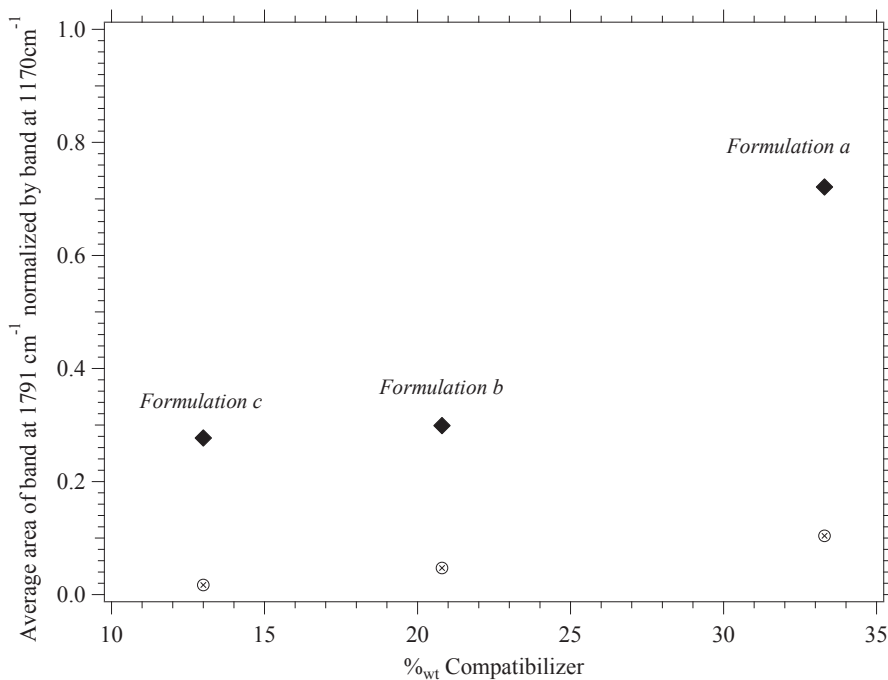
Figure III-21: Average 1791cm^{-1} band area normalized by absorbance at 1170cm^{-1} versus %$_{wt}$ of compatibilizer MA-g-HDPE introduced in the blends for unreacted (full markers) and reacted samples (empty circles).

By comparing the areas of the normalized absorption band *A* between reacted (extruded) and unreacted (unprocessed) blends at same compositions, the conversion rates were calculated:

$$MA\ Conversion\ rate = \frac{\frac{A_{unreacted\ blend}}{\%_{wt}\ sample\ in\ KBr\ plate} - \frac{A_{reacted\ blend}}{\%_{wt}\ sample\ in\ KBr\ plate}}{\frac{A_{unreacted\ blend}}{\%_{wt}\ sample\ in\ KBr\ plate}}$$

Eq. III-3

Figure III-22 shows the obtained experimental conversion rates as a function of the molar ratio of Maleic Anhydride moieties on amine end-groups of PA6 ([MA]/[NH$_2$]).
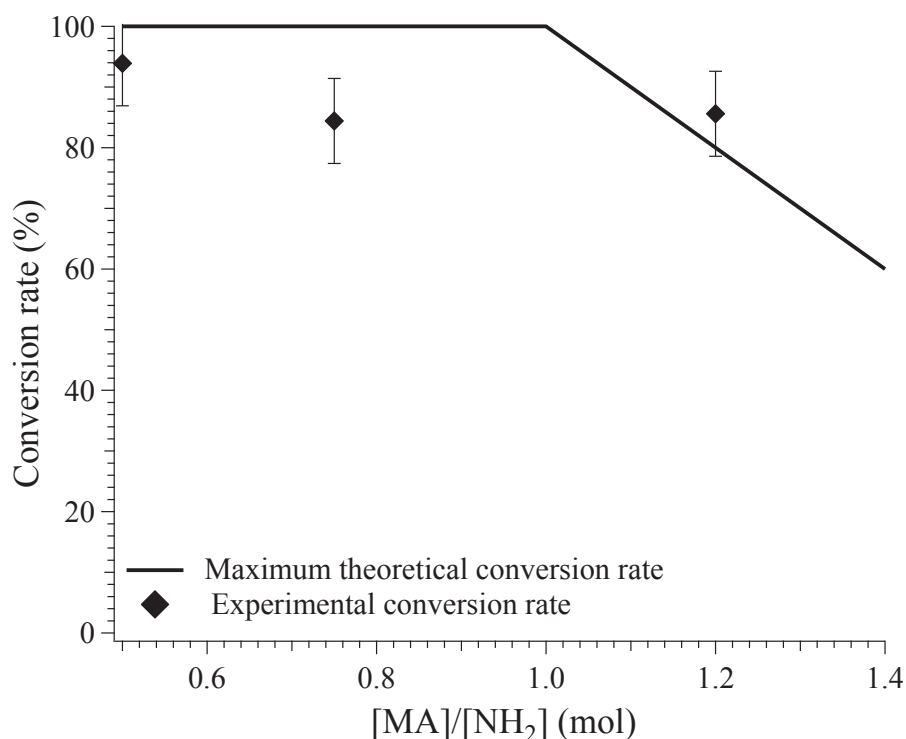
Figure III-22: Maximum theoretical and experimental conversion rates versus the molar ratio [MA]/[NH$_2$].

Given the large uncertainties in area measurements particularly in the case of reacted blends (very small area), IR spectra give only a good semi-quantitative estimate of MA conversion rate.

So, the compatibilization reaction conversion in our systems is higher than **80%** for molar ratios [MA]/[NH$_2$] from 0.5 to 1.2 which is in agreement with the literature [79,80,106]. Thus, the experimental data are quite in agreement with the maximum theoretical reaction rates.

The molar ratios [MA]/[NH$_2$] ranges from 0.5 to 1.2 in the blends tested in IR. The percentage of PA6 chains under the form of copolymer is estimated in both extreme cases:

- For [MA]/[NH$_2$] of 0.5, there are two times more NH$_2$ moieties than MA moieties in the blend. Considering that 1) each PA6 chain exhibited one NH$_2$ end-group and 2) at least 80% of MA moieties reacted, this means that at least 40% of PA6 chains should be under the form of copolymers.

- For [MA]/[NH$_2$] of 1.2, contrary to the previous case, there is an excess of MA moieties in the blend. Considering that 1) each PA6 chain exhibited one NH$_2$ end-group and 2) at least 80% of MA moieties reacted, we may expect that 80% of the PA6 chains are under the form of copolymers.

Thus, for the considered molar ratios [MA]/[NH$_2$] from 0.5 to 1.2, it may be estimated that **40 to 80% of PA6 chains are under the form of copolymers, thus anchored at interfaces**.

5. Expected size of the morphology

Considering that 40 to 80% of PA6 chains are under the form of copolymers, at thermodynamic equilibrium, all copolymer should be located at interfaces. The characteristic size of PA6 domains in the morphology should be of the order of chain dimensions, that is a few tens of nm at most. Therefore, the micrometer scale morphology does certainly not correspond to this situation, and most of the copolymers formed during processing are actually not located at this large scale domain interfaces. This is discussed in more details in this section by first estimating the expected sizes of the domains of both phases in the blends at thermodynamic equilibrium and then estimating the amount of copolymers located at the interface in our systems.

5.1. Estimation of the domains size at thermodynamic equilibrium

At each point of the ternary diagram, the theoretical quantity of interface (per unit volume) may be estimated considering that the reaction is completed up to 80% for instance.

The surface coverage at the interface between PA6 and HDPE chains of the compatibilizer is estimated according to Eq. I-54 and Eq. I-55 of *Chapter I section 2.4.1.2 Interfacial coverage Σ page 47* reminded here:

$$\Sigma = \frac{1}{s}$$

<div align="right">**Eq. III-4**</div>

With:

$$s \approx N^{1/3} a^2 \left(\frac{\chi_{12}}{54}\right)^{-1/6}$$

<div align="right">**Eq. III-5**</div>

Σ corresponds to the number of chains par unit area and s is the average area occupied by one chain.

By considering the values for each parameter estimated in *Chapter II Materials and experimental*:

-   An average polymerization degree **N of 300 monomers**. In fact, for MA-g-HDPE, N was found to be of about 350 monomers between each grafted MA. In the case of PA6, considering the average molecular mass in number M_n of 27600g.mol^{-1} and the molar mass of the PA6 monomer unit M of 113g.mol^{-1}, the polymerization degree N of PA6 was found to be about 250 monomers.

-   The average size of the monomers ***a*** was estimated to be **0.5nm**.

-   The Flory interaction parameter χ_{12} between HDPE (of compatibilizer) and PA6 was estimated to be roughly of the order of **0.7**.

The interfacial coverage Σ in our systems was found to be of the order 0.3 chain/nm², which corresponds to an average area occupied by one chain of about 3.5nm². This estimation is in the same order of magnitude as the values found in the literature, typically 0.2 chain/nm² [15] or 0.3 chain/nm² [36].

Hypothesis: We consider that the **interface coverage is constant**, except perhaps when the molar concentration [MA] tends to 0 (along the *Axis NC* in the ternary diagram of Figure III-1). It will be considered in what follows that **one copolymer chain occupies a surface s equals to 5nm²**.

By using the surface coverage previously estimated and the reaction conversion rates determined experimentally, the expected domain sizes at thermodynamic equilibrium are now estimated:

-   First along the *Axis C* in the ternary diagram of Figure III-1. This means in blends containing only PA6 and MA-g-HDPE.

-   Then, at any point of the ternary diagram. This means in blends containing PA6, MA-g-HDPE and HDPE homopolymer.

5.1.1. Expected sizes in PA6/MA-g-HDPE blends (Axis C)

This case corresponds to the blends along *Axis C* as illustrated in the following ternary diagram.
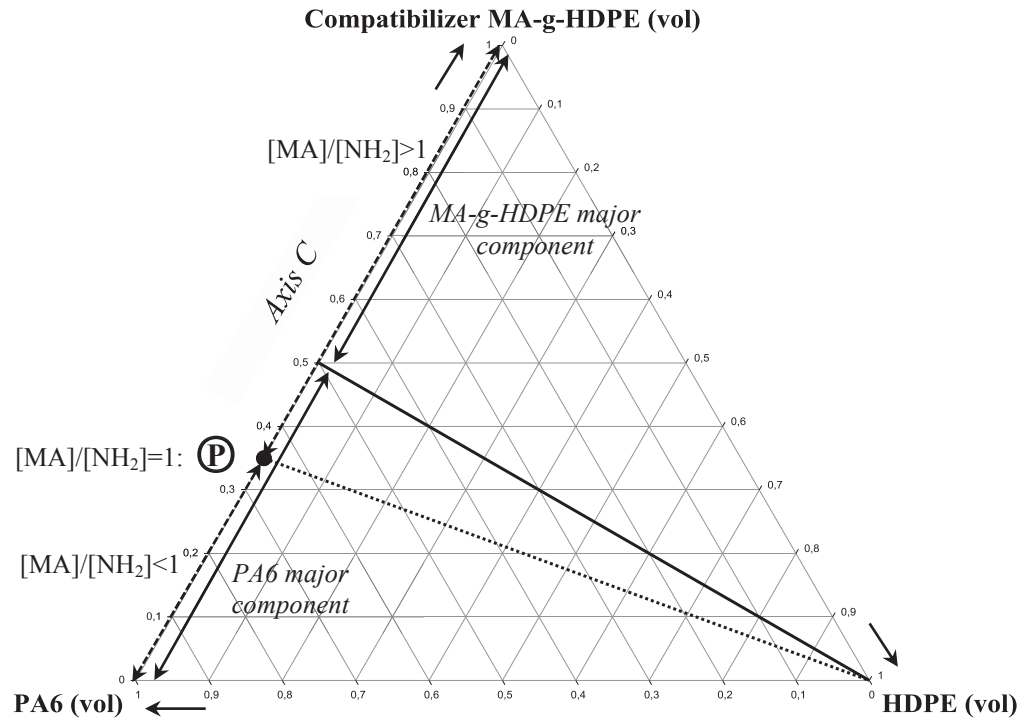
Figure III-23: Ternary diagram corresponding to the blends sizes investigated along the *Axis C*.

In this case, the quantity of surface created *A* per unit volume is given by:

$$A = s\Psi \qquad \text{Eq. III-6}$$

With:
- *s*, the surface occupied by one copolymer chain (5nm²)
- Ψ, the number of copolymer created

The number of copolymers created Ψ directly depends on the limiting reactive specie: [MA] or [NH$_2$] molar concentrations. The schematic evolution of *A* as a function of the volume fraction of MA-g-HDPE, $\phi_{MA\text{-}g\text{-}HDPE}$ is shown in Figure III-24.
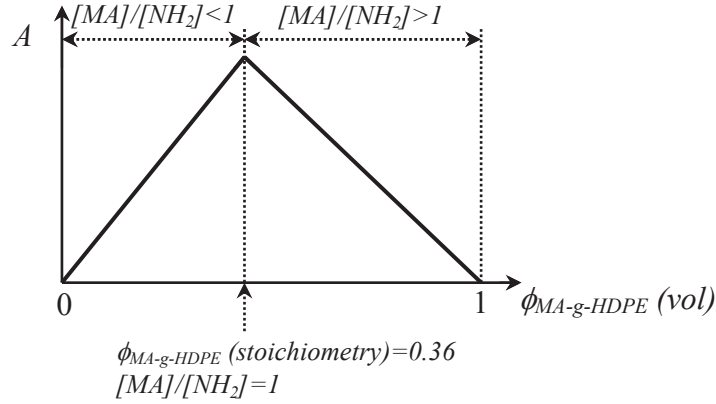
Figure III-24: Schematic evolution of the quantity of surface created A as a function of the volume fraction of MA-g-HDPE, $\phi_{MA\text{-}g\text{-}HDPE}$.

The characteristic size d for each domain (PA6 and MA-g-HDPE) is given by:

$$d \approx \frac{V}{A} = \frac{V}{s\Psi}$$

Eq. III-7

Where V is the volume of the corresponding domain.

According to Eq. III-7, the average size of the domains can be estimated quantitatively, apart from a geometrical factor, linked to the form of the domains (spherical nodules, stretched nodules, co-continuity…).

Two cases are distinguished:

1) [MA]/[NH$_2$]<1: The limiting specie is MA, there is an excess of NH$_2$.

Considering that 80% of MA moieties are consumed in the reaction, the number of copolymers created is given by:

$$\Psi = 0.8\mathcal{N}_a\, n_{MA} = 0.8\phi_{MA-g-HDPE}[MA]\mathcal{N}_a\rho_{HDPE}$$

Eq. III-8

With:
- n_{MA}, moles of MA
- $\phi_{MA\text{-}g\text{-}HDPE}$, the volume fraction of MA-g-HDPE
- $[MA]$, the molar concentration of MA in the compatibilizer: 101mmol.kg^{-1}
- $\mathcal{N}_a$, the Avogadro's number
- ρ_{HDPE}, the density of HDPE chains in the melt: 0.72g.cm^{-3}

135

The limiting specie being MA, **this average size of the domains of HDPE (of compatibilizer) should correspond to a chain length, at least in one dimension**.

The average size of the domains of PA6 is estimated by:

$$d_{PA6} \approx \frac{V}{A} = \frac{\phi_{PA}}{0.8s\phi_{MA-g-HDPE}[MA]\mathcal{N}_a\rho_{HDPE}} = \frac{1 - \phi_{MA-g-HDPE}}{2.2 \ 10^8 \phi_{MA-g-HDPE}}$$

Eq. III-9

For example, for a blend PA6/MA-g-HDPE containing 25%$_{vol}$ of MA-g-HDPE, the average size of the PA6 domains is estimated to be about 14nm. Decreasing the amount of MA-g-HDPE to 10%$_{vol}$, the average size of PA6 domains is expected to increase to about 41nm.

2) [MA]/[NH₂]>1: The limiting reactive specie is NH_2, there is an excess of MA.

Considering that 80% of NH_2 is consumed in the reaction, the number of copolymers created is estimated as:

$$\Psi = 0.8\mathcal{N}_a n_{PA6} = 0.8\phi_{PA6}[NH_2]\mathcal{N}_a\rho_{PA6}$$

Eq. III-10

With:
- n_{NH2}, moles of NH_2
- ϕ_{PA6}, the volume fraction of PA6
- $[NH_2]$, the molar concentration of NH_2 in the PA6: 40mmol.kg^{-1}
- $\mathcal{N}_a$, the Avogadro's number
- ρ_{PA6}, the density of HDPE chains in the melt: 0.96g.cm^{-3}

The average size of the domains of PA6 should correspond to a chain length, at least in one dimension.

Considering that 80% at most of NH_2 is consumed in the reaction, the average size of the domains of HDPE (of compatibilizer) is estimated by:

$$d_{HDPE} \approx \frac{V}{A} = \frac{1 - \phi_{PA6}}{0.8s\phi_{PA6}[NH_2]\mathcal{N}_a\rho_{PA6}} = \frac{1 - \phi_{PA6}}{9.2 \ 10^7 \phi_{PA6}}$$

Eq. III-11

For example, for a blend PA6/MA-g-HDPE containing 40%$_{vol}$ of MA-g-HDPE, the average size of the HDPE domains is estimated to be about 7nm. Increasing the amount of MA-g-HDPE to 70%$_{vol}$, the size of HDPE domains is expected to increase to about 25nm.

The evolution of the domain size d as a function of the volume fraction $\phi_{MA\text{-}g\text{-}HDPE}$ is schematized in Figure III-25.
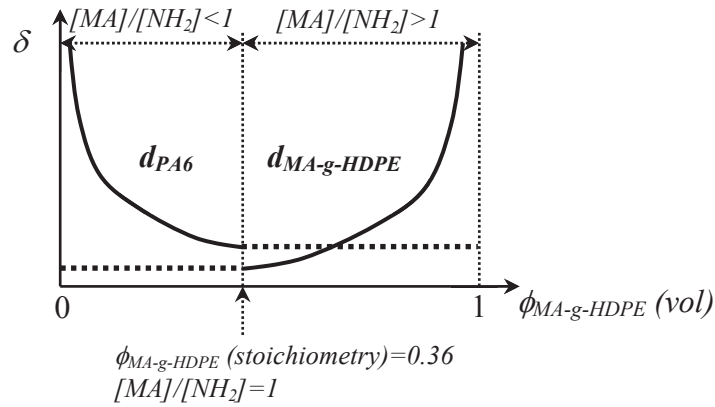
Figure III-25: Schematic evolution of the domain size d as a function of the volume fraction of MA-g-HDPE, $\phi_{MA\text{-}g\text{-}HDPE}$.

5.1.2. At any point of the ternary diagram

This case corresponds to any blends as illustrated in the following ternary diagram.
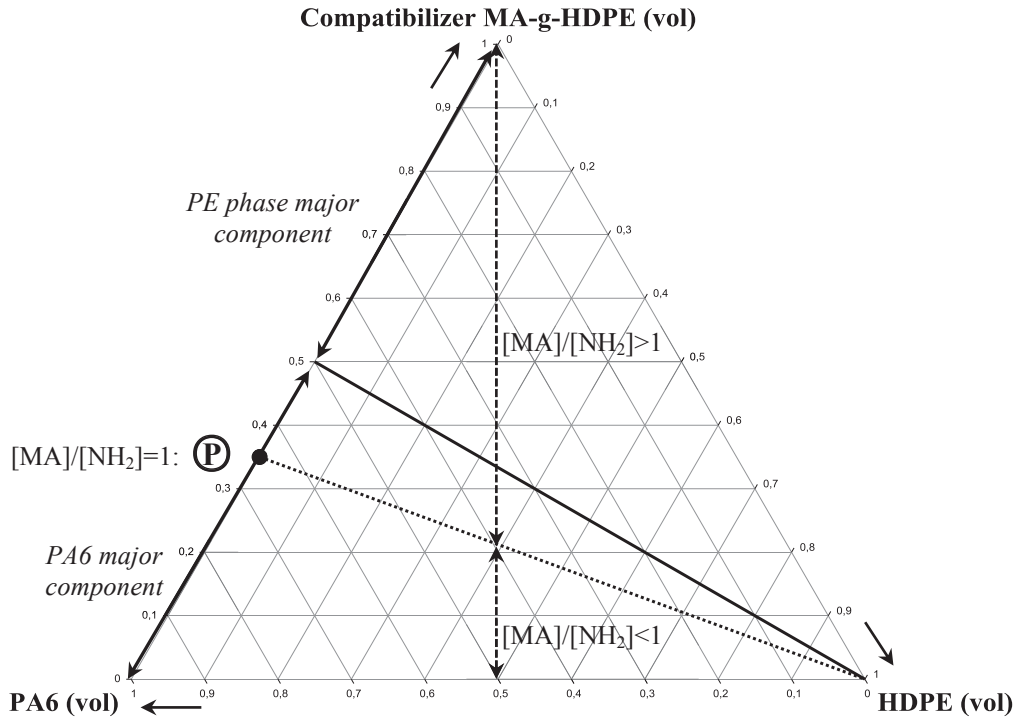
Figure III-26: Ternary diagram corresponding to any blends sizes investigated.

Like previously, two cases are distinguished.

1) **Blends in the domain [MA]/[NH$_2$]<1:** The limiting specie is MA

Considering that 80% of the MA moieties reacted, the average size of the domains of PE phase is estimated by:

$$d_{PE\ phase} \approx \frac{V}{A} = \frac{\phi_{HDPE} + \phi_{MA-g-HDPE}}{0.8s\phi_{MA-g-HDPE}[MA]\mathcal{N}_a\rho_{HDPE}} = \frac{\phi_{HDPE} + \phi_{MA-g-HDPE}}{2.2\ 10^8\phi_{MA-g-HDPE}}$$

Eq. III-12

For example, considering a blend PA6/HDPE/MA-g-HDPE 60/24/16%$_{vol}$, the average size of the domains of the PE phase is estimated to be about 11nm.

The average size of the domains of PA6 is estimated by:

$$d_{PA6} \approx \frac{V}{A} = \frac{\phi_{PA6}}{0.8s\phi_{MA-g-HDPE}[MA]\mathcal{N}_a\rho_{HDPE}} = \frac{\phi_{PA6}}{2.2\ 10^8\phi_{MA-g-HDPE}}$$

Eq. III-13

For example, considering the same blend PA6/HDPE/MA-g-HDPE 60/24/16%$_{vol}$, the average size of the domains of PA6 is estimated to be about 17nm.

2) **Blends in the domain [MA]/[NH$_2$]>1:** The limiting specie is NH$_2$

We suppose that at most 80% of NH$_2$ reacted.

The average size of the domains of PE phase is estimated by:

$$d_{PE\ phase} \approx \frac{V}{A} = \frac{\phi_{HDPE} + \phi_{MA-g-HDPE}}{0.8s\phi_{PA6}[NH_2]\mathcal{N}_a\rho_{PA6}} = \frac{\phi_{HDPE} + \phi_{MA-g-HDPE}}{9.2\ 10^7\phi_{PA6}}$$

Eq. III-14

For example, considering a blend PA6/HDPE/MA-g-HDPE 20/20/60%$_{vol}$, the average size of the domains of the PE phase is estimated to be about 43nm.

The average size of the domains of PA6 is estimated by:

$$d_{PA6} \approx \frac{V}{A} = \frac{\phi_{PA6}}{0.8s\phi_{PA6}[NH_2]\mathcal{N}_a\rho_{PA6}} = \frac{1}{9.2\ 10^7}$$

Eq. III-15

For example, considering the same blend PA6/HDPE/MA-g-HDPE 20/20/60%$_{vol}$, the average size of the domains of PA6 is estimated to be about 11nm.

So, the expected average sizes at thermodynamic equilibrium of both PA6 and PE phase domains should be at the nanometer scale. Therefore, the observed micrometer scale morphology is not consistent with the large conversion rate determined in our systems. The amount of copolymers located at this interface of micrometer scale morphology is estimated in the following section.

5.2. Amount of copolymers located at the micrometer scale morphology interface

Conversely, the relative amount of copolymers located at the interfaces of micrometer scale morphology may be roughly estimated from the observed average size of the domains.

A symmetric blend PA6/PE phase 50/50%$_{vol}$ exhibiting a co-continuous morphology of typical characteristic size a=1µm as schematized in Figure III-27 is considered.
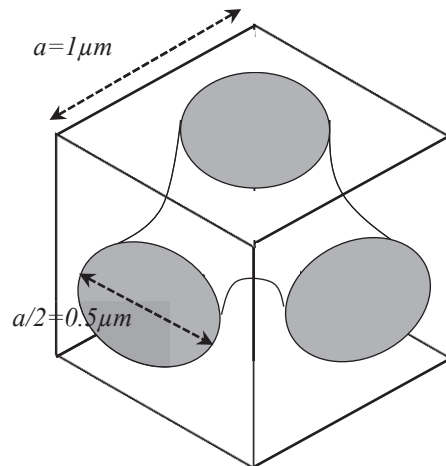
Figure III-27: Diagram of a symmetric co-continuous blend exhibiting a typical characteristic size of 1µm.

Based on geometrical arguments, the surface/volume ratio is of the order of *2.5/a*. The volume of the elementary unit is a^3=$10^{-18}m^3$. So, the area of the interface in the elementary unit is of the order of *2.5 $10^{-12}m^2$*.

On the other hand, the volume occupied by the interface is estimated using the gyration radii R_g of both PA6 chains and HDPE chains of the compatibilizer. As illustrated in Figure III-28, the interface thickness is defined as the sum of gyration radii of both PA6 and HDPE chains under the form of copolymers located at the interface.
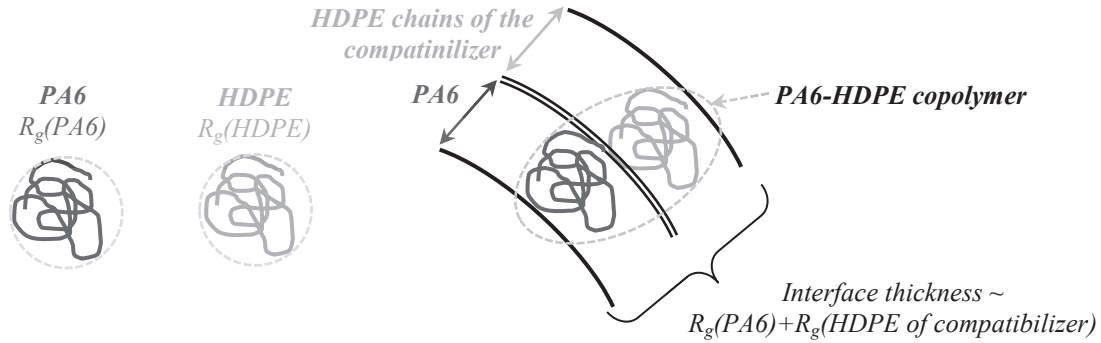
Figure III-28: Diagram of PA6/HDPE interface.

So, the gyration radii of both PA6 and HDPE chains in the compatibilizer are estimated:

- HDPE side: in compatibilized blends, HDPE chains which form the interface are ones of the compatibilizer MA-g-HDPE. As already showed previously (*Chapter II Materials and experimental section 2.5.2.2 Dynamical rheometry page 80*) there are about 350 monomers (CH_2-CH_2) between each grafted MA which represents a molar mass of 9800 g.mol^{-1}. According to Fetters et al. [98], $\langle R_g^2 \rangle = 1.25 M_n$ (Å²) which gives a PE chain gyration radius R_g of 11nm.

- PA6 side: According to Fetters et al. [98], $\langle R_g^2 \rangle = 0.853 M_n$ (Å²) with *Mn=27600g.mol^{-1}*, which gives a PA6 chain gyration radius R_g of 15nm.

Thus, the order of magnitude of gyration radii of both PA6 and HDPE chains is considered to be of the order of 10nm, which gives an **interface thickness of the order of 20nm**.

Considering the specific area of the micrometer scale morphology of 2.5 10^{-12}m^2 and an interface thickness of 20nm, the interface volume in the elementary unit is 5 10^{-20}m^3. Thus, the typical volume fraction occupied by the copolymers located at the interface of the micrometer scale morphology is given by:

$$\frac{V_{interface}}{V_{total}} = \frac{5 \cdot 10^{-20}}{10^{-18}} = 5\% \, of \, total \, volume$$

Eq. III-16

So, in the case of symmetric co-continuous micrometer scale morphology exhibiting a characteristic size of 1µm (PA6/PE phase 50/50%$_{vol}$), if the interface contains only PA6-g-HDPE copolymers, these copolymers correspond to 5% of the total volume. As we consider a symmetric blend, **PA6 chains under the form of copolymers located at the interface represent approximately 5% of the total amount of PA6.**

To summarize:

1) According to the conversion rate of the compatibilization reaction, 40 to 80% of PA6 chains are under the form of copolymers.

2) According to the typical size of the micrometer scale morphology, PA6 chains under the form of copolymers located at this large scale morphology interface represent about 5% of the overall PA6 content in the blend.

By coupling both conclusions, the fraction of the copolymers formed during extrusion which are located at the interfaces of the micrometer scale morphology is very small. According to the previous conclusions, we estimate this fraction to be 12% at most of the PA6 chains. **So, where are the other 88% of PA6 chains under the form of copolymers located?** To answer this question, we need to observe our blends at the nanometer scale.

6. Nanometer scale morphology

The morphology at the nanometer scale was observed in both compatibilized and non-compatibilized blends. The results obtained are presented in this section.

6.1. Compatibilized blends

The formation of nano-dispersions has been studied in the literature. Thus, prior to detail the experimental results, literature about the formation of the nano-dispersions via interface instabilities is described.

After a description of our blend morphologies as observed by TEM, a mechanism of formation of the nano-dispersions in our systems is proposed.

6.1.1. Literature about nano-dispersions formation mechanisms

In compatibilized systems, due to thermal fluctuations, slight deformations at random locations along interface occur. This interfacial roughening could be at the origin of the nano-dispersion formation. This phenomenon has been studied in the literature in static conditions and under shear.

6.1.1.1. In static conditions

According to Lyu et al [107], interfacial roughening was clearly observed in static conditions after 20 minutes of reaction between PS-NH$_2$ and PMMA-Anhydride as shown on Figure III-29.
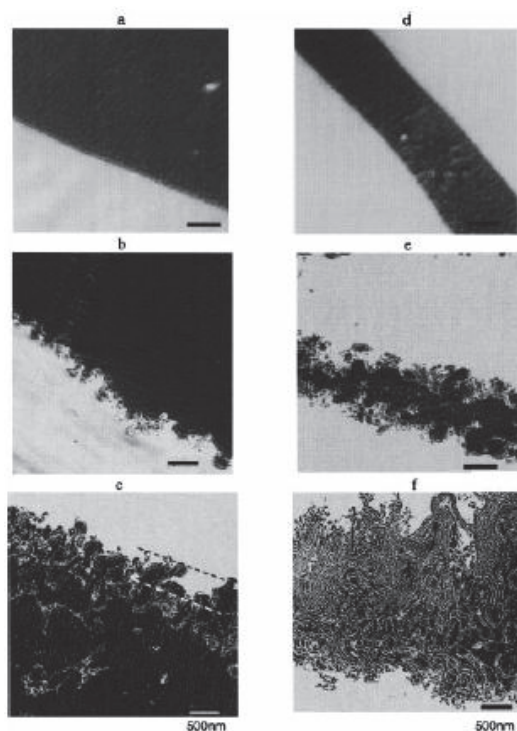
Figure III-29: Morphologies of PS-NH$_2$/PMMA-anhydride blends (in dark and light respectively) after static reaction at 200°C during a) 0, b) 20 and c) 60 min at large domain interface and during d) 0, e) 20 and f) 60 min at thin sheet interface. All scale bars are 500nm [107].

This roughening may be due to instability resulting from negative interfacial tension as explained by Jiao et al [108] in PS-NH$_2$/PS-g-MA systems. In fact, in reactively compatibilized systems, progressively as the reaction is going on, it is more and more difficult for reactive species to reach the interface due the entropy loss [109]. However, when the flat interface is saturated by in situ formed copolymers, thermal fluctuations still induce slight deformations along the interface. The associated increase of curvature is accompanied by an increase of interfacial area, leading to a local increase in interfacial tension [107]. So, this continuous interface renewal allows new reactive species reaching the interface to create more and more copolymers and so increase the interfaces area.

Some parts of PS domains (in black) pinch off at this rough interface and move to PMMA phase as shown on Figure III-29 b) and e). Thus, **interface roughening could lead to nano-dispersion formation.**

6.1.1.2. Under shear

Interface roughening under shear was also observed in the literature.

Jeon et al [110] studied PA66/PS (70%$_{wt}$ of PA66) blends prepared in cup-rotor mixer reactively compatibilized by in situ formed block copolymers PA66-b-PS. The compatibilization reaction used in this study was between amine end-groups of PA66 and anhydride end-groups of PS-Anhydride (NH$_2$ with MA like in our systems). In addition to micrometer scale dispersion of PS, sub-micron micelles were observed. The authors proposed that this sub-dispersion was formed by interfacial roughening.

Copolymers with shorter grafts would lead to greater interface instabilities and roughening [110,108]. So, the formation of nano-dispersions may be increased or decreased by adapting the copolymer architecture. χN (χ, Flory interaction parameter and N, degree of polymerization of copolymer) and Σ (interface coverage, depending notably on conversion rate and on the morphology) mainly govern interfacial roughening [110]:

- When $\Sigma > \Sigma_{max}$ (Σ_{max} corresponds to the interface coverage by pure copolymer), interfacial roughening has occured and micelles are observed.
- When χN increases (typically in the case of high molecular weight polymers and immiscible systems), the interface becomes more rigid and fluctuations may decrease.
  Jones et al [111] examined more precisely the influence of monomer structure on reactions at immiscible polymer/polymer interfaces. By changing the chemical nature of polymer backbone, the interaction parameter χ changed. So, by decreasing χ, both reaction rate and interfacial roughening increased. In fact, by decreasing χ, the interfacial tension was reduced and new interface was created by interfacial instabilities. Thus, the available interfacial area for reaction became larger. Moreover, by increasing the molecular weight (directly linked to N), the reaction rate and the interface coverage decreased. According to the authors, it was not due to a modification of viscosity or diffusion coefficient. They proposed that by increasing the molecular weight, the concentration in reactive species decreases (typically in $1/M_n$ for polymers functionalized at chains ends) which limits the ability for chains to meet and react.

During blending process, the mechanical forces applied would highly accelerate the reaction kinetics (typically over 1000 times quicker than in static conditions for reaction between NH$_2$ and MA) [109]. When interfacial roughening is going on, shear flow also accelerate the sub-dispersion formation by pinching off more easily the roughened interface.

Thus, **under shear conditions, nano-dispersions can be formed via interfacial roughening caused by the extremely fast reaction and accentuated by external flow**.

Bhadane et al [112] studied Polyamide / Brominated Poly(isobutylene-co-p-methylstyrene) blends (PA/BIMSM) prepared using a Brabender internal mixer (90/10%$_{wt}$). The in-situ formation of BIMSM-PA graft copolymer at the interface occurred following this reaction:
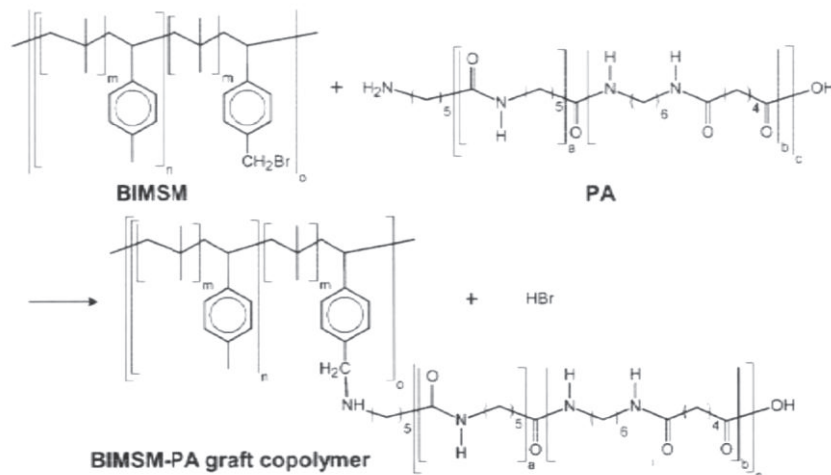
Figure III-30: Reaction between BIMSM and PA to from BIMSM-PA grafted copolymer [112].

In this case, there were 38 potential Bromine sites available for reactive grafting with PA per BIMSM molecule. Thus, 38 PA chains could react with one BIMSM and form a graft copolymer with several segments. It was estimated that about 46%$_{wt}$ of graft copolymer is produced based on the total weight of the blend. Thus, this does not allow us knowing the average number of PA6 grafts per MIMSM chain.

According to the authors, micelles of grafted copolymer were observed over the entire compositions range. As shown on Figure III-31, these micelles were pinched off from the interface.
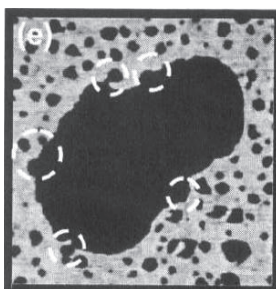
Figure III-31: AFM micrograph in BIMSM/PA blend. Scale 2.1 x 2.1 μm [112].

The authors explain the micelles formation by a mechanism of "interfacial erosion". In this case, several PA chains (up to 38) can react with one BIMSM molecule and form a graft copolymer with several segments increasing a lot the viscosity. They argued that this viscosity mismatch between interfacial region and base components would tend to pull out the copolymer away from the interface, during melt mixing.

In our case, there are in average 2.7 MA moieties per HDPE chain of the compatibilizer. Considering the reaction rate of 80%, several PA6 chains are probably grafted on one HDPE chain of the compatibilizer. This argument of 'viscosity mismatch" may also be valid in our case.

Note that this pinch off could also be due to interfacial roughening like in other studies previously described.

6.1.2. TEM observations

In compatibilized blends, both nano-dispersions of PE phase in PA6 and PA6 in PE phase were simultaneously observed. Two blends are used to illustrate these nano-dispersions as shown in Figure III-32.
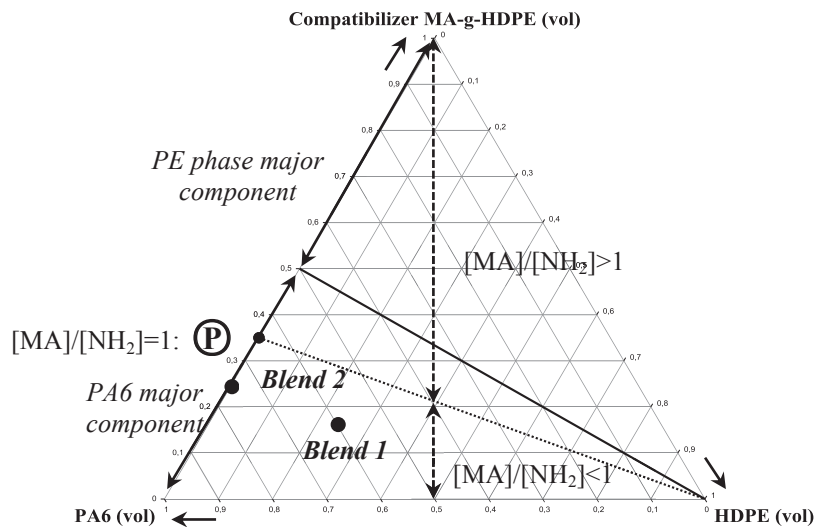
Figure III-32: Ternary diagram showing blends 1 and 2 used to illustrate the nano-dispersions in compatibilized systems.

An example of TEM micrographs for blend 1: PA6/HPDE 3/MA-g-HDPE (60/24/16%vol) which exhibits co-continuous morphology at the micrometer scale is shown in Figure III-33.
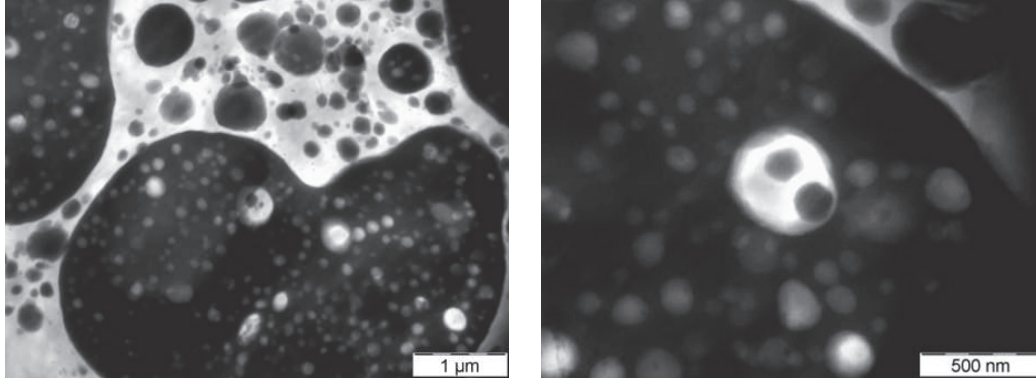
Figure III-33: Examples of TEM micrographs of blend 1: PA6/HDPE 3/MA-g-HDPE blends (60/24/16%$_{vol}$) after PA6 staining during 15 minutes (black domains).

So, according to Figure III-33, the typical minimum sizes of both nano-dispersions which were observed are:
- For PA6 in PE phase: 50nm
- For PE phase in PA6: 40nm

Moreover, as shown in Figure III-33, the distance between the small nodules did not exceed a few hundreds of nm.

According to the previous estimations of the domain sizes (see *section 5 page 132*):
- for PE phase, the size would be 11nm (Eq. III-12)
- for PA6, the size would be 17nm (Eq. III-13)

So, the sizes and the distances between nano-dispersions experimentally observed were a little larger than expected.

Figure III-34 shows an example of TEM micrographs for blend 2: PA6/MA-g-HDPE (75/25%vol) which exhibits only PE domains at the nanometer scale.
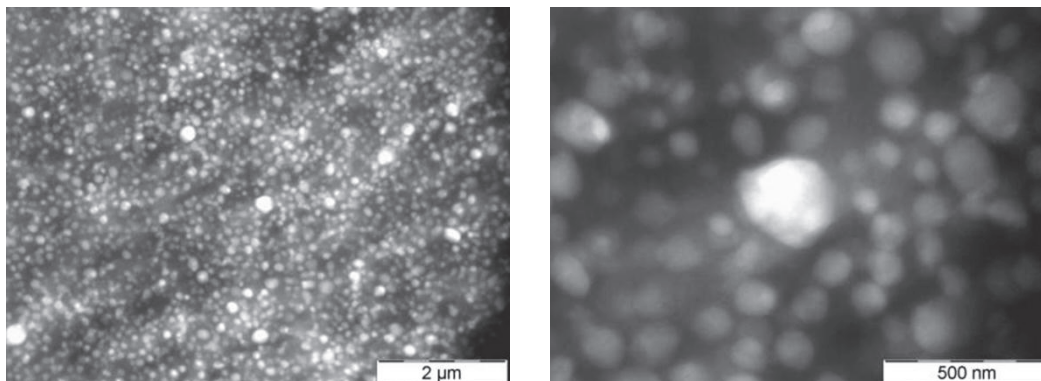
Figure III-34: Example of TEM micrograph of blend 2: PA6/MA-g-HDPE blends (75/25%$_{vol}$) after PA6 staining during 15 minutes (black domains).

In blend 2 which contains only PA6 and MA-g-HDPE (along *Axis C*), according to our previous estimations (see *section 5 page 132*):
-    for PE phase, the size would be of the order of the size of the chains, typically $2R_g \sim 22$nm
-    for PA6, the size would be 14nm (Eq. III-9)

Experimentally, the maximum sizes observed were of the order of 200nm, larger than the expected ones.

The conditions of preparation and of observation in TEM being delicate, we may not observe all the nano-dispersions present in the samples, which could explain the differences obtained between the experimental data and the expected sizes from our previous estimations (see *section 5 page 132*).

In fact, note that PA6 staining conditions need to be well adapted in order to avoid underestimate nano-dispersion of PE. After 15 minutes staining, both nano-dispersions of PE (white nodules) and PA6 (black nodules) were clearly observed. After 1 hour staining, nano-dispersion of PE in PA6 was less visible. This is illustrated in Figure III-35.
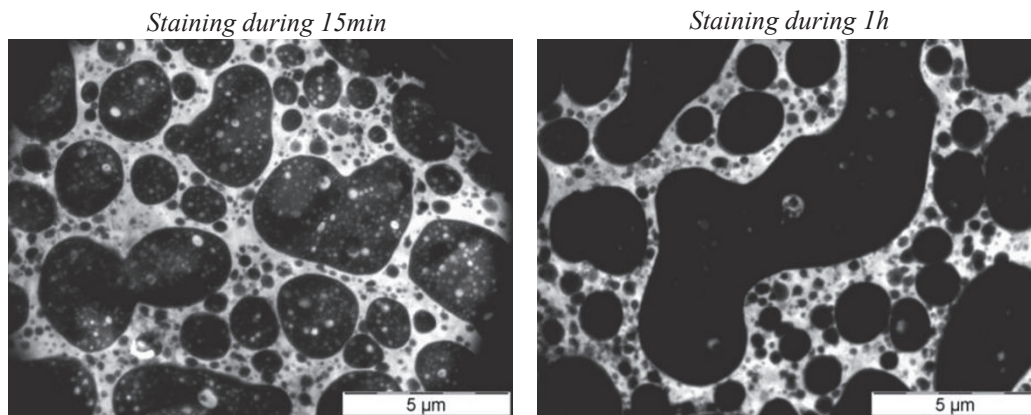
Figure III-35: Example of TEM micrograph of blend 1: PA6/HDPE 3/MA-g-HDPE blends (60/24/16%$_{vol}$) after PA6 staining during 15 minutes and 1 hour (black domains).

Moreover, the contrast between PA6 and PE phase changes depending on where the small nodules of PE phase were cut.

a)   b)
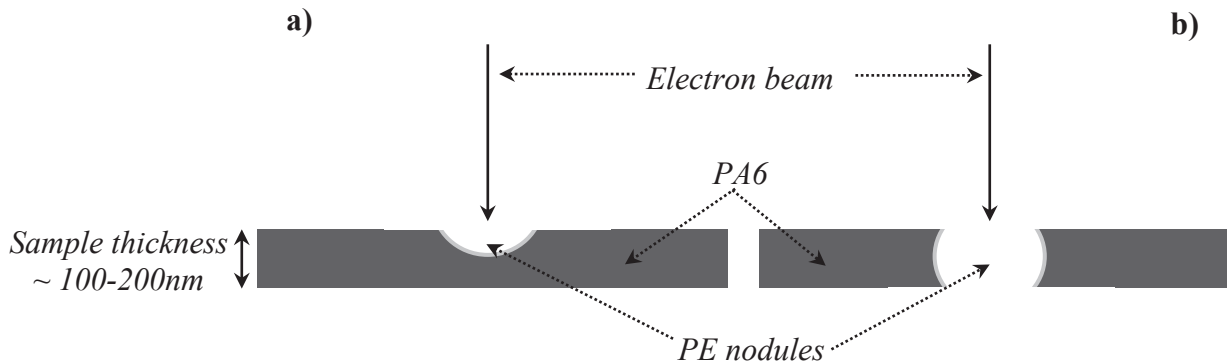
Figure III-36: Illustration of the difference of contrast in TEM.

In the case a), the nodule of PE is not cut at the medium position: the electron beam goes through a thickness of PE (white) and a thickness of stained PA6 (black). This results in black PA6 with a grey nodule of PE. Depending on the crossed PA6 thickness, the nodule of PE would appear more or less dark.

On the contrary, in the case b), the nodule of PE is cut at the medium position and is large enough: the electron beam crosses only the PE which appears in white.

To conclude, PA6 chains under the form of copolymers are anchored at the interfaces of both micrometer and nanometer scale morphologies. The nano-dispersions would represent a very large volume of interface. This would explain where were localized the 88% of PA6 under the form of copolymers which could not be located at the interface of the micrometer scale morphology.

6.1.3. Summary of nano-dispersion formation in PA/PE compatibilized blends

Experimentally, TEM observations revealed a kind of pinch off from the interface as shown in Figure III-37, as well as nano-dispersions (as presented previously on Figure III-33).

Pinch off from the interface
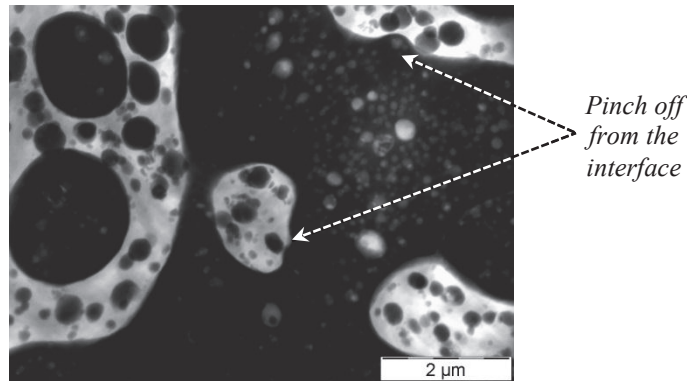
Figure III-37: Example of TEM micrograph of PA6/HDPE 3/MA-g-HDPE blends (60/24/16%$_{vol}$) after PA6 staining during 1 hour (black domains).

The size of these pinch off's ranges from 70 to 250nm in the micrograph of Figure III-37 which well corresponds to the minimum nano-dispersion size observed of ~50nm (Figure III-33).

In our systems, the interaction parameter χ_{12} between PA6 and HDPE was estimated to be roughly of the order of 0.7. The degrees of polymerization N of each block of the graft copolymer formed at the interface are the following:

- PA6 block: $N \approx 250$.
- HDPE chains of compatibilizer block: $N \approx 350$ monomers between each grafted MA.

Thus, the overall degree of polymerization can be considered to be of the order of 600, which corresponds to $\chi N \approx 420$.

So, in our case, the conversion rate was estimated to be higher than 80% and the kinetics was observed to be very fast, leading to the formation of nano-dispersions in spite of our large χN, which is in agreement with Jeon et al [110].

The following diagram summarizes the interfacial instabilities mechanism which leads to nano-dispersion formation.

Initial flat interface

Interfacial roughening

Very fast reaction (kinetics highly accelerated by shear during melt blending):
Interfacial tension decreases

Difficult for more reactive species to reach the interface by penetrating in the already formed copolymers brush

Interfacial instabilities due to thermal fluctuation + very fast reaction (interfacial tension close to 0): Available interface area for reaction allowing new reactive species to reach the interface:
Continuous interface creation

Nano-dispersion

Pinch off from roughened interface (facilitated by shear):
Nano-dispersion formation

Figure III-38: Mechanism of nano-dispersion formation via interface roughening.

As described in the *Chapter I section 2.4.2.1 Physical compatibilization page 50*, the homopolymer chains must not be too long to be able to interpenetrate in copolymer brush at the interface [46]. In our case, the chains of PA6 homopolymers exhibit the same length as the copolymer grafted chains of PA6 in average. Thus, a few homopolymer PA6 chains may be solubilized into the nano-domains of PA6 formed by the copolymer, but may not swell the brush of PA6 grafted chains [40]. On the other hand, the chains of HDPE homopolymers are much longer than the HDPE blocks of the compatibilizer between each PA6 graft in average. In this case, the chains of HDPE homopolymers cannot penetrate into the nano-dispersions of PE formed by the copolymer [40]. Thus, the size of both nano-dispersions of PA6 and PE phase in our compatibilized blends should be quite constant. Obviously, these assumptions do not take into account the large polydispersity of our polymers.

6.1.4. Estimation of the nano-dispersion sizes

This section is dedicated to the estimation of the typical size of both nano-dispersions of PA6 and PE phase. We did not precisely analyze theses interfacial instabilities, and this point could be studied in more details in future work. However, the parameters which play a role during the interfacial instabilities are essentially the interfacial tension Γ and the shear rate $\dot{\gamma}$. Thus, we may expect that the nano-dispersions sizes may be estimated in a first approximation by Taylor's equation [9] (*Chapter I section 2.3.1 Drop break-up page 31*). In fact, Taylor's theory studies the deformation and break-up of a Newtonian fluid droplet in a Newtonian liquid in a simple shear field $\dot{\gamma}$ and proposes that the smallest droplet diameter d_{min} accessible is linked to this shear rate and to the interfacial tension by the following equation:

$$d_{min} = \frac{\Gamma}{\dot{\gamma}\eta_m} f(R_v) = \frac{\Gamma(R_v + 1)}{\dot{\gamma}\eta_m \left(\frac{19}{16}R_v + 1\right)}$$

Eq. III-17

With:
- Γ, the interfacial tension (typically 1mN/m in compatibilized system as described in the literature for PA6/LDPE compatibilized using Maleic Anhydride [94,93,101])
- R_v, the viscosity ratio
- $f(R_v)$, a function of the viscosity ratio R_v with values close to one
- η_m, the matrix viscosity (PA6 for sub-dispersions of PE, and PE phase for PA6 sub-dispersions).

According to Eq. III-17, the characteristic minimum size at a shear rate $\dot{\gamma}$ of 100s^{-1} was estimated in the blend 1 in Figure III-32 PA6/HDPE 3/MA-g-HDPE blend (60/24/16%$_{vol}$). The considered matrix viscosities η_m at 290°C are 580 and 280Pa.s for PA6 and PE phase 3 respectively.

The calculated Taylor sizes and the experimentally measured typical diameters of sub-dispersions are reported in Table III-2.

	Taylor size	Experimentally observed diameter
PA6	33	50
PE phase 3	16	40

Table III-1: Minimal diameters d_{min} in nm calculated by Taylor's theory and experimentally observed (Figure III-33).

Thus, the order of magnitude of the sizes estimated by Taylor's theory is the same range as the experimentally observed values.

6.2. Non-compatibilized blends

After a description of our blend morphologies characterized by TEM, the typical size of the sub-dispersions observed is then compared to the Taylor's sizes. Finally, a mechanism of formation of these sub-dispersions in non-compatibilized blends is proposed.

6.2.1. TEM observations

In non compatibilized blends, the morphology also exhibited simultaneously both sub-dispersions of PA6 in HDPE and of HDPE in PA6. An example of TEM micrographs in PA6/HDPE 3 blend (60/40%$_{vol}$) (blend C in the ternary diagram of Figure III-5 (c)) which exhibits co-continuous morphology at the large scale is shown in Figure III-39.
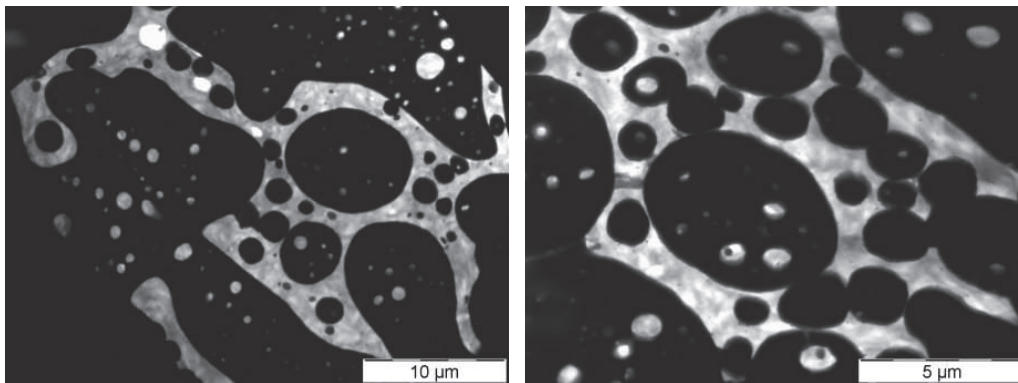
Figure III-39: Example of TEM micrograph of PA6/HDPE 3 (60/40%$_{vol}$) after PA6 staining during 45 min (black domains). Be careful that the scale is not the same as in Figure III-33.

Note that the scale of the micrographs of the non-compatibilized blend in Figure III-39 is ten times larger than the scale of the micrographs of the compatibilized blend 1 exhibiting the same volume fraction of PA6 (60%$_{vol}$) (Figure III-33).

As expected, according to Figure III-39, the typical minimum sizes of both sub-dispersions which were observed are much larger than in compatibilized systems:
- For PA6 in PE phase: 400nm
- For PE in PA6: 200nm

In the case of non-compatibilized blends, the sub dispersions are certainly formed by the Taylor droplet break-up mechanism.

6.2.2. Taylor sizes (hydrodynamic)

The sizes of the sub-dispersions observed in non-compatibilized systems were compared to the sizes d_{min} calculated from Taylor's theory [9] (*Chapter I section 2.3.1 Drop break-up page 31*).

$$d_{min} = \frac{\Gamma}{\dot{\gamma}\eta_m} f(R_v) = \frac{\Gamma(R_v + 1)}{\dot{\gamma}\eta_m \left(\frac{19}{16}R_v + 1\right)}$$

Eq. III-18

With:

- Γ, the interfacial tension (typically 10mN/m in non compatibilized system as estimated in *Chapter II Materials and experimental section 2.4 Miscibility between Polyethylene and Polyamide page 74* using the Flory interaction parameter)
- R_v, the viscosity ratio
- $f(R_v)$, a function of the viscosity ratio R_v with values close to one
- η_m, the matrix viscosity (PA6 for sub-dispersions of PE, and PE phase for PA6 sub-dispersions).

According to Eq. III-18, the characteristic minimum size at a shear rate $\dot{\gamma}$ of 100s^{-1} was estimated in the PA6/HDPE 3 blend (60/40%$_{vol}$). The considered matrix viscosities η_m at 290°C are 580 and 275Pa.s for PA6 and HDPE 3 respectively.

The calculated Taylor sizes and the experimentally measured typical diameters of sub-dispersions are reported in Table III-2.

	Taylor size	Experimentally observed diameter
PA6	340	400
HDPE 3	160	200

Table III-2: Minimal diameters d_{min} in nm calculated by Taylor's theory and experimentally observed (Figure III-39).

The order of magnitude of the sizes estimated by Taylor's theory matches quite well the experimentally observed values. So, even if the model of Taylor does not take into account the polymers viscoelasticity, the order of magnitude of the sizes calculated here clearly corresponds to the submicron-scale morphology observed in our systems.

6.2.3. Summary of sub-dispersions formation in PA/PE non-compatibilized blends

In non-compatibilized blends, systems exhibiting larger interfacial tension, the final morphology observed corresponds to an equilibrium between droplets break-up and coalescence. The minimum droplet diameter corresponds to the size estimated by Taylor's theory.

However, as observed in Figure III-39, both sub-dispersions of PA6 in HDPE and of HDPE in PA6 were simultaneously observed. The small inclusions of blend matrix may be trapped inside the minor phase during the coalescence to form larger and more easily stretchable particles [113] as illustrated in Figure III-40.
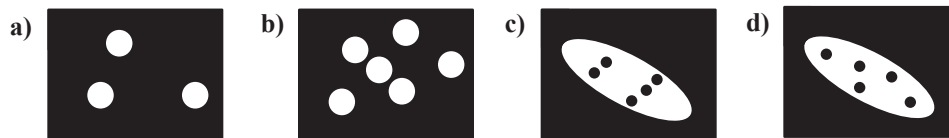
Figure III-40: Diagram of "trapping" mechanism during the coalescence of the dispersed phase.

7. Mechanisms of formation of the multi-scale morphologies: Percolation theory

As explained in *Chapter I section 2.5.3.2 Percolation theory page 56*, the phase inversion and so co-continuity can be described using the percolation theory. Many papers are dealing with percolation on several properties like electrical conductivity or mechanical properties [61,62]. However, to the best of our knowledge, this theory has rarely been used to analyze quantitatively typical sizes of the morphologies yet. Thus, this section proposes to apply the percolation theory to describe our multi-scales morphologies.

In the case of non-compatibilized blends, due to the large interfacial tension, all the domains were subjected to breaking and coalescence mechanisms. In compatibilized blends, we have seen that a large fraction of the grafted copolymer was located within droplets of small size (of the order of 50nm) generated by interface instabilities during reactive processing. However, interfaces relatively poor in copolymer remained present in the system. These interfaces formed larger domains which were subjected to breaking and coalescence equilibrium (micrometer scale morphology), driven by the high shear rate value imposed during processing and by the interfacial tension between the domains. Of course, even if a large fraction of the formed copolymers were micellized at small scale, the interfacial tension between these larger domains was significantly lowered as compared to the corresponding uncompatibilized blends, but not to the point to completely inhibit coalescence.

We propose that the observed characteristic sizes and distributions of sizes results from a breaking / coalescence equilibrium mechanism, as usually observed in blends with non-vanishing interfacial tension. In this case, it should be possible to describe the typical sizes by percolation concepts.

7.1. Evolution of the largest domain size versus composition

Let us first consider the evolution of the dominant characteristic size in the systems with variable compositions, exhibiting different morphologies, as it is the case along line L in the ternary diagram in Figure III-1. By increasing the amount of minority phase (in terms of volume fraction), the domain size increases up to the frontier at which the domains become continuous, which corresponds to the percolation threshold.

In percolation theory, the correlation length ξ (which describes the spatial extension of percolation clusters) diverges at the threshold as:

$$\xi \approx |\phi - \phi_c|^{-\nu}$$ <div style="text-align:right">**Eq. III-19**</div>

With:
- ϕ, the volume fraction
- ϕ_c, the volume fraction at threshold
- ν, the exponent equals to 0.88 in 3D [114]

Note that all the distances should be scaled by the elementary (smallest) length scale in the system. The meaning of ξ is that clusters extending over distances larger than ξ are exponentially rare. This correlation length describes the spatial extension of static clusters on a lattice. These are tenuous objects, described by a fractal dimension less than 3 (in 3D, the fractal dimension, defined as $r \approx m^{1/D}$ with m its mass, is given by D=2.53 for $r<\xi$ and D=2 for $r>\xi$) [115].

In the present case, due to non-zero interfacial tension, the observed objects are droplets of nearly spherical or ellipsoidal shapes, except perhaps very close to the continuity threshold, where they become to be highly elongated (the so-called stretched dispersion/fibrils region). Thus, it is likely that, under the effect of interfacial tension, fractal clusters may collapse in a compact shape in a fast time scale, keeping the volume nearly constant during this process. Thus, considering the variation of the largest mass m_ξ (or equivalently the volume) as a function of the distance to the threshold would be more appropriate. In percolation, the characteristic mass m_ξ diverges at the threshold as:

$$m_\xi \approx |\phi - \phi_c|^{-1/\sigma} \qquad\qquad \textbf{Eq. III-20}$$

with the exponent $1/\sigma = 1/0.45 = 2.22$ in 3D [115].

To compare the values measured in different systems (compatibilized and non-compatibilized blends) with different values of the interfacial tension Γ, the observed masses should be rescaled by the elementary (smallest) mass m_T. We have seen that the smallest size observed in our systems (elementary volume) corresponds to the Taylor's size. According to Taylor equation (Eq. III-17), the elementary mass m_T we should use to rescale the observed masses varies as:

$$m_T \approx d_{min}^3 \approx \Gamma^3 \qquad\qquad \textbf{Eq. III-21}$$

With:
- d_{min}, the minimum diameter accessible according to Taylor
- Γ, the interfacial tension

We did not measure directly the characteristic masses m_ξ in our systems. By considering that the volume of the dispersed phase domains is representative of their mass, we have estimated qualitatively on SEM micrographs the characteristic sizes of the dispersed phase domains. More precisely, we measured the characteristic sizes of the largest dispersed phase domain in systems along line *L, Axis C* and *Axis NC* of Figure III-1 in the blends prepared using the three HDPEs (ternary diagrams in Figure III-5). The blends used for this analysis all exhibited nodular dispersions or stretched dispersion, respectively considered as spheres and ellipsoids. Thus, according to the measured sizes in 2D in SEM micrographs, the largest dispersed phase volume before reaching the phase inversion and thus, co-continuity was determined using the following equations:

$$V_{sphere} = \frac{4\pi}{24} a^3 \qquad\qquad \textbf{Eq. III-22}$$

$$V_{ellipsoid} = \frac{4\pi}{24} b^2 c \qquad\qquad \textbf{Eq. III-23}$$

With:
- *a*, the average diameter of the largest droplet in blends exhibiting a nodular dispersion morphology
- *b*, the average diameter of the largest stretched dispersed domain in blends exhibiting a stretched dispersion morphology
- *c*, the average length of the largest stretched dispersed domain in blends exhibiting a stretched dispersion morphology

The evolution of the reduced largest volume (V/Γ^3) of the dispersed phase is reported as a function of the PA6 volume fraction in the blends in Figure III-42 and Figure III-44. Curves on the left of the graphs correspond to measured PA6 droplets or stretched droplets volumes (minority PA6 phase), curves on the right side correspond to measured PE phase droplets or stretched droplets volumes (minority PE phase). The fits were performed by holding the percolation exponent fixed to -2.22 (its 3D value) [115] and the percolation volume fraction ϕ_c according to the experimental co-continuous region:

$$Reduced\ V_{dispersed\ phase} = a|\phi - \phi_c|^{-2.22}$$

Eq. III-24

PE phases with HDPEs 1 or 2 (60%$_{vol}$ HDPE/40%$_{vol}$ MA-g-HDPE) and neat HDPE 2 exhibit quite the same viscosity ratios (from 0.9 to 1.5 at 100s^{-1}, see Table II-4). Thus, Figure III-42 shows the results obtained for both blends with PE phase 1 and PE phase 2 (along the line L in Figure III-41) and also for non-compatibilized blends with HDPE 2 (along *Axis NC* in Figure III-41).

Figure III-41: Ternary diagram of typical blends with HDPE 2 used to plot the reduced volume of the dispersed phase as the function of the PA6 volume fraction.

157

Figure III-42: Dispersed phase volume versus PA6 volume fraction (markers) in PA6/HDPE 1/MA-g-HDPE and PA6/HDPE 2/MA-g-HDPE blends along the line *L*. The points encircled correspond to PA6/HDPE 2 non-compatibilized blends (along *Axis NC*) whose dispersed phase volume was rescaled by dividing by the interfacial tension $\Gamma^3=3.4^3$. The domains in grey correspond to the experimentally observed co-continuity boundaries (between 40 and 45%$_{vol}$ of PA6 to 55%$_{vol}$ of PA6 according to the ternary diagrams in Figure III-5 (a) and (b)). Both percolation fits for PA6 and PE phase dispersions are plotted in red. The blue dashed lines correspond to the percolation threshold in the fits.

For points along the line *L* in the ternary diagrams (corresponding to black markers in Figure III-42), the values of the volume (measured in μm^3) are directly plotted. **For the three non-compatibilized blends** with HDPE 2 along *Axis NC* (encircled black markers in Figure III-42), **the corresponding values of the volume have been all divided by 39 to rescale them to the volume obtained in compatibilized blends along line *L*. This rescaling value corresponds to an interfacial tension at cubic square $\Gamma^3=3.4^3\approx39$.** In fact, according to Eq. III-21, the volume ($\sim d^3$) is directly proportional to Γ^3 and non-compatibilized blends exhibit larger interfacial tension than compatibilized systems. The fits match well the experimental data and **the percolation volume fractions obtained (blue dashed lines in Figure III-42), which are consistent with the experimental boundaries of the co-continuous region (grey domains in Figure III-42) are 40 and 55%$_{vol}$ in PA6.**

In the same way, PE phase 3 (60%$_{vol}$ HDPE 3/40%$_{vol}$ MA-g-HDPE) and neat MA-g-HDPE exhibit the same viscosity ratios (0.5 at 100s^{-1}, see Table II-4). Thus, Figure III-44shows the results obtained for blends with PE phase 3 (along the line *L* in Figure III-44) and also for PA6/MA-g-HDPE blends (along *Axis C* in Figure III-44).
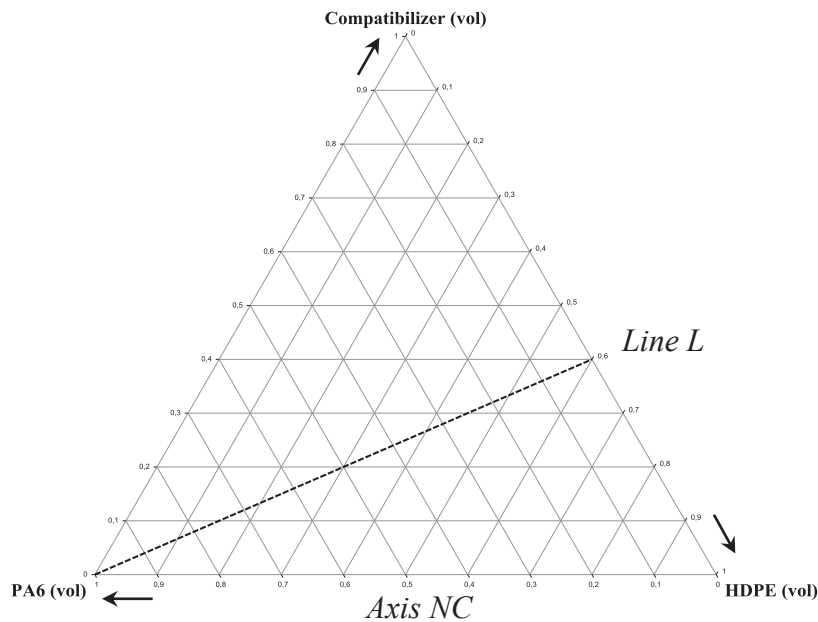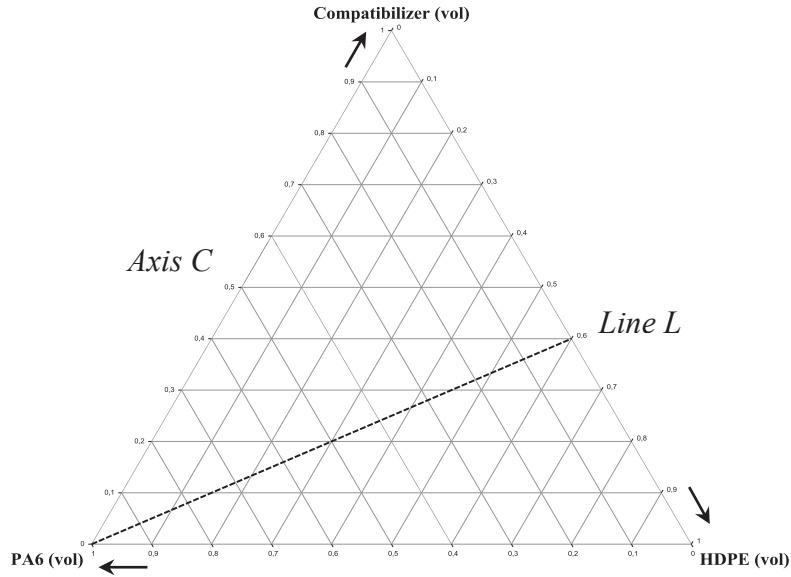
Figure III-43: Ternary diagram of typical blends with HDPE 3 used to plot the reduced volume of the dispersed phase as the function of the PA6 volume fraction.
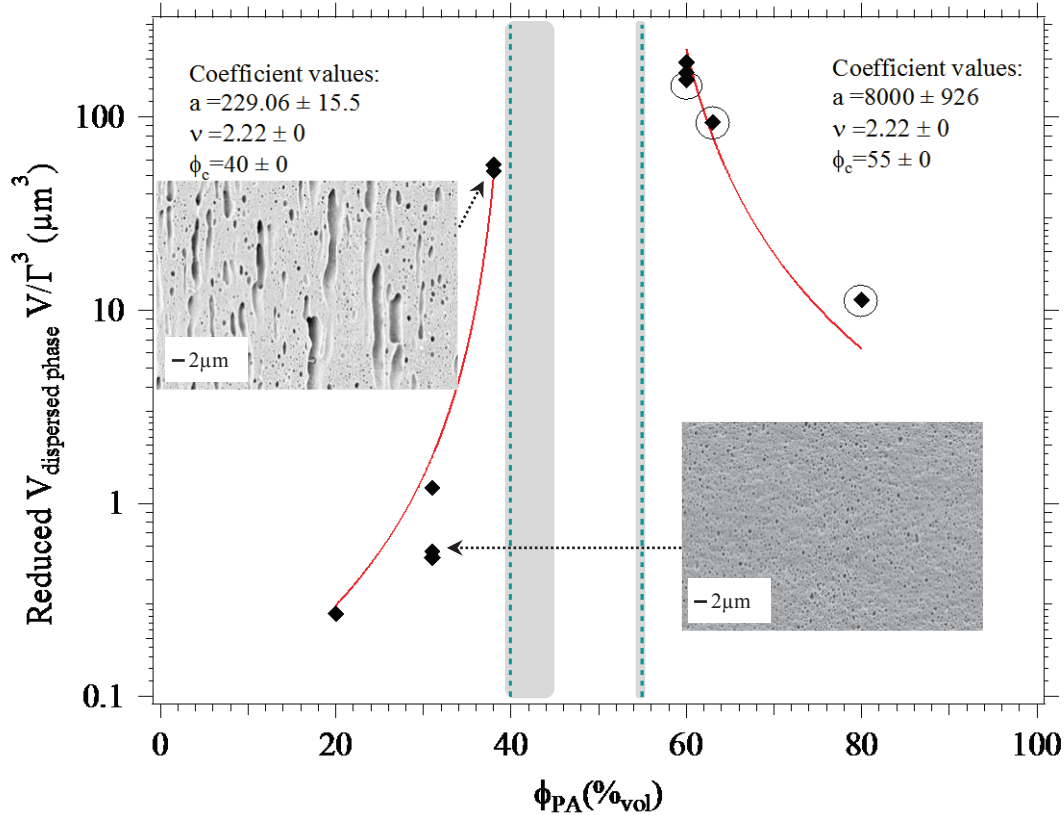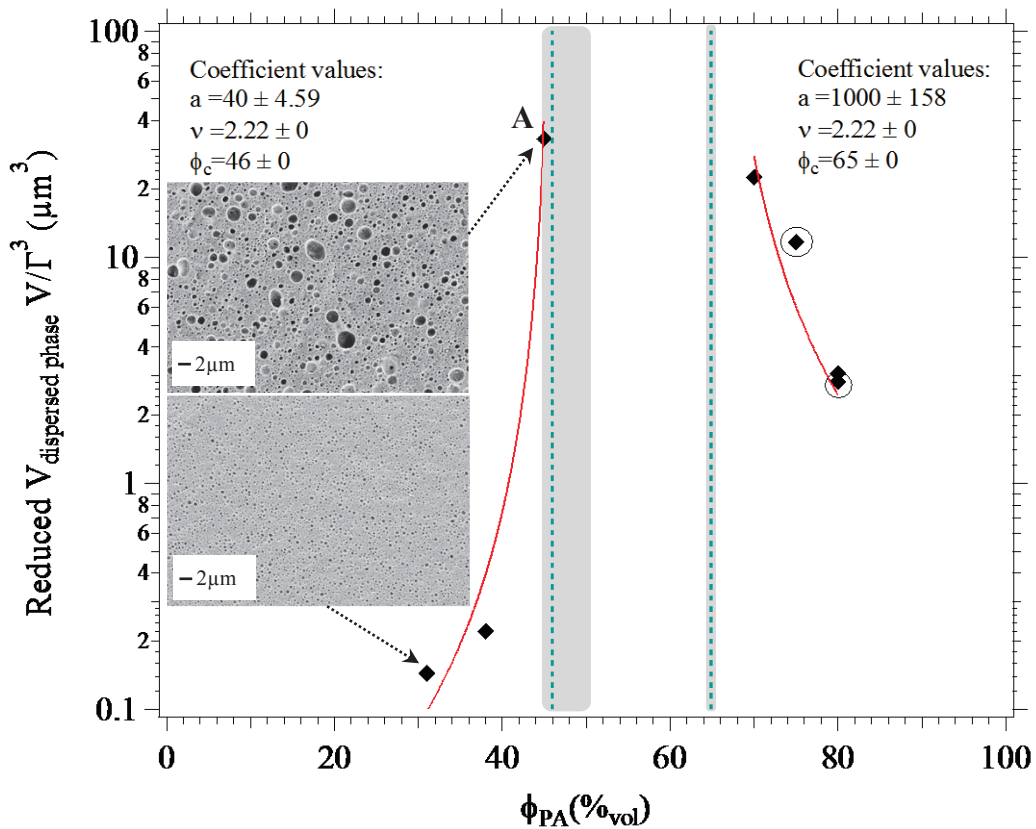

Figure III-44: Dispersed phase volume versus PA6 volume fraction (markers) in PA6/HDPE 3/MA-g-HDPE blends along the line *L*. The points encircled correspond to PA6/MA-g-HDPE blends (along *Axis C* Figure III-1) whose dispersed phase volume was rescaled by multiplying by the interfacial tension $\Gamma^3 = 7^3$. The domains in grey correspond to the experimentally observed co-continuity boundaries (between 45 and 50%$_{vol}$ of PA6 to 65%$_{vol}$ of PA6 according to the ternary diagram in Figure III-5 (c)). Both percolation fits for PA6 and PE phase dispersions are plotted in red. The blue dashed lines correspond to the percolation threshold in the fits.

For points along the line *L* in the ternary diagrams (corresponding to black markers in Figure III-44), the values of the volume (measured in μm^3) are directly plotted. **For the two PA6/MA-g-HDPE blends** along *Axis C* (encircled black markers in Figure III-44), **the corresponding values of the volume have been multiplied by 343 to rescale them to the volume obtained in compatibilized blends along line *L*. This rescaling value corresponds to an interfacial tension at cubic square $\Gamma^3=7^3=343$.** In fact, in this case, the interfacial tension is smaller in PA6/MA-g-HDPE blends than in blends with PE phase 3 along the line *L*. Like for the other HDPEs, the fits match well the experimental data and **the percolation volume fractions obtained (blue dashed lines in Figure III-44), which are consistent with the experimental boundaries of the co-continuous region (grey domains in Figure III-44) are 46 and 65%$_{vol}$ in PA6.**

As expected, the percolation thresholds are shifted to larger amount of PA6 in the case of HDPE 3 and MA-g-HDPE which exhibit a lower viscosity than HDPEs 1 and 2 (see *section 3.4 Influence of the viscosity ratios on micrometer scale* morphology *page 122*).

All together, **the rescaling used** for the reduced volumes plotted in Figure III-42 and Figure III-44 **correspond to relative values of the interfacial tension scaling from 10mN.m^{-1} (uncompatibilized blends along the *Axis NC*) down to about 2.9mN.m^{-1} (compatibilized blends along the line *L*) down to about 0.4mN.m^{-1} (binary PA6/MA-g-HDPE blends along the *Axis C*)** as illustrated in Figure III-45. These values of interfacial tensions are quite in agreement with ones expected from the literature [94,93,101].
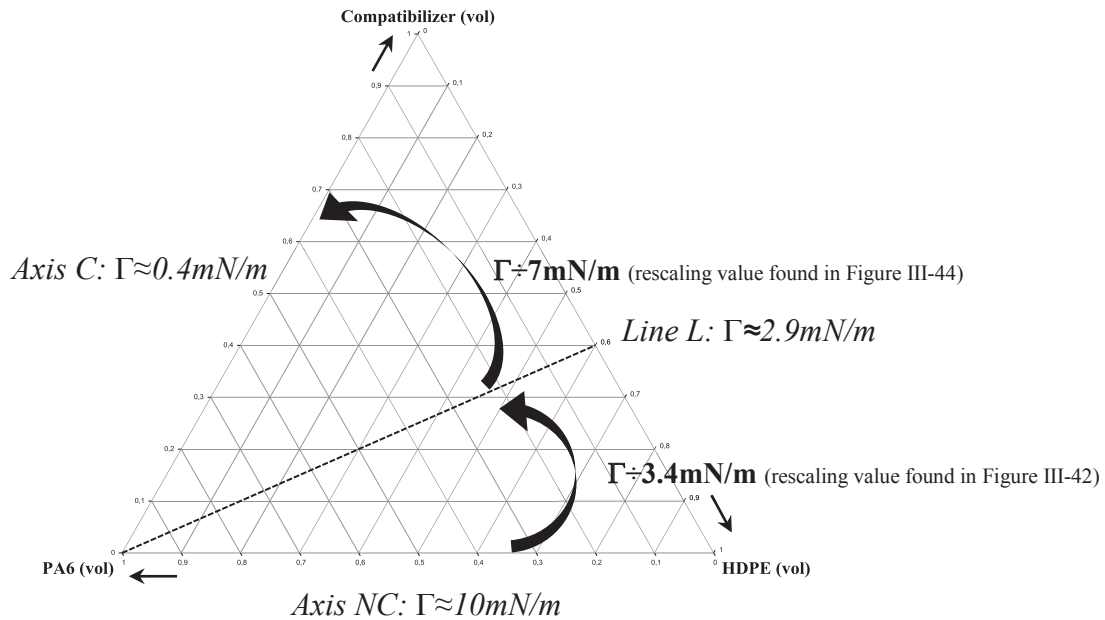
Figure III-45: Illustration of the estimations of the interfacial tensions in blends along *Line L* and *Axis C* by using the rescaling values found in Figure III-42 and Figure III-44.

7.2. Distribution of sizes

Then, the distribution of domain sizes has been analyzed in a blend close to the percolation threshold (A in Figure III-44). The SEM micrograph was binarized and treated as follows using the ImageJ software:

- The image with various grey levels was first converted into a binary image by adjusting the threshold (Image – Adjust – Threshold). This step to obtain a binary image similar to the initial image is the trickiest.
- Then, the scale between pixels and μm was holded.
- Finally, the particles area was analyzed by the software in order to obtain a distribution.

Figure III-46 shows the initial SEM micrograph of blend A and the binarized image used to compute the distribution of sizes shown in Figure III-48.
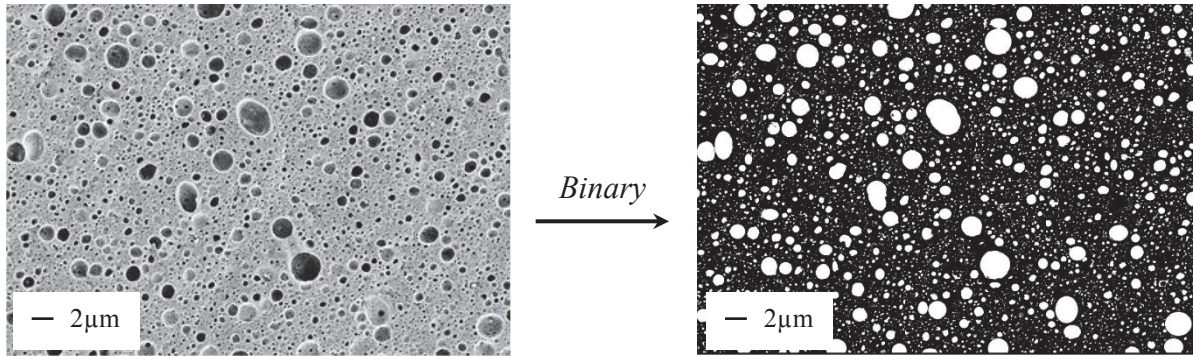
Figure III-46: SEM micrograph of blend A in Figure III-44 PA6/HDPE 3/ MA-g-HDPE (45/33/22%$_{vol}$) before and after binarization.

In a 3D system, the distribution of cluster masses $P_{3D}(m)$ is a function of the following form [115]:

$$P_{3D}(m) \approx m^{-\tau} f\left(\frac{m}{m_\xi}\right)$$

Eq. III-25

With:

- τ, the critical exponent whose value is 2.18 in 3D [115].

Where $f\left(\frac{m}{m_\xi}\right)$ decreases exponentially for the cluster mass $m > m_\xi$:

$$f\left(\frac{m}{m_\xi}\right) \approx e^{-\frac{m}{m_\xi}}$$

Eq. III-26

161

In our case, the distribution of the domains in the range of sizes smaller than the largest size (previously analyzed, see section 7.1) $m < m_\xi$ was observed, i.e. in the range in which the power law dominates in Eq. III-25:

$$P_{3D}(m) \approx m^{-\tau}$$

<div align="right">Eq. III-27</div>

With:

- τ, the critical exponent whose value is 2.18 in 3D [115].

In this range of sizes, the domains may collapse to compact objects. Indeed, it is observed in Figure III-46 that droplets of all sizes are nearly spherical. Thus, considering the distribution of volumes (or equivalently masses) is appropriate.

In our case, we measured a distribution of domain areas S. So, we need to make a change of variables between S and m (equivalent to a volume):

$$P_{3D}(S)dS = P_{3D}(m)dm$$

<div align="right">Eq. III-28</div>

Considering that $m \approx S^{3/2}$ and $dm \approx S^{1/2}dS$:

$$P_{3D}(S) \approx S^{\frac{-3\tau}{2}+\frac{1}{2}}$$

<div align="right">Eq. III-29</div>

What is directly measured by analyzing SEM binarized micrograph is the distribution of domains areas in **2D**: P_{2D} *(log S)*, i.e. the relative number of domains of area S in the plane of the picture. Figure III-47 illustrates the way to convert the measured 2D distribution into the 3D distribution of sizes (in the case of isotropic droplets).
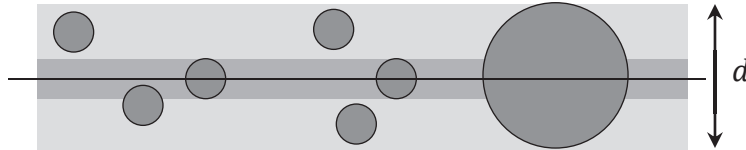
Figure III-47: Schematics illustrating the way to convert a 2D distribution into a 3D distribution of sizes.

The relative measured number of objects of size (diameter) $d \approx S^{1/2}$ within a picture of total area A is representative of a volume $d \times A$. Therefore, the relative number of small objects is larger in 3D than measured in 2D:

$$P_{2D}(S) \approx P_{3D}(S)d \approx S^{1/2}P_{3D}(S)$$

<div align="right">Eq. III-30</div>

<div align="center">162</div>

Then, by combining Eq. III-29 and Eq. III-30:

$$P_{2D}(S) = S^{1/2}P_{3D}(S) \approx S^{1/2}S^{\frac{-3\tau}{2}+\frac{1}{2}} = S^{\frac{-3\tau}{2}+1}$$

<div align="right">Eq. III-31</div>

And for the distribution in 2D of log S:

$$P_{2D}(\log S) \approx S^{-\frac{3\tau}{2}+2} = S^{-1.27}$$

<div align="right">Eq. III-32</div>

The distribution of the log of domain areas (P_{2D} *(log S)*) is plotted in Figure III-48. We did not apply a correction to take into account the fact that droplets may not be cut at equator. This correction should have negligible effect on the distribution.
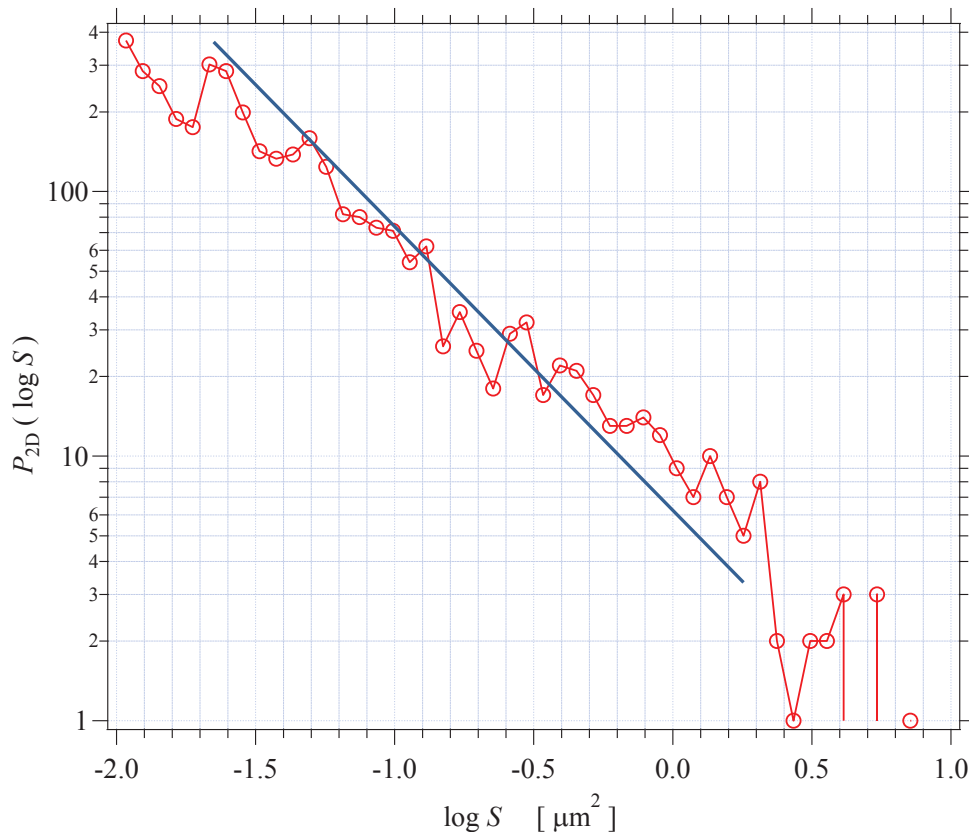
Figure III-48: Distribution of domain areas (in red) of blend A in Figure III-44: PA6/HDPE 3/MA-g-HDPE (45/33/22%$_{vol}$) computed from Figure III-46. The curve in blue corresponds to a straight line whose slope is -1.27.

So, the blue straight line which corresponds to the distribution expected from percolation theory (Eq. III-32) matched quite well the experimental distribution in red in Figure III-48.

To conclude, the percolation theory well describes the characteristic sizes and the distributions of sizes in the multi-scales morphologies observed in PA6/HDPE blends.

8. Conclusion

The development of morphologies in PA6/HDPE blends compatibilized with MA-g-HDPE was studied over a broad range of compositions in this chapter.

Several kinds of morphology were observed as the amount of PA6 increased in the blends from 1) to 5):
1) PA6 dispersion in PE phase
2) PA6 stretched dispersion in PE phase
3) Co-continuous
4) PE phase stretched dispersion in PA6
5) PE phase dispersion in PA6

These morphologies exhibit characteristic sizes from nanometer scale to micrometer scale.

Morphologies at the micrometer scale were first discussed. As the extrusion parameters on the kind of tools did not influence the morphology, the morphological regions of all the blends were summarized in ternary diagrams for each HDPE, independently from the process. The development of these morphologies is accelerated by the presence of the compatibilizer. It was observed that stretched dispersions/fibrils and an increase of domain sizes were observed near the phase inversion. We have also seen that the stretching of the morphology should be essentially due to the high shear applied in the extruder die and probably to the stretching of the strand at the exit of the die during its cooling in water. However, by increasing the volume ratio compatibilizer / HDPE, the morphology became more stable during its passage through the die. So, these stretched morphologies are certainly not steady state morphologies and would relax to nodular dispersions or co-continuity depending on the blend composition, during a second heating step (without any shear). The viscosity ratios had less influence on the phase inversion compositions range than expected from Paul and Barlow's model. **So, the composition (volume ratios PE phase / PA6) is the predominant parameter in micrometer scale morphology development.**

High conversion rates (>80% typically) for the compatibilization reaction were determined by Infrared spectroscopy. According to this result, the expected sizes of the morphology at thermodynamic equilibrium and the amount of copolymer formed at the interface were estimated. It was found that the main part of the copolymer was not located at the micrometer scale morphology interfaces. Thus, morphologies at the nanometer scale were then studied.

In the case of non-compatibilized blends, due to the large interfacial tension, all the domains were subjected to breaking and coalescence mechanisms with a minimum droplet size (of the order of few hundreds nm) which corresponds to the Taylor estimated size.

In compatibilized blends, we have seen that a large fraction of the grafted copolymer was located within droplets of small size (of the order of 50nm) generated by interface instabilities during reactive processing. However, interfaces relatively poor in copolymer remained present in the system. These interfaces formed larger domains which were subjected to breaking and coalescence equilibrium to form the micrometer scale morphology, driven by the high shear rate value imposed during processing and by the interfacial tension between the domains.

Thus, the percolation theory was applied to describe the characteristic sizes and the distributions of sizes in the multi-scales morphologies observed in PA6/HDPE blends. By rescaling the sizes experimentally measured by the interfacial tension, the reduced volume of the dispersed phase (V/Γ^3) as a function of the PA6 volume fraction was plotted in a same graph for several blends (compatibilized and non-compatibilized) exhibiting a same rheological behavior. The percolation fits performed matched well the experimental data. The expected distribution of sizes from percolation theory was also in agreement with the experimental distribution of sizes close to the percolation threshold. **Thus, the percolation theory allows estimating qualitatively interfacial tensions by measuring typical domain sizes. Conversely, it may be also useful to predict the largest size of the dispersed phase depending on the composition.**

To summarize the results obtained in this chapter, Figure III-49 shows a diagram of multi-scales morphologies development in both compatibilized and non-compatibilized blends.

① Beginning of extrusion   ② Extrusion   ③ At the end of extrusion

Large domains

Droplets break up/coalescence

Multi-scales morphology

NON-COMPATIBILIZED BLENDS:

Starting of droplets break up (Taylor) and coalescence mechanisms

NON-COMPATIBILIZED BLENDS:

All the domains can coalesce

NON-COMPATIBILIZED BLENDS:

- The smallest size corresponds to Taylor's size: ~500nm
- The largest size is determined by coalescence: ~a few tens μm

COMPATIBILIZED BLENDS:

The reaction being very fast, the *interfacial instabilities* occurred at the very early stages. According to the continuous interface renewal, the reaction ran out by forming *nano-dispersions*. A multi-scales morphology was already formed from the early stages:

Very low interfacial tension: Γ_1

Larger interfacial tension: $\Gamma_2 > \Gamma_1$

COMPATIBILIZED BLENDS:

The nano-dispersions may be stable: they do not coalesce. Only the largest domains with the larger interfacial tension Γ_2 can coalesce.

COMPATIBILIZED BLENDS:

- The smallest size corresponds to the size of the nano-dispersions formed by interfacial instabilities: ~50nm.
- The largest size is determined by the coalescence of the largest domains: ~a few μm

Figure III-49: Diagram of multi-scales morphology development in both compatibilized and non-compatibilized blends.

IV. Stability of the morphologies

1. Introduction

The final properties of polymer blends depending on morphology, the challenge is to obtain a controlled, stable and reproducible morphology. More precisely, the stability of the morphologies during a second step processing is a key point from the application point of view to insure reproducibility of properties in a final part. We have seen in the previous chapter (*Chapter III Control of blend morphologies*) the development of various morphologies in PA6/HDPE reactively compatibilized blends and the predominant factors to control them. So, this chapter will focus on the study of morphologies stability under various conditions.

For better understanding, well controlled conditions were firstly used:
- Static annealing
- Controlled shear

Then, real processes exhibiting more complex flows were tested:
- Extrusion blow molding
- Injection molding

2. Studied formulations

Six blends with HDPE 2 prepared by twin screw extrusion D40 were used to study the morphology stability. These formulations and associated morphologies in the pellets obtained at the exit of the extruder die are detailed in Figure IV-1.
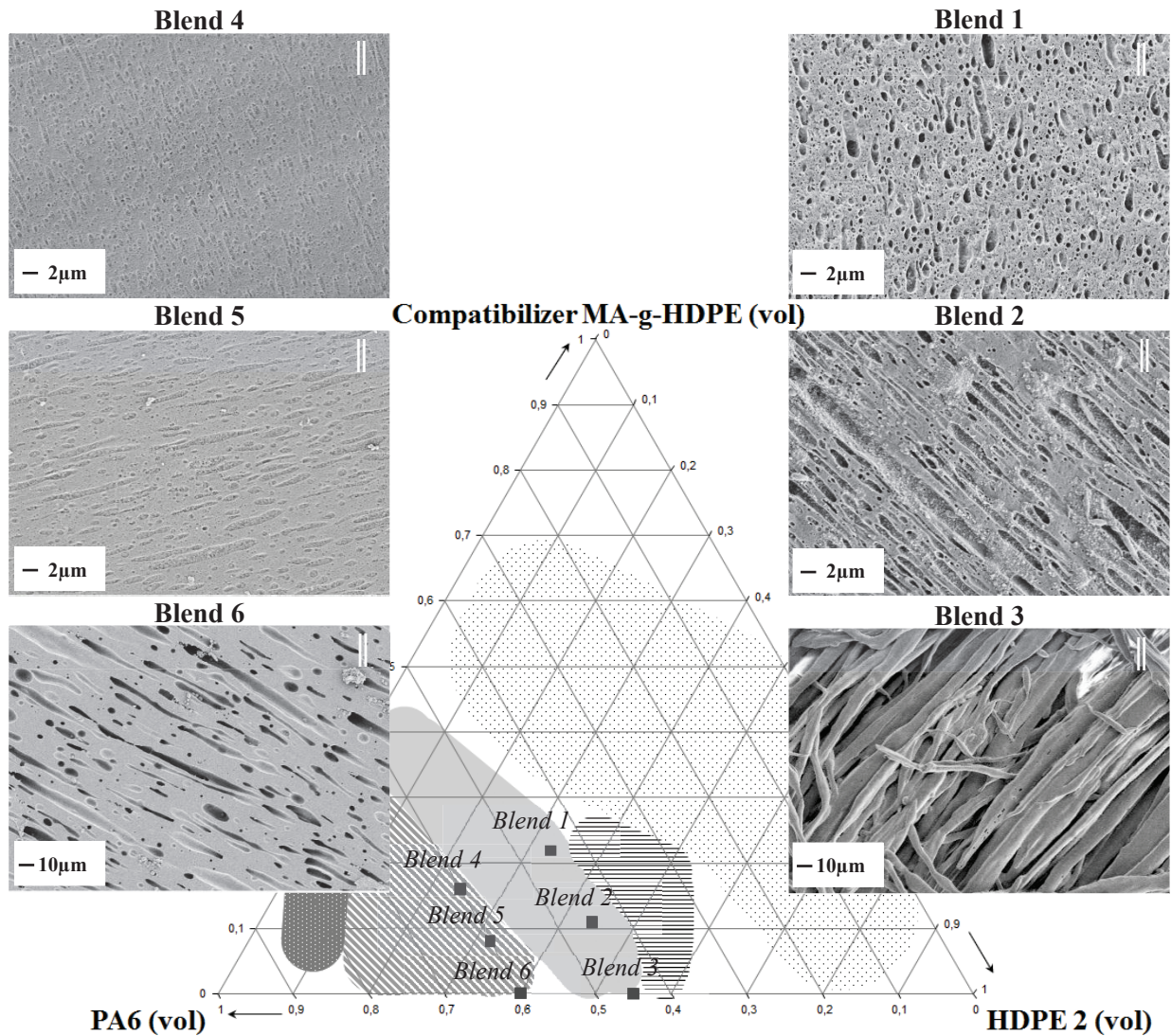
Figure IV-1: Ternary diagram of blends used for morphology stability study and associated pellets morphology (blends 1, 2 and 3: 45%$_{vol}$ PA6 (PA6 etched using formic acid), blends 4, 5 and 6: 60%$_{vol}$ PA6 (PE phase etched using Decalin)). Domains of morphology are represented using the same symbols as in Figure III-4:

- PA6 dispersion in PE phase
- PA6 stretched dispersion in PE phase
- Co-continuous
- PE phase stretched dispersion in PA6
- PE phase dispersion in PA6

As shown on Figure IV-1, two series of three blends with various compatibilizer amounts were studied. The morphologies and the qualitative characteristic domain size are:

- **Series 45: 45%$_{vol}$ PA6:**

  - Blend 1 (high compatibilizer amount): HDPE 2/MA-g-HDPE 33/22%$_{vol}$: PA6 stretched dispersion in PE phase (close to co-continuity) *(characteristic size width 1.5µm, length 4µm)*
  - Blend 2 (low compatibilizer amount): HDPE 2/MA-g-HDPE 44/11%$_{vol}$: PA6 very stretched dispersion in PE phase (close to co-continuity) *(characteristic size width 3µm, length 10µm)*
  - Blend 3 (non-compatibilized): HDPE 2/MA-g-HDPE 55/0%$_{vol}$: PA6 fibrils/HDPE 2 fibrils (close to co-continuity) *(characteristic size width 10µm, length several tens µm)*

In the case of the blends of series 45, the morphologies observed parallel to the extrusion flow seem to be stretched dispersions of PA6 in PE phase matrix. However, we could expect that the morphology is closer to co-continuity than observed in this direction. In fact, the PA6 domains in blends 1 and 2 in Figure IV-1 seem to be quite deep, indicating a probable co-continuity. Observations perpendicularly to the extrusion flow would be interesting to really confirm the morphology. Moreover, blend 1 was also made using another tool (extruder D34) and was found to be really co-continuous. Thus, the blends of series 45 could be considered close to co-continuity.

- **Series 60: 60%$_{vol}$ PA6:**

  - Blend 4 (high compatibilizer amount): HDPE 2/MA-g-HDPE 24/16%$_{vol}$: PE stretched dispersion in PA6 *(characteristic size width 500nm, length 4µm)*
  - Blend 5 (low compatibilizer amount): HDPE 2/MA-g-HDPE 32/8%$_{vol}$: PE stretched dispersion in PA6 *(characteristic size width 1.5µm, length 6µm)*
  - Blend 6 (non-compatibilized): HDPE 2/MA-g-HDPE 40/0%$_{vol}$: PE very stretched dispersion in PA6 *(characteristic size width 10µm, length 100µm)*

3. Stability of the morphologies after static annealing

As previously described in the *Chapter II section 3.1.2.1 Static annealing experiments page 86*, to study the stability of the morphology under static conditions, annealing were performed in DSC at 290°C during 5 and 15 minutes under Helium flow.

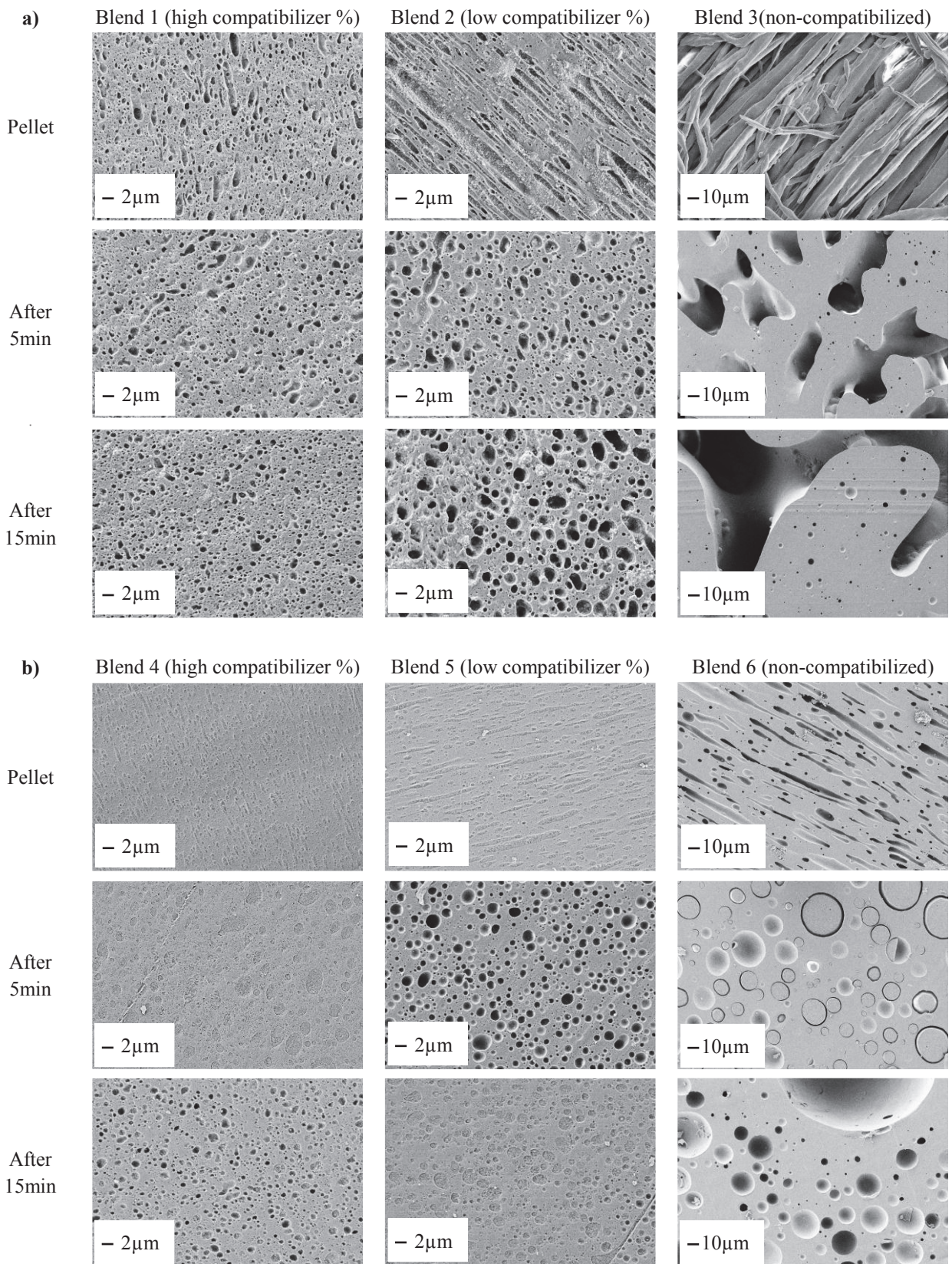The morphologies obtained after static annealing at 290°C are summarized in Figure IV-2.

Figure IV-2: SEM micrographs (‖) of a) Series 45 (PA6 etched) b) Series 60 (PE phase etched), in pellets after extrusion and after static annealing during 5 and 15min.

Thus, after static annealing at 290°C:

- In **compatibilized systems** (blends 1, 2, 4 and 5):

  As expected, the stretched morphologies being non-steady state morphologies, a stretching release was observed after static annealing. However, the domain size remains stable whatever the annealing time. So, the low compatibilizer amount seems to be sufficient to suppress the coalescence and to stabilize the micrometer scale morphology.

- In **non-compatibilized systems** (blends 3 and 6):
  - In blend 3, after extrusion, the morphology was fibrillar, very close to co-continuity domain. After annealing, the stretching was released and the morphology was co-continuous, with an important increase of the domains size with time due to coalescence.
  - In blend 6, after annealing, a stretching release was observed and a nodular PE phase dispersion was obtained with an increase of particles size with time due to coalescence.
  - The typical size increased linearly with annealing time in non compatibilized systems as observed in PS/PA6 50/50 blends by Zhang et al [15]. An example of the evolution of the typical domain volume as a function of annealing time for blend 6 is plotted in Figure IV-3. For comparison, the evolution of the characteristic domain volume in blend 5 (compatibilized) is also reported.
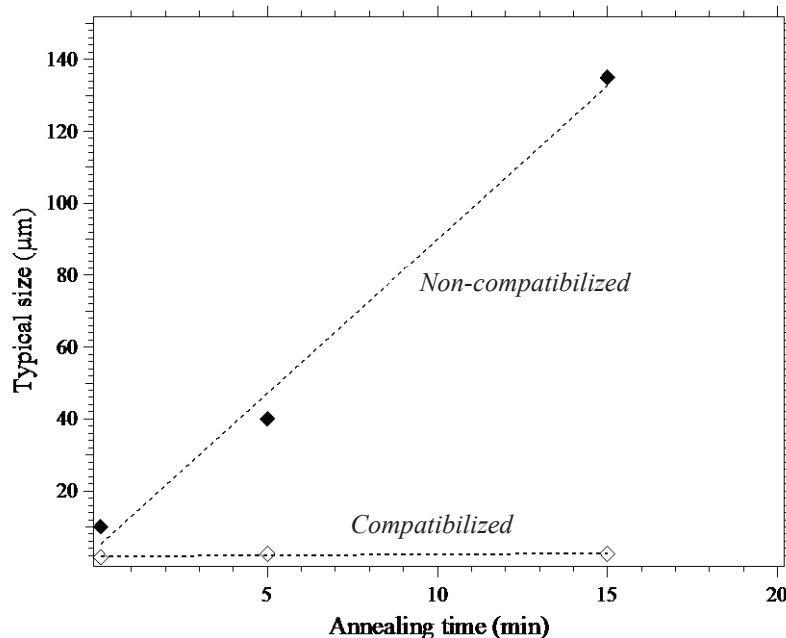

Figure IV-3: Typical domain size versus annealing time in blends 5 (compatibilized) and 6 (non-compatibilized).

Finally, the blends of series 45 seem to be more co-continuous after static annealing, which is consistent with the region of co-continuity plotted in the ternary diagram in Figure IV-1.

4. Stability of the morphologies under controlled shear conditions

As described in details in the *Chapter II section 3.1.2.2 Controlled shear experiments conditions: capillary rheometer page 86*, the stability of the morphologies was also studied in controlled shear conditions at 290°C after a static annealing of 17 minutes using a capillary rheometer, at two shear rates:

-   $200s^{-1}$: order of magnitude of extrusion shear rate.
-   $2000s^{-1}$: order of magnitude of injection molding shear rate during the passage through the nozzle and of the die shear rate in twin screw extrusion. To conduct these experiments, remind that, due to the too small quantity of material available in the capillary rheometer, a shear rate of $50s^{-1}$ was applied with peaks at $2000s^{-1}$ after 1, 5 and 10 minutes.

It was estimated in the *Chapter II section 3.1.2.2 Controlled shear experiments conditions: capillary rheometer page 86* that the shear rate of $200s^{-1}$ was applied during 0.8s and that the shear rate of $2000s^{-1}$ was applied during 0.08s.

4.1. Evolution of viscosity with time

In this section, the evolution of blends viscosity with time during the controlled shear experiments at 290°C is described. Figure IV-4 and Figure IV-5 show the viscosity as a function of time at both shear rates 200 and $2000s^{-1}$.
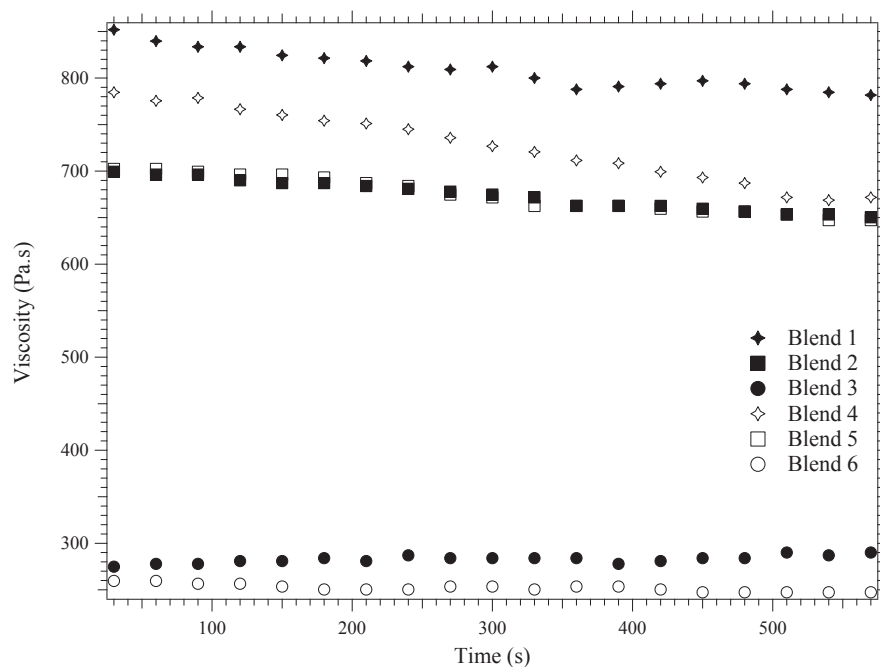
Figure IV-4: Viscosity as a function of time during controlled shear experiments at $200s^{-1}$.

In Figure IV-5, in addition to viscosity, the shear rate versus time is also represented in order to know at what time the $2000s^{-1}$ peaks were applied.
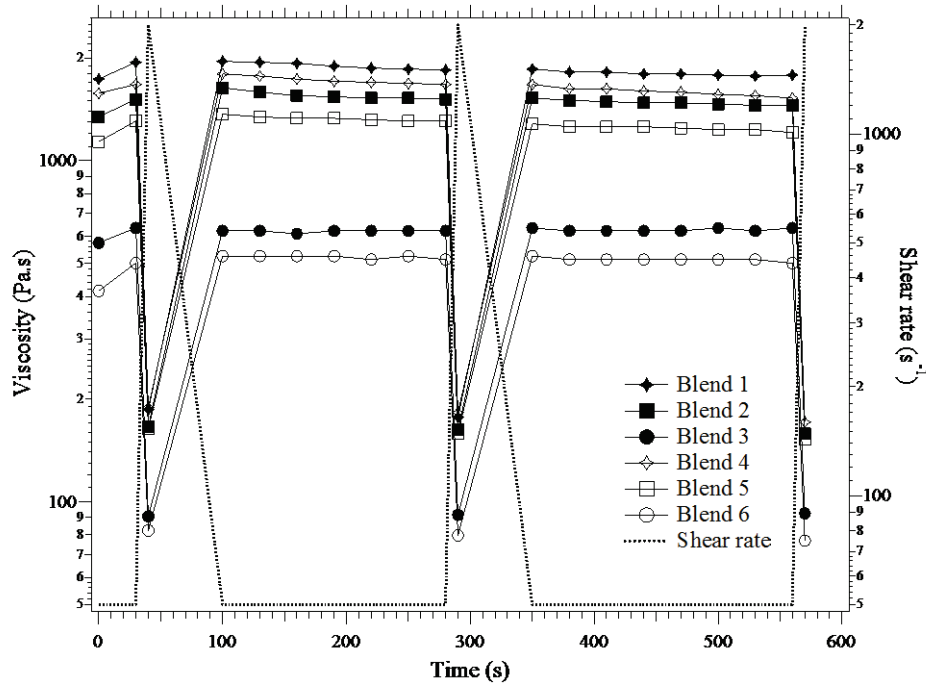
Figure IV-5: Viscosity as a function of time during controlled shear experiments at $50s^{-1}$ with the three peaks at $2000s^{-1}$ at 1, 5 and 10 minutes. The dashed line corresponds to the shear rate applied as a function of time.

As expected, when this higher shear rate was applied ($2000s^{-1}$), the viscosity immediately decreased. For both shear rates and for each series, the viscosity plateau increased with the compatibilizer amount in the blends, as expected:

$$\eta_{Blend\ 1} > \eta_{Blend\ 2} > \eta_{Blend\ 3}$$
$$\eta_{Blend\ 4} > \eta_{Blend\ 5} > \eta_{Blend\ 6}$$

Concerning the evolution of the viscosity with time, Table IV-1 summarizes the viscosity gaps $\Delta\eta$ (%) after 10minutes of controlled shear at 290°C.

	Blend 1	Blend 2	Blend 3	Blend 4	Blend 5	Blend 6
At $200s^{-1}$	8	7	6	14	8	5
At $50s^{-1}$	8	4	0	9	8	0
At $2000s^{-1}$ ($\Delta\eta$ between the first and the last peak)	7	5	2	9	7	7

Table IV-1: Viscosity gap $\Delta\eta$ in % after 10minutes of controlled shear.

The viscosity gap during 10 minutes was always lower than 10% (except for blend 4 which exhibited a viscosity decrease of 14.4% at $200s^{-1}$). So, the viscosity is considered to be stable.

173

4.2. Morphologies after controlled shear

The morphologies parallel to the flow ($\parallel$) obtained after controlled shear experiments at 200 and $2000s^{-1}$ are summarized in Figure IV-6.

a)

	Blend 1 (high compatibilizer %)	Blend 2 (low compatibilizer %)	Blend 3 (non-compatibilized)

b)

	Blend 4 (high compatibilizer %)	Blend 5 (low compatibilizer %)	Blend 6 (non-compatibilized)

Pellet

— 2µm   — 2µm   —10µm   —100µm

After
200s⁻¹

— 2µm   — 2µm   —10µm   —100µm

After
2000s⁻¹

— 2µm   — 2µm   —10µm   —100µm
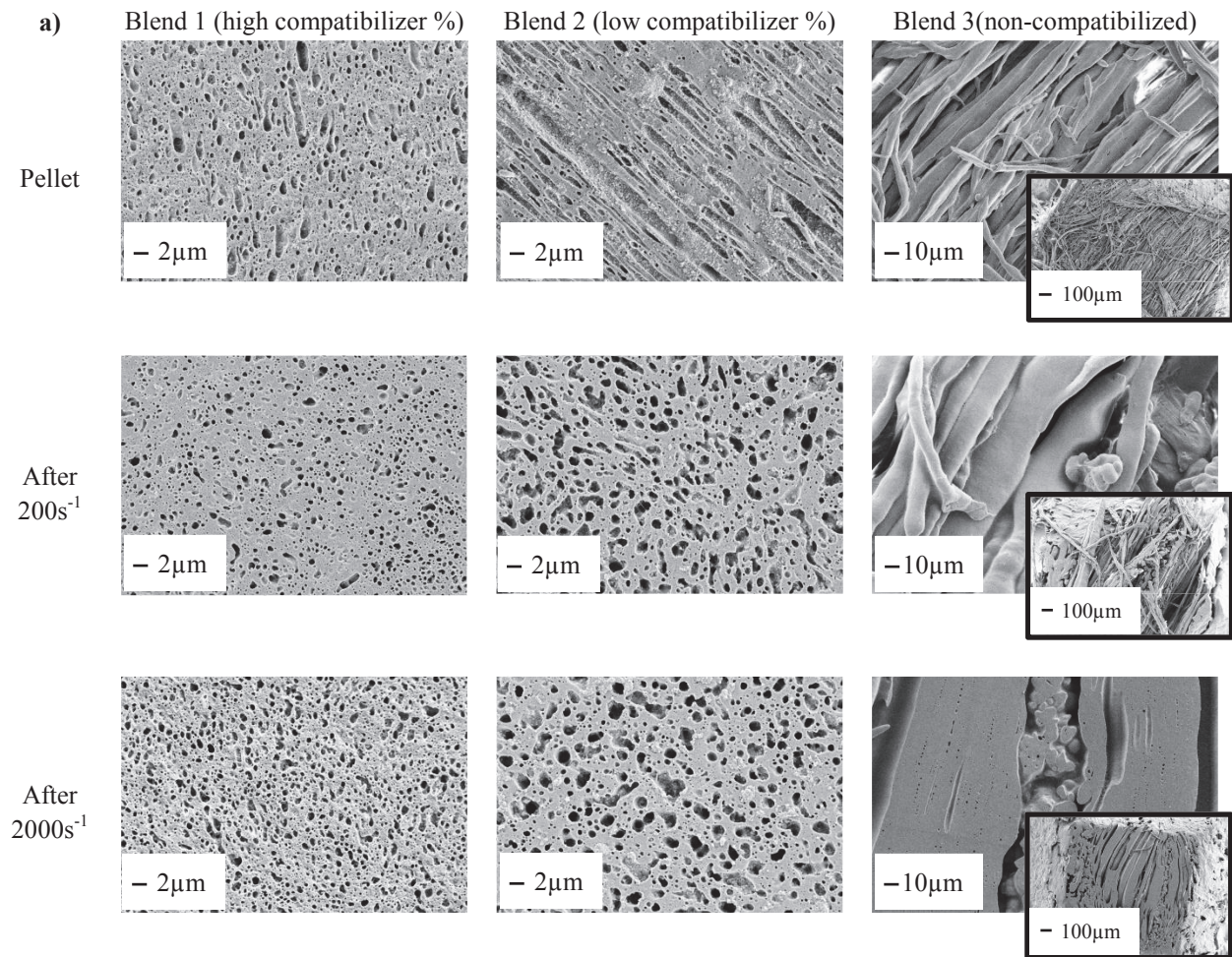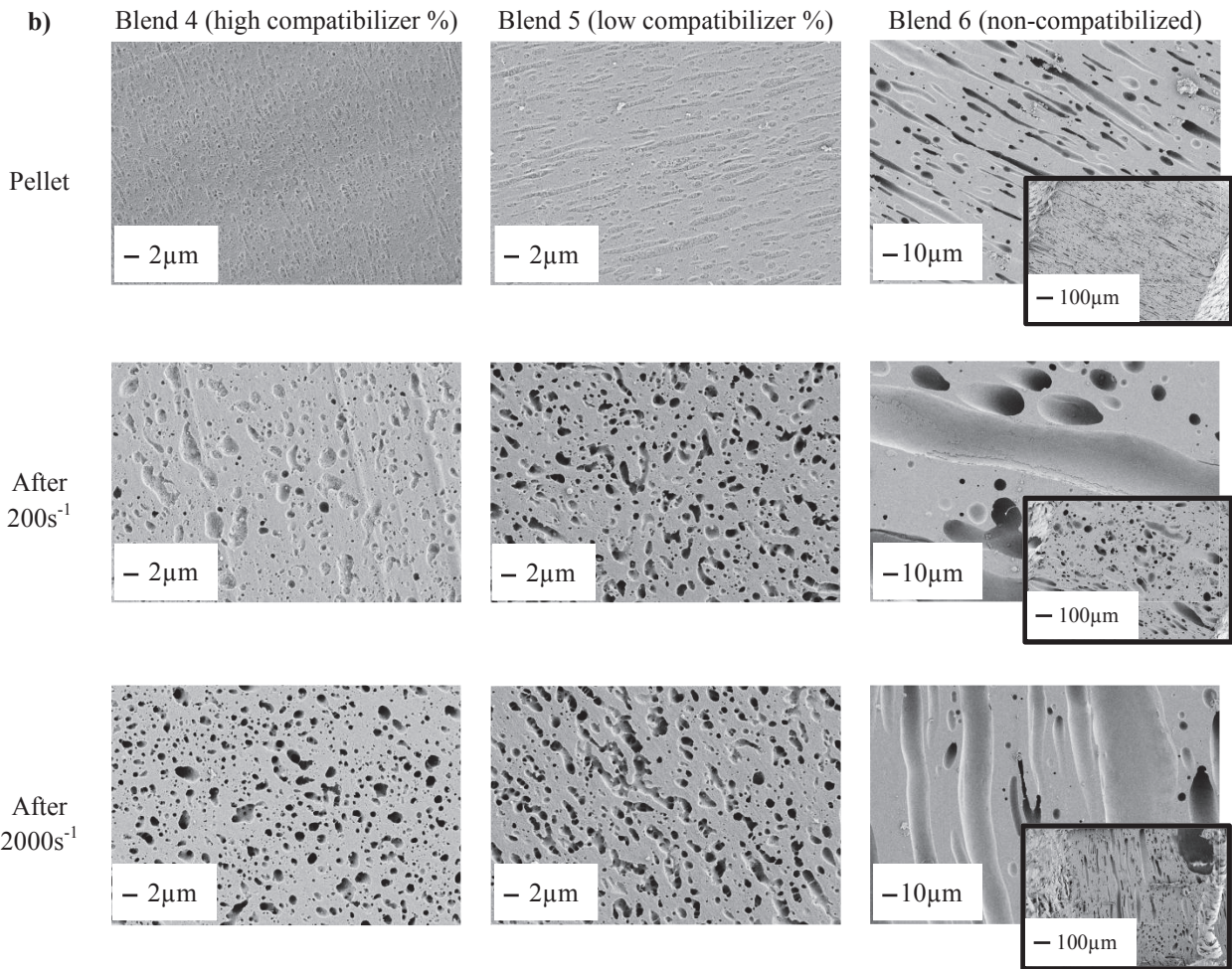
Figure IV-6: SEM micrographs (‖) of a) Series 45 (PA6 etched) b) Series 60 (PE phase etched), in pellets after extrusion and after controlled shear at 200 and 2000s⁻¹, 290°C.

- **In compatibilized systems** (blends 1, 2, 4 and 5), **whatever the shear rate applied, a stretching release was observed but the domain size remained quite stable. However, the morphology evolved to be closer to co-continuity.** In fact, all these blends were at the boundaries between stretched dispersions and co-continuous regions after extrusion (Figure IV-1). So, the additional shear applied can bring the morphology to co-continuity.

- **In non-compatibilized systems** (blends 3 and 6), the kind of morphology was not modified after controlled shear compared to pellets obtained after extrusion. However, **the domains size dramatically increased due to coalescence and the morphology was more heterogeneous then in pellets. However, with shear, the coalescence was less important than in static annealing.** After controlled shear, the largest width of the stretched domains was observed to be about 45µm whereas after static annealing, this width could reach 135µm typically. Contrary to static annealing, the stretching was kept, but the aspect ratio (length/width) seems to be smaller after shearing.

175

The shear rates values applied in these controlled shear experiments are comparable to those in extrusion ($200s^{-1}$) and in the extruder die ($2000s^{-1}$). We have seen in the *Chapter III section 3.5 Summary of the micrometer scale* morphology *page 125* that the stretching of the morphology would be due to the high shear applied in the extruder die. So, it may seem surprising that the morphologies were not stretched during their passage in the capillary rheometer, at least at $2000s^{-1}$. However, at the exit of the extruder die, the strand was also stretched during its cooling in water, which was not the case at the exit of the capillary rheometer. Thus, we may speculate that the morphology relaxed very fast at the exit of the capillary during its cooling at air, in the absence of post stretching.

5. Stability of the morphologies after a second step processing

From an applicative point of view, it is interesting to study the stability of the morphologies after a second step processing. In fact, morphology stability is needed to insure reproducibility of the properties in a final part. Two processes of interest were used in this study:
1) Extrusion blow molding
2) Injection molding

The morphologies obtained after both these second step processes are discussed in this section.

5.1. Extrusion blow molding

As detailed in the *Chapter II section 3.1.2.3 Extrusion blow molding page 88*, bottles were prepared by extrusion blow molding and the morphologies obtained were compared to the morphologies in pellets. This section is divided into three parts:
1) Skin/Core effect
2) Influence of position in the bottle
3) Summary of the morphology stability study after extrusion blow molding

5.1.1. Skin/Core effect

In order to determine if there is a skin/core effect in blow molded parts, the samples were observed as described in Figure IV-7.
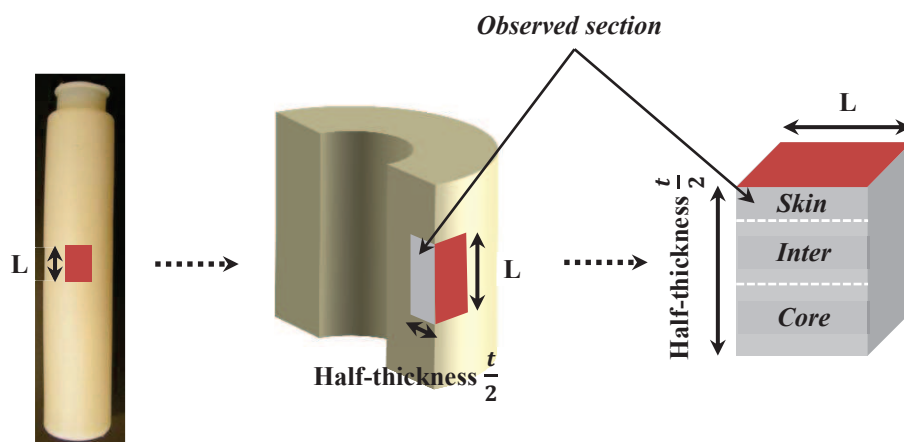
Figure IV-7: Diagram of bottle sample.

A skin/core effect with three regions was observed in all blends (see Figure IV-8):

- **Core**: the morphology in core region after blow molding was quite similar to the morphology obtained after controlled shear at $200s^{-1}$ (order of magnitude of the shear rate applied during the extrusion blow molding process), 290°C (see Figure IV-9).

- **Inter**: the morphology exhibited the same size as in core region but was still more stretched.

- **Skin** (~100µm thick): in compatibilized blends, the morphology exhibited a larger domain size than in core region and was more stretched. In non compatibilized blends, the skin region was more difficult to distinguish.

Two effects may contribute to the apparent stretching observed in the skin (and also in inter region):
1) The high shear rate applied to these regions close to the wall of the annular die
2) The fast cooling close to the cold mold wall.

An example of the morphologies obtained for Blend 2 of series 45 with low amount of compatibilizer (sufficient to stabilize the size of the morphology according to static annealing) is presented in Figure IV-8 and Figure IV-9.
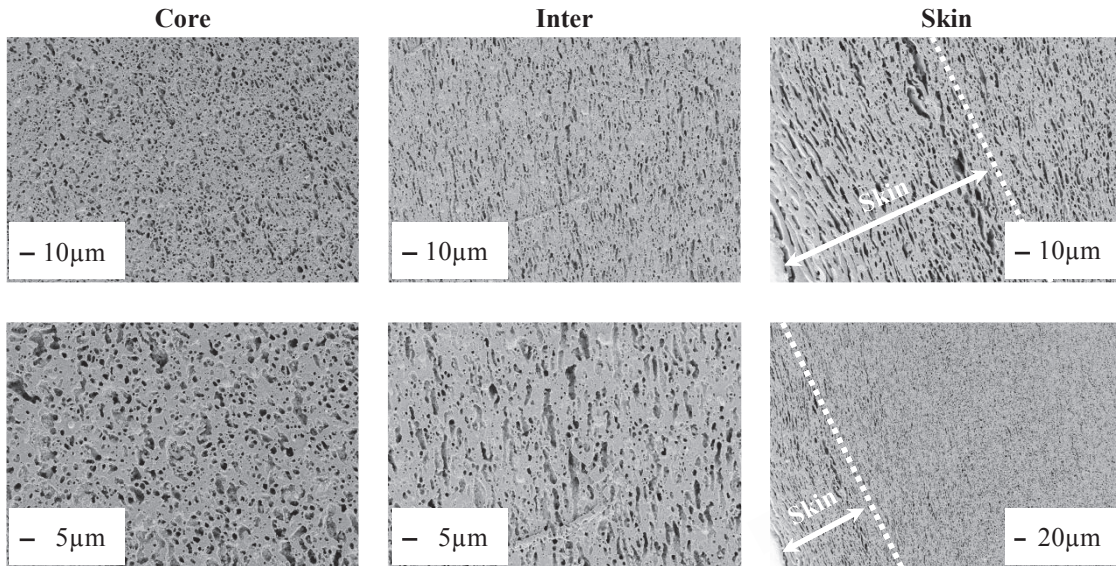
Figure IV-8: SEM micrographs of Blend 2 (PA6 etched) after extrusion blow molding: skin/inter/core regions on sample in medium position in the bottle.
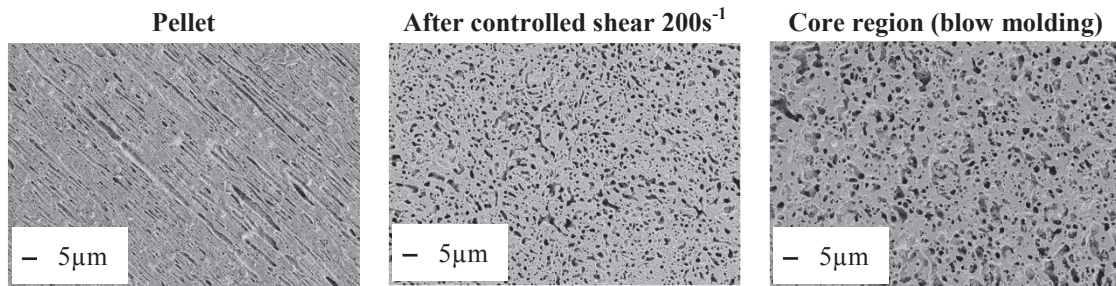
Figure IV-9: SEM micrographs x1000 of Blend 2 (PA6 etched) in a pellet obtained at the exit of twin screw extrusion, after controlled shear at 200s[-1] and after extrusion blow molding in core region.

When it is not specified, only the morphologies in core regions are used in what follows.

5.1.2. Influence of position on the morphology

5.1.2.1. Morphologies at various positions along the bottle

Blend's morphology in several positions along the bottles was characterized as illustrated on Figure IV-10 in order to determine if there is an influence of the parison drop on morphology, more precisely on stretching.
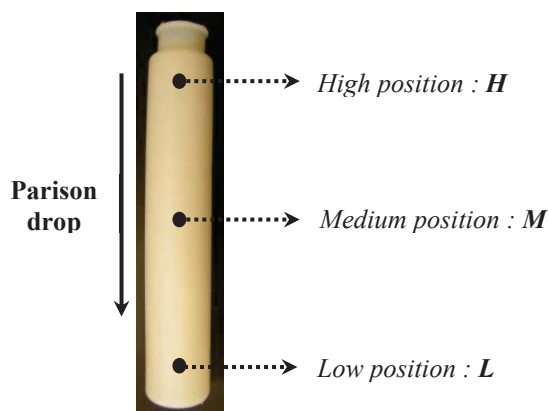
Figure IV-10: Bottle's positions used for morphology observations in SEM.

The influence of position on the morphology was studied on three blends:

- Series 60: **Blends 5** with the low amount of compatibilizer, sufficient to stabilize the size of the morphology according to static annealing.
- Series 45: **Blend 2** also with the low amount of compatibilizer, and **Blend 3** without any compatibilizer in order to determine if there is an effect of the compatibilization.

As shown in Figure IV-11, the blends exhibited some differences depending on the position along the bottle:

- In all cases, **the morphology was more stretched at the bottom of the bottle** (*L* position) than in the medium position (*M* position). This may be due to the mold closing which extends the part at the bottom.

- For blends 3 and 5, a little stretching was also observed at the top of the bottle (*H* position). In fact, as the parison length increases, it becomes heavier. As it gets heavier, if the melt strength of the polymers is not large enough, the parison starts to extend itself, which should lead to stretching of the morphology particularly at the top of the part. Thus, contrary to blend 2, in the case of blends 3 and 5, the melt strength may not be high enough.
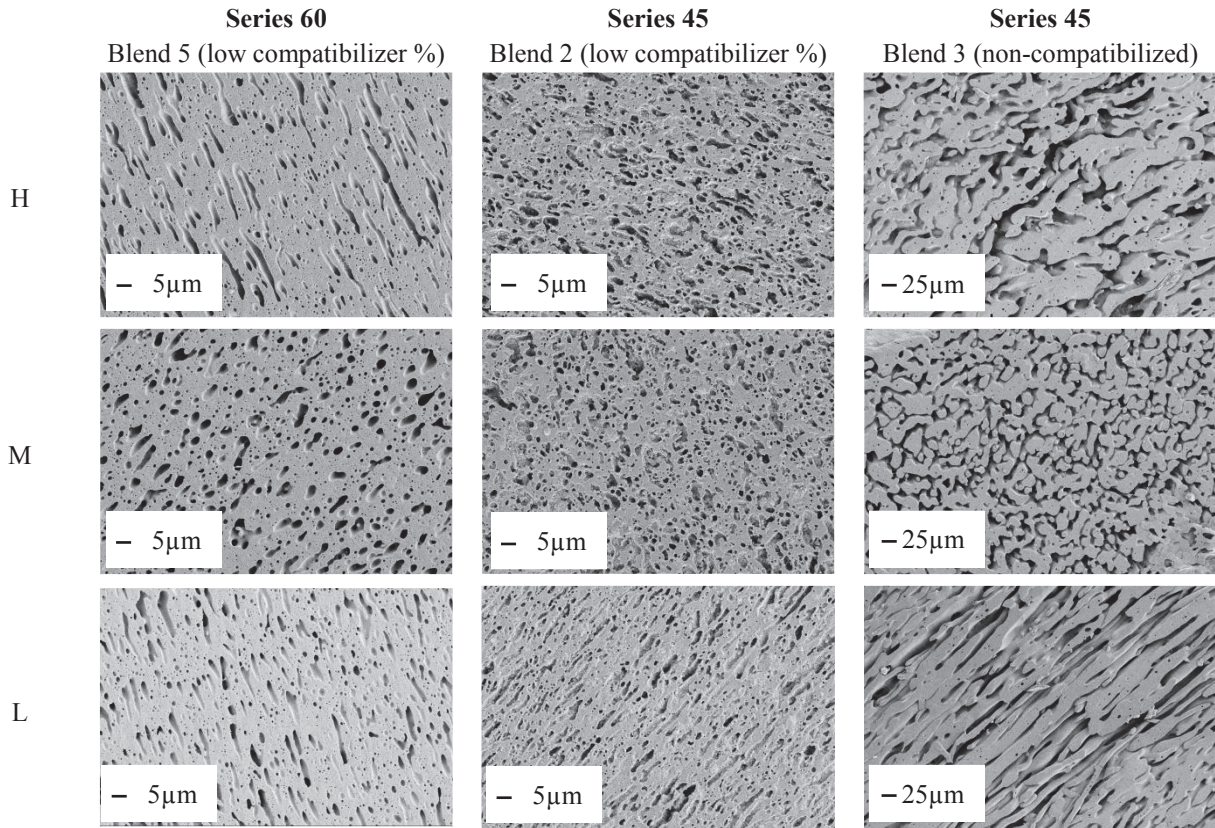
Figure IV-11: SEM micrographs of core regions of blend 5 (PE phase etched) and of blends 2 and 3 (PA6 etched) for the three positions along the bottle.

To characterize the melt strength of the polymers, the drop time was measured for all blends during the trials (see Figure IV-12).

As shown in Figure IV-12, **for blends 1, 2 and 4** (dashed lines), the evolution of drop time versus the distance from the annular die was linear. This means that the speed of parison drop was constant. **So the melt strength was high enough to avoid parison sag and stretching of the morphology at the top of the bottle.**

On the contrary, **for blend 5, 3 and 6** (full lines), the evolution of drop time versus the distance from the annular die was not linear. The speed of parison drop increased as the parison became longer and so heavier. Thus, in these cases, **the melt strength was too small and a stretching of morphology could be observed at the top of the bottle.**

Blends' melt strengths characterized via drop times measurements are in agreement with the stretching of the morphology observed. **Thus, the blends which showed morphology stretching at the top of the bottles** (blends 5 and 3) **also exhibited too small melt strengths.**
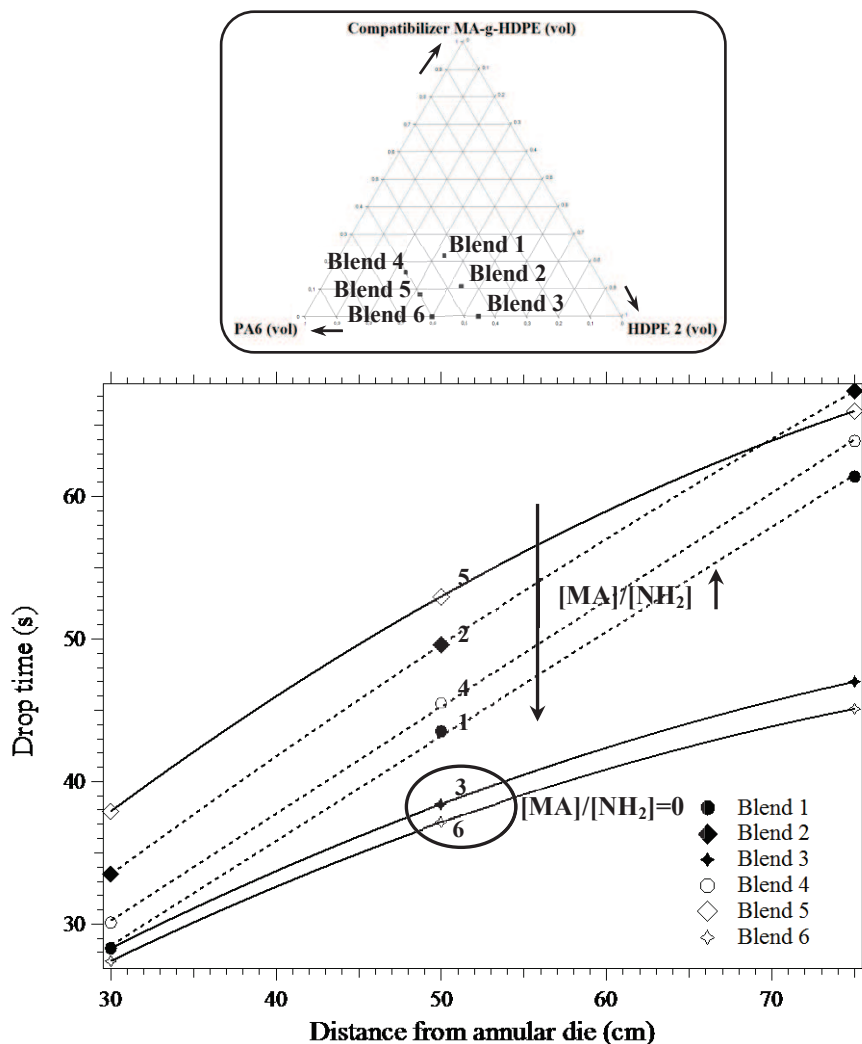
Figure IV-12: Drop time as a function of the distance from the annular die.

Note that the compatibilized blends exhibited longer drop times than the non-compatibilized ones. This should be due to the increase of compatibilized blends' viscosity due the compatibilization reaction. In compatibilized blends, the molar ratios $[MA]/[NH_2]$ are:

	Blend 1	Blend 2	Blend 4	Blend 5
$[MA]/[NH_2]$	0.9	0.45	0.5	0.25

Table IV-2: Molar ratios $[MA]/[NH_2]$ in the compatibilized blends.

So, by increasing the molar ratio $[MA]/[NH_2]$, the drop time decreased. The viscosity of the compatibilizer is lower than the viscosity of HDPE 2 used in these blends (see *Figure II-22 in Chapter II*). By increasing the amount of compatibilizer in the blends, the fraction of HDPE chains exhibiting a lower viscosity increases. Thus, the overall viscosity may decrease, leading to smaller drop times.

181

5.1.2.2. Morphologies perpendicularly to the flow

For the most stretched morphologies in pellets (blends with low compatibilizer amount in each series: blend 2 for series 45 and blend 5 for series 60), the morphology after extrusion blow molding was observed parallel and perpendicular to the parison drop for medium position (*M*) in order to determine whether there is stretching into two dimensions during air blowing inside the parison (formation of platelets).

The diagram in Figure IV-13 shows both directions of observation. Figure IV-14 shows examples of SEM micrographs of core, inter and skin regions of both blends 2 and 5 perpendicularly and parallel to the parison drop.
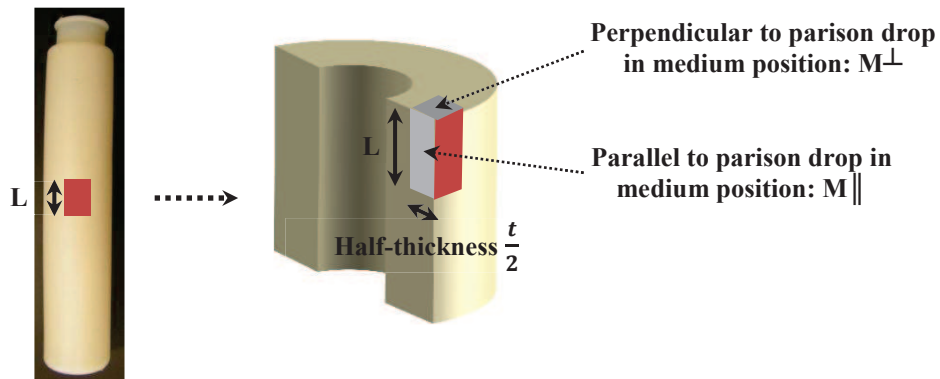
Figure IV-13: Directions of observation to determine if there is a bi-dimensional stretching.

b)

| Core | Inter | Skin |

M‖

M⊥
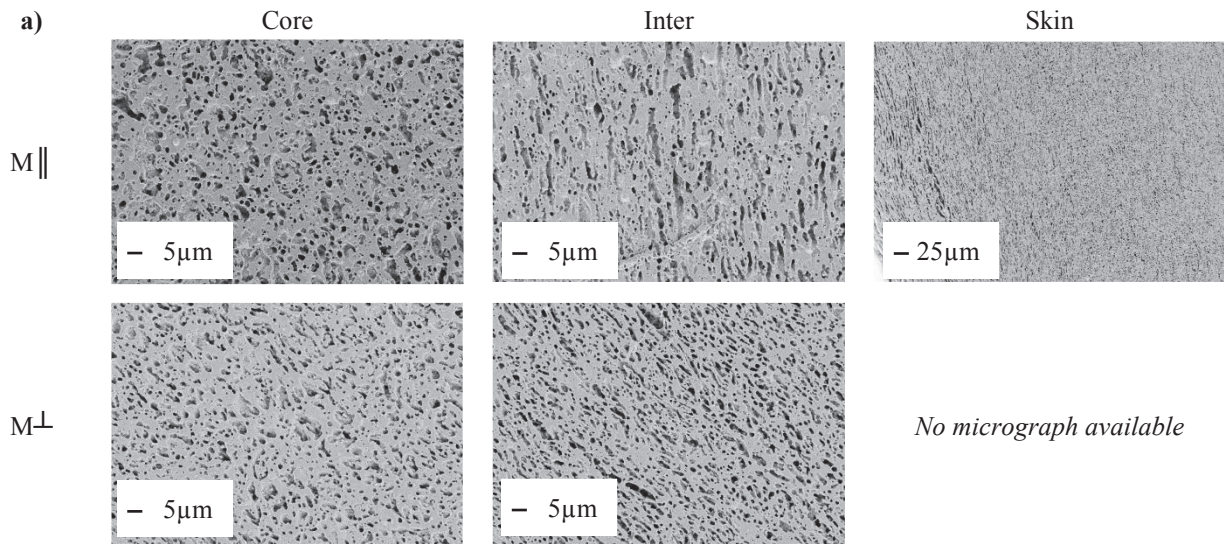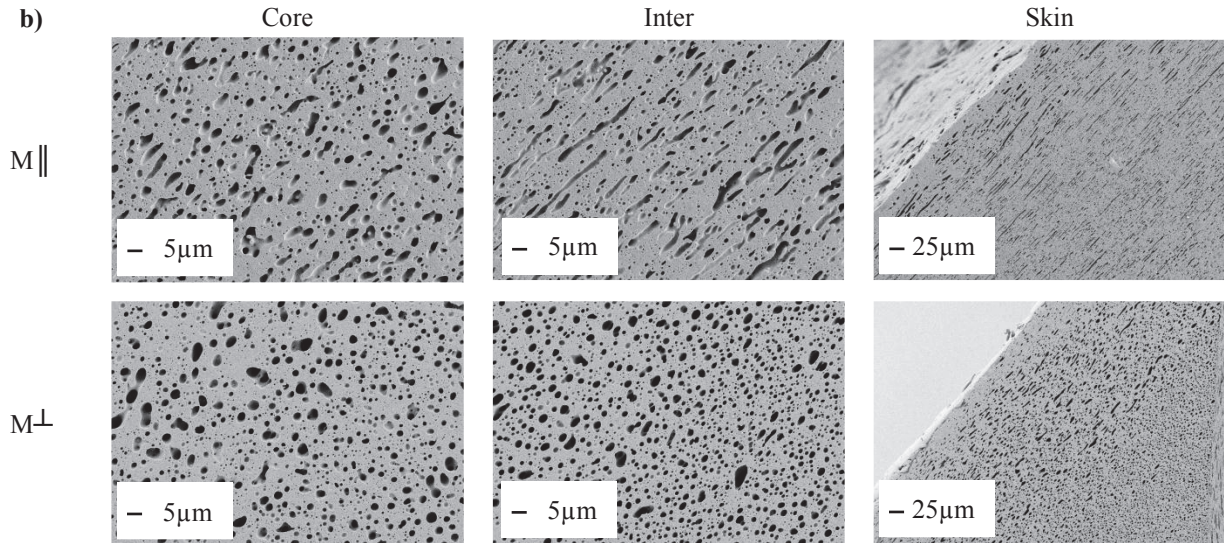
Figure IV-14: SEM micrographs of core/inter/skin regions perpendicular and parallel to the parison drop in medium position along the bottle for a) Blend 2 (PA6 etched) and b) Blend 5 (PE phase etched).

A little stretching was observed on external regions perpendicularly to the parison drop. However, this stretching was less large than parallel to the parison drop, which is consistent with the almost similar diameters between the annular die and the final bottle. **So, a little bi-dimensional stretching was formed during air blowing inside the parison.**

5.1.3. Summary of the morphology stability study after extrusion blow molding

We have seen that a skin/core effect was observed after extrusion blow molding. If the external regions are more stretched due to the process, core region seems to be more representative of blend morphology without additional stretching. Moreover, the position along the bottle can influence the morphology. In fact, additional stretching was observed at the top and at the bottom of the bottle due to too small melt strength and to the mold closing respectively.

Thus, in order to summarize the morphologies obtained after extrusion blow molding without taking into account additional stretching, the morphologies of core region in medium position parallel to the parison drop ($M‖$) are presented in Figure IV-15 and compared to the morphologies in the pellets obtained after extrusion, morphologies after static annealing and morphologies after controlled shear at 200s^{-1} (order of magnitude of shear rate applied during the extrusion blow molding process).

a)

	Blend 1 (high compatibilizer %)	Blend 2 (low compatibilizer %)	Blend 3 (non-compatibilized)
Pellet	2μm	2μm	10μm
After static annealing 15min	2μm	2μm	10μm
After 200s^{-1} controlled shear	2μm	2μm	10μm
Blow molding: M∥ core	2μm	2μm	10μm

184

b)

	Blend 4 (high compatibilizer %)	Blend 5 (low compatibilizer %)	Blend 6 (non-compatibilized)
Pellet	2μm	2μm	10μm
After static annealing 15min	2μm	2μm	10μm
After 200s^{-1} controlled shear	2μm	2μm	10μm
Blow molding: M∥ core	2μm	2μm	10μm
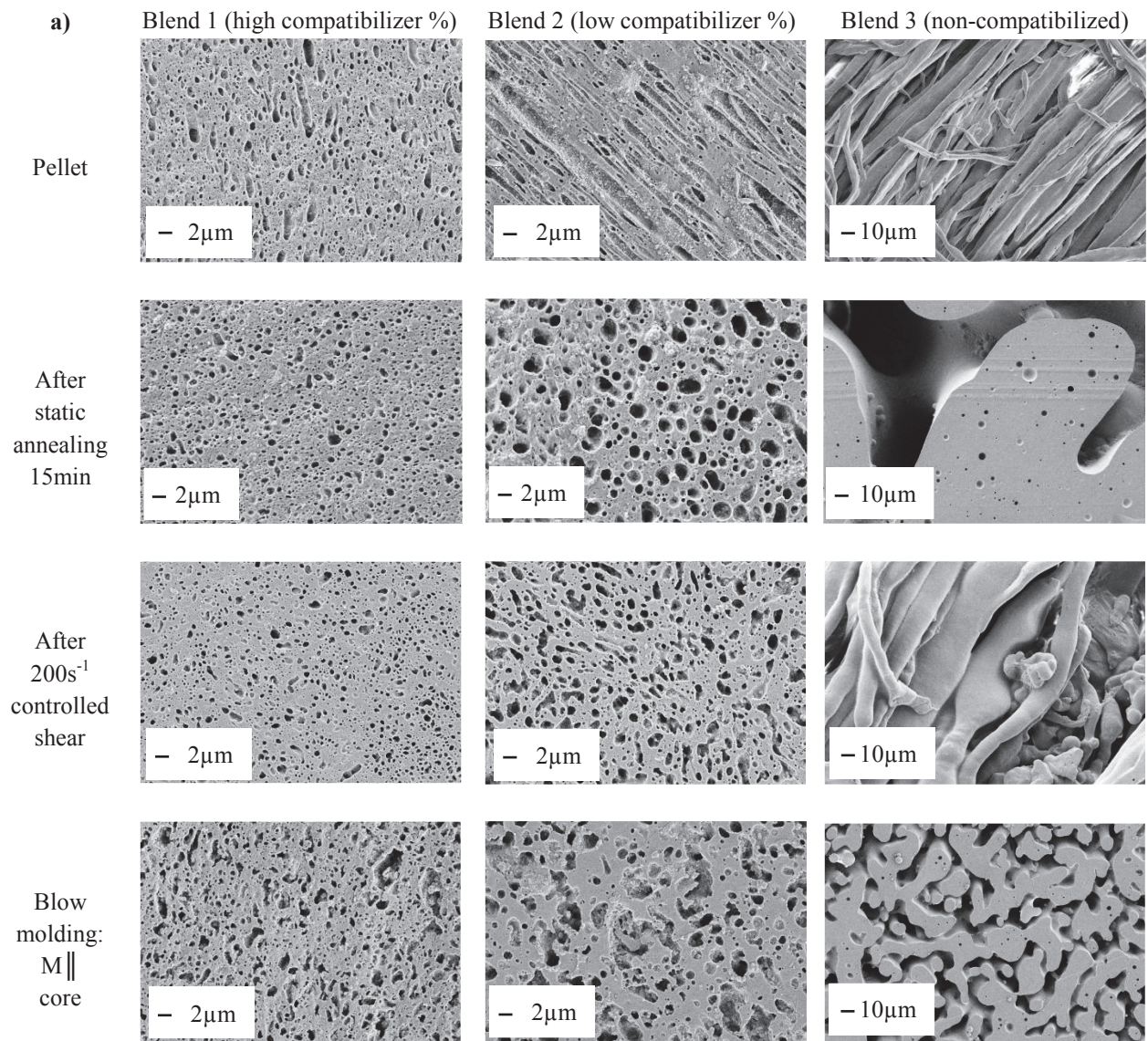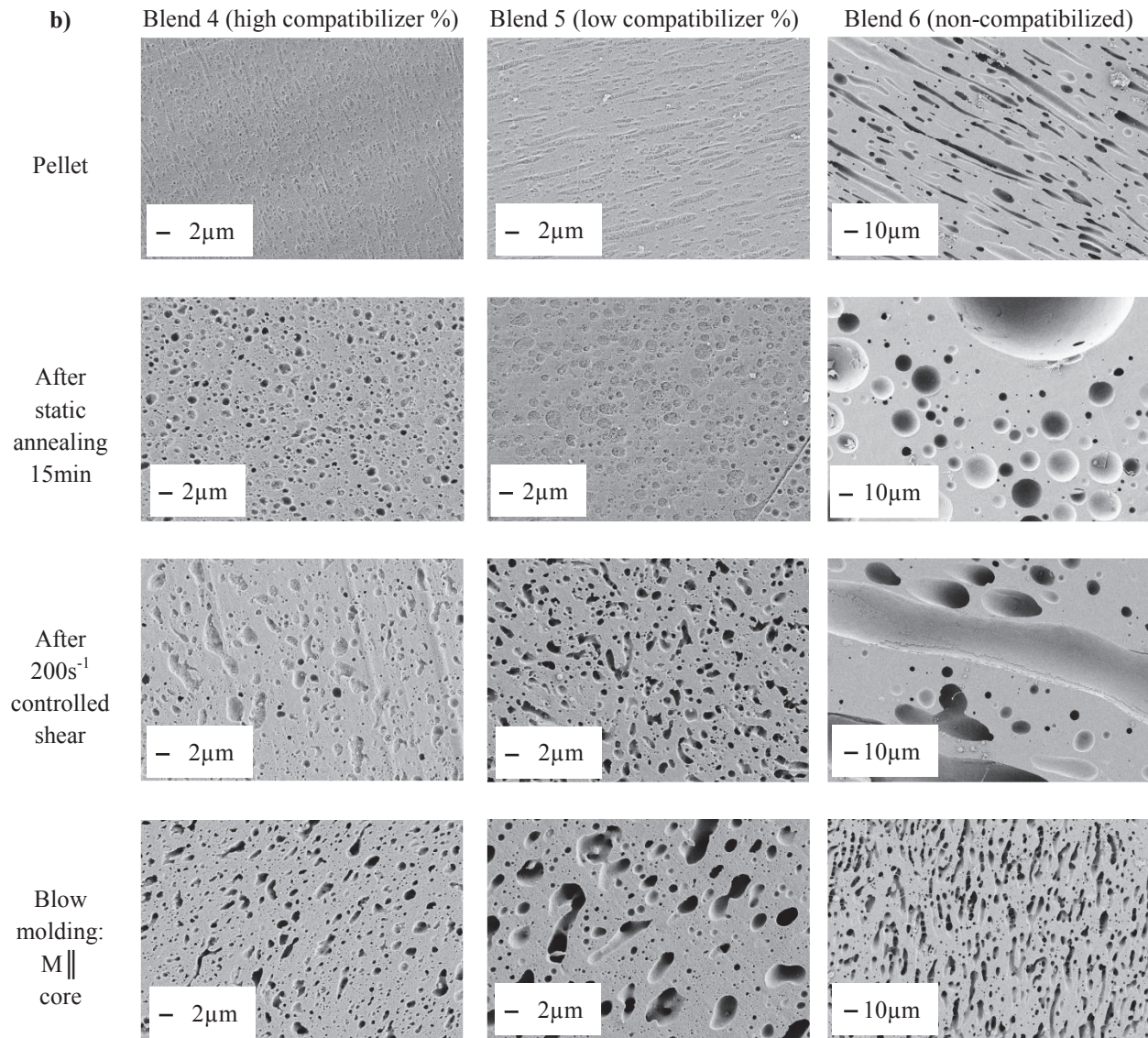
Figure IV-15: SEM micrographs of a) Series 45 (PA6 etched) b) Series 60 (PE phase etched), in pellets after extrusion, after static annealing during 15min, after controlled shear at 200s^{-1} and after extrusion blow molding ($M\parallel$ position, core region).

To conclude on the stability of the morphologies after extrusion blow molding, two cases are proposed:

- **Compatibilized blends** (1, 2, 4 and 5):

    - The morphology observed after extrusion blow molding was quite **similar to** one observed **after controlled shear** at 200s^{-1}, with a little coarsening in the case of blends with low amount of comaptibilizer (blends 2 and 5).
    - A **stretching release** was observed in core as compared to pellet morphology.

185

- **Non-compatibilized blends** (2 and 6):

  - Contrary to static annealing, the **stress applied to the blends during extrusion blow molding process limited the coalescence of the domains size in non-compatibilized systems.**
  - The characteristic size of the morphology was smaller after extrusion blow molding than after controlled shear at $200s^{-1}$. In fact, in extrusion blow molding, the polymers were always submitted to shear whereas the controlled shear experiments were preceded by a static annealing of 17 minutes which may lead to coalescence.
  - In blend 3, the morphology observed after extrusion blow molding was co-continuous without any stretching. In blend 6, the morphology was quite the same as in pellet with less stretching.

5.2. Morphologies after injection molding

Another process largely used to produce polymer parts is the injection molding. Stability of the morphologies after this process was also studied. As detailed in *ChapterII section 3.1.2.4 Injection molding page 88*, tensile specimens and plates were prepared by injection molding and the morphologies obtained were compared to the morphologies in pellets obtained after extrusion. This section is divided into two parts:
1) Tensile specimens
2) Plates

5.2.1. Tensile specimens

Tensile specimens were injected and the morphology was observed perpendicularly to injection flow in order to detect any 2D stretching (we assume that there was stretching parallel to the injection flow). Various positions on the tensile specimens were observed. Three injection speeds were tested on few blends in order to determine the influence of the shear rate on morphology. Thus, this section is divided into four parts:
1) Skin/core effect
2) Influence of the position
3) Influence of the injection speed
4) Summary of the morphology stability study after injection molding of tensile specimens

5.2.1.1. Skin/core effect

In order to determine if there is a skin/core effect on injected tensile specimens, the morphology was observed as described in Figure IV-16.
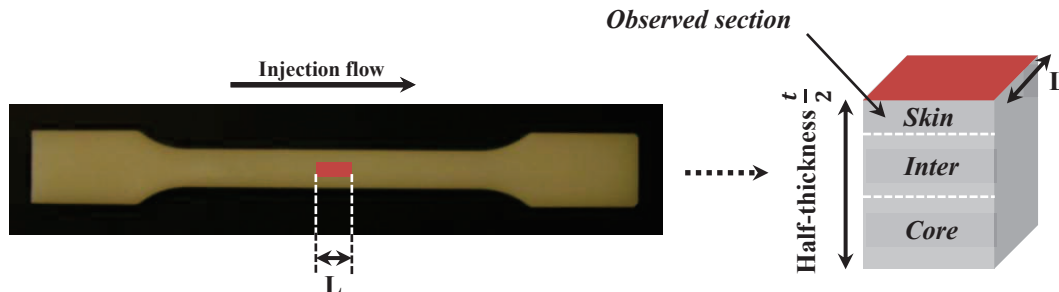

Figure IV-16: Diagram of tensile specimens.

A skin/core effect with three regions was observed for all blends (see Figure IV-17) [19]:

- **Core**: the morphology was **close to the morphology obtained after controlled shear at 2000s^{-1}** (order of magnitude of shear rate applied in injection molding process during the passage through the nozzle) without any stretching perpendicularly to the flow (see Figure IV-18). A coarsening of the characteristic domain size was observed in the case of non-compatibilized blends (blends 3 and 6) and of blends exhibiting low compatibilizer amount (blend 2, as illustrated in Figure IV-18 and blend 5).

- **Inter**: the morphology presented many cracks. To explain the origin of these cracks, a sample of blend 2 was prepared without etching and cracks were not observed in this case. Thus, **the cracks should be due to residual stress release after etching**. Differences of crystallization temperatures between PA6 and PE phase could lead to stresses appearance during the cooling step. Barrel buckling also proved the existence of these internal stresses.

- **Skin** (~100µm thick): in compatibilized blends, the morphology exhibited a smaller characteristic domain size than in core region and was more stretched perpendicularly to the flow. In non-compatibilized blends, the skin region was more difficult to distinguish.

We cannot conclude on stretching in the main flow direction because the injected samples were observed only perpendicularly to the flow, contrary to controlled shear experiment and pellet.

Figure IV-17 and Figure IV-18 show an example of the morphologies obtained for Blend 2 of series 45 with the low amount of compatibilizer (sufficient to stabilize the size of the morphology according to static annealing).

Core	Inter	Skin
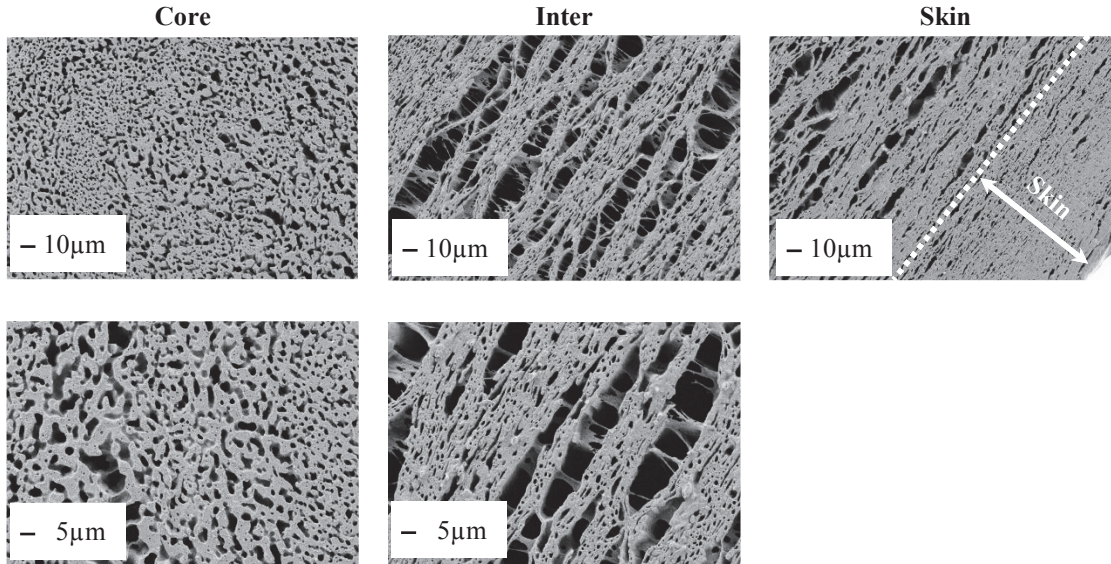
Figure IV-17: SEM micrographs of skin/inter/core regions in Blend 2 (PA6 etched) of injected tensile specimens (medium position, injection speed 88mm.s^{-1}).

Pellet	After controlled shear 2000s^{-1}	Core region (injection molding)
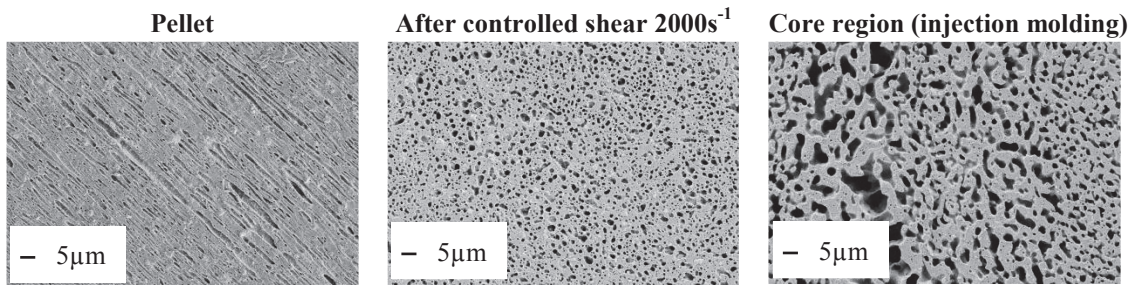
Figure IV-18: SEM micrographs x1000 of Blend 2 (PA6 etched) in the pellets obtained after extrusion, after controlled shear at 2000s^{-1} and after injection molding in core region.

When it is not specified, the morphologies obtained in core region are used in what follows.

5.2.1.2. Influence of the position

Blend's morphology in several positions along the tensile specimen was characterized as illustrated in Figure IV-19 in order to determine if there is an influence on the morphology.

Figure IV-19: Tensile specimens' positions used for morphology observations in SEM.

The influence of the position on morphology was studied on **Blend 2** of series 45 with the low amount of compatibilizer, sufficient to stabilize the size of the morphology according to static annealing.

The morphologies obtained after injection molding (injection speed 88mm.s^{-1}) are summarized in Figure IV-20. As skin regions (~100µm thick) were always similar, only, core and intermediate regions morphologies are described.
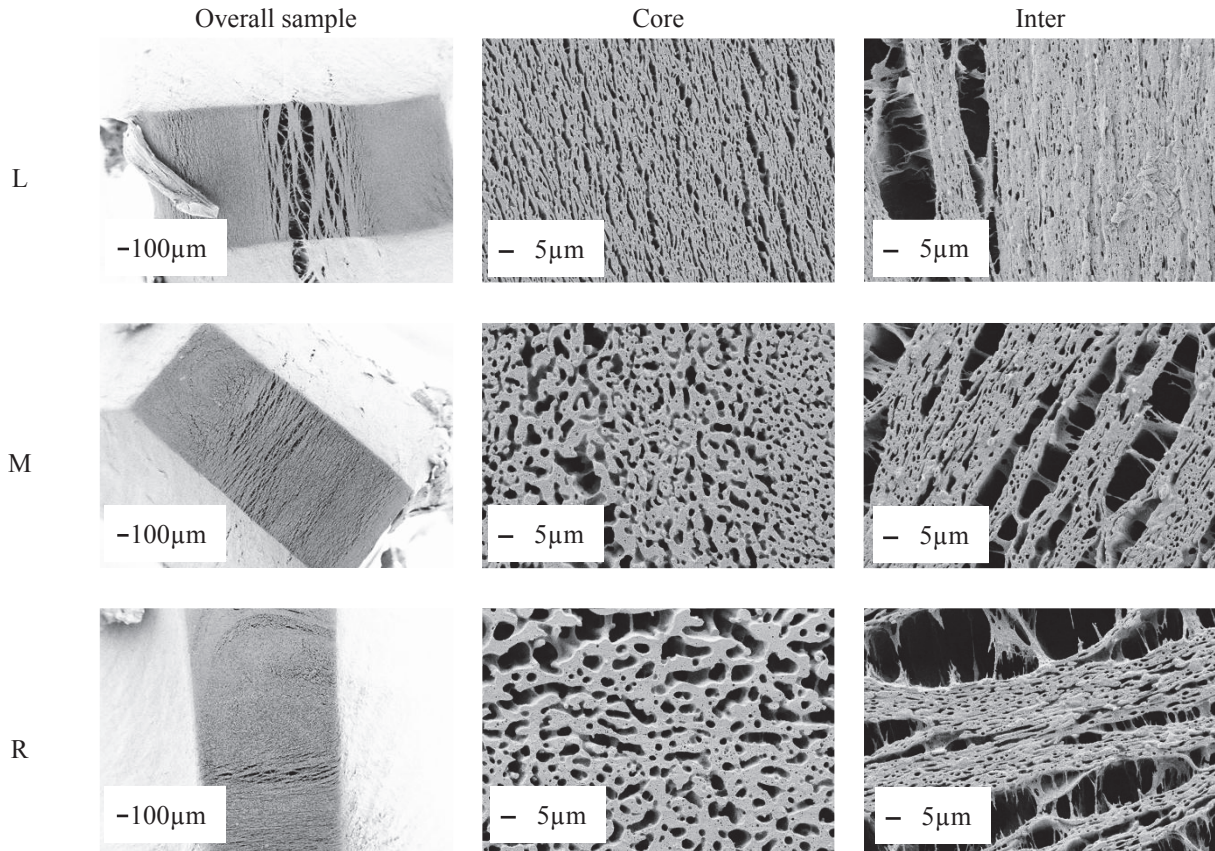
Figure IV-20: SEM micrographs of core and inter regions of Blend 2 (PA6 etched) for the three positions along the tensile specimen.

So, the morphologies obtained in medium (M) and right (R) positions are quite similar.

At the left side of the tensile specimen, the closest from the injection point **(position L), the morphology in core region was finer and more stretched perpendicularly to the flow. Moreover, inter region exhibited much more cracks than in medium and right positions (M and R).**

We have seen that cracks were due to internal stresses release during etching. Concerning the origin of these cracks:

1) As already mentioned, a hypothesis for the apparition of stresses was the difference of the crystallization temperatures between PA6 and PE phase.

2) Here, there were much more cracks at the beginning of the injection flow; so stresses should be larger. During injection molding, there is a fountain flow inside the mold as schematized in Figure IV-21 [19]. Thus, in left position (L), the back flow from the fountain flow was larger than in medium and right positions (M and R) which should cause more internal stresses.
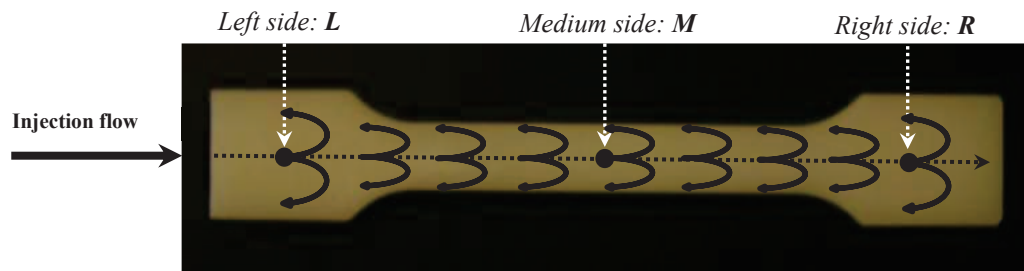
Figure IV-21: Fountain flow in injected tensile specimens.
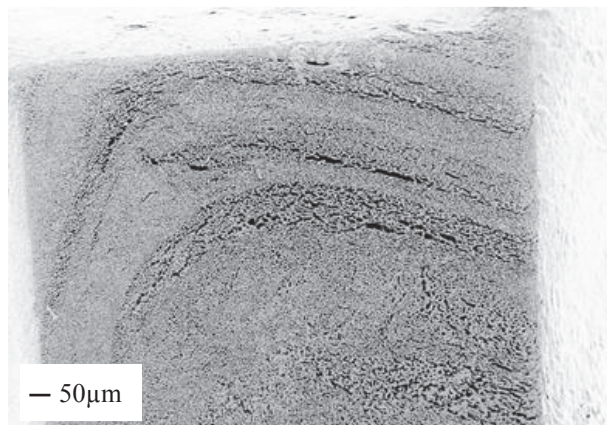
Figure IV-22: SEM micrograph of the fountain flow in core region, right position of Blend 2 (PA6 etched).

5.2.1.3. Influence of the injection speed

The influence of the injection speed was studied on two blends of series 45:
- **Blend 2** with the low amount of compatibilizer, sufficient to stabilize the size of the morphology according to static annealing
- **Blend 3** without any compatibilizer

The injection speeds tested are:
- 15% of the maximum speed: 26mm.s^{-1}: *V15*
- 50% of the maximum speed: 88mm.s^{-1}: *V50*
- 85% of the maximum speed: 149mm.s^{-1}: *V85*

The morphologies obtained in core region of medium position *M* are summarized in Figure IV-23.

Blend 2 (low compatibilizer %)   Blend 3 (non-compatibilized)
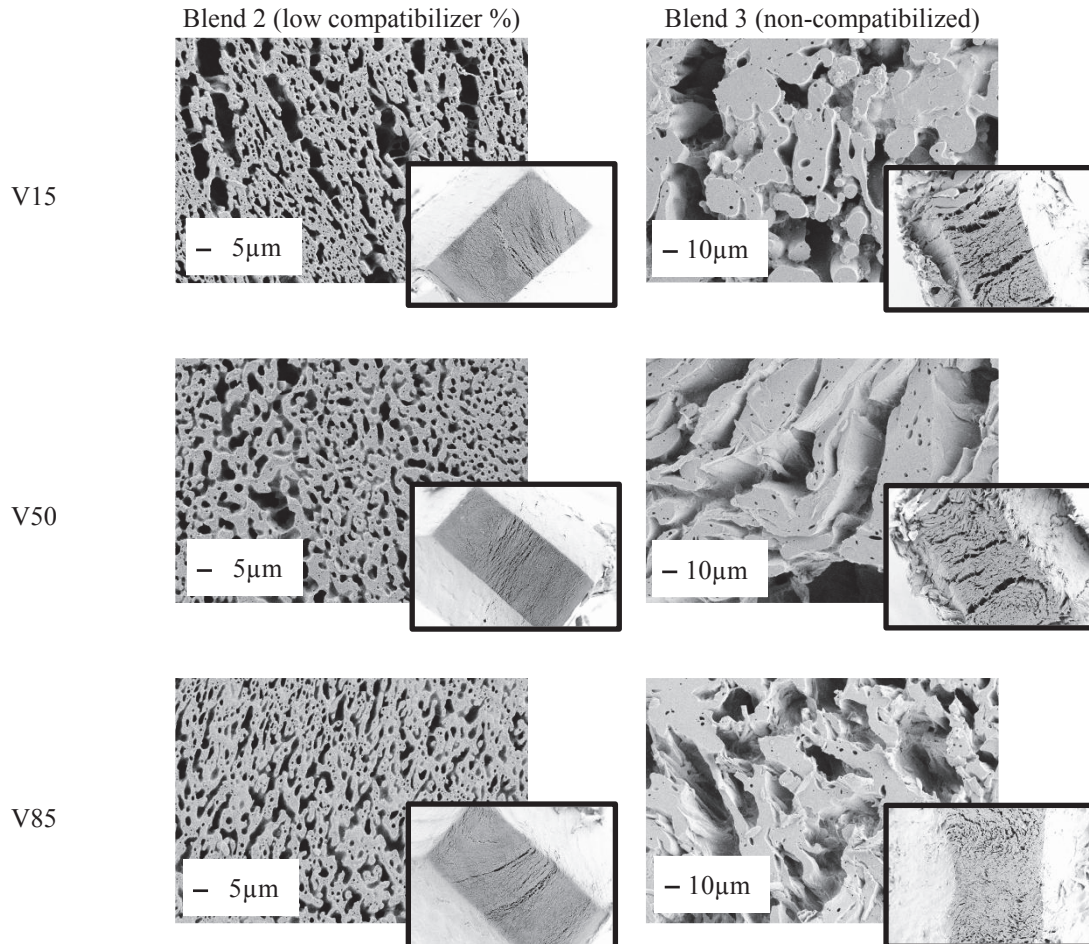
Figure IV-23: SEM micrographs of Blends 2 and 3 (PA6 etched) in core region, position *M* at various injection speeds. The small micrographs all exhibit the same scale: ⎯ 500µm.

So, **no significant influence of the injection speed between V50 and V85 on the morphology was observed**. However, in the case of low injection speed (*V15*), the morphology of blend 2 seems to be more heterogeneous with some cracks even in core region. Thus, at low injection speed, cracks may be more distributed along the thickness, which may be due to less defined injection flow.

5.2.1.4. Summary of the morphology stability study after injection molding of tensile specimens

The SEM observations were performed perpendicularly to the injection flow.

We have seen that a skin/core effect was observed after injection molding of tensile specimens. External regions were more stretched perpendicularly to the flow and finer, intermediate region exhibited cracks due to internal stress release after etching. So, it seems that the core region were the most representative of blend morphology without cracks and additional stretching. Moreover, depending on the position along the tensile specimen and on the injection speed, the distribution of cracks due to residual stresses release after etching was different. This may lead to different final properties.

Thus, in order to summarize the characteristic sizes of the morphologies obtained after injection molding of tensile specimens, the morphologies of core region in medium position (M) are presented and compared to the morphologies in pellets obtained after extrusion, morphologies after static annealing and morphologies after controlled shear at $2000s^{-1}$ (order of magnitude of shear rate applied during injection molding process). The results are summarized in Figure IV-24.

a)

	Blend 1 (high compatibilizer %)	Blend 2 (low compatibilizer %)	Blend 3 (non-compatibilized)
Pellet			
After static annealing 15min			
After $2000s^{-1}$ controlled shear			
Tensile specimen: M core			

193

b)

	Blend 4 (high compatibilizer %)	Blend 5 (low compatibilizer %)	Blend 6 (non-compatibilized)
Pellet	2µm	2µm	10µm
After static annealing 15min	2µm	2µm	10µm
After 2000s^{-1} controlled shear	2µm	2µm	10µm
Tensile specimen: M core	2µm	2µm	10µm

Figure IV-24: SEM micrographs of a) Series 45 (PA6 etched) b) Series 60 (PE phase etched), in the pellets obtained after extrusion, after static annealing during 15min, after controlled shear at 2000s^{-1} and in injected tensile specimens (M position, core region).

To conclude on the stability of the morphologies after injection molding, two cases are proposed:

- **Compatibilized blends** (1, 2, 4 and 5):

 The morphology observed after injection molding was quite **similar to** one observed **after controlled shear** at 2000s^{-1}, with coarsening in case of blends with low amount of compatibilizer (blends 2 and 5).

- **Non-compatibilized blends** (3 and 6):

  - Like in extrusion blow molding, the **stress applied to the blends during injection molding process of tensile specimens limited the coalescence of the domains size in non-compatibilized blends.**

  - The characteristic size of the morphology was a little smaller after injection molding than after controlled shear at $2000s^{-1}$. In fact, in injection molding, the polymers were always submitted to shear whereas the controlled shear experiments were preceded by a static annealing of 17 minutes which may lead to coalescence.

Note that no conclusions can be given about stretching differences between pellet and injected tensile specimens. In fact, contrary to pellets and to samples after controlled shear, injected tensile specimens were observed perpendicularly to the injection flow.

5.2.2. Plates

Plates of 0.8mm thickness were also injected. This section is divided into three parts:
1) Skin/Core effect
2) Stretching: Observations parallel and perpendicular to the injection flow
3) Summary of the morphology stability study after injection molding of plates

5.2.2.1. Skin/Core effect

In order to determine if there is a skin/core effect on injected plates, the morphology was observed parallel to the flow as described in Figure IV-25.
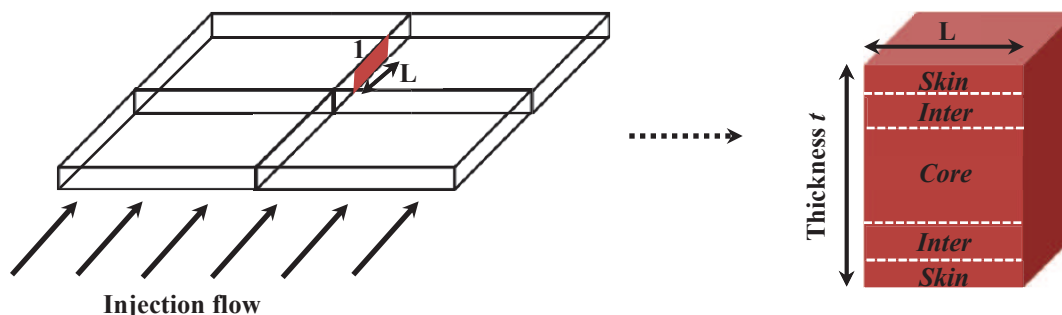
Figure IV-25: Diagram of injected plates.

Like in tensile specimens, **a skin/core effect with three regions** (along the plate half-thickness) **was observed for all blends** (see Figure IV-26):

- **Core:** the morphology was close to the morphology observed in pellet (stretched in the flow direction) (see Figure IV-27).

- **Inter:** the morphology was stretched a lot and presented many cracks. Like in tensile specimens, these cracks would be due to internal stress release after etching.

- **Skin** (~100μm thick): in compatibilized blends, the morphology exhibited a very smaller characteristic domain size and was a little more stretched than in core region. In non-compatibilized blends, the skin region was more difficult to distinguish.

An example of the morphologies obtained for Blend 2 of series 45 with low amount of comaptibilizer (sufficient to stabilize the size of the morphology according to static annealing) is presented in Figure IV-26 and Figure IV-27.
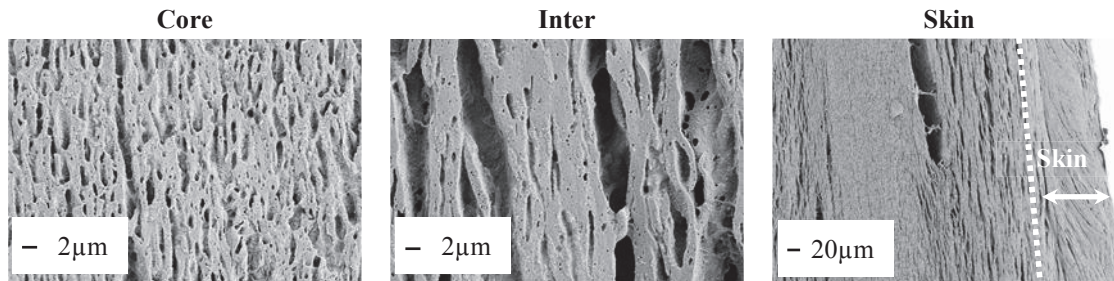
Figure IV-26: SEM micrographs of Blend 2 (PA6 etched) after injection molding of plates: skin/inter/core regions parallel to the flow.
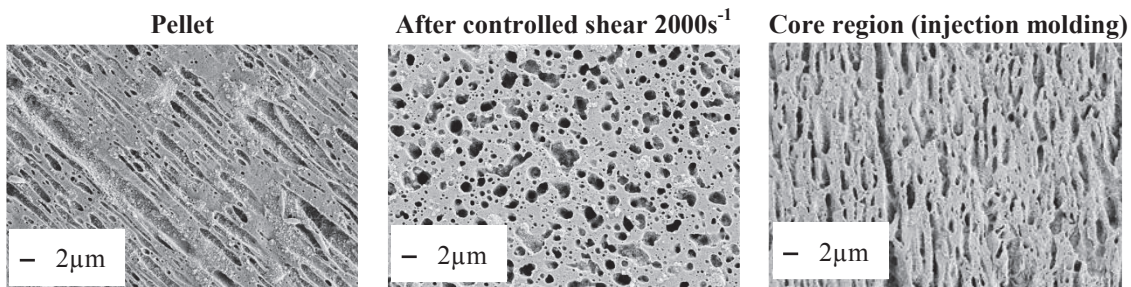
Figure IV-27: SEM micrographs x2500 of Blend 2 (PA6 etched) in the pellets obtained after extrusion, after controlled shear at 2000s^{-1} and after injection molding of plates parallel to the flow in core region.

Only core regions are represented in what follows when it is not specified.

5.2.2.2. Stretching: Observations parallel and perpendicular to the injection flow

Contrary to the injection of tensile specimens, for plates, the polymers were injected over all plate's width. Thus, there was an injection layer which could lead to stretching in two dimensions. In order to determine if there is 2D stretching, morphology was observed parallel ($\parallel$) and perpendicular ($\perp$) to the injection flow as schematized in Figure IV-28.
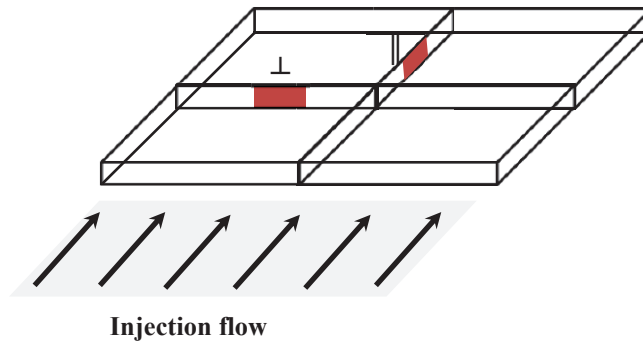
Injection flow

Figure IV-28: Plates' positions observed in SEM to determine if there is 2D stretching.

Morphologies in both positions (parallel and perpendicular to the injection flow) were observed for all blends. A representative example of the morphologies obtained for Blend 2 is presented in Figure IV-29.
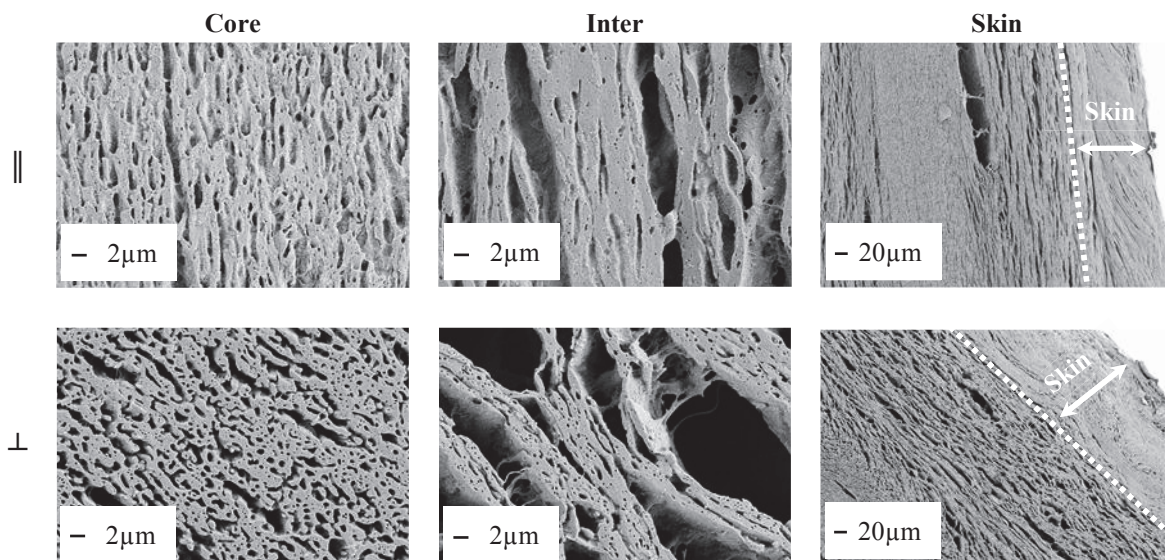
Figure IV-29: SEM micrographs of Blend 2 (PA6 etched) parallel ($\parallel$) and perpendicular ($\perp$) to the injection flow.

As it can be seen in Figure IV-29:

- **In core region, the morphologies were quite similar in both directions. However, as we could expect, a larger stretching was observed parallel to injection flow ($\parallel$).**

- **In inter and skin regions, there was a 2D stretching and the morphology consisted of PA6 platelets.**

5.2.2.3. Summary of the morphology stability study after injection molding of plates

We have seen that a skin/core effect was observed after injection molding of plates. Skin and intermediate regions were 2D stretched. More precisely, skins exhibited finer domains size and intermediate regions exhibited cracks due to internal stress release after etching (no cracks were observed in sample before etching). As it was explained for injected tensile specimens, the internal stresses would be due to the difference of crystallization temperatures between PA6 and PE phase and to the fountain flow occurring in injection molding. So, it seems that the core regions were the most representative of blend morphology without cracks or additional stretching.

Thus, to summarize the morphologies obtained after injection molding of plates, the morphologies of core region parallel and perpendicular to the injection flow are presented and compared to the morphologies in pellets obtained after extrusion, morphologies after static annealing and morphologies after controlled shear at $2000s^{-1}$ (order of magnitude of shear rate applied during injection molding process). The results are summarized in Figure IV-30.

	Blend 1 (high compatibilizer %)	Blend 2 (low compatibilizer %)	Blend 3 (non-compatibilized)
Pellet	— 2μm	— 2μm	— 10μm
After static annealing 15min	— 2μm	— 2μm	— 10μm
After $2000s^{-1}$ controlled shear	— 2μm	— 2μm	— 10μm
Injected plates: ‖ core	— 2μm	— 2μm	— 10μm
Injected plates: ⊥ core	— 2μm	— 2μm	— 10μm

a)
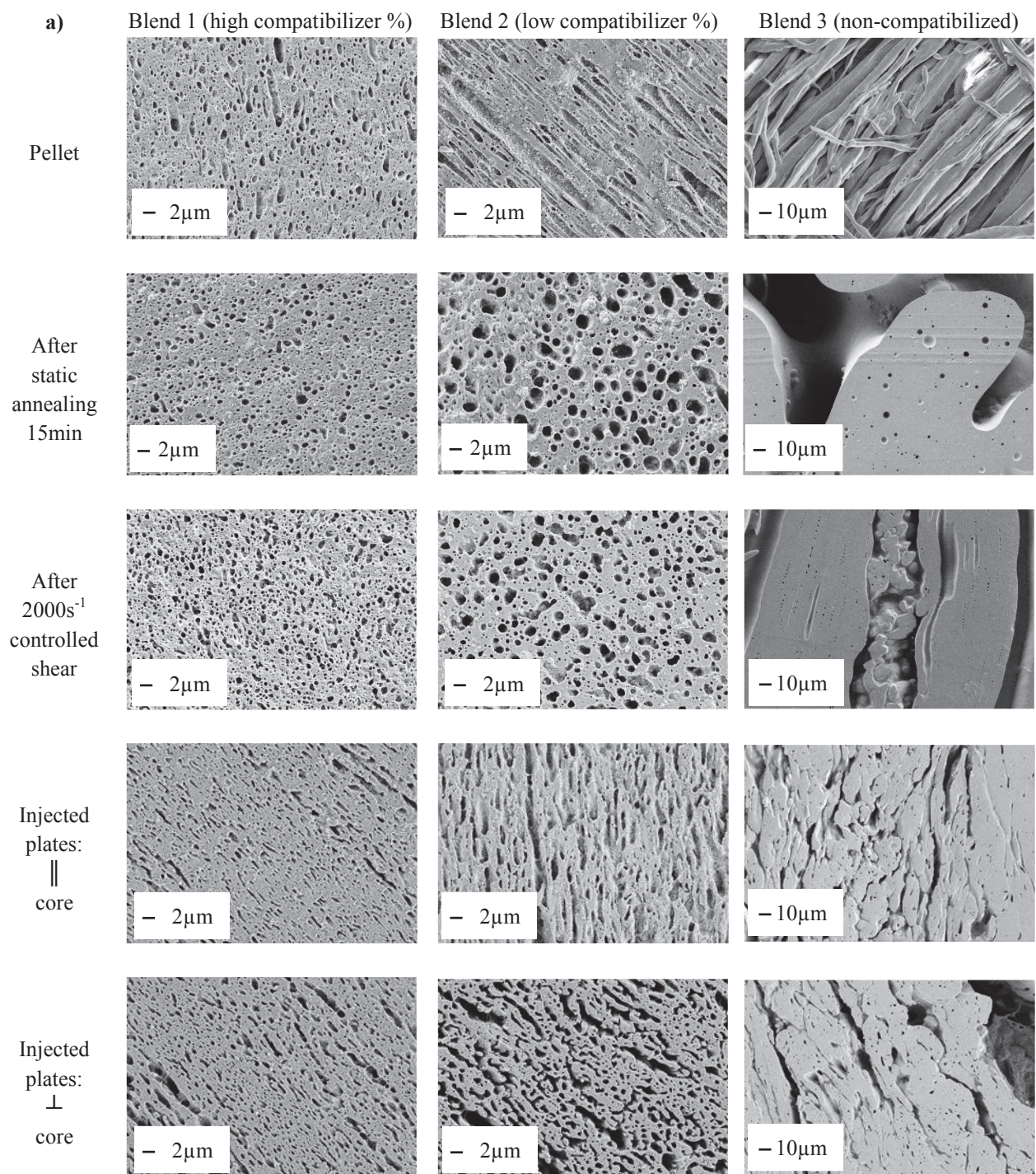
Figure IV-30: SEM micrographs of a) Series 45 (PA6 etched) b) Series 60 (PE phase etched), in pellets obtained after extrusion, after static annealing during 15min, after controlled shear at 2000s⁻¹ and in injected plates.

To conclude on the stability of the morphologies after injection molding of plates, two cases are considered:

- **Compatibilized blends** (1, 2, 4 and 5):

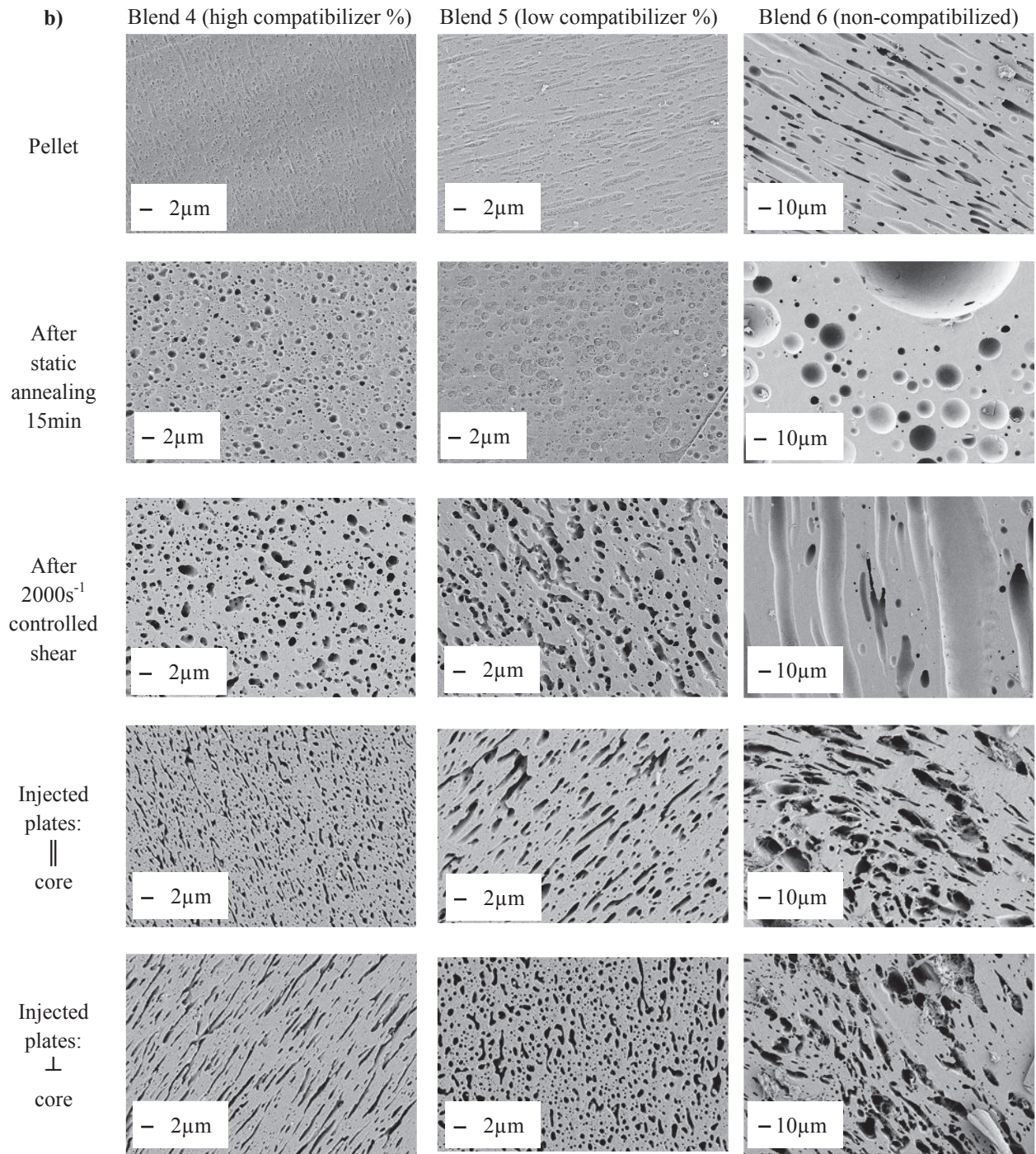 The morphology observed in injected plates was **quite** similar to one observed in **pellet** with the same domains sizes. Due to the layer injection, a **stretching in two dimensions** was obtained. Moreover, like after controlled shear at 2000s^{-1}, the morphology was also **more co-continuous**.

- **Non compatibilized blends** (3 and 6):

  - Like for tensile specimens, the **stress applied during injection molding of plates limited the coalescence of the domains size in non-compatibilized blends**.

  - In blend 3, the morphology observed in plates was co-continuous and a stretching in two dimensions was observed. In blend 6, the morphology was close to pellet's one but more heterogeneous with quite the same domains sizes.

5.3. Comparison between extrusion blow molding and injection molding

The morphology stability has been described after two kinds of processes: extrusion blow molding and injection molding. Two kinds of parts were prepared by injection molding: tensile specimens and plates. Results obtained in both processes are compared in this section.

First of all, differences in term of injection process can be emphasized depending on the molded part:
- For tensile specimens:
  - Polymer injection into the mold was done by a canal (1D).
  - Final barrels were thick: 4mm.
  - The average shear rate into the mold was estimated to be between 5 and 28s^{-1} depending on the injection speed (see *Chapter II section 3.1.2.4 Injection molding page 88*).
- For plates:
  - Polymer injection into the mold was done by a layer (2D).
  - Final plates were thin: 0.8mm.
  - The average shear rate into the mold was estimated to be 520s^{-1} (see *Chapter II section 3.1.2.4 Injection molding page 88*).

In both processes, morphology exhibited a skin/core effect. The differences observed for external layers are summarized in Table IV-3.

Injection molding	Extrusion blow molding
Skin: finer domains size and more stretched than in core	*Skin:* larger domains size and more stretched than in core
Inter: stretching and cracks due to stress release after etching	*Inter:* stretching

Table IV-3: Comparison between morphologies obtained in extrusion blow molding and in injection molding.

The stretching observed in the external layers could lead to interesting barrier properties even in the case of co-continuous morphology in core region.

In core region, differences were observed between tensile specimens and plates in injection molding. The main conclusions are the following:

- **Compatibilized blends:**

For compatibilized blends, the results are summarizes in Table IV-4.

Injection molding		
Tensile barrels	**Plates**	**Extrusion blow molding**
Morphology is more co-continuous than in pellet (like after controlled shear)		
Coarsening in case of low compatibilizer %	No coarsening	Coarsening in case of low compatiblizer %
No stretching perpendicularly to the flow	2D stretching	No stretching

Table IV-4: Summary of core morphologies after injection molding and extrusion blow molding for compatibilized blends.

Thus, by comparing both injected parts, injection of plates seems to limit coarsening and to stretch in two dimensions the morphology. In fact, due to the smaller thickness of the sample (0.8mm vs 4mm for tensile specimens), the shear rate applied to polymers was found to be larger than in tensile specimens. So, the stress applied in core region of plates may be larger which may limit the coarsening. On the other hand, as the injection was done by a layer (2D), 2D stretching was also observed.

- **Non-compatibilized blends:**

The stress applied by both processes limited the coalescence in core region.

6. Conclusion

The final properties of polymer blends depending on morphology, the challenge was to obtain a controlled and stable morphology after a second step processing in a final part. Thus, the stability of the morphologies was studied under various conditions. For better understanding, well controlled conditions were firstly tested:

- Static annealing at 290°C
- Static annealing followed by controlled shear at 200 and 2000s^{-1}, 290°C

Then, real second steps processing were tested:

- Extrusion blow molding
- Injection molding of tensile specimens and plates

The morphologies obtained are summarized on the following ternary diagrams.
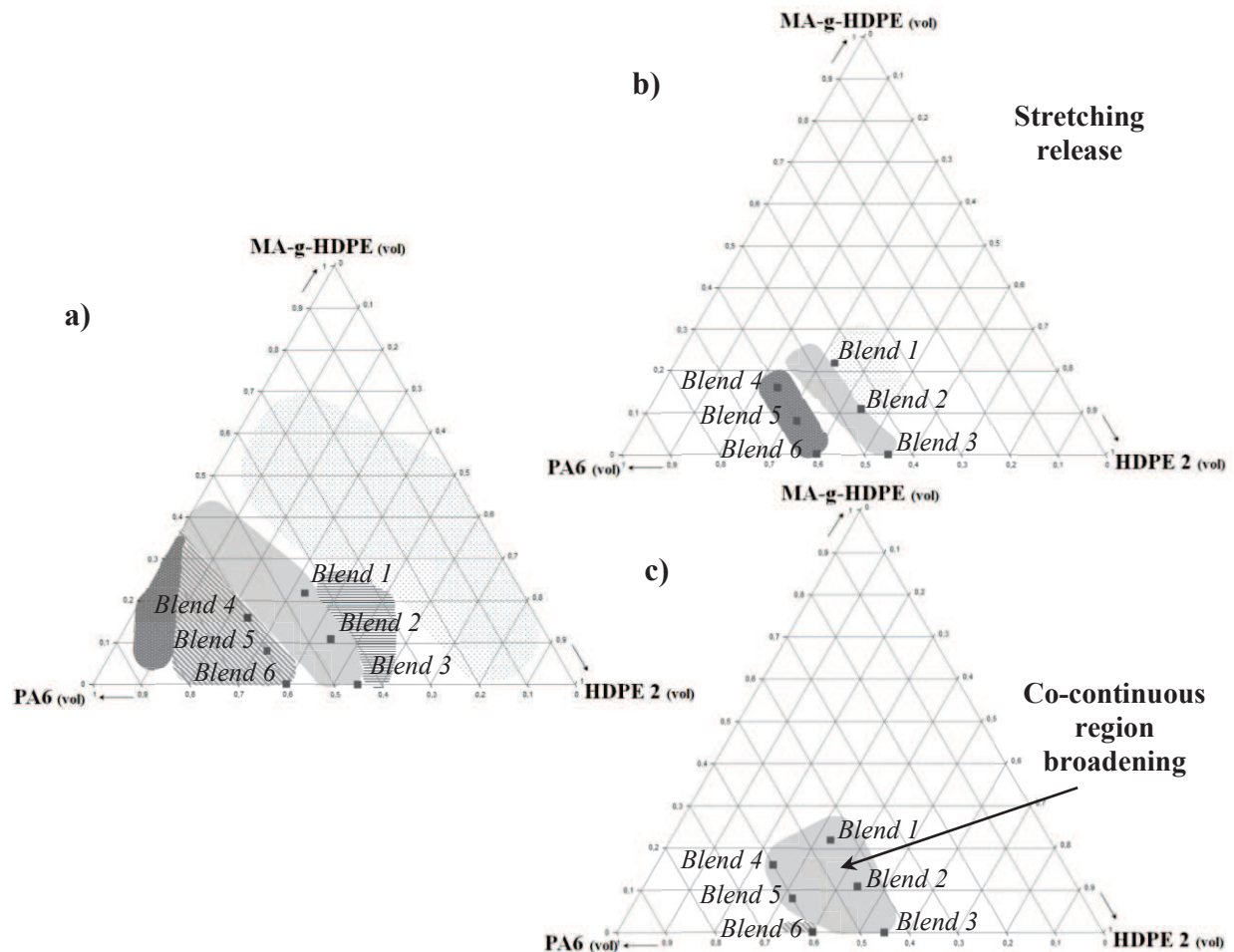

Figure IV-31: Ternary diagrams of morphologies: a) initially in pellet obtained after extrusion, b) after static annealing at 290°C, c) after shear in core region controlled shear, injection molding and extrusion blow molding), using same symbols as in Figure III-4:☐ PA6 dispersion, ☐ PA6 stretched dispersion, ☐ co-continuity, ☐ PE phase stretched dispersion, ☐ PE phase dispersion.

Compared to pellet obtained after extrusion in which all the morphologies were stretched, a stretching release was observed in all blends after static annealing (Figure IV-31 (a) and (b)). This confirms that **stretched dispersions are not steady state morphologies** (see *Chapter III 3.5 Summary of the micrometer scale* morphology *page 125*). Note that the non-compatibilized blend 3, which was at the boundary with the co-continuous region evolved during annealing to co-continuity.

Whatever the shear applied (controlled shear, in extrusion blow molding or in injection molding), the morphology always evolved in the same way and can be represented in a same ternary diagram in Figure IV-31 (c). In pellets (Figure IV-31 (a)), the morphologies were close to boundaries with the co-continuous region. **Under shear, all the morphologies evolved to co-continuity leading to broadening of this region to higher amounts of PA6.**

The results obtained in term of characteristic domain sizes are summarized in the following table.

	Static annealing	Controlled shear	Blow molding (core)	Injection of tensile barrels (core)	Injection of plates (core)
Compatibilized blends	Stability of size	Stability of size	Little coarsening for low amount of compatibilizer	Little coarsening for low amount of compatibilizer	Stability of size
Non-compatibilized blends	Coalescence	Less coalescence than in static	Limitation of coalescence	Limitation of coalescence	Limitation of coalescence

Table IV-5: Summary of domain sizes stability.

To conclude, the graft copolymer PA6-g-HDPE formed in situ stabilizes the size of the morphology whatever the conditions applied, static [15] or under shear. However, a little coarsening was observed with low amount of compatibilizer. In non-compatibilized blends, coalescence was observed after static annealing. Applying shear limits this coalescence. However, even if the domain size does not evolve much, the interface between PA6 and PE phase is still weak which cannot lead to good final properties.

Finally, the effects observed on the kinds of morphologies are probably due to the fact that the blends used were all close to boundaries between regions of different morphologies. In fact, as already emphasized (*Chapter III*), in this particular case, depending on the process parameters, the morphology could evolve to one or the other morphology.

V. Crystallization in the blends

1. Introduction

As the final properties of immiscible polymer blends depend on morphology, the predominant parameters which control the morphology development were determined and the stability of the morphologies was studied under various conditions in the previous chapters. Crystallinity will also play an important role on properties. In fact, high crystallinity amount will lead to higher stiffness and better barrier properties for example.

The crystallization takes place in three steps:
1) Nucleation
2) Crystal growth
3) Crystal perfectionning

The first step of nucleation can be homogeneous in the medium. It can also be heterogeneous, which means that the nuclei are initiated on heterogeneities (impurities, interfaces…). In this last case, the barrier of energy to overcome to initiate the nucleation and thus the crystallization is much lower. In polymers, the crystallization by cooling from the melt is generally initiated by heterogeneities available in the melt: heterogeneous nucleation [20]. In polymer blends, the presence of the second component can disturb the crystallization process of the first one, including nucleation, spherulite growth rate, overall crystallization kinetics, degree of crystallinity and crystalline final morphology. Several factors influence the crystallization including notably blend composition, morphology, phase interaction (for example in presence of reactive compatibilizer), crystallization conditions… [20].

So, this chapter deals with blends crystallization. Temperature sweeps were performed by Differential Scanning Calorimetry (DSC) to study the influence of blends composition and morphology on the transition temperatures (melting and crystallization) and on the crystalline structure of each phase in the blends.

This chapter is divided into two sections, one dedicated to Polyamide and the other dedicated to Polyethylene.

2. Characterization method

To characterize the crystallinity, temperature sweeps were performed by Differential Scanning Calorimetry (DSC). The principle is based on the measure of heat flow difference between a pan containing the sample and an empty pan (reference) during temperature sweeps. All phenomena consuming (endothermic) or releasing (exothermic) heat are detected and measured: melting, crystallization, glass transition… To prepare the samples, approximately 10mg of pellet's sections were cut and placed into an Aluminum non-hermetic pan. The thermal treatment applied under a nitrogen flow is presented in Figure V-1. To carry out these experiments, the equipment used was a *DSC TA Q2000*.
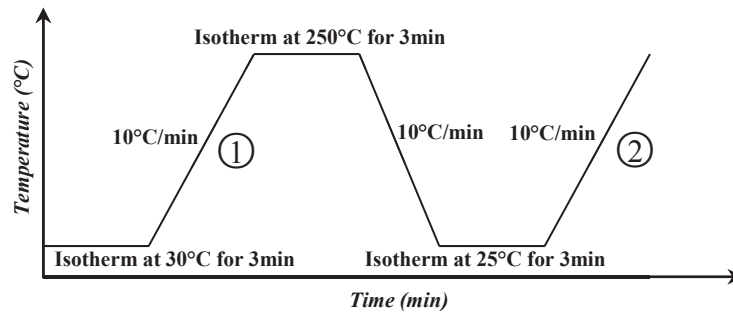
Figure V-1: Thermal treatment applied in DSC for temperature sweep.

The phenomena observed during the first heating ramp (①) depend on the thermal history of the sample and thus, on process conditions used. So, an isothermal plateau at 250°C, above the melting temperatures of both HDPE and PA6 was applied during three minutes in order to eliminate the thermal history of the samples [116,117]. Then, a cooling ramp at 10°C/min was performed in all the samples to measure crystallization temperatures T_c in the same conditions. Finally, the second heating ramp (②) allows measuring the intrinsic melting temperatures T_m and enthalpies ΔH_m, independent on the thermal history.

In our case, the melting temperatures T_m were measured during the second heating ramp (②). The melting enthalpies ΔH_m obtained by integrating the melting peak during the second heating ramp (②) were used to calculate the crystallinity amount χ_c (in %) of each phase:

$$\chi_c = \frac{\Delta H_m}{\Delta H_\infty . \phi_{phase}(wt)} \times 100$$

Eq. V-1

ΔH_∞ is defined as the reference melting enthalpy of the theoretical polymer "100% crystalline". In the case of HDPE, the crystalline structure is orthorhombic, T_m=*137-145°C* [91] and the value of ΔH_∞ is 293J.g^{-1} [118,119].

For PA6, two polymorphic forms α and γ can be observed [86,87]:

- α phase: generally considered to be the most thermodynamically stable phase as it is obtained by slow cooling [88]. It has a monoclinic crystalline structure. $T_m=223°C$, $\Delta H_\infty(\alpha) = 191 J.g^{-1}$ [119,120].

- γ phase: generally obtained by fast cooling. It has a pseudo-hexagonal crystalline structure [88]. $T_m=214°C$, $\Delta H_\infty(\gamma) = 175 J.g^{-1}$ [119,120].

The transition temperatures were measured at peak maximum.

3. Polyamide 6 crystallization

The crystallization of PA6 is described in this section. Bulk PA6 crystallinity and the influence of process are first described in order to define the most relevant reference. Then, the influence of PA6/PE phase blends morphology on PA6 crystallization is discussed.

3.1. Bulk PA6

3.1.1. Typical thermogram obtained

An example of typical thermogram obtained for bulk PA6 in classical DSC during cooling ramp and second heating ramp is shown in Figure V-2.
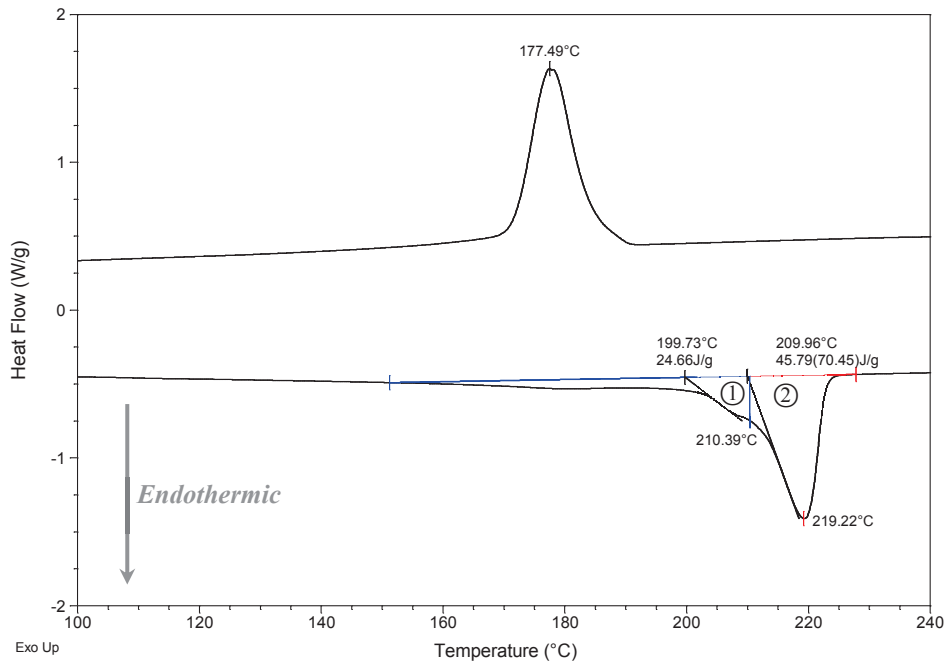

Figure V-2: Typical thermogram (cooling ramp and second heating ramp: 10°C.min⁻¹) obtained for bulk PA6 in classical DSC.

According to Figure V-2, the crystallization temperature of neat PA6 is T_c~177°C.
Then, PA6 melting exhibits two peaks whose T_m are a little lower than in the literature:
- Peak ① which corresponds to γ phase: T_m~210°C
- Peak ② which corresponds to α phase: T_m~219°C

To determine the crystallinity amount of each crystalline phase, a vertical drop was used to separate the overall melting peak area into two areas as illustrated in Figure V-2. According to the PhD work of M. Sabard, this method was more consistent than deconvolution [88].

Thus, the calculated crystallinity amounts of both phases, according to the thermogram in Figure V-2 are:
- χ_c(γ phase)=14%
- χ_c (α phase)=24%
- χ_c (total)=38%

In order to determine if there is crystal perfectioning in bulk PA6 during heating (exotherm in the same time as melting endotherm), Modulated Differential Scanning Calorimetry was performed (MDSC). The advantage of this technique is to divide the total heat flow obtained in classical DSC into two components: calorific capacity (reversing) and kinetic capacity (nonreversing):

$$\frac{dH}{dt} = \underbrace{C_p \frac{dT}{dt}} + \underbrace{f(T,t)}$$

Eq. V-2

$$Heat\ flow = Reversing\ flow + Non\text{-}reversing\ flow$$

With C_p, the calorific capacity.

Glass transition and often melting are observed in the reversing flow. On the other hand, crystallization is observed in the non-reversing flow (kinetic event).

In our case, we used the mode "heat only" in order to avoid any cooling during oscillations of the modulated temperature as shown in Figure V-3, which seems more judicious to observe eventual crystal perfectioning during heating.
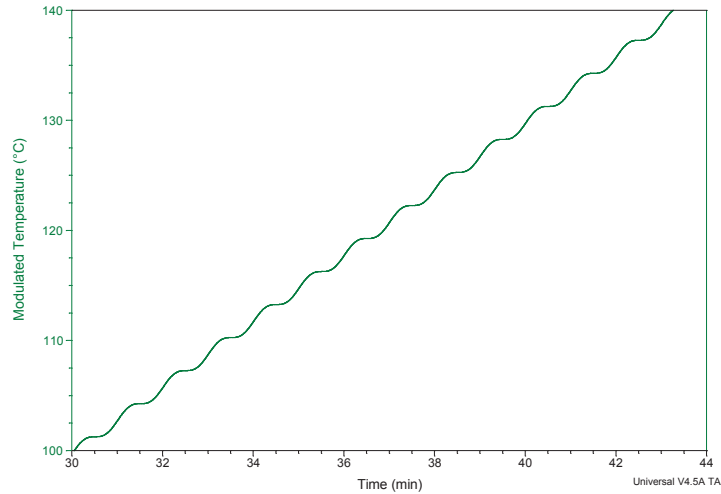
Figure V-3: Modulated temperature versus time for MDSC "heat only".

The period of oscillations (60s) was chosen in order to have several cycles during the transition observed. The heating ramp applied was 3°C/min, slow enough to have a good resolution. Using the "heat only" mode, the oscillations amplitude was defined automatically according to the oscillations period and to the heating ramp, here 0.477°C.

Figure V-4 shows a typical thermogram of the second heating ramp obtained in MDSC for bulk PA6. The full line represents the reversing heat flow and the dashed line, the non-reversing heat flow.
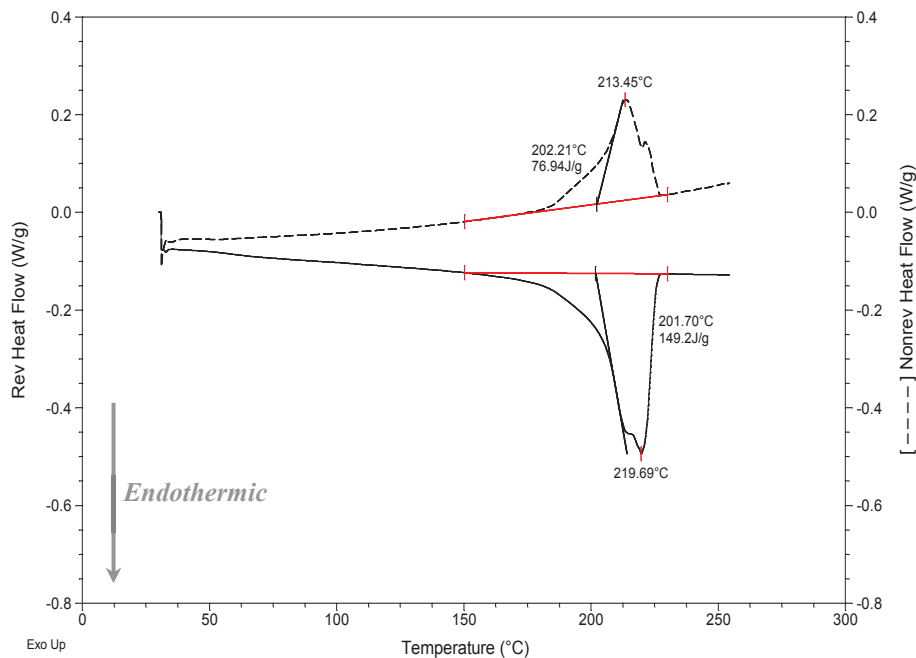
Figure V-4: Typical thermogram (second heating ramp) obtained for bulk PA6 in MDSC. Full line: reversing heat flow, dashed line: non-reversing heat flow.

As in classical DSC, both α and γ phases were observed in the melting peak (endotherm in reversing heat flow signal). In the same time, an exotherm due to crystal perfectioning was observed in the non-reversing heat flow signal. By subtracting the exotherm area to the endotherm area, the melting enthalpy was found to be 72 J.g^{-1} like in classical DSC (70.5 J.g^{-1}), which will lead to the same crystallinity amounts for both crystalline phases. Thus, even if crystal perfectioning was evidenced by MDSC during PA6 melting, as the melting enthalpies measured were similar in both techniques, classical DSC was sufficient to determine the crystallinity amounts. So, only classical DSC was performed on blends, and only classical DSC results are shown in what follows.

3.1.2. Influence of the process

Neat PA6 was extruded in the same conditions as the blends. Both references, PA6 before extrusion and extruded PA6 (extruder D34), are compared in this section. The thermograms obtained for PA6 before and after extrusion in classical DSC during the cooling ramp and the second heating ramp are shown in Figure V-5 and Figure V-6 respectively.

Figure V-5: Thermograms (cooling ramp 10°C/min) obtained for neat PA6 before (full line) and after (dashed line) extrusion.
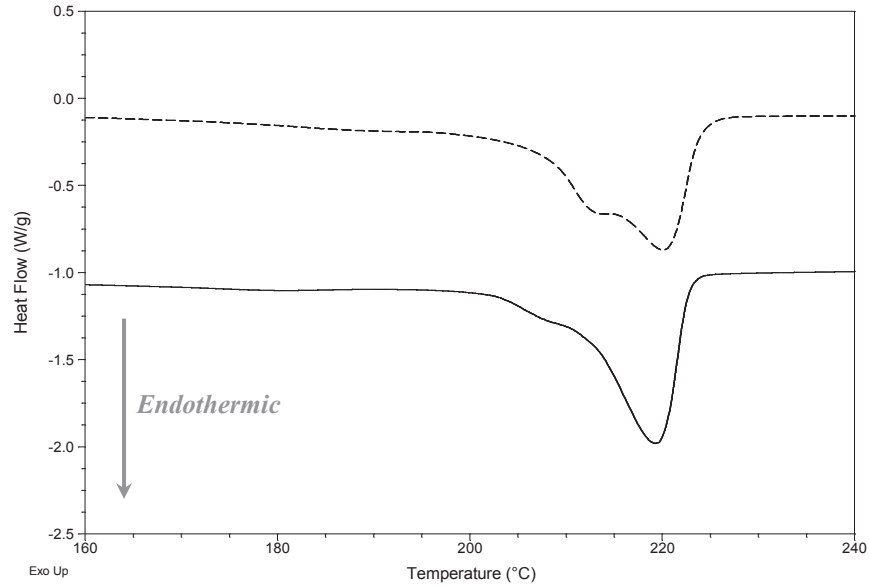
Figure V-6: Thermograms (second heating ramp 10°C/min) of neat PA6 before (full line) and after (dashed line) extrusion.

The following table summarizes the results obtained in both samples.

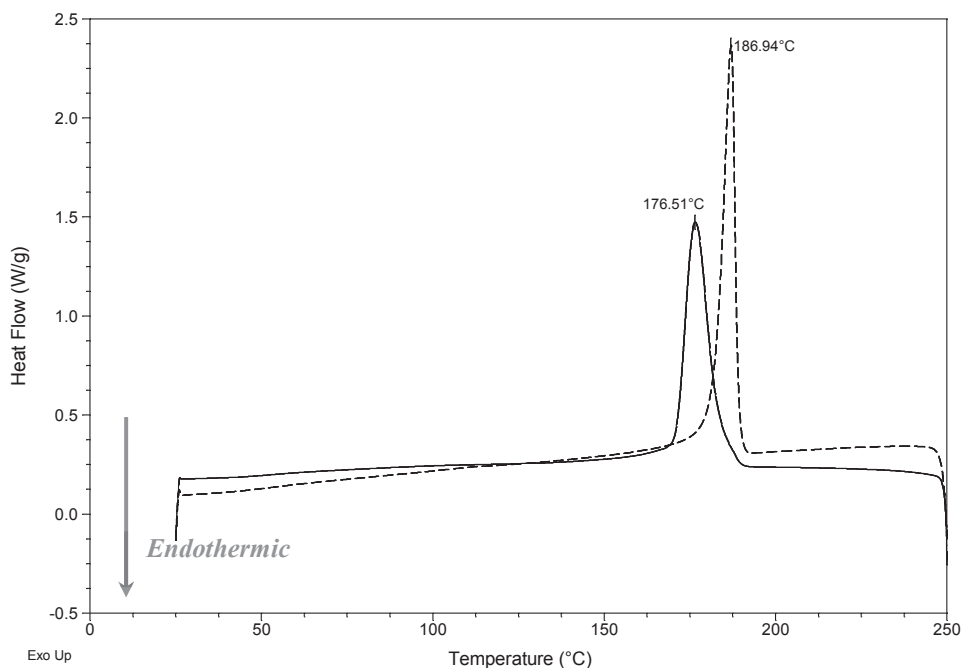|	T_c	$T_m(\alpha)$	$T_m(\gamma)$	$\chi_c(\alpha)$	$\chi_c(\gamma)$	$\chi_c(total)$
Unprocessed PA6	177°C	219°C	210°C	25%	13%	38%
Processed PA6	187°C	220°C	214°C	17%	27%	44%

Table V-1: Crystallization and melting temperatures, and crystallinity amounts of α and γ phases in PA6 before and after extrusion.

PA6 crystallization temperature after extrusion (T_c~187°C) is higher than before extrusion (T_c~177°C). To explain this difference, the extrusion process may bring more impurities in the material, which could facilitate the crystallization of PA6.

The overall crystallinity amount of PA6 is larger after extrusion. This is in agreement with the higher crystallization temperature of processed PA6, probably due to the presence of more impurities which may facilitate the crystallization and thus increase the crystallinity amount.

The melting temperature $T_m(\alpha)$ of PA6 α phase is considered to be the same before and after extrusion. It is difficult to conclude on the influence of extrusion process on the melting temperature $T_m(\gamma)$ of PA6 γ phase because of the bad resolution of the peak, leading to large uncertainties. Then, the ratio γ phase/α phase fraction is higher after extrusion.

Thus, in order to compare materials with the same thermal history, processed PA6 will be used as the reference in the following section dealing with PA6 crystallization in PA6/PE phase blends.

3.2. Blends with PE phase

The influence of morphology on PA6 crystallization (determined from the cooling ramp) and crystallinity amount (determined from the second heating ramp) is presented in this section. Two aspects are analyzed:

1) The influence of the kind of morphology
2) The influence of the morphology size

3.2.1. Influence of the kind of morphology

To study the influence of the kind of morphology on (1) PA6 crystallization temperature, (2) PA6 crystallinity amount and (3) PA6 crystalline phases, compatibilized blends with constant PE phase composition (HDPE/MA-g-HDPE=60/40%$_{vol}$) and various PA6 fractions were used and compared to the processed PA6 reference. These blends follow the dashed line (which corresponds to line *L* in *chapter III*) in Figure V-7. Blends based on HDPEs 1, 2 and 3 were studied.
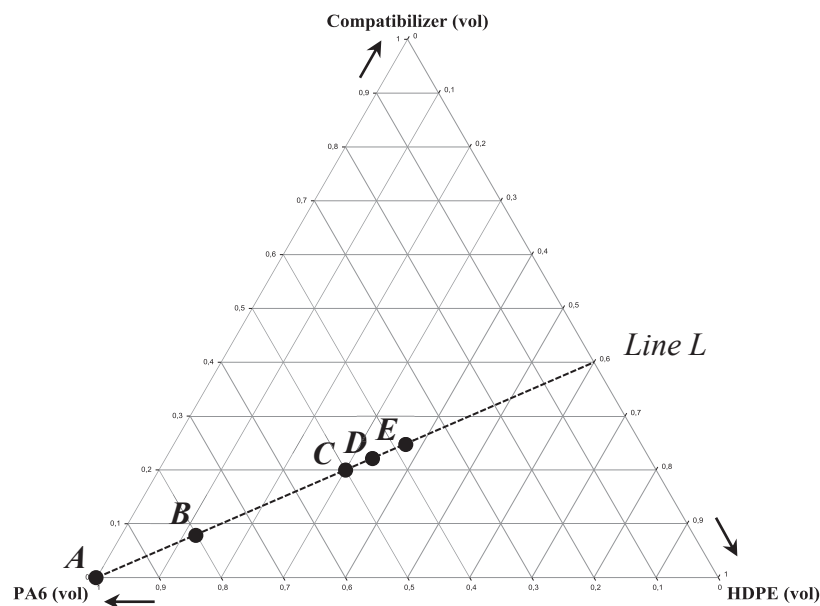
Figure V-7: Blends with constant PE phase composition HDPE/Compatibilizer (60/40%$_{vol}$) used to study the influence of blend morphology on PA6 crystallization. Several blends based on HDPEs 1, 2 and 3 all located on line L were studied. The formulations (*B* to *E* with HDPE 3, processed using the extruder D34) used in Figure V-8 to illustrate the influence of PA6 amount on the crystallization temperature of PA6 are also included.

3.2.1.1. Crystallization temperature

Figure V-8 shows the thermograms (during cooling ramp) for the five systems *A* to *E* reported in Figure V-7, which exhibit different morphologies.
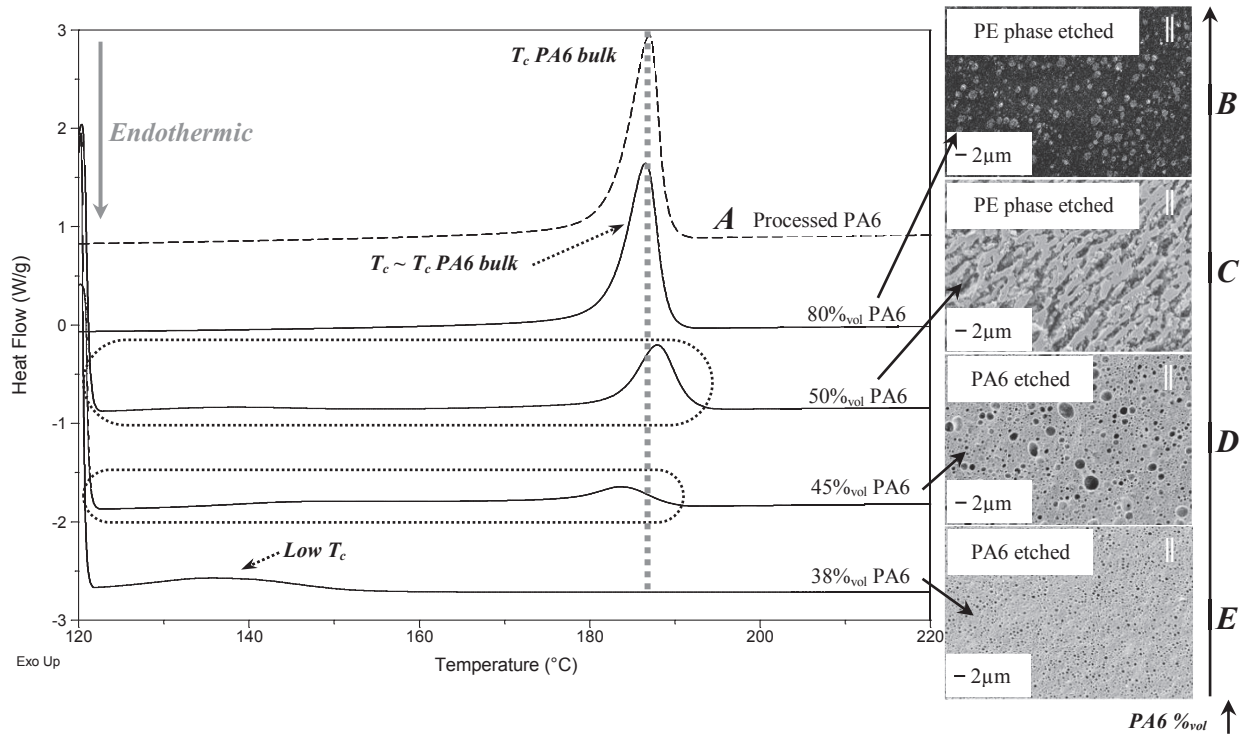
Figure V-8: Crystallization peak(s) of PA6 depending on the PA6 amount in blends *B* to *E* (with HDPE 3) and in the processed PA6 reference (*A*).

To discuss the influence of the morphology on PA6 crystallization, three cases are proposed:

1) <u>Morphologies with continuous PE phase matrix:</u>

In the blend with $38\%_{vol}$ of PA6, the size of dispersed PA6 domains is much smaller than $1\mu m$ (typically $<600nm$) (see Figure V-8 *E*). The crystallization exotherm of PA6 is drastically shifted to lower temperature ($\sim135°C$). This behavior was also observed in literature for PA6 dispersed in polyolefins functionalized with acrylic acid [121].

In the blend with $45\%_{vol}$ of PA6, the size of dispersed PA6 domains ranges from sub-micron scale to droplet diameters of about $2\mu m$ (see Figure V-8 *D*). In this case, the PA6 crystallization is spread over a very large temperatures range. The flattened exotherm at low temperature (between 130 and 170°C) is still present, most probably associated to the smallest PA6 droplets. An exotherm close to the bulk crystallization temperature appears, probably associated to the largest PA6 droplets.

This fractionated crystallization behavior can be explained as follows:

In the case of the dispersed PA6 morphology, the nucleation of PA6 in the droplets is restricted to the volume of the droplet and each droplet will crystallize according to the number and the type of heterogeneities in it [63,122]. The spectrum of undercoolings at which the crystallization steps occur reflects the difference in nucleating activity of the various heterogeneities available in the melt [20]. Thus, when the droplet size decreases below the average distance between nucleating sites leading to a crystallization temperature of 187°C, the probability to have such a nucleus inside all the droplets decreases. The droplets which do not crystallize like in bulk can contain another type of heterogeneous nuclei which become active at lower temperature.

Typically, when the PA6 droplet size becomes smaller than 2μm, the crystallization temperature is a little shifted to a lower temperature (see Figure V-8 *D*). By decreasing more and more the PA6 droplet size, this shift becomes more and more large.

Thus, when the PA6 is dispersed in PE phase matrix, fractionated crystallization was observed when the droplets size becomes fine enough.

2) Co-continuous morphologies:

In the blend with 50%$_{vol}$ of PA6, the morphology is co-continuous (see Figure V-8 *C*). Thus, as PA6 is considered as a matrix, it can crystallize like in bulk. However, a flattened exotherm is still observed down to a temperature close to 120°C.

The presence of these fractionated crystallization peaks are due to the multi-scale morphology. The sub-dispersions of PA6 formed in addition to the micrometer scale co-continuous morphology lead to the confinement of a fraction of the PA6 [63].

3) Morphologies with continuous PA6 matrix:

In the blend with 80%$_{vol}$ of PA6, the morphology is PE phase nodular dispersion in PA6 (see Figure V-8 *B*). In this case, by decreasing the temperature from the melt, the PA6 matrix firstly crystallizes in the presence of a molten dispersed PE phase. Heterogeneous nucleation by heterogeneities (like impurities) can occur as in the bulk.

As PA6 constitutes the matrix, PA6 "domains" are large enough to crystallize like in the bulk: T_c blends ~ T_c bulk.

3.2.1.2. Crystallinity amount

The overall crystallinity amount of PA6 in PA6/PE phase blends is now discussed depending on morphology, by observing the second heating ramp on the thermograms.

Whatever the PE phase (1, 2 or 3), the melting temperatures of PA6 during the second heating ramp were always about 212°C for γ phase and 219°C for α phase, close to T_m in processed PA6 reference (Table V-1). Figure V-9 shows the overall ($\alpha + \gamma$) crystallinity amount of PA6 as a function of PE phase content in the blends (along line *L* in Figure V-7).
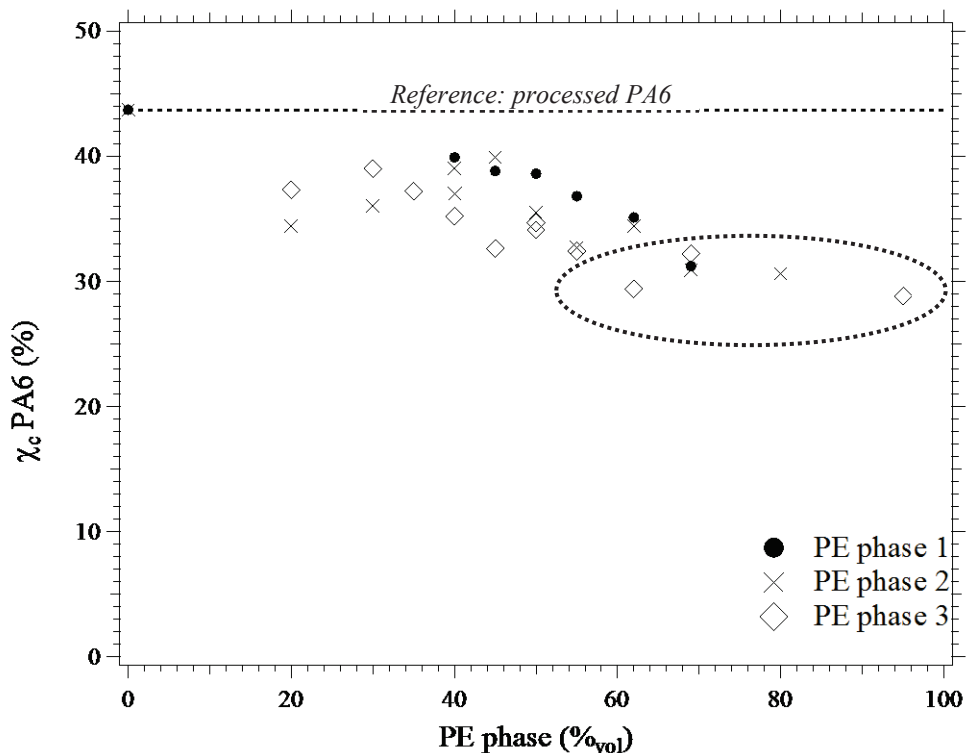
Figure V-9: Overall ($\alpha + \gamma$) crystallinity amount of PA6 χ_c versus PE phase amount in the blends along line *L* (see Figure V-7), processed using the three tools (extruders D34 and D40, batch mini-extruder).

The crystallinity amount of the reference (processed PA6) is 44%. It clearly appears that **blending with PE phase decreases the PA6 crystallinity amount** to a maximum value of about 35%.

The blends encircled in Figure V-9 exhibit smaller PA6 crystallinity (~29%) than the other blends. In fact, in these blends, the morphology is always PA6 dispersed in PE phase with a domain size smaller than 1µm. As described previously, depending on the droplet size, the crystallization may be disturbed by PA6 confinement.

3.2.1.3. Crystalline phases

As some final properties of blends depend on the kind of crystalline phase (α of γ) which is formed [88], it is of great interest to determine how the PE phase can favor one or the other of the PA6 crystalline phases. The fraction of the overall PA6 crystallinity amount which corresponds to γ phase is plotted as a function of the PE phase content in Figure V-10.
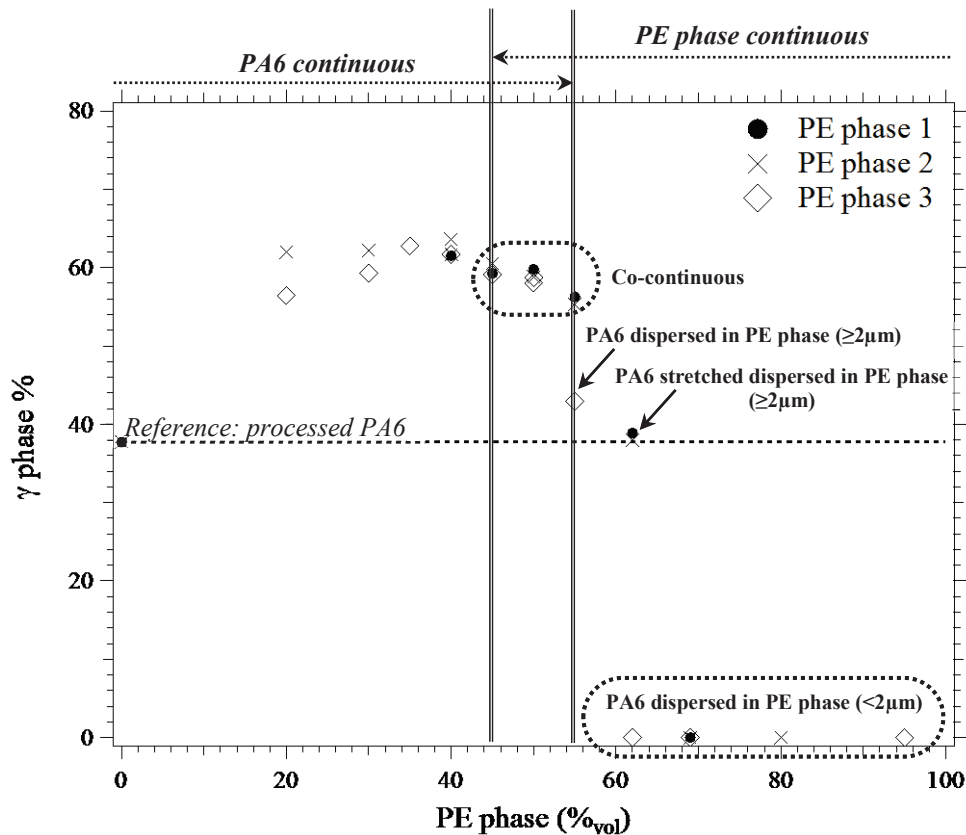
Figure V-10: γ phase fraction in PA6 crystalline phase versus PE phase amount in the blends along line *L* (see Figure V-7), processed using the three tools (extruders D34 and D40, batch mini-extruder).

Two cases are proposed to discuss the results obtained in Figure V-10:

1) Morphologies with continuous PA6 matrix:

In this case, the blends exhibit PE phase dispersion, PE phase stretched dispersion or co-continuous morphologies. The fraction of γ as compared to the overall crystallinity amount of PA6 is always much larger (~60% of the overall PA6 crystal phase) than in the reference processed PA6 (39%) for all the PE phases (1, 2 and 3).

So, the PE phase seems to favor the formation of γ phase in the blends with PA6 continuous (morphologies with PA6 matrix and co-continuity).

216

2) <u>Morphologies with continuous PE phase matrix:</u>

Two typical sizes of morphology are distinguished:

a) *<u>Morphologies with some PA6 domains exhibiting a large size (≥ 2μm):</u>* In this case, the fraction of γ phase is nearly the same (about 40%) as in the reference (processed PA6).

b) *<u>Morphologies with only small domain size of PA6 (<2μm):</u>* In this case, only α phase is obtained.

So, the morphologies with continuous PE phase seem to favor the formation of α phase in the small PA6 droplets (typically <2μm).

3.2.2. Influence of the morphology size

To study more precisely the influence of the morphology size on (1) PA6 crystallization temperature, (2) PA6 crystallinity amount and (3) PA6 crystalline phases, blends with HDPE 3 were used. As already explained, it is a particular case in which the viscosity ratio is always equal to 0.5 (*see Table II-4 in Chapter II*) whatever the volume ratio MA-g-HDPE/HDPE 3 and whatever the shear rate. Moreover, HDPE 3 and MA-g-HDPE exhibit very similar molecular mass distributions (*see Figure II-6 in Chapter II Section 2.5 Materials of the study page 76*). Thus, by comparing blends with same PA6 content and same morphology, **the only changing parameter is the compatibilizer amount, or more precisely the amount of MA moieties.**

Two series of blends with a constant PA6 volume fraction (along lines *N* as described in *Figure III-1 in Chapter III*) were studied, one with PA6 continuous and one with PE phase continuous in order to compare both cases as summarized in Figure V-11:

- *Series 60:* Blends *a* to *e*, processed by extrusion D34: 60%$_{vol}$ of PA6, co-continuous morphology
- *Series 38:* blends *f* and *g*, processed by extrusion D34 and batch mini-extrusion respectively: 38%$_{vol}$ of PA6, PA6 dispersed or stretched dispersed in PE phase
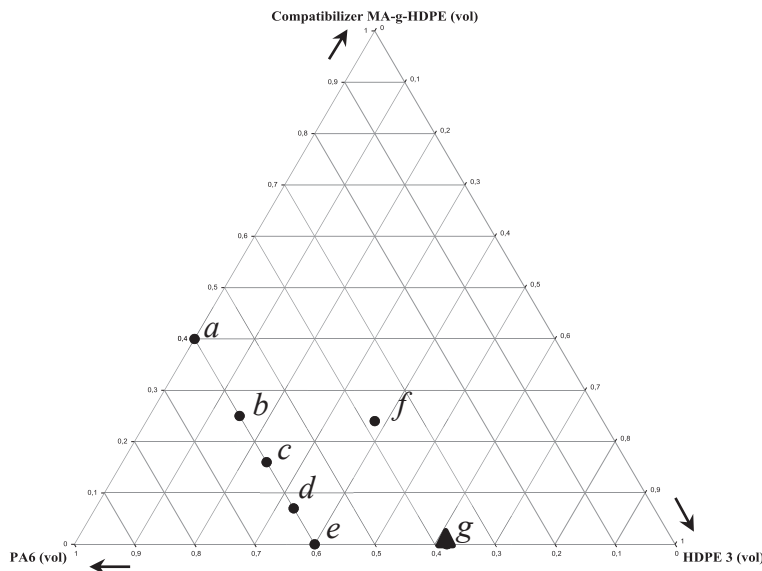
Figure V-11: Blends with HDPE 3 used to study the influence of compatibilizer amount on the crystallization of PA6.

3.2.2.1. Crystallization temperature

The crystallization behavior was firstly compared in both series. Figure V-12 and Figure V-13 show the thermograms obtained during the cooling ramp in both series.
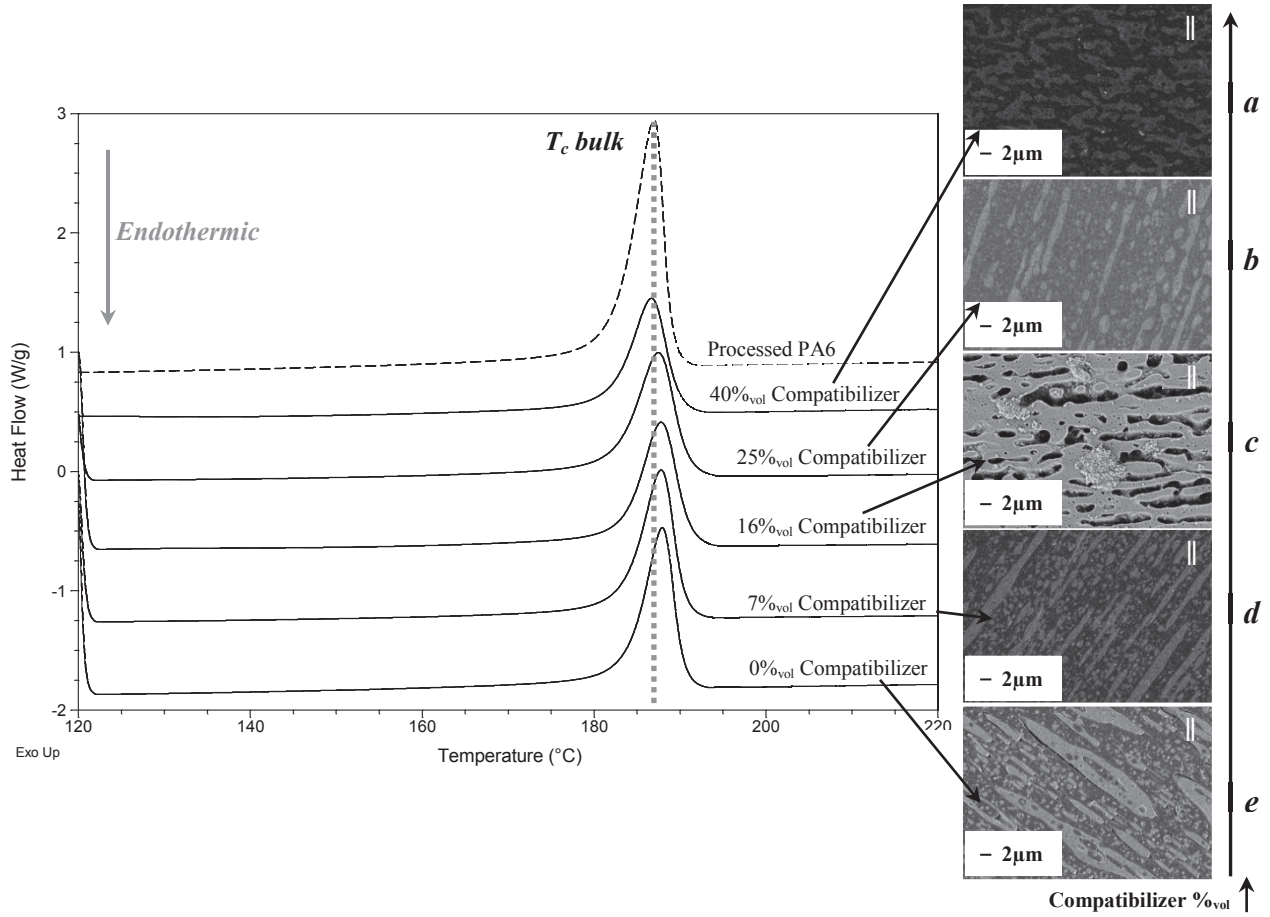
Figure V-12: Thermograms (cooling ramp) of blends *a* to *e* of series 60 in Figure V-11 (PE phase etched).
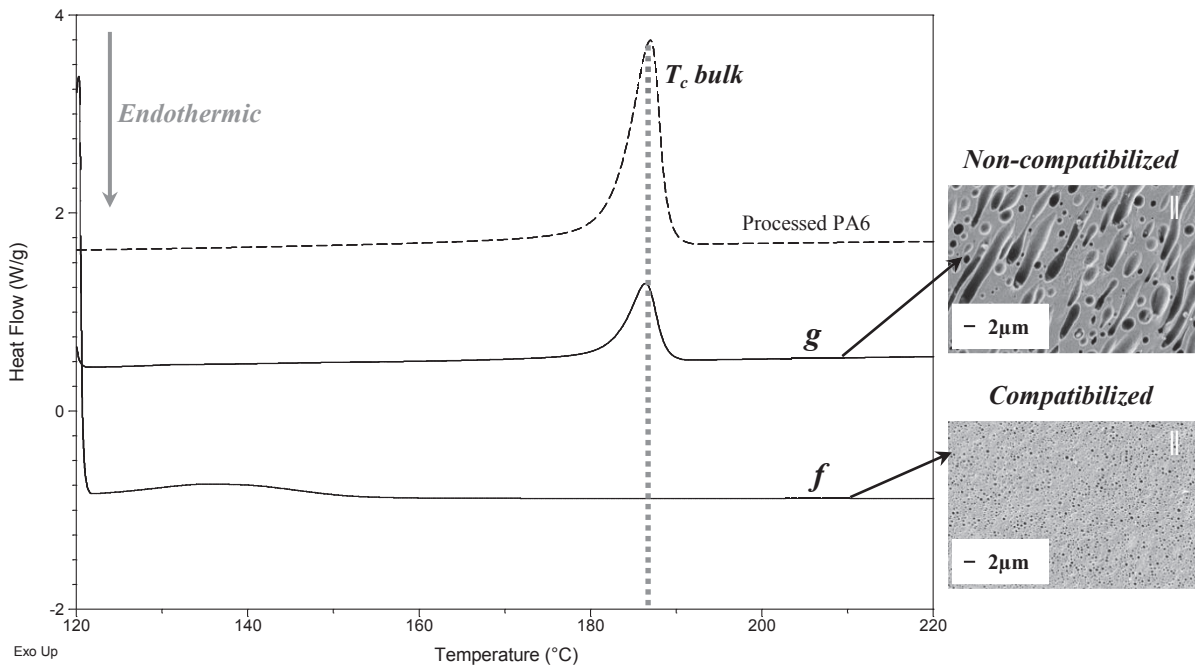
Figure V-13: Thermograms (cooling ramp) of blends *f* to *g* of series 38 in Figure V-11 (PA6 etched).

Series 60: PA6 continuous (Figure V-12):

All the blends exhibit co-continuous morphology. As expected, the domains size decreases down to 1µm as the compatibilizer amount increases. **Whatever the compatibilizer amount, PA6, considered as matrix crystallizes like in bulk.**

No additional flattened exotherm at lower temperature is observed in these cases. However, TEM was performed on blend *c* (16%$_{vol}$ of compatibilizer) and nano-dispersions of PA6 (in black) were clearly observed in the PE phase matrix:
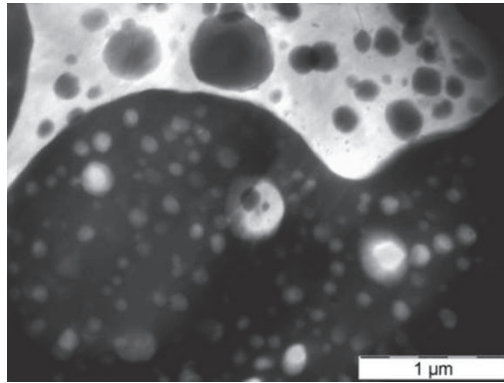
Figure V-14: Example of TEM micrograph of blend c in Figure V-11 after PA6 staining (domains in black).

Thus, in these blends, PA6 nano-dispersions may be present in too small quantity for detection in DSC. However, a small decrease of the enthalpy of crystallization of the peak at T_c *bulk* (from 44 to 36J/g) is observed as the compatibilizer amount increases. This could be an indication of the increase of the nano-dispersions of PA6 quantity as the compatibilizer amount increases.

Series 38: PE phase continuous (Figure V-13):

The morphology of non-compatibilized blend (*g*) is much coarser and also more stretched than the one of the compatibilized blend (*f*). Contrary to compatibilized blend (PA6 domains size always <2µm) which presents fractionated crystallization (with an exotherm around 125-130°C), **PA6 domains size in the non-compatibilized blend is large enough to allow PA6 crystallizing like in the bulk (almost all the PA6 domains exhibit a size ≥2µm).**

3.2.2.2. Crystallinity amount

The influence of the morphology size on the crystallinity amount of PA6 was also studied comparing the melting behaviors during the second heating ramp of blends in both series.

Series 60: PA6 continuous:

Whatever the amount of compatibilizer (PA6 domains remained always >2μm), the melting temperatures of PA6 during the second heating ramp were always about 214°C for γ phase and 219°C for α phase, like in the reference processed PA6 (Table V-1). The overall crystallinity amount was always about 39% in average, a little lower than in the reference (Table V-1). **So, in blends with PA6 continuous, the morphology size does not influence much the melting temperatures and the overall crystallinity amount of PA6.**

Series 38: PE phase continuous:

Whatever the size of the morphology, the melting temperatures of PA6 during the second heating ramp were about 213°C for γ phase and 219°C for α phase, like in the reference processed PA6 (Table V-1). The compatibilized blend (*f*), which presents a PA6 dispersion morphology (<2μm), exhibited a lower overall PA6 crystallinity amount (29%) than the non-compatibilized blend (*g*) (33%), which presents coarser morphology. As already explained, **the PA6 crystallization is hindered when the PA6 is confined in small droplets (typically <2μm).**

3.2.2.3. Crystalline phases

We now focus more precisely on the crystalline phases: α and γ.

Series 60: PA6 continuous:

The fraction of the overall PA6 crystallinity amount which corresponds to γ phase is plotted as a function of compatibilizer content in Figure V-15.
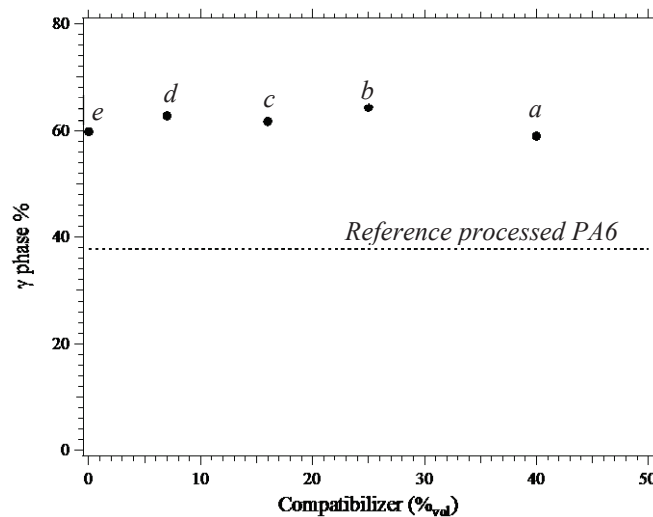
Figure V-15: γ phase fraction of PA6 crystalline phase versus compatibilizer amount in blends *a* to *e* of series 60.

Thus, whatever the compatibilizer amount, the typical size of the PA6 domains being always larger than 2µm, the γ phase fraction is constant (~60%).

Note that as PA6 is continuous in these blends, as expected from the previous section, γ phase formation is favored.

Series 38: PE phase continuous:

In the compatibilized blend (*f*), PA6 is confined in small droplets (<2µm) and only α phase was formed. On the other hand, in the non-compatibilized blend (*g*), a large part of PA6 is not confined (≥2µm) and the γ phase was favored (54%), which is consistent with the series 60 with PA6 continuous and with the results from previous section (see *section 3.2.1 Influence of the kind of morphology page 212*).

3.2.3. Summary of PA6 crystallization in the blends with PE phase

Depending on the PA6 confinement, various crystallization behaviors were observed:

- PA6 not confined (typically >2µm):
    - PE phase reduces the overall crystallinity amount of PA6 as compared to the reference processed PA6 (from 44% to 35% typically)
    - Crystallization like in bulk
    - γ phase is favored

- PA6 confined (typically <2µm):
    - The overall crystallinity amount of PA6 is much more decreased (down to 29%).
    - Crystallization is shifted to lower temperature and this shift becomes larger as the PA6 domain size decreases (down to 135°C instead of 187°C in the case of PA6 domain size <600nm, see Figure V-8 *E*).
    - Only α phase is formed

4. Polyethylene crystallization

Like for PA6, bulk HDPEs, MA-g-HDPE and one example of PE phase (HDPE/MA-g-HDPE 60/40%$_{vol}$) are described. The influence of process is described in order to define the most relevant references. The influence of adding compatibilizer to HDPEs to obtained PE phases is also detailed. Then, the influence of the morphology of PA6/PE phase blends on the crystallization of PE phase is discussed.

4.1. Bulk HDPE

4.1.1. Typical thermograms obtained

An example of thermogram obtained for bulk HDPE 3 during the cooling ramp and the second heating ramp, both at 10°C/min is shown in Figure V-16.

Figure V-16: Example of thermogram (cooling ramp and second heating ramp at 10°C/min) obtained for bulk HDPE 3 (unprocessed).
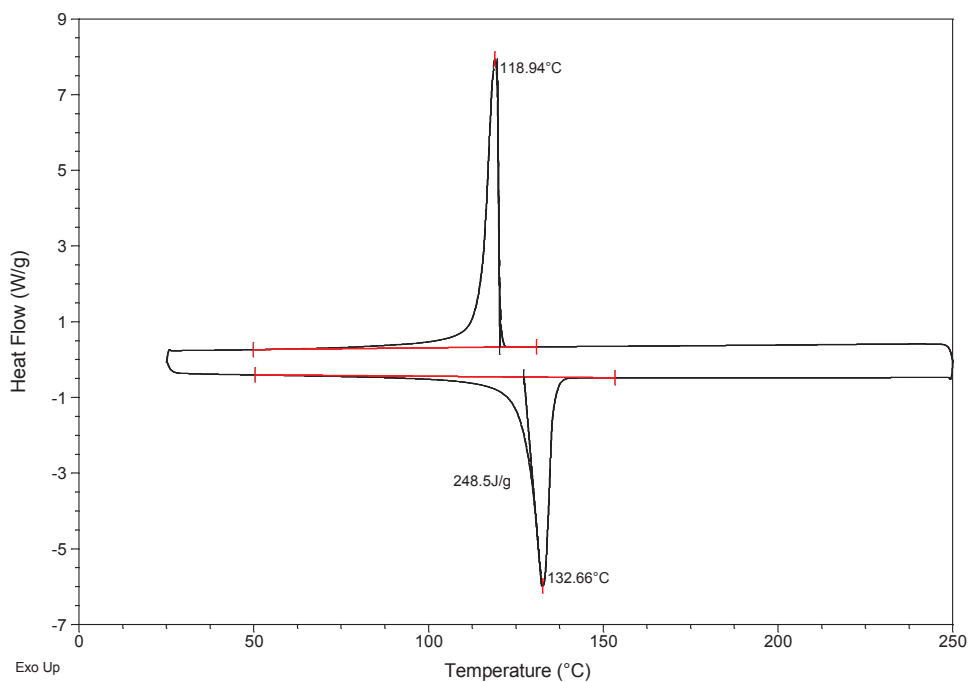
The cooling ramp was used to determine the crystallization temperature (T_c). The second heating ramp, after elimination of thermal history, was used to determine the melting temperature (T_m) and the crystallinity amount of PE phase (χ_c).

223

4.1.2. Influence of the process

Bulk HDPEs and MA-g-HDPE were processed in the same conditions as the blends using the twin screw extruder D34 and the batch mini-extruder. As no blend with HDPE 1 was prepared by batch mini extrusion, the reference HDPE 1 was not processed using this tool.

The results obtained are summarized in the following table:

	T_m (°C)	T_c (°C)	χ_c (%)
Bulk HDPE 1 before extrusion	126	115	60
Processed HDPE 1 (extruder D34)	127	115	64
Bulk HDPE 2 before extrusion	130	119	78
Processed HDPE 2 (extruder D34)	131	117	75
Processed HDPE 2 (batch mini-extruder)	133	117	75
Bulk HDPE 3 before extrusion	133	119	87
Processed HDPE 3 (extruder D34)	133	119	84
Processed HDPE 3 (batch mini-extruder)	135	118	84
Bulk MA-g-HDPE before extrusion	126	115	66
Processed MA-g-HDPE (extruder D34)	128	116	66
Processed MA-g-HDPE (batch mini-extruder)	128	117	69

Table V-2: Transitions temperatures and crystallinity amounts in bulk HDPEs and MA-g-HDPE before and after extrusion.

The melting temperatures after processing were always a little higher than in neat materials. Some differences were also observed in crystallization temperatures. In fact, the crystallization notably depends on the impurities present in the melt to initiate heterogeneous nucleation. Thus, depending on the tool used, on the quality of the cleaning prior to the experiments… the material crystallization temperature can vary. Finally, the crystallinity amounts measured during the second heating ramp also exhibited few differences.

To conclude, the processes have slight influence on the transitions temperatures and the crystallinity amounts. Thus, in order to compare materials with the same thermal history, processed HDPEs and MA-g-HDPE will be used as references in what follows.

4.1.3. Influence of the compatibilizer

The compatibilizer and HDPEs exhibit different transitions temperatures and crystallinity amount. In this section, the behavior of PE phases (HDPE/MA-g-HDPE 60/40%$_{vol}$) is analyzed. As the PE phases were prepared by extrusion D34, references processed in this tool are used for comparison. The results are summarized in Table V-3.

	T_m (°C)	T_c (°C)	χ_c (%)
HDPE 1	127	115	64
HDPE 2	131	117	75
HDPE 3	133	119	84
MA-g-HDPE	128	116	66
PE phase 1	127	115	62
PE phase 2	129	119	76
PE phase 3	131	119	79

Table V-3: Transitions temperatures and crystallinity amounts in processed references (extruder D34) and in PE phases (HDPE/MA-g-HDPE 60/40%$_{vol}$).

The presence of Maleic Anhydride moieties (MA) in the compatibilizer could impede the crystallization of HDPE chains, leading to a lower crystallinity amount as observed by comparing HDPE 2 and HDPE 3 to MA-g-HDPE [123]. However, we can note that HDPE 1 exhibits lower crystallinity amount than MA-g-HDPE. In TGA, a larger mass loss was observed in HDPE 1 than in the other HDPEs and in MA-g-HDPE after 30 minutes at 290°C (*see Chapter II section 4.1.1 ThermoGravimetric Analyses (TGA) page 94*). This larger mass loss was probably due to the degradation of PE additives in this very formulated commercial grade. Thus, the lower crystallinity amount observed in HDPE 1 may be also associated to the degradation of the additives during the extrusion.

The experimental crystallinity amounts χ_c were compared to the calculated ones by a classic mixing law between HDPE and MA-g-HDPE:

$$\chi_c(PE\ phase)_{calc} = \%_{wt}(HDPE).\chi_c(HDPE) + \%_{wt}(MA\text{-}g\text{-}HDPE).\chi_c(MA\text{-}g\text{-}HDPE) \qquad \textbf{Eq. V-3}$$

The results obtained are presented in Table V-4.

	$\chi_c(exp)$ (%)	$\chi_c(calc)$ (%)
PE phase 1	62	65
PE phase 2	76	72
PE phase 3	79	77

Table V-4: Experimental and calculated crystallinity amounts in PE phases (HDPE/MA-g-HDPE 60/40%$_{vol}$).

By comparing the experimental crystallinity amounts and the calculated ones, no significant differences were observed.

Thus, the PE phase crystallinity follows a mixing law between HDPE and MA-g-HDPE (using processed references). This means that the PE chains of HDPE and MA-g-HDPE are able to co-crystallize which is essential for the compatibilization effectiveness.

4.2. Blends with PA6

The influence of the morphology on PE phase crystallization (determined from the cooling ramp) and crystallinity amount (determined from the second heating ramp) was also investigated. The influence of the kind of morphology is first discussed. Then, the influence of the compatibilizer amount is detailed.

4.2.1. Influence of the kind of morphology

To study the influence of the kind of morphology on (1) PE phase crystallization temperature and (2) PE phase crystallinity amount, compatibilized blends with constant PE phase composition (HDPE/MA-g-HDPE=60/40%$_{vol}$) and various PA6 fractions were used and compared to the processed references (HDPEs, MA-g-HDPE and PE phases). These blends follow the dashed line (which corresponds to line *L* in *chapter III*) in Figure V-17. Blends based on HDPEs 1, 2 and 3 were studied.
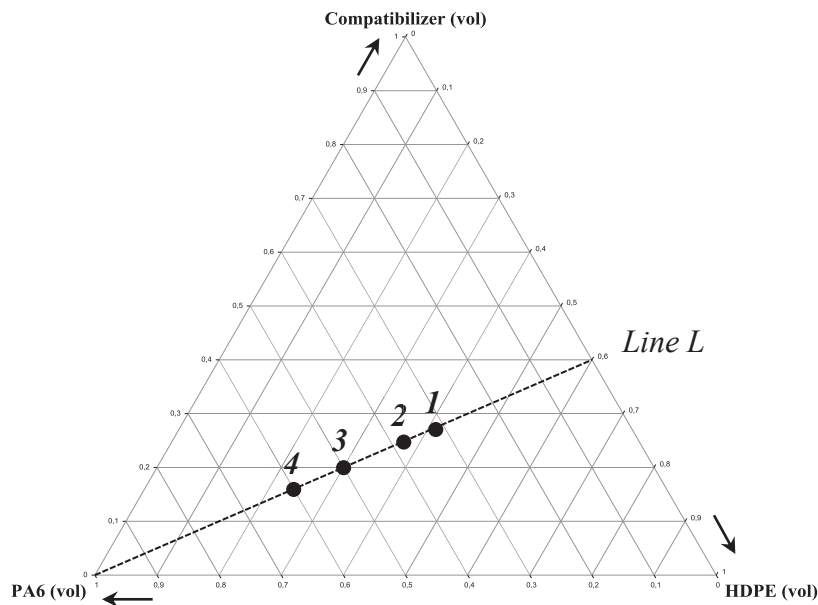
Figure V-17: Blends with constant PE phase composition HDPE/Compatibilizer (60/40%$_{vol}$) used to study the influence of blend morphology on PE phase crystallization. Several blends based on HDPEs 1, 2 and 3 all located on line *L* were studied. The formulations (*1* to *4* with HDPE 1, processed using the extruder D34) used in Figure V-18 to illustrate the influence of PA6 amount on the crystallization of PE phase are also included.

4.2.1.1. Crystallization temperature

Depending on the morphology, various PE phase crystallization peaks were observed in the thermograms as illustrated in Figure V-18.
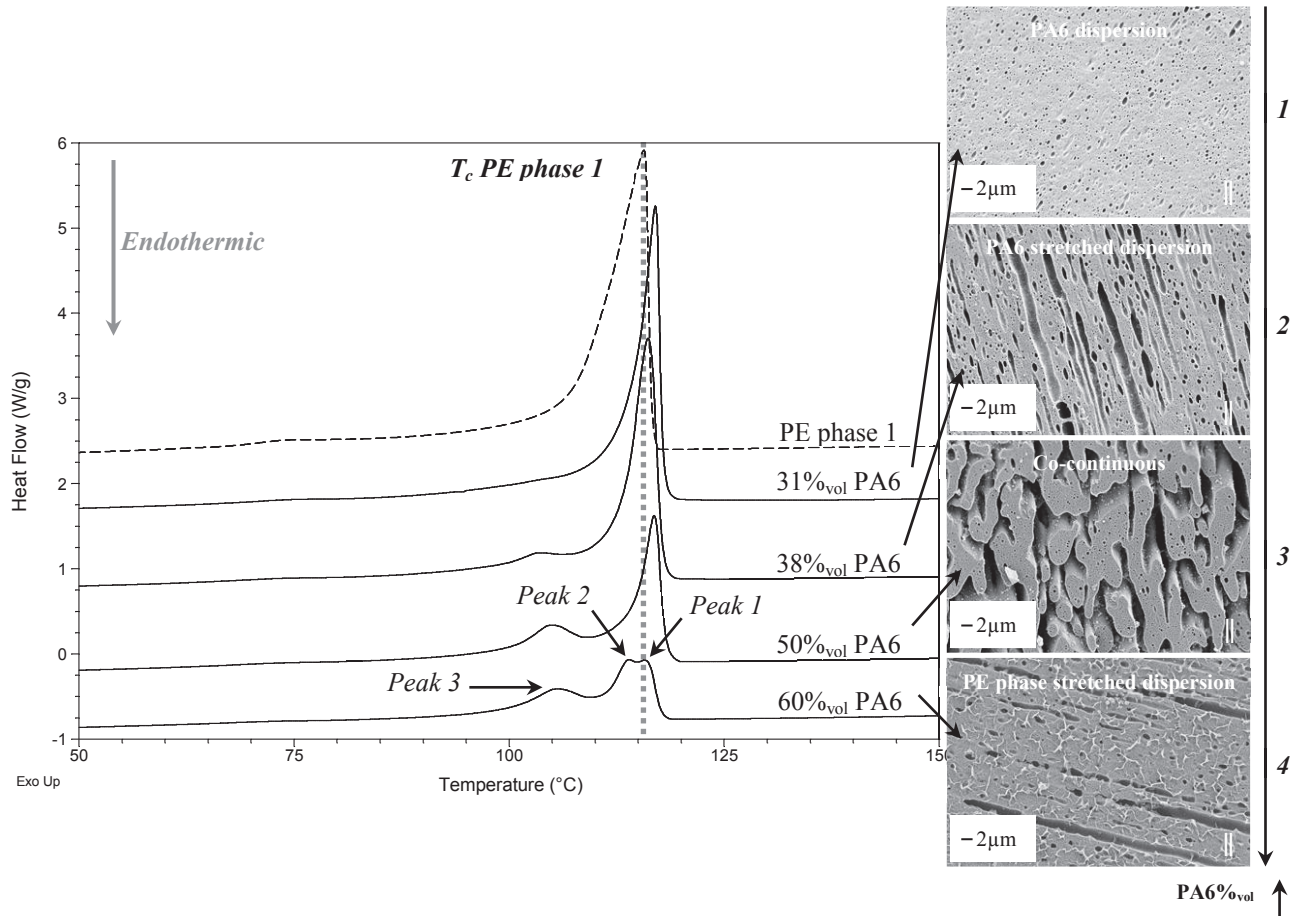
Figure V-18: Thermograms (cooling ramp 10°C/min) of blends *1*, *2* (PA6 etched), *3* and *4* (PE phase etched) with HDPE 1 exhibiting various morphologies along line *L*.

So, depending on the morphology, one to three peaks corresponding to the crystallization of PE phase were observed. Like previously, to quantify the fraction of the overall crystallization which corresponds to peak 1, 2 or 3, vertical drops were used to separate the overall crystallization peak as illustrated in Figure V-19.
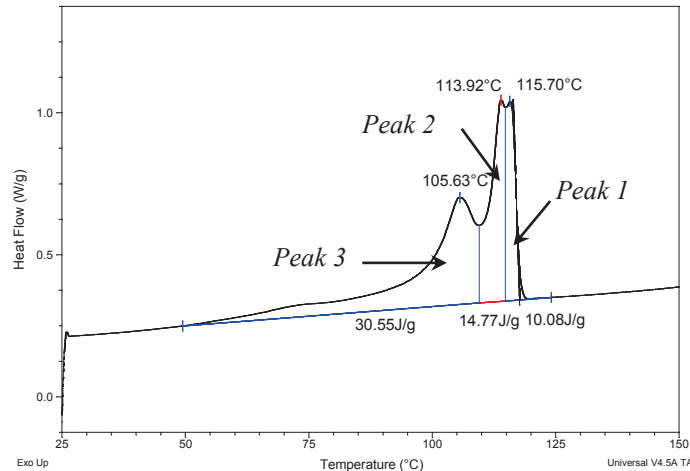
Figure V-19: Method used to quantify the fraction of the overall crystallization corresponding to each peak.

To explain the three peaks corresponding to the PE phase crystallization, three cases are distinguished:

1) Morphologies with continuous PE phase matrix:

In the blend with $31\%_{vol}$ of PA6, the morphology is PA6 dispersion within a PE phase matrix (see Figure V-18 *1*). In this case, the heterogeneous nucleation by heterogeneities (like impurities) can occur as in bulk. **Thus, the PE phase crystallizes like in bulk: T_c blends ~ T_c bulk.**

In the blend with $38\%_{vol}$ of PA6, the morphology is PA6 stretched dispersion in PE phase matrix (see Figure V-18 *2*). An additional crystallization peak at a lower temperature (from 102 to 106°C) is observed. Two hypotheses are formulated to explain the presence of the peak 3 of crystallization at lower temperature:

1) The fraction of the PE phase chemically linked to the PA6 by the compatibilization reaction may be hindered to crystallize by the PA6 already crystallized.

2) As described in the *Chapter III*, nano-dispersions of PE phase in the stretched domains of PA6 were observed. As already explained for PA6 crystallization, as the size of the domains becomes smaller than the typical distance between the nucleation sites present within the bulk phase, a fraction of the domains does not contain any nucleus leading to crystallization at 116°C. The crystallization within those domains should be shifted to lower temperature, at which other types of heterogeneities with larger nucleation barriers may become active. Such heterogeneities are likely located at the interfaces. Thus, the peak 3 may be associated to the crystallization of the fraction of PE phase confined in sub-dispersions.

228

Additional experiments with HDPE 3 were performed to validate one or the other of these hypotheses. A blend PA6/MA-g-HDPE (64.3/35.7%$_{vol}$) exhibiting a molar ratio [MA]/[NH$_2$]=1 (corresponding to point Ⓟ in Figure III-1 (*see Chapter III page 104*)) was first prepared in batch mini-extrusion (called blend *0*). Then, this blend was diluted using two amounts of HDPE 3 in order to obtain the following mixtures:

- Blend *d$_1$*: PA6/HDPE 3/MA-g-HDPE 60/6.8/33.3%$_{vol}$
- Blend *d$_2$*: PA6/HDPE 3/MA-g-HDPE 40/37.8/22.2%$_{vol}$

In the same time, the blend *0* was also reprocessed to get a reference thermogram having the same thermal history as the blends *d$_1$* and *d$_2$*.

As blends *d$_1$* and *d$_2$* were diluted only with HDPE 3, no more reaction could occur. Figure V-20 shows the thermograms (in cooling ramp) obtained for these blends.
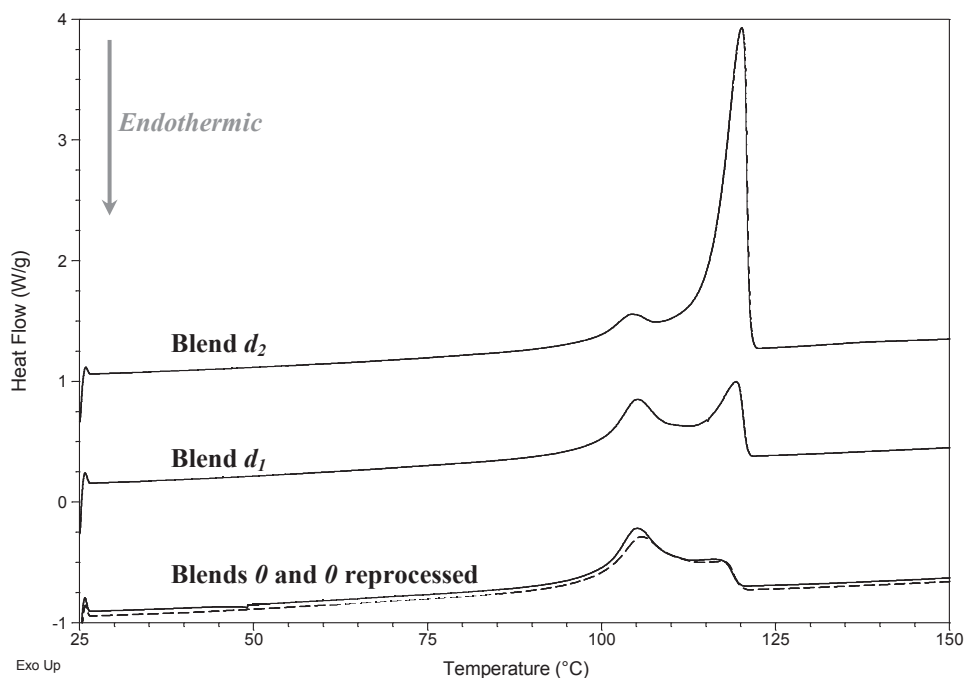
Figure V-20: Thermograms (cooling ramp) of blend *0* (dashed line), blend *0* reprocessed (solid line) and blends *d$_1$* and *d$_2$*.

In all the blends, both peak 1 and peak 3 are observed. According to Figure V-20, it clearly appears that the fraction of peak 3 is the same in the blends *0* and *0* reprocessed (84%). This fraction corresponds to a fixed reaction conversion (>80% in both cases according to InfraRed spectroscopy). Then, by diluting HDPE 3, no more reaction could occur, thus the fraction of the PE phase chemically linked to PA6 is the same. Thus, if the peak 3 is due to these HDPE chains of the compatibilizer linked to PA6 at the interface, the fraction of peak 3 should be directly proportional to the fraction of MA-g-HDPE in the PE phase. By comparing this expected fraction of peak 3 to the experimentally observed one in blends *d$_1$* and *d$_2$*, we will conclude on the origin of this peak.

The expected fraction of peak 3 is calculated using the fraction of peak 3 in blend *0* (84%):

$$Expected\ \%\ of\ peak\ 3 = 84\ \frac{\%_{MA-g-HDPE}}{\%_{PE\ phase}} \qquad \textbf{Eq. V-4}$$

The results obtained are summarized in the following table:

	% MA-g-HDPE in PE phase	% peak 3 calculated	% peak 3 experimentally observed
Blend d_1	83%	70	61
Blend d_2	37%	32	22

Table V-5: Fraction of peak 3 expected if this peak is only due to the PE chains linked to PA6 at the interface compared to the fraction of peak 3 experimentally observed in blends d_1 and d_2.

It clearly appears that the fraction of peak 3 experimentally observed is smaller than the one expected if this peak was only due to the HDPE chains of the compatibilizer chemically linked to PA6 at the interface. Moreover, by diluting HDPE in blend *0*, the characteristic size of the PE phase domains increases and the fraction of confined PE phase decreases, which is in agreement with the observed reduction of peak 3.

Thus, the peak 3 is not associated to the fraction of the PE phase chemically linked to the PA6 by the compatibilization reaction in which the crystallization may be hindered by the PA6 already crystallized (hypothesis 1).

So, we attribute the fractionated crystallization peaks at T_c bulk (peak 1) and at lower T_c (peak 3) to the fraction of PE phase within the continuous matrix and within confined sub-dispersions respectively (hypothesis 2).

The density of nucleating sites in neat processed HDPE 3 was estimated to be of the order of $10^{14}m^{-3}$ in a forthcoming paper [124]. This corresponds to an average distance between nucleating sites of the order of two tens of µm. The density of nucleating sites in PE phase 3 was found to increases up to $10^{17}m^{-3}$ in blends with PA6 [124]. When it crystallizes, PA6 may expulse some impurities to the PE phase, increasing the nucleating sites density. This density corresponds to an average distance between nucleating sites of the order of two µm. **It is thus expected that the crystallization temperature will be shifted down (peak 3) in droplets smaller than this typical size of the order of µm.**

2) Co-continuous morphology:

In the blend with 50%$_{vol}$ of PA6, the co-continuity is reached and the quantity of nano-dispersions of PE phase in PA6 should be larger. The additionnal peak at 105°C (peak 3) increases.

3) PA6 continuous:

In the blend with 60%$_{vol}$ of PA6, the morphology is PE phase stretched dispersion in PA6 matrix. In this case, the additional peak at 105°C is still observed, due to the sub-dispersions of PE phase. Then, the crystallization peak corresponding to the one in the bulk is splitted into two peaks at 116 and 114°C respectively. **This may be due to a mechanism of local slowing down of the crystallization kinetics.** This slowing down may occur in the entanglements formed when the stretched domains undergo Rayleigh instabilities to break up into smaller droplets as illustrated in Figure V-21.

Slowing down of crystallization in
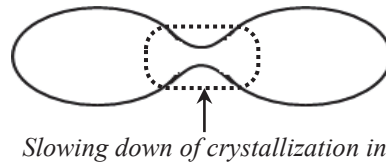
Figure V-21: Diagram of entanglements in PE phase stretched domains.

In order to summarize the results obtained with the three PE phases in the blends along line *L* (Figure V-17), the fraction of the overall PE phase crystallization corresponding to peak 3 (crystallization within the small PE phase droplets) is plotted as a function of PE phase amount in the blends in Figure V-22.
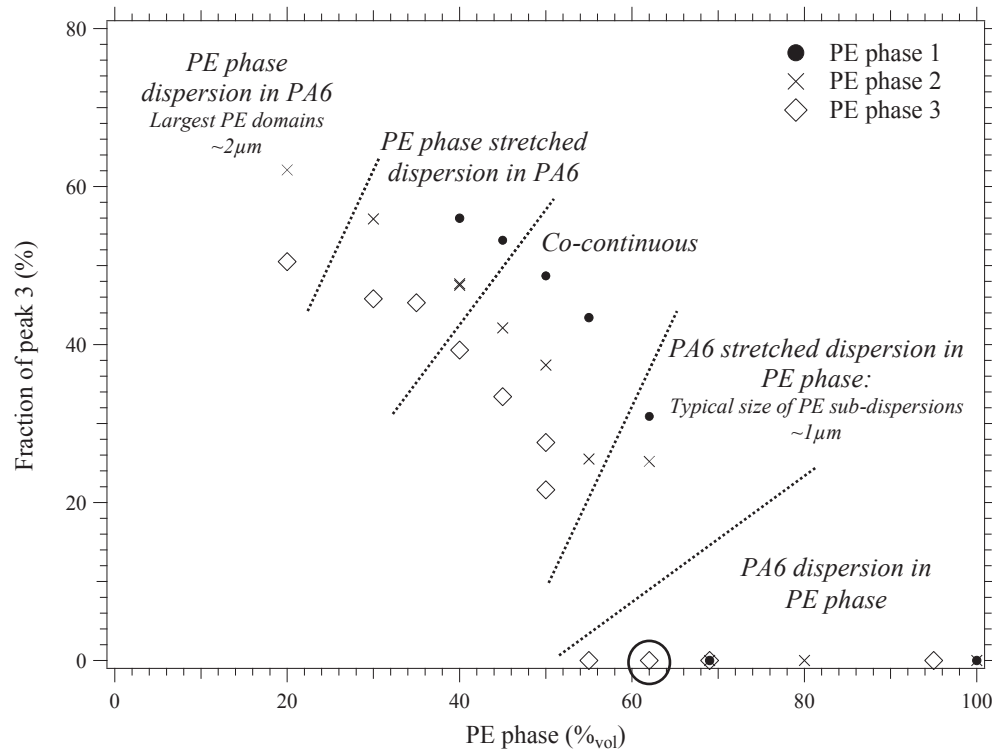
Figure V-22: Fraction of the overall crystallization corresponding to peak 3 versus the PE phase amount in the blends (along line *L*).

231

According to Figure V-22, it seems that **the crystallization is shifted down to peak 3 in PE phase droplets smaller than 1µm typically**, which is agreement with the estimation performed according to the nucleating sites density.

Note that no peak 3 is observed in the case of the blend encircled in Figure V-22. However, TEM was performed on this blend (PA6/HDPE 3/MA-g-HDPE 38/38/24%$_{vol}$) and a few nano-dispersions of PE phase (in white/grey) were clearly observed in the PA6 domains:
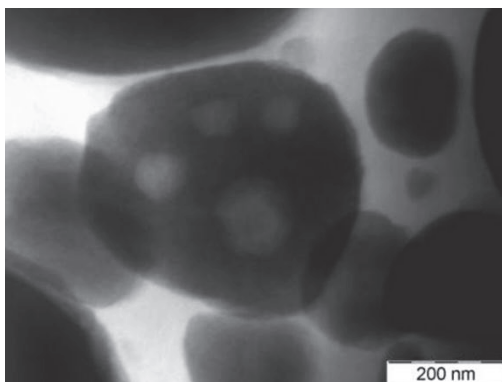
Figure V-23: Example of TEM micrograph of blend encircled in Figure V-22 after PA6 staining (domains in black).

Thus, in this blend, PE phase nano-dispersions may be present in too small quantity for detection in DSC (as already observed in the case of PA6 nano-dispersions, see Figure V-14).

In the same way, the fraction of the overall PE phase crystallization corresponding to peak 2 (slowing down in entanglements of PE phase stretched domains) is plotted as a function of PE phase amount in Figure V-24.
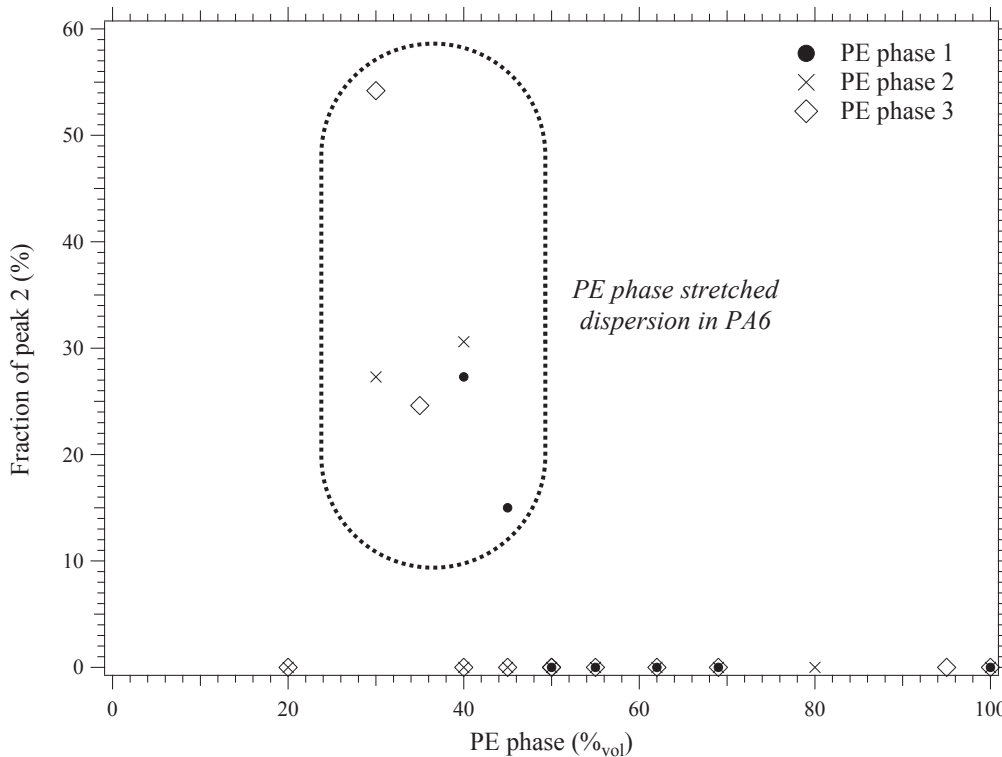
Figure V-24: Fraction of the overall crystallization corresponding to peak 2 versus the PE phase amount in the blends (along line *L*).

To summarize, three PE phase crystallization peaks were observed depending on the morphology:

- **Peak 1:** T_c *1~HDPE T_c bulk (~116°C)*. It corresponds to the crystallization as in the bulk of the *fraction of PE phase within a continuous matrix*.

- **Peak 2:** Split of peak 1 into two peaks: T_c *2 (114°C)<T_c bulk*. It appears when the morphology is *PE phase stretched dispersion in PA6 matrix*. It may be due to a slowing down of the crystallization kinetics in entanglements of PE phase stretched domains.

- **Peak 3:** T_c *3 (105°C)<<T_c bulk*. It is due to crystallization of *PE phase confined into sub-dispersions smaller than 1µm typically*.

233

4.2.1.2. Crystallinity amount

By observing the second heating ramp on the thermograms, the overall crystallinity amount of PE phase in the blends with PA6 is now discussed.

The melting temperatures of PE phases in the blends with PA6 were always quite similar to ones measured in neat HDPEs and PE phases.
Figure V-25 shows the overall crystallinity amount of PE phase as a function of PE phase amount in the blends with PA6.
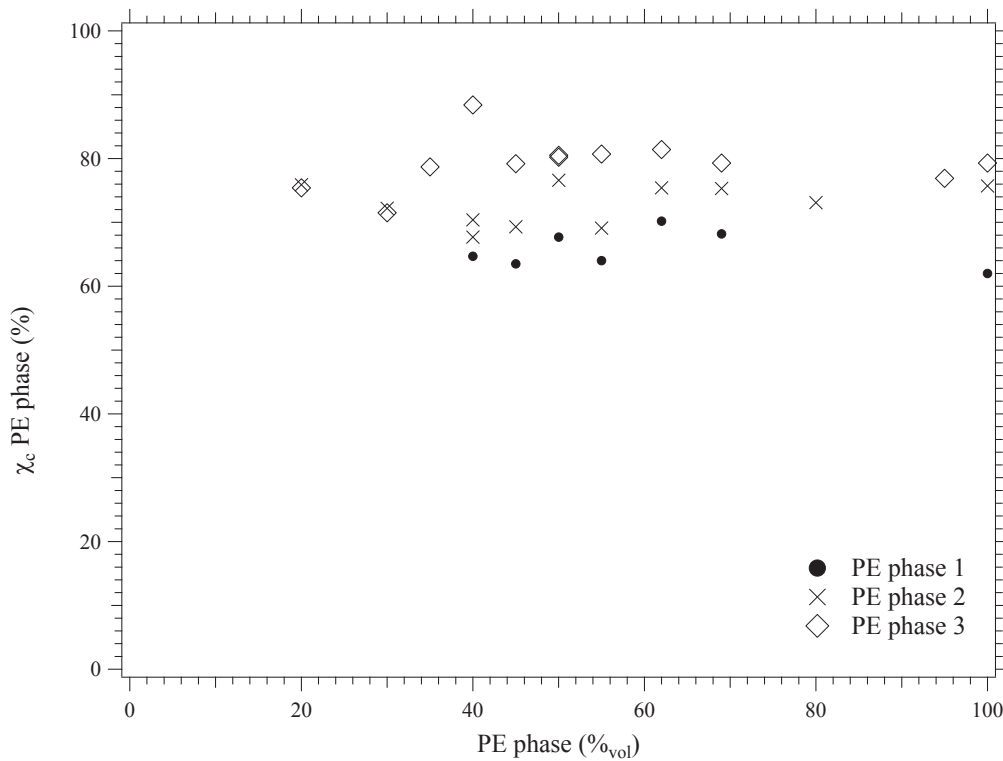
Figure V-25: Crystallinity amount of PE phase versus PE phase content in the blend (along line *L*).

Whatever the composition and the morphology of the blends, the crystallinity amount of PE phase is always quite similar to the one observed in neat PE phase.

Thus, PA6 does not seem to influence crystallinity amount of PE phases.

4.2.2. Influence of the compatibilizer amount

To study the influence of the compatibilizer amount on (1) PE phase crystallization temperature and (2) PE phase crystallinity amount, blends with HDPE 3 were used. In fact, as already explained, it is a particular case in which the viscosity ratio is always equal to 0.5 (see *Table II-4 in Chapter II*) whatever the volume ratio MA-g-HDPE/HDPE 3 and whatever the shear rate. Moreover, HDPE 3 and MA-g-HDPE exhibit almost the same molecular masses distribution (see *Figure II-6 in Chapter II Section 2.5 Materials of the study page 76)*. Thus, by comparing blends with same PA6 content and same morphology, **the only changing parameter is the compatibilizer amount, or more precisely the amount of MA moieties.**

Like for PA6 crystallization, two series of blends with a constant PA6 volume fraction (along lines *N* as described in *Figure III-1 in Chapter III*) were studied, one with PA6 continuous and one with PE phase continuous in order to compare both cases as summarized in Figure V-26:
- **Series 60:** Blends *a* to *e*, processed by extrusion D34: 60%$_{vol}$ of PA6, co-continuous morphology
- **Series 38:** blends *f* and *g*, processed by extrusion D34 and batch mini-extrusion respectively: 38%$_{vol}$ of PA6, PA6 dispersed or stretched dispersed in PE phase

Blends *a* and *h*, which contain only PA6 and compatibilizer will be also compared in this section.
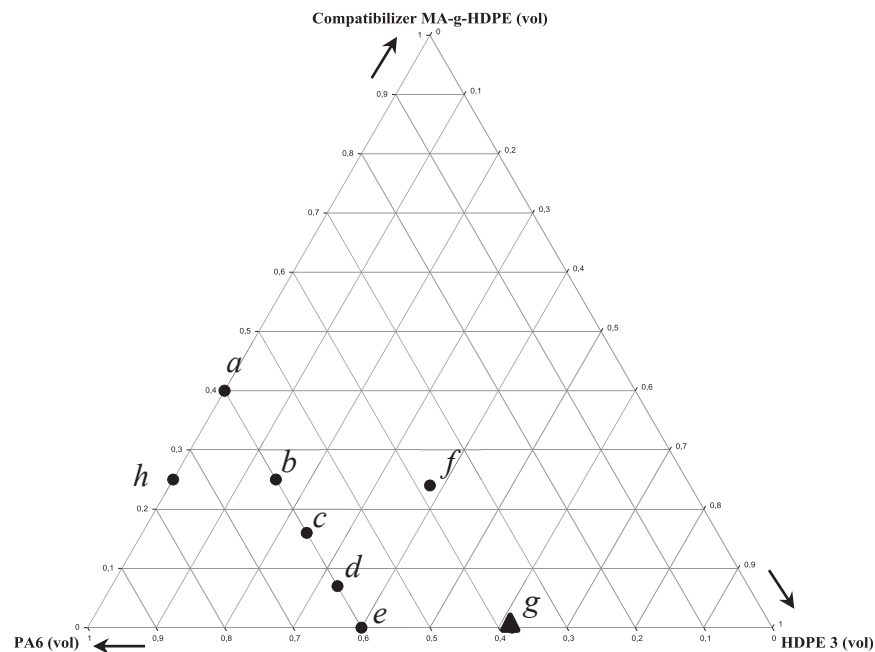
Figure V-26: Blends with HDPE 3 used to study the influence of the compatibilizer amount on the crystallization of PE phase 3.

235

4.2.2.1. Crystallization temperature

The two series 38 and 60 are firstly discussed.

Series 60: PA6 continuous:

Figure V-27 shows the thermograms obtained during the cooling ramp of blends *a* to *e*.
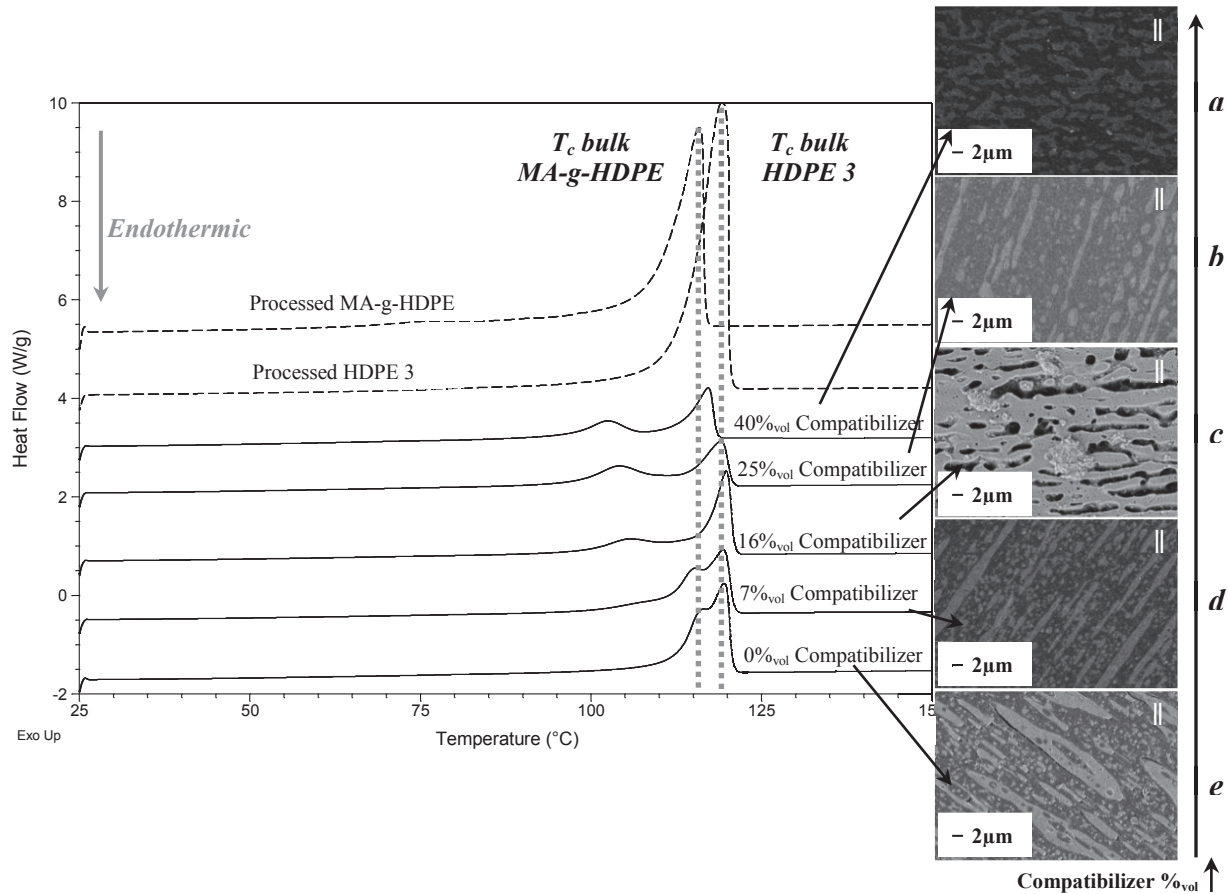
Figure V-27: Thermograms (cooling ramp) of blends *a* to *e* of series 60 (PE phase etched) and of the processed references MA-g-HDPE and HDPE 3.

All the blends exhibit co-continuous morphologies. In the cases of blends *e* and *d* (0 and 7%$_{vol}$ of compatibilizer respectively), peak 2 is also observed. In fact, the morphology is quite stretched.

Figure V-28 shows the fraction of overall PE phase crystallization corresponding to peak 3 as a function of the compatibilizer amount in blends *a* to *e* of the series 60.
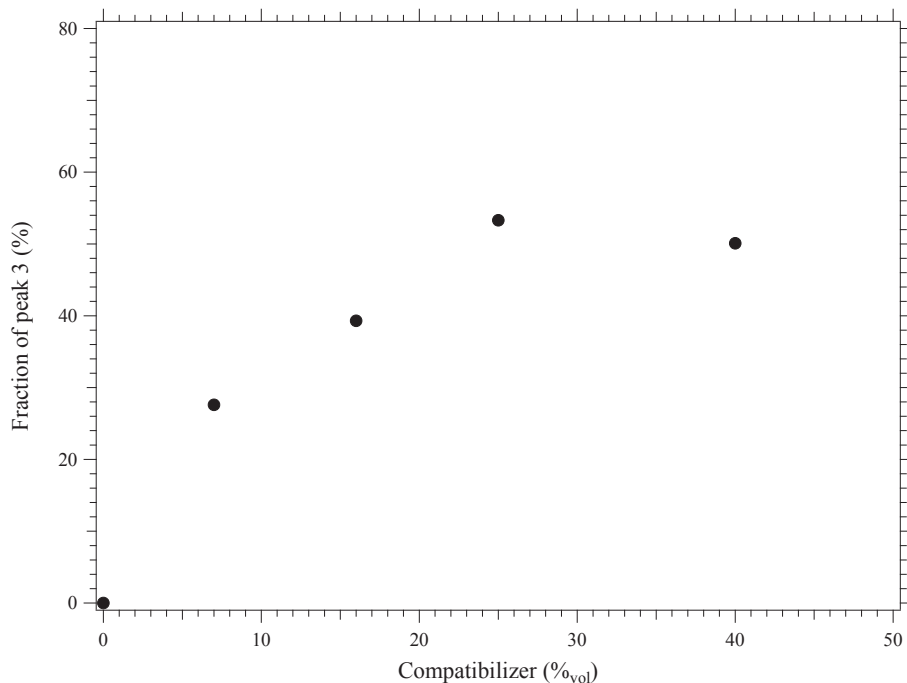
Figure V-28: Fraction of the overall PE phase crystallization corresponding to peak 3 versus the compatibilizer amount in blends *a* to *e* of series 60.

By adding compatibilizer, the typical size of the smallest PE phase droplets decreases below to 1µm and the peak 3 appears. The fraction of peak 3 increases by increasing the compatibilizer amount until it reaches a maximum fraction of about 55% of the overall PE phase crystallization. In fact, by increasing the compatibilizer amount, the formation of sub-dispersions of PE phase (<1µm) responsible of peak 3 is favored.

Series 38: PE phase continuous:

Figure V-29 shows the thermograms obtained during cooling ramps of blends *f* and *g*.
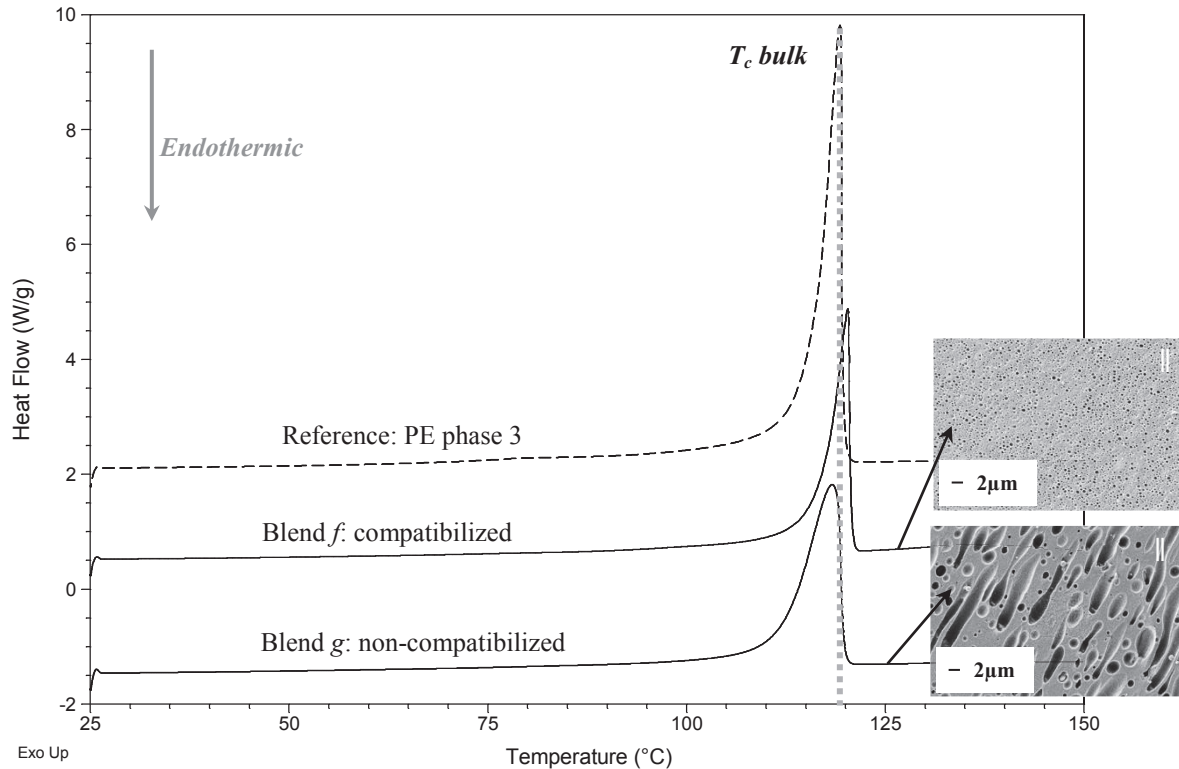
Figure V-29: Thermograms (cooling ramp) of blends *f* to *g* of series 38 (PA6 etched) and of the processed references PE phase 3.

The morphology of the compatibilized blend (*f*) is PA6 dispersed in PE phase matrix. The morphology of the non-compatibilized blend (*g*) is much coarser and more stretched. In both cases, only peak 1 corresponding to bulk crystallization is observed. In fact, **as PE phase is the continuous matrix, it can crystallize like in bulk.**

Comparison between PA6/Compatibilizer blends *a* and *h*:

Blends *a* and *h* without any neat HDPE are compared in this section.

Figure V-30 shows the thermograms obtained during cooling ramp of blends *a* (60%$_{vol}$ of PA6) and *h* (75%$_{vol}$ of PA6).
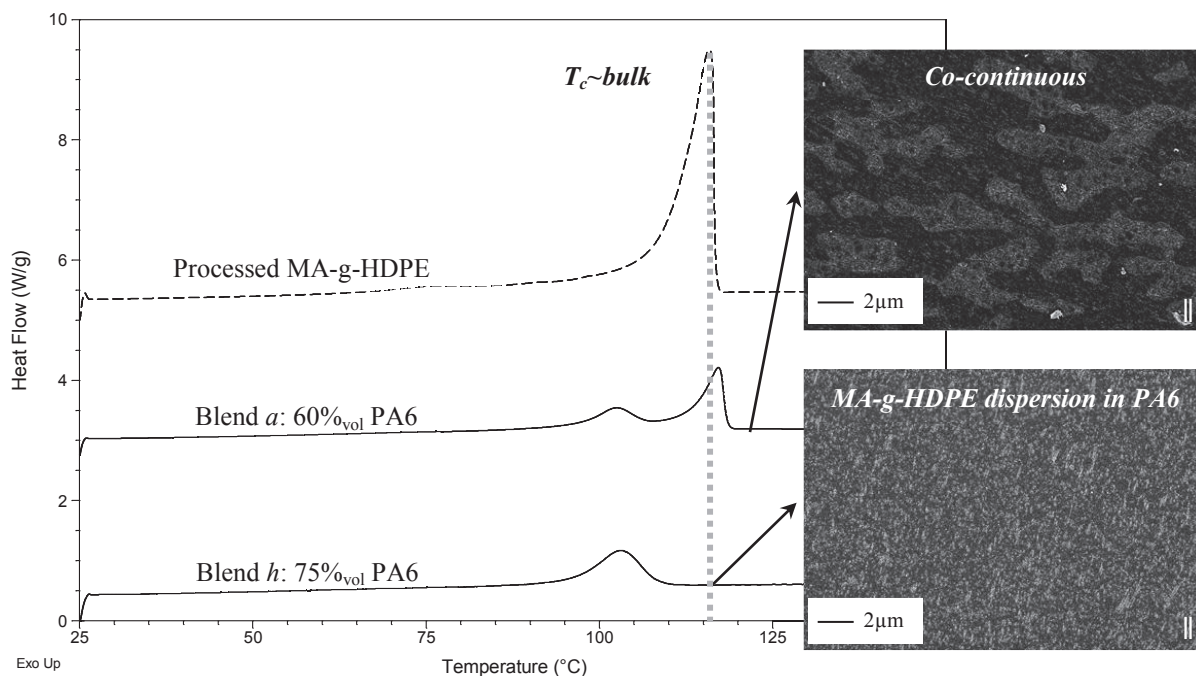
Figure V-30: Thermograms (cooling ramp) of PA6/MA-g-HDPE blends *a* and *h* containing respectively 60 and 75%$_{vol}$ of PA6 (MA-g-HDPE etched, light grey domains).

In the blend *a* (60%$_{vol}$ of PA6), the morphology is co-continuous (>1µm) with MA-g-HDPE nano-dispersions (<1µm). Thus, fractionated crystallization with peaks 1 and 3 is observed.

In the blend *h* (75%$_{vol}$ of PA6), the morphology is a very small dispersion of MA-g-HDPE in PA6 (<500nm). In this case, the crystallization only occurs at lower temperature than in bulk, corresponding only to peak 3.

4.2.2.2. Crystallinity amount

By using the second heating ramp, the overall PE phase crystallinity amount is now discussed in both series and in blends PA6/MA-g-HDPE *a* and *h*.

Series 60: PA6 continuous:

The melting temperature T_m of blend *e* (non-compatibilized) was 133°C, corresponding to the melting temperature of neat processed HDPE 3. Then, by increasing the amount of compatibilizer, the melting temperature of the PE phase decreased down to 127°C, close to one of neat processed MA-g-HDPE (128°C).

The overall PE phase crystallinity amount is plotted as a function of the compatibilizer amount in blends *a* to *e* of the series 60 in Figure V-31.
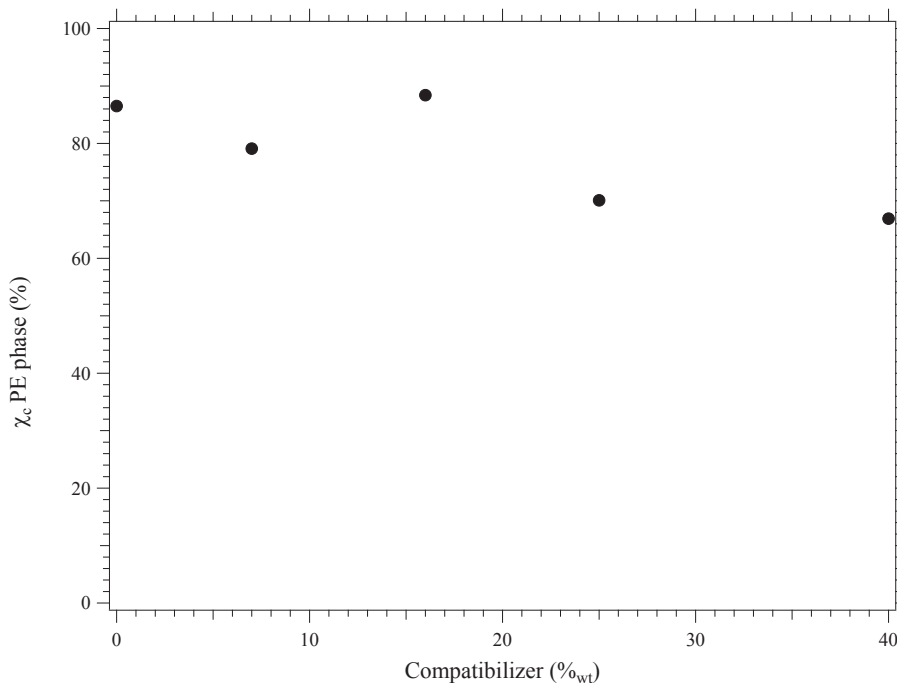
Figure V-31: Crystallinity amount of PE phase 3 versus the compatibilizer amount.

By increasing the amount of compatibilizer, a decrease of the overall PE phase crystallinity amount from 87 to 67% is observed. In fact, the PE phase crystallinity amount approaches the one of neat processed compatibilizer (66%).

Series 38: PE phase continuous:

The overall PE phase crystallinity amounts are quite similar in both blends:
- In the compatibilized blend (*f*): the melting temperature (T_m) is the same as in the reference PE phase 3 (131°C). The crystallinity amount χ_c is 81%, close to the one in the reference PE phase 3 (79%).
- In the non-compatibilized blend (*g*): the melting temperature (T_m) is the same as in the reference HDPE 3 (133°C). The crystallinity amount χ_c is 83%, close to the one in the reference HDPE 3 (84%).

Comparison between PA6/Compatibilizer blends *a* and *h*:

In blend *a* (60%$_{vol}$ of PA6), the melting temperature of the PE phase was 127°C, close the one of neat processed MA-g-HDPE (128°C). In blend *h* (75%$_{vol}$ of PA6), the melting temperature of PE phase was 124°C, a little lower than in the reference MA-g-HDPE.

In blends *a* and *h* the overall MA-g-HDPE crystallinity amount is 67%, close to the one of neat processed MA-g-HDPE (66%).

4.2.3. Summary of PE phase crystallization in the blends with PA6

To conclude, PA6 does not influence the overall crystallinity amount of PE phase whatever the blend composition. Then, depending on the PE phase confinement, fractionated crystallization was observed:

- **Peak 1:** *T_c 1~HDPE T_c bulk (~116°C)*. It corresponds to the crystallization as in the bulk of the ***fraction of PE phase within a continuous matrix***.

- **Peak 2:** Split of peak 1 into two peaks: *T_c 2 (114°C)<T_c bulk*. It appears when the morphology is ***PE phase stretched dispersion in PA6 matrix***. It may be due to a slowing down of the crystallization kinetics in entanglements of PE phase stretched domains.

- **Peak 3:** *T_c 3 (105°C)<<T_c bulk*. It is due to the crystallization of ***PE phase confined into sub-dispersions smaller than 1µm typically***.

5. Conclusion

In addition to the morphology, the final properties of blends also highly depend on the crystallinity. Thus, this chapter dealt with blend crystallization. Temperature sweeps were performed by Differential Scanning Calorimetry (DSC) to study the influence of the morphology on (1) the crystallization (determined from the cooling ramp) and (2) the final crystallinity amount (determined from the second heating ramp) of each phase in the blends.

Prior to characterize the blends, neat polymers (PA6 and HDPEs) unprocessed and processed using the same conditions as the blends were studied in order to determine the most relevant references. Thus, as the extrusion slightly influences the thermal behavior of raw materials, processed references were used. The following table summarizes the characteristics of the extruded references.

	T_m (°C)		T_c (°C)	χ_c (%)
HDPE 1	127		115	64
HDPE 2	131		117	75
HDPE 3	133		119	84
MA-g-HDPE	128		116	66
PE phase 1 (HDPE 1/MA-g-HDPE 60/40%$_{vol}$)	127		115	62
PE phase 2 (HDPE 2/MA-g-HDPE 60/40%$_{vol}$)	129		119	76
PE phase 3 (HDPE 3/MA-g-HDPE 60/40%$_{vol}$)	131		119	79
PA6	α: 220	γ: 214	187	44 (α: 17, γ:27)

Table V-6: Transition temperatures and crystallinity amounts of the processed references (extrusion D34).

Then, the crystallization of PA6 and of PE phases was described.

PA6 crystallization:

Depending on the PA6 confinement, various crystallization behaviors were observed:
- PA6 not confined (typically >2µm):
    - PE phase reduces the overall crystallinity amount of PA6 as compared to the reference processed PA6 (from 44% to 35% typically)
    - Crystallization like in bulk
    - γ phase is favored compared to bulk processed PA6
- PA6 confined (typically <2µm):
    - The overall crystallinity amount of PA6 is much more decreased (down to 29%).
    - Crystallization is shifted to lower temperature and this shift becomes larger as the PA6 domain size decreases (down to 135°C instead of 187°C in the case of PA6 domain size <600nm, see Figure V-8 *E*).
    - Only α phase is formed

PE phase crystallization:

PA6 does not influence the overall crystallinity amount of PE phase whatever the blend composition. Then, depending on the PE phase confinement, fractionated crystallization was observed:

- **Peak 1:** T_c *1~HDPE T_c bulk (~116°C)*. It corresponds to the crystallization as in the bulk of the ***fraction of PE phase within a continuous matrix***.

- **Peak 2:** Split of peak 1 into two peaks: T_c *2 (114°C)<T_c bulk*. It appears when the morphology is ***PE phase stretched dispersion in PA6 matrix***. It may be due to a slowing down of the crystallization kinetics in entanglements of PE phase stretched domains.

- **Peak 3:** T_c *3 (105°C)<<T_c bulk*. It is due to the crystallization of ***PE phase confined into sub-dispersions smaller than 1µm typically***. In fact, as the size of the domains becomes smaller than the typical distance between the nucleation sites present within the bulk phase (estimated to be of the order of µm), the fraction of domains which does not contain any nucleus leading to crystallization at 116°C (peak 1) becomes non-zero. The crystallization within those domains is shifted to a lower temperature, at which other types of heterogeneities (like the interface with the PA6) with larger nucleation barriers may become active.

General conclusion

The main objective of this work was to study Polyamide 6 (PA6) / High Density Polyethylene (HDPE) compatibilized blends in the framework of a DURAMAT sub-project whose target was to develop materials for biofuel tanks and pipes applications. In fact, Polyamide (PA) is known for its barrier properties. It exhibits a high resistance to hydrocarbon products. However, the polar groups which constitute the Polyamide make it sensitive to polar solvents. Today, the biofuels used in automotive market contains 10% of ethanol, but this rate may increase in the next years. Moreover, the future standards controlling the allowed fuel tank permeability will be more and more restrictive. Thus, blending Polyamide with a non-polar polymer impermeable to polar solvents like Polyethylene (PE) was the strategy in this work to develop a material with improved barrier properties to alcoholized gas.

The performances of polymer blends depending on the morphology, this study focused on the relationships between (1) the formulation and process parameters and (2) the obtained morphologies and microstructure of the blends. One Polyamide 6 (PA6), three High Density Polyethylene (HDPE) of various viscosities and one standard compatibilizer Maleic Anhydride grafted High Density Polyethylene (MA-g-HDPE) have been used. The compatibilization reaction occurs between Maleic Anhydride moieties (MA) of the compatibilizer and amine end-groups (NH_2) of PA6. High amounts of compatibilizer have been used. The molar ratio [MA]/[NH_2] in the blends ranged from 0 to 13.7.

The extrusion temperature (290°C) was high, especially for HDPEs, and PA6 is sensitive to moisture. Thus, the stability of the used polymers during the process was first checked, essentially by ThermoGravimetric Analyses (TGA) and Size Exclusion Chromatography (SEC). It was found that HDPEs and MA-g-HDPE could evolve during the process, whereas PA6 was quite stable. Thus, the processed HDPEs and MA-g-HDPE and the unprocessed PA6 were used as references as regards the rheological behavior.

The development of the different kinds of morphologies in co-rotating twin screw extrusion using tools of different scales and various operating conditions (screw speed, temperature and residence time) was then studied in these PA6/HDPE reactively compatibilized blends over a broad range of compositions. The morphologies were observed by Scanning Electron Microscopy (SEM) after minor phase etching. They exhibited characteristic sizes from the nanometer scale to the micrometer scale. Thus, one of the objectives was to propose a global mechanism to describe the development of these multi-scales morphologies.

Several kinds of morphologies at the micrometer scale were observed as the amount of PA6 increased in the blends:

1) PA6 dispersion in PE continuous phase
2) PA6 stretched dispersion in PE continuous phase
3) Co-continuous
4) PE phase stretched dispersion in PA6 continuous phase
5) PE phase dispersion in PA6 continuous phase

The development of these morphologies during extrusion was accelerated by the presence of the compatibilizer. As the process parameters did not influence the kind of morphologies, the regions corresponding to each type of observed morphology were summarized on ternary diagrams (representing the volume fractions of PA6, HDPE and MA-g-HDPE) for each HDPE, whatever the processing tool used. The viscosity ratios between phases had less influence on the co-continuity range than predicted by the phase inversion model of Paul and Barlow. Thus, the blend composition was the predominant parameter driving the morphology development at the micrometer scale.

As expected, by increasing the volume ratio MA-g-HDPE/HDPE, the morphology became finer (from $10 - 20\mu m$ to $\sim 1\mu m$). On the other hand, it was checked by FTIR that the conversion of MA moieties during the compatibilization was larger than 80%. So, in many of the studied blends that contained a high amount of MA-g-HDPE, a large fraction of the obtained material consist of a graft copolymer which was formed in-situ. The major part of the copolymer was not localized at the interfaces between the micrometric domains.

In the compatibilized blends, a large fraction of the grafted copolymer was located within nano-dispersions of both PE in PA6 and PA6 in PE, which were simultaneously observed in blends by Transmission Electron Microscopy (TEM). These nano-dispersions (of the order of 50nm) were generated by interface instabilities during the reactive processing. As this interfacial roughening ran out the reaction little by little, interfaces relatively poor in copolymer remained present in the system. These interfaces formed larger domains which were subjected to breaking and coalescence equilibrium to form the micrometer scale morphology.

Sub-dispersions were also observed in the non-compatibilized blends. In this case, due to the large interfacial tension, all the domains were subjected to breaking and coalescence mechanisms with a minimum droplet size (of the order of few hundreds nm) which corresponds to the Taylor estimated size.

Both the evolution of the largest size as a function of the composition, and the distribution of sizes in a blend close to co-continuity, were modeled using percolation concepts. By rescaling the experimentally measured sizes by the interfacial tension, the reduced volume of the dispersed phase (V/Γ^3) was plotted as a function of the PA6 volume fraction in a same graph for several blends exhibiting a same rheological behavior (compatibilized and non-compatibilized). The fits performed using percolation theory matched well the experimental data.

Thus, percolation theory was found to be very useful for the description of polymer blends even if they are reactively compatibilized and a large amount of copolymer is formed. In fact, it allows estimating qualitatively interfacial tensions by measuring typical domain sizes. Conversely, it may be also useful to predict the largest size of the dispersed phase depending on the composition.

The stability of the morphologies was then studied using various amount of compatibilizer. In fact, the stability of the morphologies during a second step processing is a key point from the application point of view to insure reproducibility of the properties in a final part. Various conditions were tested including static annealing, controlled shear and second step processing (injection molding and extrusion blow molding). Ternary diagrams of the morphologies were plotted after static annealing and after a second heating and shearing step (whatever the shear experiment, controlled shear or second step processing).

First of all, the stretching was released during the static annealing, indicating that the stretched morphologies are not steady state morphologies. Then, the graft copolymer PA6-g-HDPE formed in situ stabilized the size of the morphology whatever the conditions applied, static or under shear. However, a little coarsening was observed with low amount of compatibilizer. In non-compatibilized blends, coalescence was observed after static annealing. Applying shear limited this coalescence.

The blends studied were all close to boundaries between regions of different morphologies. After a second step heating (and shearing), the morphologies evolved to one or the other morphology. This effect was also observed in other cases during the first step of blending, by changing the extrusion parameters on blends at the boundaries between two regions of different morphologies.

In a last part, as the crystallinity also plays an important role on properties, the influence of the composition and the morphology of the blends on the mechanism of crystallization and the crystallinity amount in both PA6 and PE phases was also studied by Differential Scanning Calorimetry (DSC).

PE phase was found to reduce the overall crystallinity amount of PA6. Fractionated crystallization at lower temperature was observed when PA6 was confined in domains smaller than 2μm typically. In this case, only α crystalline phase was formed. When PA6 was not confined, the PE phase was found to favor the formation of γ crystalline phase, which could lead to a modification of the PA6 phase properties as compared to the PA6 bulk.

On the other hand, PA6 did not influence the overall crystallinity amount of PE phase. As soon as a fraction of the phase was confined in domains smaller than 1μm typically, a distinct crystallization peak at lower temperature was observed, corresponding to confined crystallization. It was checked that this is coherent with the density of nucleating sites estimated. Moreover, the peak associated to the bulk crystallization of PE was splitted into two peaks in stretched PE dispersions within a PA6 continuous matrix. A mechanism of slowing down of the crystallization kinetics in entanglements of PE stretched domains was proposed to explain this split.

To conclude, the relationships between (1) the formulation, the process conditions and (2) the morphology and crystallization of PA6/HDPE reactively compatibilized blends have been established. It will be now of great interest to characterize the targeted properties depending on the morphology in these systems. So, this study can constitute a basis for the design of new polymer blends with given controlled and stabilized morphology according to the desired set of properties.

Bibliography

[1]   UTRACKI L.A., Introduction to polymer blends, In *Polymer blends handbook,* Utracki LA (eds.), Kluwer Academic Publishers, Dordrecht, Boston, London, pp 1-122 **(2003).**

[2]   CASTRO M., CARROT C. and PROCHAZKA F., Experimental and theoretical description of low frequency viscoelastic behaviour in immiscible polymer blends, *Polymer,* **2004**, 45 (12), 4095-4104

[3]   OMONOV T.S., HARRATS C., GROENINCKX G. and MOLDENAERS P., Anisotropy and instability of the co-continuous phase morphology in uncompatibilized and reactively compatibilized polypropylene/polystyrene blends, *Polymer,* **2007**, 48 (18), 5289-5302

[4]   PERNOT H., BAUMERT M., COURT F. and LEIBLER L., Design and properties of co-continuous nanostructured polymers by reactive blending, *Nat. Mater.,* **2002**, 1 (1), 54-58

[5]   BOURRY D. and FAVIS B.D., Cocontinuity and Phase Inversion in HDPE/PS Blends: Influence of Interfacial Modification and Elasticity, *Journal of polymer science part B: polymer physics,* **1998**, 36 (11), 1889-1899

[6]   LYNGAAE-JORGENSEN J. and UTRACKI L.A., Dual phase continuity in polymer blends, *Makromolekulare Chemie, Macromolecular Symposia,* **1991**, 48/49 (1), 189-209

[7]   LYNGAAE-JORGENSEN J. and VALENZA A., Structuring of polymer blends in simple shear flow, *Makromolekulare Chemie, Macromolecular Symposia,* **1990**, 38 43-60

[8]   LYNGAAE-JORGENSEN J. and UTRACKI L.A., Structuring polymer blends with bicontinuous phase morphology. Part II. Tailoring blends with ultralow critical volume fraction, *Polymer,* **2003**, 44 (5), 1661-1669

[9]   WU S., Formation of Dispersed Phase in Incompatible Polymer Blends: Interfacial and Rheological Effects, *Polym. Eng. Sci.,* **1987**, 27 (5), 335-343

[10] HUITRIC J., MEDERIC P., MOAN M. and JARRIN J., Influence of composition and morphology on rheological properties of polyethylene/polyamide blends, *Polymer,* **1998**, 39 (20), 4849-4856

[11] SERPE G., JARRIN J. and DAWANS F., Morphology-Processing Relationships in Polyethylene-Polyamide Blends, *Polym. Eng. Sci.,* **1990**, 30 (9), 553-565

[12]   BOURRY D. and FAVIS B.D., Cocontinuity and phase inversion in HDPE/PS blends: influence of interfacial modification and elasticity, *J. Polym. Sci. , Part B: Polym. Phys.,* **1998**, 36 (11), 1889-1899

[13]   WILLIS J., CALDAS V. and FAVIS B., Processing-morphology relationships of compatibilized polyolefin/polyamide blends, *Journal of Materials Science,* **1991**, 26 (17), 4742-4750

[14]   LYU S.P., JONES T.D., BATES F.S. and MACOSKO C.W., Role of block copolymers on suppression of droplet coalescence, *Macromolecules,* **2002**, 35 (20), 7845-7855

[15]   ZHANG C.L., FENG L.F., ZHAO J., HUANG H., HOPPE S. and HU G.H., Efficiency of graft copolymers at stabilizing co-continuous polymer blends during quiescent annealing, *Polymer,* **2008**, 49 (16), 3462-3469

[16]   MACOSKO C.W., GUÉGAN P. and KHANDPUR A.K., Compatibilizers for melt blending: Premade block copolymers, *Macromolecules,* **1996**, 29 5590-5598

[17]   GALLOWAY J.A., JEON H.K., BELL J.R. and MACOSKO C.W., Block copolymer compatibilization of cocontinuous polymer blends, *Polymer,* **2005**, 46 (1), 183-191

[18]   ZHANG J., COLE P.J., NAGPAL U. and MACOSKO C.W., Direct correlation between adhesion propotion and coupling reaction at immiscible polymer-polymer interfaces, *The journal of adhesion,* **2006**, 82 887-902

[19]   FELLAHI S., FAVIS B.D. and FISA B., Morphological stability in injection-moulded high-density polyethylene/polyamide-6 blends, *Polymer,* **1996**, 37 (13), 2615-2626

[20]   GROENINCKX G., VANNESTE M. and EVERAERT V., Crystallization, morphological structure, and melting of polymer blends, In *Polymer blends handbook,* Utracki LA (eds.), Kluwer Academic, Dordrecht, Boston, London, pp 203-294 **(2002).**

[21]   COLBEAUX A. Compatibilisation de mélanges Polypropylène/Polyéthylène par extrusion réactive. Thèse. Lyon : Institut National des Sciences Appliquées de Lyon, **2001**, 338 p.

[22]   UTRACKI L.A., Thermodynamics of polymer blends, In *Polymer blends handbook,* Utracki LA (eds.), Kluwer Academic Publishers, Dordrecht, Boston, London, pp 123-201 **(2003).**

[23]   UTRACKI L.A., Polymer/polymer miscibility, In *Polymer alloys and blends: Thermodynamics and rheology,* Utracki LA (eds.), Hanser, Munich, Vienne, New York, pp 29-129 **(1989).**

[24] MASNADA E. Mélange de polymères ou polymère-solvant. Thermodynamique et dynamique à l'approche de la trnasition vitreuse. PhD thesis. Lyon : Université Claude Bernard Lyon 1, **2010**, 320 p.

[25] AJJI A., Interphase and compatibilization by addition of a compatibilizer, In *Polymer blends handbook,* Utracki LA (eds.), Kluwer Academic Publishers, Dordrecht, Boston, London, pp 295-338 **(2003).**

[26] GRACE H., Dispersion phenomena in high viscosity immiscible fluid systems and applications of static mixers as dispersion devices in such systems, *Chemical Engineering Communications,* **1982**, 14 225-277

[27] UTRACKI L.A. and SHI G.Z.H., Compounding polymer blends, In *Polymer blends handbook,* Utracki LA (eds.), Kluwer academic publishers, Dordrecht, Boston, London, pp 577-652 **(2002).**

[28] DEYRAIL Y. Evolution de la morphologie sous cisaillement dans les mélanges de polymères non miscibles : cristallisation, solidification et réticulation de la phase dispersée. Thèse. Lyon : Université Claude Bernard, **2003**, 149 p.

[29] FAVIS B.D. and CHALIFOUX J.P., The effect of viscosity ratio on the morphologie of polypropylene/polycarbonate blends durong processing, *Polymer Engineering and Science,* **1987**, 27 (20), 1591-1600

[30] FORTELNY I. and ZIVNY A., Coalescence in molten quiescent polymer blends, *Polymer,* **1995**, 36 (21), 4113-4118

[31] FORTELNY I. and KOVAR J., Theory of coalescence in immiscible polymer blends, *Polymer Composites,* **1988**, 9 (2), 119-124

[32] SONDERGAARD K. and LYNGAAE-JORGENSEN J., Coalescence in an interface-modified polymer blend as studied by light scattering measurements, *Polymer,* **1996**, 37 (3), 509-517

[33] CHESTERS A.K., The modelling of coalescence processes in fluid-liquid dispersions: A review of current understanding, *Chemical Engineering Research and Design. Transaction of the institution of chemical engineers. Part A,* **1991**, 69 (A4), 259-270

[34] ELMENDORP J.J. and VAN DER VEGT A.K., A study on polymer blending microrheology: Part IV. The influence of coalescence on blend morphology origination, *Polym. Eng. Sci.,* **1986**, 26 (19), 1332-1338

[35]   GONZALEZ-NUÑEZ R., DE KEE D. and FAVIS B.D., The influence of coalescence on the morphology of the minor phase in melt-drawn polyamide-6/HDPE blends, *Polymer,* **1996**, 37 (21), 4689-4693

[36]   HUITRIC J., MOAN M., CARREAU P.J. and DUFAURE N., Effect of reactive compatibilization on droplet coalescence in shear flow, *Journal of Non-Newtonian Fluid Mechanics,* **2007**, 145 (2-3), 139-149

[37]   BROWN S.B., Reactive compatibilization of polymer blends, In *Polymer blends handbook,* Utracki LA (eds.), Kluwer Academic Publishers, Dordrecht, Boston, London, pp 339-415 **(2003).**

[38]   SCAFFARO R., MISTRETTA M.C. and LA MANTIA F.P., Compatibilized polyamide 6/polyethylene blend-clay nanocomposites: Effect of the degradation and stabilization of the clay modifier, *Polymer Degradation and Stability,* **2008**, 93 (7), 1267-1274

[39]   VILLE J. Alliages de thermoplastiques immiscibles polyéthylène/polyamide chargés de nanoparticules d'argile : relations structure - morphologie - rhéologie. Thèse. Brest : Université européenne de Bretagne, **2009**, 137 p.

[40]   PERNOT H. Polymères nanostructurés à base de polyéthylène et de polyamide synthétisés par extrusion réactive : Conception et propriétés. Thèse. Paris : Université Pierre et Marie Curie, **2003**, 239 p.

[41]   SEGALMAN R.A., Patterning with block copolymer thin films, *Materials science and engineering,* **2005**, R 48 191-226

[42]   HELFAND E. and TAGAMI Y., *Journal of Polymer and Science,* **1971**, 39 471-

[43]   LEIBLER L., Block copolymers at interfaces, *Physica A,* **1991**, 172 258-268

[44]   UTRACKI L.A., Compatibilization of Polymer Blends, *The Canadian Journal of Chemical Engineering,* **2002**, 80 (6), 1008-1016

[45]   SHULL K.R. and KRAMER E.J., Segregation of block copolymers to interfaces between immiscible homopolymers, *Macromolecules,* **1990**, 23 4780-4787

[46]   LEIBLER L., Emulsifying effects of block copolymers in incompatible polymer blends, *Makromolecular Chemistry, macromolecular symposia,* **1988**, 16 1-17

[47]   GONZALEZ-NUÑEZ R., PADILLA H., DE KEE D. and FAVIS B.D., Barrier properties of polyamide-6/high density polyethylene blends, *Polymer Bulletin,* **2001**, 46 (4), 323-330

[48] LEEWAJANAKUL P., PATTANAOLARN R., ELLIS J.W., NITHITANAKUL M. and GRADY B.P., Use of Zinc-Neutralized Etylene/Methacrylic Acid Copolymer Ionomers as Blend Compatibilizers for Nylon 6 and Low-Density Polyethylene, *Journal of Applied Polymer Science,* **2003**, 89 (3), 620-629

[49] CHEN Z.B., LI T.S., YANG Y.L., ZHANG Y. and LAI S.Q., The Effect of Phase Structure on the Tribological Properties of PA66/HDPE Blends, *Macromolecular Materials and Engineering,* **2004**, 289 (7), 662-671

[50] MILAN M.L. Nanocomposites thermoplastiques/silicates lamellaires : gestion des morphologies par le contrôle des intéractions aux interfaces et des conditions de mise en oeuvre. Thèse. Lyon : Institut National des Sciences Appliquées de Lyon, **2007**, 266 p.

[51] HOLSTI-MIETTINEN R.M., PERTTILÄ K.P., SEPPÄLÄ J.V. and HEINO M.T., Oxygen Barrier Properties of Polypropylene/Polyamide 6 Blends, *Journal of Applied Polymer Science,* **1995**, 58 (9), 1551-1560

[52] ARAUJO J.R., VALLIM M.R., SPINACE M.A.S. and DE PAOLI M.A., Use of postconsumer polyethylene in blends with polyamide 6: effects of the extrusion method and the compatibilizer, *Journal of Applied Polymer Science,* **2008**, 110 (3), 1310-1317

[53] POTENTE H. and MELISCH U., Theoretical and Experimental Investigations of the Melting of Pellets in Co-Rotating Twin-Screw Extruders, *International Polymer Processing,* **1996**, 11 (2), 104-108

[54] GONZALEZ-NUÑEZ R., FAVIS B.D., CARREAU P.J. and LAVALLÉE C., Factors influencing the formation of elongated morphologies in immiscible polymer blends during melt processing, *Polym. Eng. Sci.,* **1993**, 33 (13), 851-859

[55] LEE J.K. and HAN C.D., Evolution of polymer morphology during compounding in a twin-screw extruder, *Polymer,* **2000**, 41 (5), 1799-1815

[56] VOCKE C., ANTTILA U. and SEPPÄLÄ J.V., Compatibilization of Polyethylene/Polyamide 6 Blends with Oxazoline-Functionalized Polyethylene and Styrene Ethylene/Butylene Styrene Copolymer (SEBS), *Journal of Applied Polymer Science,* **1999**, 72 (11), 1443-1450

[57] UTRACKI L.A., DUMOULIN M.M. and TOMA P., Melt Rheology of High Density Polyethylene/Polyamide-6 Blends, *Polym. Eng. Sci.,* **1986**, 26 (1), 34-44

[58] KAMAL M.R., GARMABI H., HOZHABR S. and ARGHYRIS L., The Development of Laminar Morphology During Extrusion of Polymer Blends, *Polymer Engineering and Science,* **1995**, 35 (1), 41-51

[59] RODRIGUEZ-VELOZ O. and KAMAL M.R., The development of laminar morphology in a co-rotating twin screw extruder, *Advances in polymer technology,* **1999**, 18 (2), 89-108

[60] MIN K., WHITE J.L. and FELLERS J.F., Development of Phase Morphology en Incompatible Polymer Blends during Mixing and its Variation in Extrusion, *Polym. Eng. Sci.,* **1984**, 24 (17), 1327-1336

[61] GALLOWAY J.A. and MACOSKO C.W., Comparison of methods for the detection of cocontinuity in polyethylene oxide/polystyrene blends, *Polym. Eng. Sci.,* **2003**, 44 (4), 714-727

[62] KOLARIK J., Simultaneous prediction of the modulus and yield strength of binary polymer blends, *Polym. Eng. Sci.,* **1996**, 36 (20), 2518-2524

[63] DEDECKER K. and GROENINCKX G., Reactive compatibilisation of A/(B/C) polymer blends. Part 2. Analysis of the phase inversion region and the co-continuous phase morphology, *Polymer,* **1998**, 39 (21), 4993-5000

[64] LI J., MA P.L. and FAVIS B.D., The role of the blend interface tye on morphology in cocontinuous polymer blends, *Macromolecules,* **2002**, 35 2005-2016

[65] OMONOV T.S., HARRATS C., MOLDENAERS P. and GROENINCKX G., Phase continuity detection and phase inversion phenomena in immiscible polypropylene/polystyrene blends with different viscosity ratios, *Polymer,* **2007**, 48 (20), 5917-5927

[66] MILES I.S. and ZUREK A., Preparation, structure, and properties of two-phase co-continuous polymer blends, *Polym. Eng. Sci.,* **1988**, 28 (12), 796-805

[67] PAUL D.R. and BARLOW J.W., Polymer blends (or alloys), *Journal of Macromolecular Science: Review macromolecular chemistry,* **1980**, C18 109-168

[68] CASTRO M., CARROT C. and PROCHAZKA F., Morphologie co-continue dans un mélange de polymères incompatibles: POE/PVdF-HFP, *Rheologie,* **2003**, 4 (1), 32-39

[69] HUANG H.X., HUANG Y.F. and YANG S.L., Developing laminar morphology in higher-viscosity-ratio polyblends by controlling flow fields in a single-screw extruder, *Polymer International,* **2005**, 54 (1), 65-69

[70] UTRACKI L.A., Polyolefin Blends, In *Polymer Alloys and Blends: Thermodynamics and Rheology,* Hanser, Munich;Vienna;New York, pp 201-209 **(1989).**

[71] HOLSTI-MIETTINEN R.M., SEPPÄLÄ J.V., IKKALA O.T. and REIMA I.T., Functionalized Elastomeric Compatibilizer in PA 6/PP Blends and Binary Interactions Between Compatibilizer and Polymer, *Polym. Eng. Sci.,* **1994**, 34 (5), 395-404

[72] LAMNAWAR K. and MAAZOUZ A., Rheology and morphology of multilayer reactive polymers: effect of interfacial area in interdiffusion/reaction phenomena, *Rheologica Acta,* **2008**, 47 (4), 383-397

[73] LAMNAWAR K. and MAAZOUZ A., Rheological study of multilayer functionalized polymers: characterization of interdiffusion and reaction at polymer/polymer interface, *Rheologica Acta,* **2006**, 45 (4), 411-424

[74] SUBRAMANIAN P.M. and MEHRA V., Laminar Morphology in Polymer Blends: Structure and Properties, *Polymer Engineering and Science,* **1987**, 27 (9), 663-668

[75] JIANG C., FILIPPI S. and MAGAGNINI P., Reactive compatibilizer precursors for LDPE/PA6 blends. II: maleic anhydride grafted polyethylenes, *Polymer,* **2003**, 44 (8), 2411-2422

[76] SHENG J., MA H., YUAN X.B., YUAN X.Y., SHEN N.X. and BIAN D.C., Relation of Chain Constitution with Phase Structure in Blends: Compatibility of Two Phases in Blends of polyamide with Low-Density Polyethylene and its Ionomers, *Journal of Applied Polymer Science,* **2000**, 76 (4), 488-494

[77] BAOUZ T. and FELLAHI S., Interfacial Modification of High Density Polyethylene/Glass Fiber Reinforced and Non Reinforced Polyamide 66 Blends, *Journal of Applied Polymer Science,* **2005**, 98 (4), 1748-1760

[78] WILLIS J.M. and FAVIS B.D., Processing-Morphology Relationships of Compatibilized polyolefin/Polyamide Blends. Part I: The Effect of an Ionomer Compatibilizer on Blend Morphology, *Polymer Engineering and Science,* **1988**, 28 (21), 1416-1426

[79] MACOSKO C.W., JEON H.K. and HOYE T.R., Reactions at polymer-polymer interfaces for blend compatibilization, *Progress in Polymer Science,* **2005**, 30 (8-9), 939-947

[80] ORR C.A., ADEDEJI A., HIRAO A., BATES F.S. and MACOSKO C.W., Flow-induced reactive self-assembly, *Macromolecules,* **1997**, 30 1243-1246

[81] HUANG Y., LIU Y. and ZHAO C., Morphology and Properties of PET/PA-6/E-44 Blends, *Journal of Applied Polymer Science,* **1998**, 69 (8), 1505-1515

[82] KAMAL M.R., GARMABI H., HOZHABR S. and ARGHYRIS L., The development of laminar morphology during extrusion of polymer blends, *Polym. Eng. Sci.,* **1995**, 35 (1), 41-51

[83] SUBRAMANIAN P.M. and MEHRA V., Laminar morphology in polymer blends: structure and properties, *Polym. Eng. Sci.,* **1987**, 27 (9), 663-668

[84] LYNGAAE-JORGENSEN J. and UTRACKI L.A., Structuring polymer blends with bicontinuous phase morphology. Part II. Tayloring blends with ultralow critical volume fraction, *Polymer,* **2003**, 44 (5), 1661-1669

[85] GUÉRIN B., Polyamides, In *Techniques de l'Ingénieur, traité Matériaux non métalliques,* **(1994).**

[86] XENOPOULOS A. and CLARK E.S., Physical structure, In *Nylon plastics handbook,* Kohan MI (eds.), Carl Hanser Verlag, Munich, Vienna, New York, pp 107-138 **(1995).**

[87] STARKWEATHER H.W., Transitions and relaxations, In *Nylon plastics handbook,* Kohan MI (eds.), Carl Hanser Verlag, Munich, Vienna, New York, pp 139-150 **(1995).**

[88] SABARD M. Etude de films PA6 et nanocomposites. Effet des conditions de procédé et des nanocharges sur la morphologie et les propriétés des sorption à l'eau et à l'éthanol. PhD thesis. Lyon **2011**, 295 p.

[89] DOSSOGNE R., Polyéthylène Haute Densité PE-HD, In *Techniques de l'Ingénieur, traité Matériaux non métalliques,* **(1994).**

[90] SCHNEIDER B. and DOSKOCILOVA D., Structure of Polyolefins, In *Handbook of polyolefins,* Vasile C & Seymour R.B. (eds.), Marcel Dekker, New York, Basel, Hong Kong, pp 117-132 **(1993).**

[91] MILLER R.L., Crystallographic data and melting points for various polymers, In *Polymer handbook,* Brandrup J, Immergut E.H. & Grulke E.A. (eds.), John Wiley & Sons, Inc., New York, Chichester, Weinheim, Brisbane, Singapore, Toronto, pp VI/1-VI/192 **(1999).**

[92] BRANDRUP J., IMMERGUT E.H. and GRULKE E.A., *Polymer handbook,* Brandrup J., Immergut E.H. & Grulke E.A. (eds.), John Wiley & sons, **(1999).**

[93] ELEMANS P.H.M., JANSSEN J.M.H. and MEIJER H.E.H., The measurement of interfacial tension in polymer/polymer systems: The breaking thread method, *Journal of Rheology,* **1990**, 34 (8), 1311-1325

[94] CHAPLEAU N., FAVIS B.D. and CARREAU P.J., Measuring the Interfacial Tension of polymers in the Presence of an interfacial Modifier: Migrating the Modifier to the Interface, *J. Polym. Sci. , Part B: Polym. Phys.,* **1998**, 36 (11), 1947-1958

[95] BOGDANOV B.G. and MICHAILOV M., Structure and properties, In *Handbook of polyolefins,* Vasile C & Seymour R.B. (eds.), Marcel Dekker, New York, Basel, Hong Kong, pp 295-470 **(1993).**

[96] MULLER R., L'apport des modèles d'émulsions en rhéologie des systèmes polyphasés, *Rheologie,* **2007**, 11 1-12

[97] GRAEBLING D., MULLER R. and PALIERNE J.F., Linear viscoelastic behavior of some incompatible polymer blends in the melt. Interpretation of data with a model of emulsion of viscoelastic liquids, *Macromolecules,* **1993**, 26 (2), 320-239

[98] FETTERS L.J., LOHSE D.J., RICHTER D., WITTEN T.A. and ZIRKEL A., Connection between polymer molecular weight, density, chain dimensions, and melt viscoelastic properties, *Macromolecules,* **1994**, 27 (17), 4639-4647

[99] VERGNES B. and CHAPET M., Extrusion: Procédés d'extrusion bivis, In *Techniques de l'ingénieur, traité plastiques et composites,* **(2008).**

[100] MICHLER G.H., *Electron microscopy of polymers,* Pash H. (eds.), Springer laboratory manuals in polymer science, Berlin, pp 473 **(2008).**

[101] MINKOVA L., YORDANOV H., FILIPPI S. and GRIZZUTI N., Interfacial tension of compatibilized blends of LDPE and PA6: the breaking thread method, *Polymer,* **2003**, 44 (26), 7925-7932

[102] UTRACKI L.A., Interphase, diffusion and compatibility, In *Polymer alloys and blends : thermodynamics and rheology,* Hanser Publishers, Munich,Vienna,New York, pp 117-129 **(1989).**

[103] MACHADO A.V., COVAS J.A. and VAN DUIN M., Chemical and morphological evolution of PA6/Epm/Epm-g-MA blends in a twin screw extruder, *Journal of Polymer Science: Part A: Polymer chemistry,* **1999**, 37 (9), 1311-1320

[104] PINHEIRO L.A., BITTENCOURT C.S. and CANEVAROLO S.V., Real time assessment of the compatibilization of polypropylene/polyamide 6 blends during extrusion, *Polym. Eng. Sci.,* **2010**, 50 (4), 826-834

[105] SCOTT C. and MACOSKO C., Model Experiments for the Interfacial Reaction Between polymers During Reactive Polymer Blending, *J. Polym. Sci. , Part B: Polym. Phys.,* **1994**, 32 (2), 205-213

[106] YQUEL V., MACHADO A.V., COVAS J.A. and FLAT J.J., Contribution of the melting stage to the evolution of the morphology and chemical conversion of immiscible polyamide/polyethylene blends in twin-screw extruders, *Journal of Applied Polymer Science,* **2009**, 114 (3), 1768-1776

[107] LYU S.P., CERNOHOUS J.J., BATES F.S. and MACOSKO C., Interfacial reaction induced roughening in polymer blends, *Macromolecules,* **1999**, 32 (1), 106-110

[108] JIAO J., KRAMER E.J., DE VOS S., M÷LLER M. and KONING C., Polymer interface instability caused by a grafting reaction, *Polymer,* **1999**, 40 (12), 3585-3588

[109] JEON H.K., MACOSKO C.W., MOON B., HOYE T.R. and YIN Z., Coupling reactions of end- vs mid-functional polymers, *Macromolecules,* **2011**, 37 2563-2571

[110] JEON H.K., FEIST B.J., KOH S.B., CHANG K., MACOSKO C.W. and DION R.P., Reactively formed block and graft copolymers as compatibilizers for polyamide 66/PS blends, *Polymer,* **2004**, 45 (1), 197-206

[111] JONES T.D., SCHULZE J., MACOSKO C.W. and LODGE T.P., Effect of thermodynamic interactions on reactions at polymer/polymer interfaces, *Macromolecules,* **2003**, 36 7212-7219

[112] BHADANE P.A., TSOU A.H., CHENG J. and FAVIS B.D., Morphology developement and interfacial erosion in reactive polymer blending, *Macromolecules,* **2008**, 41 7549-7559

[113] SUNDARARAJ U. and MACOSKO C.W., Evidence for inversion of phase continuity during morphology development in polymer blending, *Polym. Eng. Sci.,* **1996**, 36 (13), 1769-1781

[114] STAUFFER D. and AHARONY A., *Introduction to percolation theory,* Stauffer D. & Aharony A. (eds.), Taylor and Francis Inc., London, **(1994).**

[115] SOTTA P. and LONG D., The crossover from 2D to 3D percolation: Theory and numerical simulations, *European Physical Journal E,* **2003**, 11 375-388

[116] MAUS A., HEMPEL E., THURN-ALBRECHT T. and SAALWÄCHTER K., Memory effect in isothermal crystallization of syndiotactic polypropylene - Role of melt structure and dynamic?, *European Physical Journal E,* **2007**, 23 91-101

[117] HERTLEIN C., SAALWÄCHTER K. and STROBL G., Low-field NMR studies of polymer crystallization kinetics: Changes in the melt dynamics, *Polymer,* **2006**, 47 7216-7221

[118] CHATREENUWAT B., NITHITANAKUL M. and GRADY B.P., The effect of zinc oxide addition on the compatibilization efficiency of maleic anhydride grafted high-density polyethylene compatibilizer for high-density polyethylene/polyamide 6 blends, *Journal of Applied Polymer Science,* **2007**, 103 (6), 3871-3881

[119] YEH J.T., CHANG S.S., YAO H.T., CHEN K.N. and JOU W.S., The permeation resistance of polyethylene/polyamide and polyethylene/modified polyamide blown tubes against unleaded gasoline, *Journal of Materials Science,* **2000**, 35 1321-1330

[120] CAMPOY I., GOMEZ M.A. and MARCO C., Structure and thermal properties of blends of nylon 6 and a liquid crystal copolyester, *Polymer,* **1998**, 39 (25), 6279-6288

[121] PSARSKI M., PRACELLA M. and GALESKI A., Crystal phase and crystallinity of polyamide 6/functionalized polyolefin blends, *Polymer,* **2000**, 41 (13), 4923-4932

[122] TOL R.T., MATHOT V.B.F. and GROENINCKX G., Confined crystallization phenomena in immiscible polymer blends with dispersed micro - and nanometer sized PA6 droplets, part 1: uncompatibilized PS/PA6, (PPE/PS)/PA6 and PPE/PA6 blends, *Polymer,* **2005**, 46 369-382

[123] WANG Y., JI D., YANG C., ZHANG H., QIN C. and HUANG B., Structure and properties of maleated High Density Polyethylene, *Journal of Applied Polymer Science,* **1994**, 52 1411-1417

[124] CECCIA S., ARGOUD A., HYNSTOVA K., JANCAR J., TROUILLET-FONTI L., LONG D. and SOTTA P., Crystallization kinetics of PE in compatibilized HDPE/PA6 blends, *Forthcoming paper,* **2011**,

Appendix A

<u>Size Exclusion Chromatography (SEC)</u>

Molar mass distribution of studied materials was determined by Size Exclusion Chromatography (SEC). The principle of separation of different macromolecules is based on the size of these macromolecules in solution in term of hydrodynamic volume. The gel stationary phase in the column contains pores which will retain molecules depending on their hydrodynamic volume. Thus, macromolecules exhibiting the largest hydrodynamic volume will elute first, followed by the smallest ones.

In the case of Polyethylene, High Temperature Size Exclusion Chromatography was needed. PE was solubilized in Trichlorobenzene (TCB) at 150°C (about 1mg/ml) during 2h. After stirring, samples were filtered at 1μm and then injected in the column. The equipment used was a chromatograph *Waters GPCV2000* at 150°C with refractometer and viscosimeter as detectors. The combination of both detectors allowed performing universal calibration and so obtaining exact average molar masses. Analyses were performed by Olivier Boyron in an external laboratory: "Laboratoire de Chimie, Catalyse, Polymères et Procédés" in CPE Lyon.

Concerning Polyamide, Size Exclusion Chromatography was performed with a *GPC PL120* at room temperature. A refractometer and a viscosimeter were used as detectors when absolute masses were needed. Otherwise, a UV detector (*UV2000 Spectra physique*) was used to obtain masses in Polystyrene (PS) equivalents. The samples were filtered at 0.2μm. Analyses were performed by Nadia Delon-Anik and Sabrina Paillet in Rhodia Research Center in Lyon (CRTL).

Number average molar mass M_n and weight average molar mass M_w were obtained:

$$M_n = \frac{\sum_i N_i M_i}{\sum_i N_i}$$

$$M_w = \frac{\sum_i N_i M_i^2}{\sum_i N_i M_i}$$

With N_i the number of macromolecules of mass M_i. M_n is more sensitive to molecules of low molecular mass, while M_w is more sensitive to molecules of high molecular mass. The Polydispersity Index (IP) is a measure of the distribution of molecular masses in the polymer and is defined as:

$$IP = \frac{M_w}{M_n}$$